On the Properties of Cirrus clouds over the Tropical West Pacific

By
Cristian Mitrescu and Graeme L. Stephens

Department of Atmospheric Science
Colorado State University
Fort Collins, Colorado

Research supported by DOE grant DE-FG03-94ER61748, and DE-FG03-98ER62569.
PI: G. Stephens

Colorado State University

Department of Atmospheric Science

Paper No. 737

ON THE PROPERTIES OF CIRRUS CLOUDS OVER THE TROPICAL WEST PACIFIC

CRISTIAN MITRESCU AND GRAEME L. STEPHENS

Research supported by Department of Energy,
Contracts # DE-FG03-94ER61748 and # DE-FG03-98ER62569

Principal Investigator: Graeme L. Stephens

Department of Atmospheric Science
Colorado State University
Fort Collins, CO

June, 2002

Atmospheric Science Paper No. 737

This page intentionally blank.

ABSTRACT

ON THE PROPERTIES OF CIRRUS CLOUDS OVER THE TROPICAL WEST PACIFIC

Understanding Earth's climate is a complex undertaking, and requires the development of accurate simulations that combine all the natural elements that can affect climate. The data that goes into these models needs to be as precise as possible, and collecting reliable data is an important and sometimes difficult step in this research. Clouds, in particular tropical thin cirrus clouds, exert a major influence on climate through cloud radiative forcing (CRF). These clouds, with their variable height, optical depth and particle distribution, make collecting accurate data difficult. Investigation by remote sensing techniques, in particular by LIDARs alone or in combination with other instruments, has become a popular way of retrieving cirrus cloud physical and microphysical properties such as particle concentration (N), characteristic diameter (D), ice water content (IWC) and ice water path (IWP).

The aim of this study is to document the properties of tropical thin cirrus using combinations of data collected from various remote sensing systems. A new method for determining cloud optical depths along with a new parameterization that treats multiple scattering effects in the LIDAR equation is introduced. A novel "inverse" model applied to lidar measurements produces profiles for IWC and N. A new, simple analytical method developed for the combination of RADAR and LIDAR system is also presented. This combination of data provides vertical profiles for D, N, and IWC. One key finding derived from the measured data is the observed relationship between optical depth and IWP. Two different methods that combine active and passive techniques are explored. The first is the LIRAD technique, which combines LIDAR and IR radiometric data. A new approach towards the LIRAD

method is introduced and from this approach we are able to identify three distinct cloud backscatter regimes correlated with the mid-cloud temperature. Second, the combination between the NASA Cloud Physics Lidar and MODIS Airborne Sensor data is examined. A new method, developed to analyze MODIS data, alleviates the complex problem of asymmetric scattering induced by ice crystals through the use of *similarity* and *scaling*. What is new is the way the ambiguities in defining key scaling parameters are overcome.

There are a number of limitations that have to be applied to the results of this study. First, the new lidar analysis tools developed are only applicable to thin cirrus clouds through which the lidar can penetrate. This corresponds to optical depth of approximately 1.5 and IWP of 27 g/m^2, assuming a 30 μm effective radius particle. Second, the cloud physical information derived from lidar alone, is subject to the imposed assumption of particle size. This assumption is relaxed in the radar-lidar method which is used to determine the credibility of the value of particle size used.

The results obtained using these new analyses tools are used to study the radiative budget of tropical thin cirrus. It is shown that thin cirrus radiatively heat the atmosphere both within the layer of cloudiness as well as within the atmosphere below. A convenient parameterization of the LW and SW CRF as a function of the IWP is tested against measured data.

Cristian Mitrescu
Atmospheric Science Department
Colorado State University
Fort Collins, CO 80523
Summer 2002

ACKNOWLEDGEMENTS

We would like to acknowledge the following people who, in various ways, helped in pursuing this research. They are : Drs. Philip Gabriel and Richard Austin for their unlimited help in solving the difficult task of getting a PhD degree; Mr. Ian Wittmeyer for his indispensable assistance in resolving various computer related problems; Professors David Randall, William Cotton and David Krueger for their time and advice in completing this dissertation; Mr. William Hart and Mr. Dennis Hlavka from NASA Goddard Space Flight Center for providing much needed data.

Data were obtained from the Atmospheric Radiation Measurement (ARM) Program sponsored by the U.S. Department of Energy, Office of Science, Office of Biological and Environmental Research, Environmental Sciences Division, as part of the Atmospheric Radiation Measurement (ARM) Program.

This page intentionally blank.

Contents

List of Figures

List of Tables

This page intentionally blank.

Chapter 1

Introduction

1.1 Introduction

Atmospheric science is the field of science that studies the structure and dynamics of the Earth's atmosphere. Of particular interest here are: (1) meteorology that focuses on study the day-to-day, hour-to-hour changes in the weather within troposphere and lower stratosphere and (2) climatology that concentrates on the statistical description of the weather.

A main goal of atmospheric science is to understand how all the components involved in the climate system, interacting in a complex and non-linear way determine the evolution of the system.

We know that climate has undergone many changes in the past and that tendency will continue in the future. In order to understand the mechanisms and the physical processes responsible for the climate, first it is necessary to identify the characteristic features of the structure and behavior of the climate. The climate system is modulated by both external and internal factors. The external factors may be identified as i) general factors such as solar radiation, Earth's sphericity, revolution around the sun and its rotation, the existence of sea and land; and ii) regional and local factors such as topography, distance to sea, vegetation cover, etc. Internal factors deal with the intrinsic properties of the atmosphere, such as the composition of the atmosphere, various instabilities, and the general circulation. This built-in variability of the climate results from the varying time lag between any single cause and effect, from the interaction of multiple factors, and from mechanisms set in motion by one or more variables operating over different time scales. Climate is never stable, instead it is subject to continuing oscillations with various

periods. For these reasons it is necessary to define climatic variations of different periods and amplitudes and to decide which qualify as short- or long-term fluctuations and which are part of the built-in, year-to-year or longer variability and thus deserving of the rank of oscillations.

1.2 Clouds: An active element in the Climate System

The major energy sources and sinks for Earth are the solar radiation and the terrestrial radiation, respectively. Incoming solar radiation is partially absorbed, scattered, and reflected by the various gases, aerosols, and clouds. What is left is partially reflected back into the atmosphere by the Earth's surface where most of it is absorbed. In order for this system to be in a quasi-state of equilibrium, the amount of absorbed energy must be very closely balanced by the amount of energy that is lost to space. Most of the incoming solar energy of interest ranges in wavelenghts from 0.1 to 2.0 μm, while most of the outgoing terrestrial radiation ranges from 4.0 to 60 μm. This gives the rationale of breaking down of the energy spectra in two distinct types: the solar radiation, or short wave (SW) and the terrestrial radiation, or long wave (LW). A schematic diagram of the sources and sinks of radiation in the atmosphere is presented in Figure 1.1.

As part of the energy and hydrological cycle, clouds play an important, active role in the climate system. Clouds are associated with the release of latent heat, and with small-scale convective motions that are responsible for the major vertical redistributions of sensible heat, moisture and momentum. These processes are more complex due to the fact that clouds interact with radiation in a very different way, depending on their location, height, thickness, and microphysical properties such as particle size, shape and chemical composition. The atmosphere controls the radiative energy exchanges between earth and space, by determining the spatial and temporal distributions of clouds and water vapor, and in so doing creates a feedback effect.

In addition to the latent heat processes, clouds, due to their complex radiative characteristics, affect the Earth's energy budget by interacting with both visible and infrared radiation. In the visible, a cloudy region, due to the clouds high albedo,

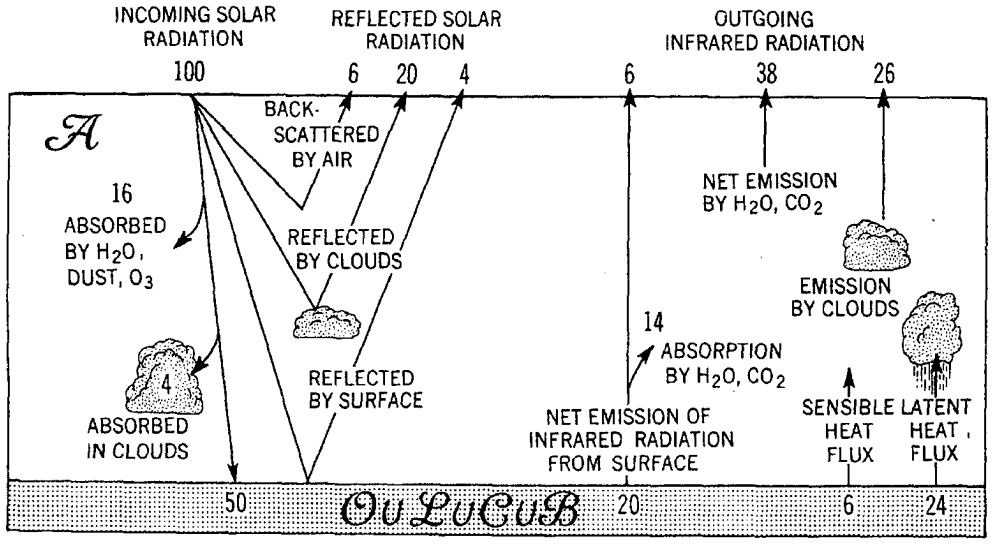

Figure 1.1: Schematic diagram of the global radiation budget in the climatic system. (From Peixoto and Oort, 1995)

reflects more radiation than a clear sky region. This process leads to a cooling effect for the Earth's surface. In the infrared region, however, the opposite effect occurs: due to their composition, clouds absorb more upwelling radiation than a "clear" atmosphere and consequently re-emit part of this radiation to space at values corresponding to their lower than surface temperatures, thus having a warming effect on the surface and atmosphere below. It is understandable that depending on their characteristics, different clouds will have different effects: thin, high-level clouds will influence more the infrared portion of the spectra leading to a warming effect, while thick, lower latitudes low level clouds will dominate the energetics of the visible spectra, inducing a cooling effect on the surface. To summarize, it is the change in net cloud radiative forcing, associated with a change in climate, that governs the cloud feedback.

Radiation, latent heating, and small-scale transport are of equal importance in the cloud-climate problem due to their strong interaction processes amongst each other, in the larger context of the large-scale circulation.

1.3 Efforts in Understanding the Climate System

As stated above, one of the most important problems in atmospheric science today is predicting the rate and spatial distribution of future climate changes caused by anthropogenic effects. In order to accomplish these goals, we accept that the processes occurring in the climate system obey the laws of physics, which can be expressed in terms of mathematical equations (with the level of approximation that is consistent with the state of our knowledge about them). We must keep in mind that climatology is also an observational science and its growth depends on the improvement of the measurements and observing systems, both in a quantitative and qualitative way.

The following paragraphs summarize our current level of understanding of the climate system in the area of modeling and measuring.

1.3.1 Understanding the Cloud-Climate Feedback

Presently, General Circulation Models (GCMs) are the most comprehensive tools for studying Earth's climate system. A GCM includes among other effects the interactions between cloud radiative and convective processes and their effects on large scale dynamics, and also includes the capability for clouds to transport chemical species.

Depending on the scale of focus, two different types of cloud models are required in order to increase confidence in cloud/climate feedback predictions (see Figure 1.2):

- Cloud Resolving Models (CRMs) that simulate all processes involved in the lifetime of a cloud [Khairoutdinov and Randall (2001)]. Part of the CRMs, the Radiative Transfer (RT) models determine the effects of a given distribution of cloud ice and liquid water on radiative heating/cooling rates;

- GCMs that portray the collective effects of an ensemble of such clouds on the large-scale energy balance and general circulation.

In order to assess their capability for describing the Earth's climate system, GCMs must be compared with observational data on various scales. Unfortunately,

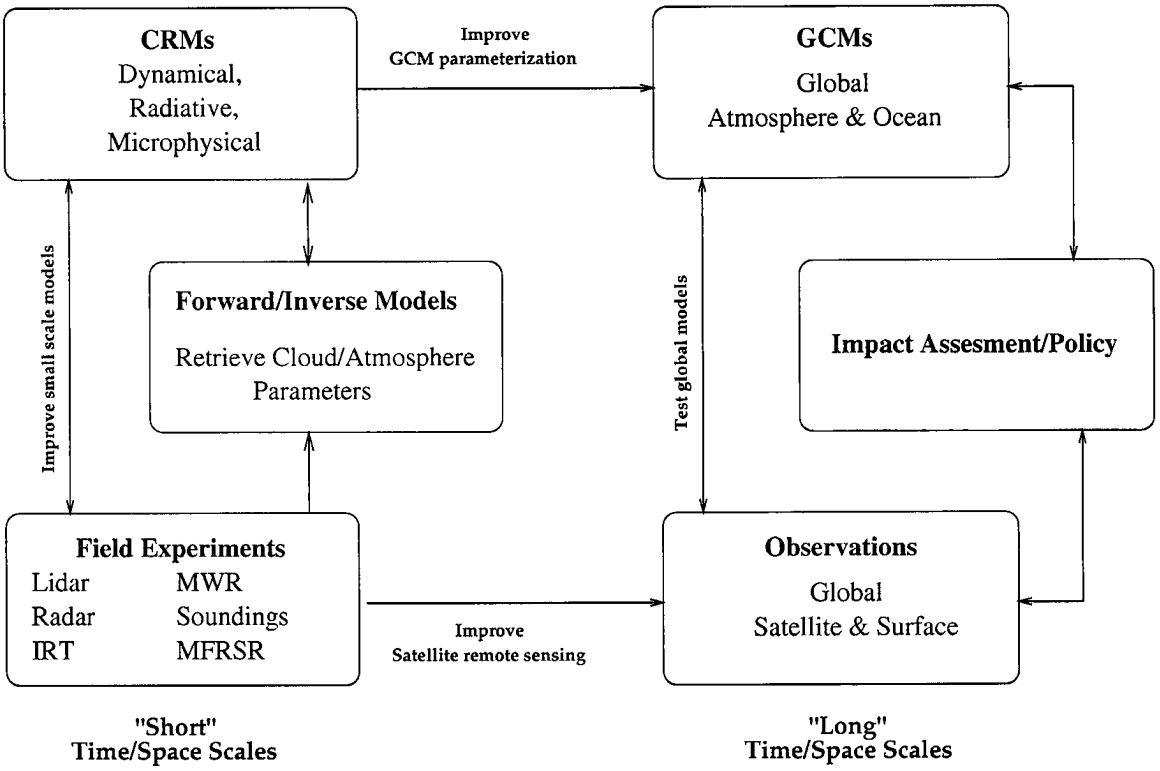

Figure 1.2: Observational strategy for the determination of the role of clouds and radiation in climate (After Wielicki et al., 1995)

the predictions for various variables that are important in describing climate changes varies widely among various GCMs. For example, (1) equilibrium warmings range from 1.7 to 5.3° C, and the rate and spatial distribution depend on the type of climate forcing and type of ocean representation assumed [DelGenio (1996)]); (2) many of the GCM's are unable even to reproduce the intra-seasonal variations observed in ERBE data [Cess et al. (1990)]; (3) among various GCM's the predicted column of precipitable water varied from 17 to 27 mm [Randall et al. (1992)].

Clouds play a major role in the Earth's energy budget. Their cooling effect due to reflection of solar radiation amounts to about 50 Wm^{-2}, while their warming effect, caused by the absorption and emission of terrestrial radiation, is about 30 Wm^{-2} in a global annual average [Hartmann (1994)]. Both effects have large variations in time and space and are furthermore strongly sensitive to cloud height, with lower

latitude low clouds typically exhibiting strong net cooling, while high clouds may have a net warming effect. The radiative properties of clouds are a central issue in studies of the climate change, but the magnitude and even the sign of cloud feedback to greenhouse warming is not agreed upon [Cess et al. (1996)].

Radiative effects of clouds can be explored using RT models. A major question addressed with these models is whether or not the small-scale variability can be accounted for in a larger-scale model. This may be accomplished by either finding a better parameterization for sub-scale processes or by identifying an "inhomogeneity parameter" that is invariant under scaling and also is applicable to various types of clouds.

1.3.2 The Climatic Importance of Thin Cirrus Clouds

Particular attention has been drawn to the importance of high cirrus clouds, especially in tropical regions, where they cover large areas. Thin high cirrus clouds (with optical depths less than 3), are believed to cause a significant warming of the equilibrium climate, particularly in the tropics [Stephens and Greenwald (1991)]. These clouds are the coldest class of tropospheric clouds and lay above the world's warmest waters. They have the potential to cause the greatest warming to the climate through cloud-radiation interaction processes [Ramaswamy and Ramanathan (1989)]. The importance of these cirrus clouds has been highlighted through their possible control of sea surface temperature in the Tropical West Pacific [Ramanathan and Collins (1991)], while the temperature and stability of the atmosphere will certainly be affected [Arkin and Ziskin (1994)]. They also induce vertical circulations due to differential heating (heating at the base and cooling at the top [Lilly (1988)]) and can influence the water vapor concentrations in the upper troposphere and lower stratosphere [Danielsen (1982)].

Observations of crystal shapes and sizes in such clouds, although scarce, are now leading to a better characterization of cloud crystals shapes and sizes, while the application of theoretical advances in remote sensing can be expected to lead to methods of retrieving reliable information with more global coverage.

To obtain accurate estimates of ice crystal radiative properties, variations in particle size, shape, and number concentration need to be considered. In a study by Kristjansson et al. (2000), the radiative effects of clouds were estimated using two GCMs (CCM3 and UKMO). The authors' conclusion was that there is a large sensitivity to both sizes and shapes, particularly in the tropics (see Figure 1.3). Smaller sizes lead to enhanced SW and LW cloud forcings, where the former effect tends to dominate. For a given IWP, size, and thus number concentration, non-spherical crystals are significantly brighter in the SW and more absorbing in the LW than spherical crystals, but the relative change in SW and LW is shape dependent. Observations also suggest that particle size is grossly dependent on temperature: colder temperatures lead to smaller crystals in the upper troposphere, particularly in the tropics, and larger crystals when warmer. As a result, there is significant radiative warming effect in the upper tropical troposphere and at high latitudes. The LW effect dominates this change in radiative heating/cooling.

These results suggest that climate models need to pay more attention to the radiative and microphysical properties of ice crystals than considered to this point, and in order to evaluate these radiative properties, intense efforts must be directed to gather relevant cloud properties. This has been and is still pursued by means of field campaigns.

1.3.3 Measuring Thin Cirrus Cloud Properties

To test our understanding of the life-cycle of large-scale thin cirrus, we must rely on observations and experiments to test hypothesies, and develop or modify various theories relating to the evolution of clouds. From such efforts, it is possible to infer the mechanisms responsible for various processes, such as transports of energy, water vapor or angular momentum. Through diagnostic and prognostic equations, combined with measurements of various state variables and other variables, we are able to describe not only the processes that are responsible for the climate system, but also provide some idea about the magnitude and occurrence of some external constraints and forcings.

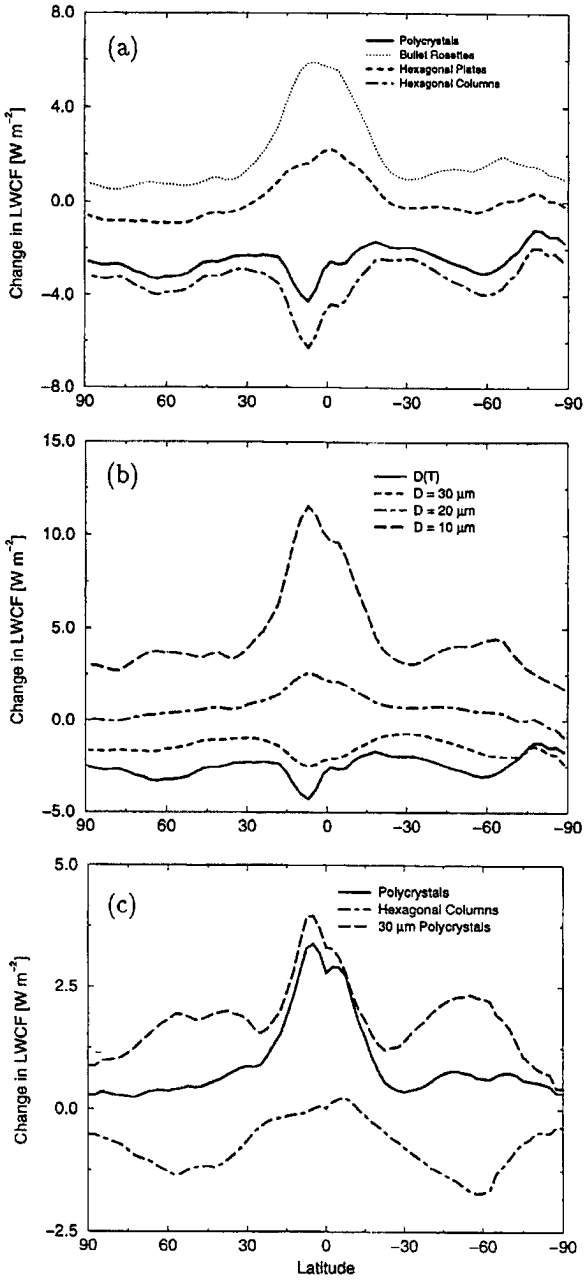

Figure 1.3: Change in the zonal mean LW cloud forcing due to a new ice optics scheme. (a) Effects of crystal shape and (b) of crystal size in CCM3. (c) Effect of shape and size in UKMO. (From Kristjansson et al., 2000)

On the average, 55 to 60 percent of the Earth's surface is covered by clouds [Matveev (1984), Rossow and Schiffer (1991)], the preponderance of which is due to middle and high clouds. Among these clouds, it is now understood that cirrus clouds play a significant role in the climate system. It follows that the measurement and inference of the optical and microphysical properties of these clouds together with knowledge about their environment and life-cycle is of fundamental importance.

From its first launch in the early 1960s, when cloud pictures where essentially the only available product, now, a multitude of meteorological satellites travel in various orbits and carry a wide variety of sensors. With advancing technology, new instruments (especially active sensors such as lidars and radars) can be carried by satellites. Their proven ability to penetrate and profile atmospheric constituents, will add new dimensions to our observations on a global scale. These satellite platforms will collect data to continue old programs like Tropical Ocean Global Atmosphere (TOGA) or International Satellite Cloud Climatology Project (ISCCP), or contribute to new ones like the Tropical Rainfall Measuring Mission (TRMM) or the CloudSat.

Since the location of cirrus clouds is at altitudes that make most of the traditional sounding procedures very difficult to perform, remote sensing techniques become an attractive alternative. In particular, high altitude thin cirrus represent a challenge for observers since they are quite inaccessible, and when they are, the ice crystals they are composed of are often too small or irregular in shape to be properly counted and sized. In fact these clouds are characterized by non-homogeneity throughout their radiative and microphysical properties, adding up to the complexity of any model describing them.

Radiative characteristics of these clouds can be measured by both active and passive sensors. By combining measurements from these instruments in a variety of spectral bands, it is possible to infer key optical and microphysical properties. However, these techniques are limited numerically by the vertical resolution of the profiles or by the spectral band resolution, and often by the estimation/retrieval methods themselves.

1.4 Purpose of this Research

From the *big picture* (see Figure 1.2), we see that the use of new instruments (lidars, radars) adds a new dimension to our ability to infer more detailed information about the structure and properties of the atmosphere, especially clouds. Remote sensors measure radiation; therefore a physical model of the interaction in a cloudy atmosphere is needed to retrieve cloud properties. The radiation processes involved determine the type of radiative transfer model used. With the advent of active sensors, that use either coherent or incoherent radiation which can be easily separated from natural sources of radiation, the properties of the medium are more easily identified. This is the case with lidars and radars. Along with the active sensors, passive sensors, by using natural emitted or scattered radiation, can add information about the radiative properties of the atmosphere, thus proving to be a useful tool in investigating our climate system.

The present research will focus on the properties of cirrus clouds over the TWP, with a particular interest in developing tools for extracting these properties from remote sensing instruments, with a special attention dedicated to the lidar system. However, this is not an easy job, given both the variability in the cirrus cloud properties and limitations of the instrument itself.

The central aim of this research is:

> *to document the properties of thin cirrus clouds and examine the relationship between cloud microphysical and radiative properties.*

The approach adopted to meet this goal centers on the analysis of lidar measurements of cirrus. Key aspects involving calibration, noise level, multiple scattering (MS) effects, and other factors will be addressed in this analysis. Finally, the mathematical description of all these physical processes, linking together measured quantities with key cloud properties, makes possible the inference of the latter. Of course, it is desirable that such a mathematical description be as simple as possible, and provide a unique set of cloud properties for a given set of measurements. Combinations of several instruments measuring the same scene in different spectral

ranges, can increase both the quantity and quality of these cloud properties. Increased quality cloud properties can then be used into atmospheric models helping to understand the role that clouds have on our climate.

It is the purpose of this thesis, that by using a mathematical description of the detailed physical processes involved in the interaction of the radiative field with clouds, to develop a model for deriving key optical and microphysical cirrus cloud parameters for the lidar observing system alone or in conjunction with other active or passive sensing systems. Aside from providing a useful tool for interpreting remote sensing measurements, this research addresses the question regarding the role and influence of clouds in the climate system by identifying key relationships between retrieved cloud characteristics and atmospheric parameters. It is our hope that the retrieved cloud characteristics along with parameterizations will be used in both CRMs and GCMs to evaluate the complex interactions represented in these models and hopefully in the real climate system.

1.5 Thesis Outline and Key Results

A description of the instruments and data sources is reviewed in Chapter 2. Data from passive and active remote sensing instruments along with more traditional sensors are used. Analyses of the lidar system is presented in Chapter 3. A new method for lidar calibration and cloud detection is introduced, and cloud transmittance and optical depth are derived. A new model describing lidar MS effects is proposed and tested against both synthetic and measured data. Unlike published results, the MS model introduced in Chapter 3, not only provides an analytical expression for the MS effects, but also makes the distinction between the MS effects on the backscatter signal and those on the cloud transmittance. This new analytical "forward" model is used in the "inverse" model to determine the vertical profile for the extinction coefficient and ice water content given assumptions about the particle size.

A new algorithm that uses a combination of radar and lidar is presented in Chpter 4. Unlike the lidar alone algorithm, this new alogorithm provides profiles of characteristic diameter and particle concentration. The algorithm is applied to

three months of data collected in the Tropical West Pacific. A key result of this research is the relationship between optical depth and IWP.

The combination of lidar, an active instrument, with passive instruments is examined in Chapter 5 as an alternative for investigating atmospheric properties. A new approach to the LIRAD method of Platt (1979) is introduced. A second active-passive method is examined when lidar data are combined with MAS radiances.

The culmination of the research described in the previous chapters is presented in Chapter 6. An important result of this work demonstrates how thin cirrus radiatively heat the atmosphere both within the layer of cloudiness as well as the atmosphere below. A convenient parameterization of the longwave and the shortwave cloud radiative forcing as function of the ice water path is also presented.

Summary and conclusions as well as some suggestions for future research are addressed in Chapter 7.

Chapter 2

Observation System for Cirrus Clouds

2.1 Introduction

There are two main categories of atmospheric observations: (1) *in situ* observations, and (2) remote sensing observations. The first category refers to the more conventional type of measurements, including pressure, temperature, wind speed and direction, specific humidity, cloud and aerosol microphysics and chemical properties. The second category of data include the passive/active remote sensing techniques applied to sensors on the ground, aircrafts and on satellite. These remote sensing methods take advantage of the spectral-dependence of absorption/emission and vertical distribution of the atmospheric constituents. For example, use of the solar spectral band relies on particle scattering properties to selectively reflect incoming radiation, yielding insightful information about particle size and optical depth in the case of clouds. On the other hand, infrared measurements rely mostly on the ability of particles to absorb and re-emit radiation, providing useful information about the particle temperature, emission coefficient, or other parameters.

Remote sensing constitutes an important part of the strategy employed in any field campaign measurement. Use of millimeter-wave radars from both aircraft and ground gives insightful information about the spatial and temporal structure of ice water. Doppler radars (centimeter wavelength) enable quantification of convective mass and water fluxes transported from the lower atmosphere into cirrus layers. Three-dimensional profiles of the wind velocity can be obtained by wind-profiling radars. Lidar observations can give information about cloud heights and cloud tops, and characterize the spatial/temporal variability of cloud layers and, in a limited way, their radiative properties.

The purpose of this chapter is to describe the data sources used in this research. This data is primarily obtained from surface measurements as part of the US Department of Energy Atmospheric Radiation Measurement Program.

2.2 The Atmospheric Radiation Measurement (ARM) Program

In 1989 the US Department of Energy set up the Atmospheric Radiation Measurement Program (ARM) to improve the parameterization of clouds and radiation used in climate models. The program's goals (http://www.arm.gov) are to:

- *Relate observed radiative fluxes and radiances in the atmosphere, spectrally resolved and as a function of position and time, to the temperature and composition of the atmosphere, specifically including water vapor and clouds, and to the surface properties, and to sample sufficient variety of situations so as to span a wide range of climatologically relevant possibilities;*

- *Develop and test parameterizations that can be used to accurately predict the radiative properties and to model the radiative interactions involving water vapor and clouds within the atmosphere, with the objective of incorporating these parameterization into General Circulations Models (GCMs).*

To achieve these goals, the researcher must work with both theoretical models and actual measurements. On the one hand, measurements are needed to verify the accuracy of the models; on the other, the models allow for an understanding of the data obtained from measurements. The ARM Program primarily uses remote sensing (satellite and/or ground-based) and surface observations to take measurements of radiation as well as optical, dynamical and thermodynamical properties of the atmosphere throughout its vertical extent. Measurements are currently being taken at multiple sites:

- Southern Great Plains (SGP),

- Tropical Western Pacific (TWP) — including Darwin, Nauru and Manus,

- North Slope of Alaska (NSA).

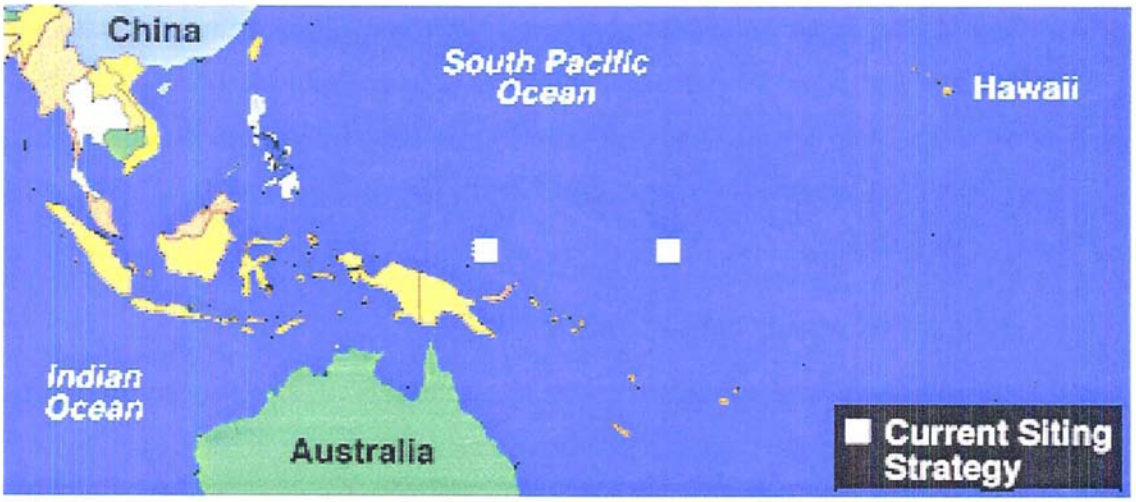

Figure 2.1: ARM TWP: Siting Strategy.

The sites located within the TWP feature the warmest ocean waters, highest atmospheric water vapor content, most active convective cloud regimes in the world, and strong coupling between the atmosphere and ocean. It is roughly bounded by 10°N and 10°S and 120°E and 150°W (see Figure 2.1).

In 1996, the ARM Program implemented its first site in the TWP locale in Manus Province, Papua New Guinea (PNG). It was chosen because of its location within the heart of the Pacific warm pool, the existence of a NOAA Integrated Sounding System, and the support of the PNG National Weather Service (NWS). The site is located at the NWS station at the Momote airport on Los Negros Island at 2.058°S, 147.425°E. The second ARM site in the TWP region is on Nauru Island, which is located in the western South Pacific approximately 1,200 miles northeast of Papua, New Guinea at 0.521°S, 166.916°E. ARM chose this site because of its location on the eastern edge of the warm pool under La Niña conditions. As a curiosity, Nauru is the world's smallest republic with more than 10,000 people living on the island, which is 8.2 square miles in size. From June 16 through July 15, 1999, an international research collaboration called **Nauru99** was conducted on and around the island of Nauru, and we mainly use the data collected during this period. A third site has now recently been implemented at Darwin, Australia.

The ARM Program is also concerned with instrumentation necessary for measurements and uses the Instrument Development Program (IDP) to upgrade existing research instrumentation required by routine operations and to develop new instruments. Currently, retrieval procedures obtain required data by the following instruments:

- Balloon-Borne Sounding System (BBSS)

  It provides on site measurements (vertical profiles) of both the thermodynamic and the dynamic state of the atmosphere:

  - Pressure (hPa)
  - Temperature (degC)
  - Relative Humidity (percents)
  - Wind speed (m/s)
  - Wind direction (deg)

  The raw sampling rate of thermodynamic sensors is approximately 1.5 per second. The nominal ascent rate is approximately 5 m/s, although this is variable during the flight.

- Micropulse Lidar (MPL)

  This is a ground-based optical remote sensing system that operates at a wavelength of 523.5 nm with a vertical resolution of 90 m. It works by sending a short pulse of light from the telescope. As the photons travel, some of them are scattered by molecules, water droplets, or other atmospheric constituents. The photons that are scattered back are measured by a photo-diode. The detected signal is stored in bins according to how long it took for the pulse to return since it was transmitted, thus producing a profile. The field of view is very narrow (0.1 mrad), thus the backscattered radiation comes from a small region within the cloud.

- Millimeter Wave Cloud Radar (MMCR)

  The MMCR is a zenith-pointing radar operating at a frequency of 34.86 GHz (Ka-band) with a vertical resolution depending on the operating mode (commonly 90 m). It reports radar reflectivity (dBZ) of the atmosphere up to 20 km. Its main purpose is to determine cloud boundaries.

- Infrared Thermometer (IRT)

  This is a ground-based radiation pyrometer that measures the equivalent black body brightness temperature. It has a narrow field of view for measuring sky temperature and for detecting clouds. The up-looking IRT reports the effective black body temperature of the sky in the portion of the infrared spectrum sensed by the instrument (9.6 – 11.5 μm).

- Microwave Water Radiometer (MWR)

  Cloud liquid water in the atmosphere emits in a continuum that increases with frequency, dominating the 31.4 GHz observation, whereas water vapor dominates the 23.8 GHz channel. MWR operates at 23.8 GHz and 31.4 GHz (microwave). It has a resolution of 0.25 K and a radiometric range from 0 to 700 K. It measures all sky radiation.

It is useful to combine measurements from more than one sensor, as these can provide cloud parameters not accessible by a single sensor. Also, novel theoretical approaches can identify new possible parameters that better describe the atmospheric behavior. In the present work, we combine the MPL and MMCR data to provide vertical profile of particle concentration and characteristic diameters assuming a gamma distribution function for the particle size distribution. These quantities can then be used to derive the vertical profiles for IWC, radiative heating rates and other radiative properties of the clouds.

2.2.1 The SAFARI Field Experiment

We also provided some analysis of field campaign data collected in the SAFARI 2000 experiment. This program, like its predecessor SAFARI-92, was intended to help

researchers understand the relations between physical, chemical, biological and anthropic processes that affect the southern African climate system. However, unlike its predecessor, this program included comprehensive observations such as: analyses and integration of land processes, ground use and cover change, surface radiation, cloud characterization and radiative effects, aerosols and trace gas chemistry and transport, hydrology, and ecology. In order to make these detailed observations, the program employed a variety of ground-based, airborne and remote sensing instruments. Intensive field campaigns were used to collect comprehensive data that could be meshed together with periods of long term, less inclusive data. These campaigns took place during the dry (August–September) and wet (February–March) seasons. The ultimate goal of the program was to help researchers understand the southern African climate system and to develop computer models that would accurately represent it. As the factors that drive climate are very complex, the primary objective was to characterize and understand the processes behind biological and anthropogenic emissions, as well as to establish a basis for long-term monitoring of climatic and hydrological processes. Once this was achieved, research could move on to modeling the southern African climate, by combining atmospheric transport and chemistry models with the observations made during the program, to corroborate the models and broaden the understanding of these emissions.

Of the remote sensing techniques, active lidar profiling is particularly helpful because the cloud height configuration is clearly determined, up to the limit of signal attenuation. One of the available lidar instruments is the Cloud Physics Lidar (subsequent to the Cloud Lidar System). It is an airborne lidar designed expressly for the study of clouds and aerosols using the ER-2 High Altitude Aircraft. This aircraft usually flies at 65,000 feet (20 km), allowing them to work as spaceborne instrument simulators. Because this instrument is small and low-cost, it can be included in multiple instrument missions, thus providing independent and accurate particle size data for cloud modeling, radiation and satellite measurements validation. The Cloud Physics Lidar (CPL) uses photon-counting detectors with a high repetition rate laser to sustain a large signal dynamic range. This produces comprehensive and dependable data sets in less time. The information provided by the instrument

is sufficient to allow for a complete analysis of radiative and optical properties of optically thin clouds. The data collected by the CPL includes:

- Cloud profiling with 30 m vertical by 200 m horizontal resolution at 1064 nm, 532 nm, and 355 nm, providing cloud location and internal backscatter structure;
- Aerosol, boundary layer, and smoke plume profiling at all three wavelengths;
- Depolarization ratio to determine the phase (e.g., ice or water) of clouds using the 1064 nm output;
- Cloud particle size determined from a multiple field-of-view measurement using the 532 nm run output;
- Direct determination of the optical depth of cirrus clouds using the 355 nm output.

The cloud optical depth can be analyzed without the need to use other instruments because only lidar data is necessary. By using attenuation of Rayleigh and aerosol scattering, together with the integrated backscatter, the extinction-to-backscatter ratio can be obtained. This ratio can then be used to determine the internal cloud extinction profile.

The CPL was first used during the SAFARI campaign in southern Africa throughout August and September 2000. The CPL data included cloud height and configuration and also aerosol and smoke plume structure. The cloud and smoke layer quantitative optical characteristics were established. CPL can also be employed together with airborne, ground-based instrumentation, and satellite data to validate regional emissions and to understand the connections between ground and atmosphere.

Together with the CPL, the MODIS Airborne Simulator (MAS) was flown on the NASA ER-2 high-altitude research aircraft during the SAFARI experiment. By acquiring high spatial resolution radiances from cloud and surface, this airborne

scanning spectrometer helps in defining and developing algorithms for the MODIS spectroradiometer in EOS satellite.

By combining both MAS and CPL data we are able to assess the advantages or limitations in determining cloud optical properties using RT models.

2.3 Moderate Resolution Imaging Spectroradiometer (MODIS)

The MODIS (Moderate Resolution Imaging Spectroradiometer) instrument and its airborne equivalent, provides information on cloud properties (area coverage, cloud droplet size, cloud top temperature, liquid water content) and aerosols. Understanding clouds is important because they play a role in the transport, transformation, and removal of chemicals in the atmosphere. As for aerosols, they change the radiative properties of the atmosphere by absorbing or scattering radiation and they are a factor in cloud formation.

MODIS [King et al. (1992)] is flown aboard the Terra (EOS AM-1) satellite, and it scans the entire Earth's surface every one to two days, acquiring data in 36 spectral bands, or groups of wavelengths. A second MODIS is to be flown as part of the payload of the Aqua satellite. Together, the two satellites will improve the understanding of global dynamics and processes occurring on the land, oceans and lower atmosphere.

A list of the bands of MODIS and their intended usage are presented in Tables 2.1 and 2.2. In the present work we use band 4 (0.545- 0.565 μm). These bands are essentially duplicated on the MAS.

Table 2.1: MODIS Technical Specifications (I)

Primary Use	Band	Bandwidth (nm)	Spectral Radiance ($W/m^2\mu msr$)	Required SNR
Land/Cloud	1	620–670	21.8	128
Boundaries	2	841–876	24.7	201
Land/Cloud	3	459–479	35.3	243
Properties	4	545–565	29.0	228
	5	1230–1250	5.4	74
	6	1628–1652	7.3	275
	7	2105–2155	1.0	110
Ocean Color/	8	405–420	44.9	880
Phytoplankton/	9	438–448	41.9	838
Biogeochemistry	10	483–493	32.1	802
	11	526–536	27.9	745
	12	546–556	21.0	750
	13	662–672	9.5	910
	14	673–683	8.7	1087
	15	743–753	10.2	586
	16	862–877	6.2	516
Atmospheric	17	890–920	10.0	167
Water Vapor	18	931–941	3.6	57
	19	915–965	15.0	250

Table 2.2: MODIS Technical Specifications (II)

Primary Use	Band	Bandwidth (μm)	Spectral Radiance ($W/m^2\mu msr$)	Required NEΔT
Surface/Cloud	20	3.660 3.840	0.45	0.05
Temperature	21	3.929–3.989	2.38	2.00
	22	3.929–3.989	0.67	0.07
	23	4.020–4.080	0.79	0.07
Atmospheric	24	4.433–4.498	0.17	0.25
Temperature	25	4.482–4.549	0.59	0.25
Cirrus Clouds	26	1.360–1.390	6.00	150 (SNR)
Water Vapor	27	6.535–6.895	1.16	0.25
	28	7.175–7.475	2.18	0.25
	29	8.400–8.700	9.58	0.05
Ozone	30	9.580–9.880	3.69	0.25
Surface/Cloud	31	10.780–11.280	9.55	0.05
Temperature	32	11.770–12.270	8.94	0.05
Cloud Top	33	13.185–13.485	4.52	0.25
Altitude	34	13.485–13.785	3.76	0.25
	35	13.785–14.085	3.11	0.25
	36	14.085–14.385	2.08	0.35

Chapter 3

LIDAR Observation of Cirrus

3.1 Introduction

In an ongoing effort to assess the effects of cirrus clouds on climate, many field experiments have been performed to understand the radiative and microphysical properties of these clouds. Amongst the various instruments used in these experiments, lidars emerged as simple and powerful probes in the investigation of the optical and microphysical properties of clouds.

A key property measured by lidars is the transmission of the laser through cirrus clouds from which the optical depth of cirrus is determined. Although this method for determining optical depth of cirrus is limited to optically-thin clouds, data obtained from such measurements has several advantages over optical depth information extracted from reflected solar radiances or emitted IR radiances [Miller et al. (2000)]. A principal advantage is the weaker dependence of the retrieval to unknown parameters such as the scattering phase function.

3.2 LIDAR System — Classic Theory

LIDAR is the acronym for LIght Detection And Ranging. It is an instrument that illuminates an object with a short pulse of light and determines its distance from a measurement of the time of flight for the light pulse to travel to the target and return. The amplitude of the detected signal is governed by two main physical processes: scattering and absorption. By modeling these processes, we can infer various optical properties of the medium illuminated by the lidar.

The lidar equation describes the power that is measured at the receiver after being scattered back by the target at some range. In the case of an atmospheric return signal, unlike that from a solid body object such as an airplane or a mountain (hard targets), the measured power will exhibit a broader space distribution that is given by the lidar equation [Weitkamp (1996)]:

$$P(r) = \frac{c\Delta t}{2} P_0 \frac{A\,\eta\,O(r)}{r^2} \beta_\pi\, T^2 \tag{3.1}$$

where A and η are the area and efficiency of the detector, O is the overlap function, β_π is the backscatter coefficient and T is the transmission of the atmosphere at range r. Since both β_π and T depend on the wavelength, we expect that the return power will depend on it too. If this dependence is nonlinear, then it is useful to compare the return from lidars that operate at different wavelengths in order to measure the atmospheric optical properties over a broader spectral range.

The transmission through a medium is defined by:

$$T(r) = \exp\left[-\int_0^r \beta_{ext}(\lambda, r')\, dr'\right] \tag{3.2}$$

were $\beta_{ext}(\lambda, r')$ is the extinction coefficient. The extinction and the backscatter coefficients are calculated using the particle size distribution $n(D)$ and the extinction/scattering efficiencies $Q_{ext,scat}$ at that particular wavelength [Stephens (1994)]:

$$\beta_{ext,sca} = \frac{\pi}{4} \int_0^\infty Q_{ext,sca}\, D^2\, n(D)\, dD\,. \tag{3.3}$$

To solve the lidar equation that involves one measured quantity P and two unknowns β_π and β_{ext}, a relationship of the form [Klett (1981)]

$$\beta_\pi = F\beta_{ext}^n \tag{3.4}$$

is adopted, where n and F are two constants. In most lidar applications, the exponent n is commonly set to unity, although we argue this has little justification. We present below both theoretical developments and experimental evidence which suggests that n need not be unity. The inverse of F is called the lidar ratio and although it is assumed constant, observations from numerous experiments show large variations within the same cloud (see Figure 3.1). The Ricatti type differential equation

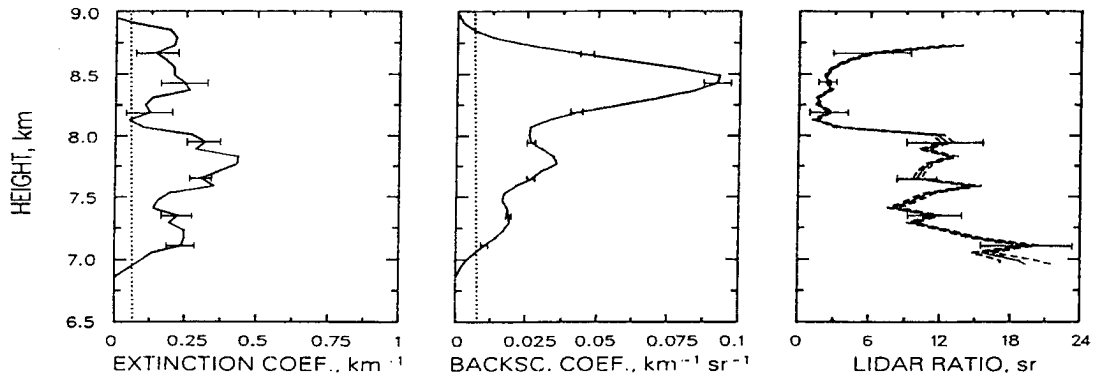

Figure 3.1: Raman lidar measurements of aerosol properties (From Ansmann et al., 1992a).

that follows from the inverse of the lidar equation can be easily solved. Its solution is given by:

$$\beta_{ext} = \frac{\exp\left[(S - S_0)/n\right]}{1/\beta_0 - 2/n \int_{r_0}^{r} \exp\left[(S - S_0)/n\right] dr'} \tag{3.5}$$

with $S(r) = \ln[r^2 P(r)]$ and $\beta_0 = \beta_{ext}(r_0)$. Unfortunately, the use of the above expression, called forward integration, is strongly influenced by the initial condition. Small uncertainties in this parameter when noise is present introduce a near singularity so that a non-physical *negative extinction coefficient occurs, unless unrealistically large values of constants F or n are used* [Weitkamp (1996)], supporting the hypothesis that the exponent n is not unity. For the backward integration, we simply reverse the order of integration, choosing as initial conditions the values at the most remote point. In contrast to forward integration, the backward integration is stable since it removes the possible singularities in the solution. However, it has the tendency to decrease the dynamic range of the data and to filter out perceptible structures. One possible resolution to this difficulty lies in the alternating use of both methods, varying the lidar ratios until the two results agree. Even so, the results can differ greatly from those inferred from other measurements as shown in Figure 3.2. In Figure 3.2(a) both the forward and inverse integration agree with the independent measurement (dotted line), while in Figure 3.2(b) this is not the case.

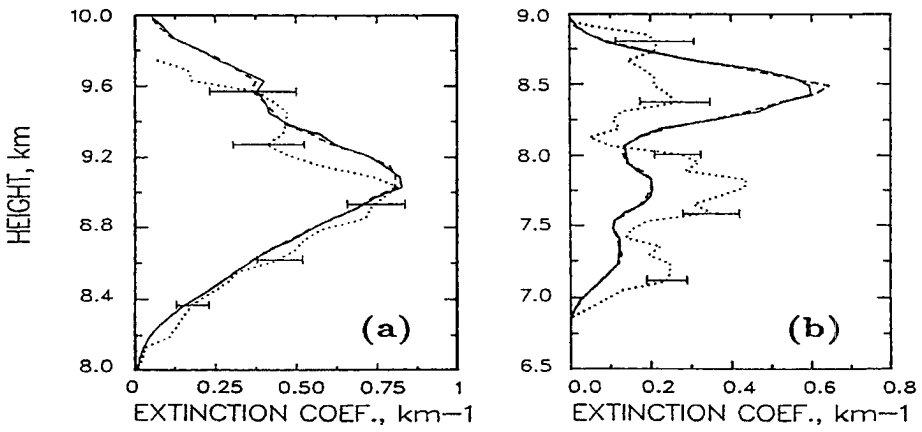

Figure 3.2: Aerosol extinction coefficient from a Raman lidar (dotted line) and from the same instrument used as an elastic-backscatter lidar (solid lines: Klett forward integration; dashed lines: Klett backward integration). (a) Lidar ratio = 15.7 sr; (b) Lidar ratio = 7.3 sr (From Ansmann et al., 1992a)

The correct solution to this problem lays in the construction of a better forward and inverse model and in understanding the limitations and possible problems that might arise from their use. But first, since what is really measured by the lidar is a voltage, the lidar signal must be calibrated. A new procedure for calibration and cloud detection is presented in the following section. We then address the problem of multiple scattering that is inherent to lidar systems. Also worthy of note, is the fact that most of the usable retrievals are performed for thin clouds, that is, when the extinction coefficient is relatively small (less than 1 km^{-1}). This limitation arises from the lidar resolution and is imposed by the forward and inverse models, as will be shown later.

3.3 Cloud Detection and Lidar Calibration

The following section describes a new algorithm developed to analyze the routinely archived lidar data collected under the US Department of Energy Atmospheric

Radiation Measurement (ARM) program by the MPL system (see section 2.2). This algorithm differs from other similar algorithms (e. g. see section 3.3.1), by the introduction of a metric that depends on three parameters: gain, offset and transmittance. The solution of this nonlinear system for the three parameters is less susceptible to noise and resolves the ambiguity in the value of the offset not achieved by existing methods.

3.3.1 Lidar Transmission Method

Young (1995) used the backscattered signal measured by a ground based lidar in conjunction with the known atmospheric backscatter to devise a simple two-independent window-fit for determining the transmittance of a cloud. Following his reasoning, we can write the measured lidar-signal voltage in a region below the cloud as:

$$y(r) = \frac{m}{r^2}\beta_m(r)T_m^2(0,r) + o\ , \tag{3.6}$$

while in a region above the cloud the relationship becomes:

$$y(r) = \frac{m}{r^2}\beta_m(r)T_m^2(0,r)T^2 + o\ . \tag{3.7}$$

Here m is a system constant, $\beta_m(r)$ is the molecular backscatter coefficient at range r, T_m and T are the molecular and the cloud transmittances respectively, and o is the offset. Here we make the assumption that aerosol is absent in these two regions, which is reasonable for high layer of cirrus well above the boundary layer, unless following volcanic erruptions or forest fires. Included in the system constant are the gain of the lidar, the overlap function, receiver area, etc. while the offset accounts for the background light, detector dark current, and amplifier and digitizer offset voltage. Molecular backscatter as well as molecular transmittance are calculated as functions of pressure and temperature, which are determined from the soundings. We have to mention that the value for the molecular backscatter coefficient is extremely small (around 0.55 $\mathrm{Mm^{-1}\ sr^{-1}}$ for altitudes around 10 km), which reduces considerably the level of measured signal for the molecular signal, thus the potential of being affected by noise. More details are presented in Appendix A.

In the above equations, the only unknowns are the aforementioned three parameters: lidar system constant (m) — or gain, lidar system offset (o), and cloud transmittance (T).

With the modeled signal introduced as:

$$x(r) = \frac{1}{r^2}\,\beta_m(r)\,T_m^2(0,r) \tag{3.8}$$

our system of equations becomes:

$$\begin{cases} y_1 &= m \cdot x_1 + o \\ y_2 &= m \cdot x_2 \cdot T^2 + o \end{cases} \tag{3.9}$$

where we introduced indices to denote the regions below the cloud (1) and above the cloud (2) respectively. At this point, a linear regression of the measured signal y against the modeled signal x can be performed for each of the two regions to yield the offset o and the system constant m for the lower region, or the product mT^2 for the higher region, respectively. The system (3.9) separates into two independent systems with two equations and two unknowns:

$$\begin{cases} \left(\overline{yx}\right)_1 - m \cdot \left(\overline{x^2}\right)_1 - o \cdot \overline{x}_1 &= 0 \\ \left(\overline{y}\right)_1 - m \cdot \left(\overline{x}\right)_1 - o &= 0 \end{cases} \tag{3.10}$$

$$\begin{cases} \left(\overline{yx}\right)_2 - m \cdot T^2 \cdot \left(\overline{x^2}\right)_2 - o \cdot \left(\overline{x}\right)_2 &= 0 \\ \left(\overline{y}\right)_2 - m \cdot T^2 \cdot \left(\overline{x}\right)_2 - o &= 0 \end{cases} \tag{3.11}$$

where over-bars indicate an average quantity, and indices are associated with low region (1) or high region (2) respectively. The two system of equations in (3.10) and (3.11) are solved independently:

$$\begin{cases} m &= \frac{\left(\overline{yx}\right)_1 - \left(\overline{y}\right)_1 \cdot \left(\overline{x}\right)_1}{\left(\overline{x^2}\right)_1 - \left(\overline{x}\right)_1^2} \\ o &= \frac{\left(\overline{y}\right)_1 \cdot \left(\overline{x^2}\right)_1 - \left(\overline{yx}\right)_1 \cdot \left(\overline{x}\right)_1}{\left(\overline{x^2}\right)_1 - \left(\overline{x}\right)_1^2} \end{cases} \tag{3.12}$$

$$\begin{cases} m \cdot T^2 &= \frac{\left(\overline{yx}\right)_2 - \left(\overline{y}\right)_2 \cdot \left(\overline{x}\right)_2}{\left(\overline{x^2}\right)_2 - \left(\overline{x}\right)_2^2} \\ o &= \frac{\left(\overline{y}\right)_2 \cdot \left(\overline{x^2}\right)_2 - \left(\overline{yx}\right)_2 \cdot \left(\overline{x}\right)_2}{\left(\overline{x^2}\right)_2 - \left(\overline{x}\right)_2^2} \end{cases} \tag{3.13}$$

From the ratio of the two system constants (mT^2 and m), the square of the transmittance can be calculated. Two values of offset are determined from this system of equations and there is no reason to expect these to be the same. This is a problem as the offset is essential in determining the cloud backscatter and transmittance from the lidar equation and thus in establishing the level of confidence in determining the two system constants by using two independent linear fits derived arbitrarily from a coupled system of equations (3.9). In the next section, we address this problem by developing a new method for computing the system constant, the offset and the transmittance from one system of equations that produce a unique solution for the above parameters.

3.3.2 A New Lidar Transmission Algorithm

To solve the problem of fitting the measured lidar signal to a model for both regions, we introduce the metric:

$$\delta^2 = \sum_{i=1}^{k_1} W_{i,1} \cdot (y_{i,1} - m \cdot x_{i,1} - o)^2 + \sum_{i=1}^{k_2} W_{i,2} \cdot \left(y_{i,2} - m \cdot T^2 \cdot x_{i,2} - o\right)^2 , \quad (3.14)$$

where the first sum is performed for the region below the cloud and the second sum is performed for the region above the cloud; k_1 and k_2, respectively are the number of points for each of these regions. The W_i's are simply weighting coefficients that account for the effects of noise. These coefficients sum to unity.

We now find the parameters (m, o, T^2) that minimize the above expression, by imposing that the partial derivatives of δ^2 with respect to each of the parameters is zero. This results in the following system of equations:

$$\begin{cases} (\overline{yx})_1 - m \cdot \left(\overline{x^2}\right)_1 - o \cdot (\overline{x})_1 & = & 0 \\ (\overline{yx})_2 - m \cdot T^2 \cdot \left(\overline{x^2}\right)_2 - o \cdot (\overline{x})_2 & = & 0 \\ (\overline{y})_1 + (\overline{y})_2 - m \cdot [(\overline{x})_1 + T^2 \cdot (\overline{x})_2] - o & = & 0 \end{cases} \quad (3.15)$$

where we used the following notation:

$$(\overline{yx})_{(1,2)} = \sum_{i=1}^{k_{(1,2)}} W_{i,(1,2)} \cdot x_{i,(1,2)} \cdot y_{i,(1,2)} \quad (3.16)$$

The above system of equations is nonlinear, consisting of three equations in three unknowns. This contrasts with (3.12) and (3.13) that are usually solved for the same unknowns. It is observed here that the first two equations in (3.15) appear identical to the first equations in (3.12) and (3.13), while the last equation in (3.15) is a weighted sum of the last equations in (3.12) and (3.13). Thus our system of equations reduces to the conventional system for particular choices of the weighting functions. It is clear that the requirement of a minimum in the proposed metric, will yield an optimal solution for the lidar calibration problem.

The unique solution for equations (3.15) is:

$$\begin{cases} T^2 &= \dfrac{(\overline{x})_1(\overline{x})_2(\overline{xy})_1+\left[\left(\overline{x^2}\right)_1-(\overline{x})_1^2\right](\overline{xy})_2-\left[(\overline{y})_1+(\overline{y})_2\right]\left(\overline{x^2}\right)_1(\overline{x})_2}{(\overline{x})_1(\overline{x})_2(\overline{xy})_2+\left[\left(\overline{x^2}\right)_2-(\overline{x})_2^2\right](\overline{xy})_1-\left[(\overline{y})_1+(\overline{y})_2\right](\overline{x})_1\left(\overline{x^2}\right)_2} \\ m &= \dfrac{(\overline{xy})_1-\left[(\overline{y})_1+(\overline{y})_2\right](\overline{x})_1}{\left(\overline{x^2}\right)_1-(\overline{x})_1^2-T^2(\overline{x})_1(\overline{x})_2} \\ o &= \dfrac{(\overline{xy})_1-m\left(\overline{x^2}\right)_1}{(\overline{x})_1} \end{cases} \tag{3.17}$$

The prescription for determining the weighting functions as well as the cloud boundaries is given by the following algorithm:

1. from preset lower and upper windows, using equal values for the weighting functions, determine the gain, offset and transmittance; the values for the lower and upper windows are chosen so that there is minimal chance that clouds are present within these boundaries: 2 to 2.8 km for the lower window and 23 to 25 km for the upper window; Define a threshold value as some percentage (currently 5 %) of the difference between the measured signals at the bottom of the lower window and top of the upper window;

2. using the values obtained from step (1), recompute the weighting functions as inverses of the distance between the measured signal and the one being modeled; this choice ensures that points that are closer to the modeled signal are given more weight than those that lie further away from the modeled signal;

3. using the above values for weighting function, recompute the values for gain, offset and transmittance;

4. define a threshold value for cloud detection. Find the maxima for the difference between signal and fit; test if it is greater than the threshold; from this level go up and down till the difference becomes less than threshold; repeat the procedure to find other cloud layers; determine the upper and lower cloud boundaries;

5. using the estimated cloud boundaries from step (4), redefine lower and upper windows; the sizes of the windows are set to 2500 m for the lower window, and 5500 m for the upper window respectively; these values ensure that we have enough points for our calculations;

6. repeat steps (1) and (2) using these new windows to determine gain, offset and transmittance;

7. repeat steps (1) through (6) for each individual profile; reject profile if transmittance is greater than unity or less than zero, or if gain is negative;

8. as an option, a filtering scheme is used: for each profile the weighting function are recomputed using a weighted sum of the averaged values for gain and offset and the computed values for the same variables; these new weighting functions are used to compute new values for gain, offset and transmittance. Use of this filtering procedure helps in reducing the level of noise in the transmittance as well as in gain and offset.

The variance of a function of two independent variables, $G(a, b)$, can be expressed as:

$$\sigma_G = \sqrt{\left(\frac{\partial G}{\partial a}\right)^2 \cdot \sigma_a^2 + \left(\frac{\partial G}{\partial b}\right)^2 \cdot \sigma_b^2} \tag{3.18}$$

Applied to our variables described in (3.12), we can deduce the following expressions:

$$\sigma_G = \sqrt{\sum_{i=1}^{k_1} \left|\frac{\partial G}{\partial y_i}\right|^2 + \sum_{i=1}^{k_2} \left|\frac{\partial G}{\partial y_i}\right|^2} \cdot \sigma_y \tag{3.19}$$

where G can be any of our retrieved variables. We also assumed that the variance in signal (σ_y) is the same for both regions and we neglected the variance in the modeled signal ($\sigma_x = 0$).

For our variables we can deduce that:

$$\left(\frac{\partial T^2}{\partial y_i}\right)_1 = \frac{W_{i,1}}{c}\left\{e + x_{i,1}\left[T^2\left(\left(\overline{x^2}\right)_2 - (\overline{x})_2^2\right) - (\overline{x})_1(\overline{x})_2\right]\right\} \tag{3.20}$$

$$\left(\frac{\partial T^2}{\partial y_i}\right)_2 = \frac{W_{i,2}}{c}\left\{e + x_{i,2}\left[T^2(\overline{x})_1(\overline{x})_2 - \left(\left(\overline{x^2}\right)_1 - (\overline{x})_1^2\right)\right]\right\} \tag{3.21}$$

$$\left(\frac{\partial m}{\partial y_i}\right)_{(1,2)} = \frac{1}{A - B^2}\left\{W_{i,(1,2)}\left(x_{i,(1,2)} - B\right) + [b - 2ma]\left(\frac{\partial T^2}{\partial y_i}\right)_{(1,2)}\right\} \tag{3.22}$$

$$\left(\frac{\partial o}{\partial y_i}\right)_1 = \frac{1}{A - B^2}\left\{W_{i,1}(A - Bx_{i,1}) + [d - 2na]\left(\frac{\partial T^2}{\partial y_i}\right)_1\right\} \tag{3.23}$$

$$\left(\frac{\partial o}{\partial y_i}\right)_2 = \frac{1}{A - B^2}\left\{W_{i,2}\left(A - BT^2x_{i,2}\right) + [d - 2na]\left(\frac{\partial T^2}{\partial y_i}\right)_2\right\} \tag{3.24}$$

where

$$A = \left(\overline{x^2}\right)_1 + T^4\left(\overline{x^2}\right)_2 \tag{3.25}$$

$$B = (\overline{x})_1 + T^2(\overline{x})_2 \tag{3.26}$$

$$C = (\overline{y})_1 + (\overline{y})_2 \tag{3.27}$$

$$D = (\overline{xy})_1 + T^2(\overline{xy})_2 \tag{3.28}$$

$$a = T^2\left(\overline{x^2}\right)_2 - B(\overline{x})_2 \tag{3.29}$$

$$b = (\overline{xy})_2 - C(\overline{x})_2 \tag{3.30}$$

$$c = (\overline{x})_1(\overline{x})_2(\overline{xy})_2 + \left[\left(\overline{x^2}\right)_2 - (\overline{x})_2^2\right](\overline{xy})_1 - C(\overline{x})_1\left(\overline{x^2}\right)_2 \tag{3.31}$$

$$d = 2CT^2\left(\overline{x^2}\right)_2 - B(\overline{xy})_2 - D(\overline{x})_2 \tag{3.32}$$

$$e = \left(\overline{x_1^2}\right)_1(\overline{x})_2 - T^2(\overline{x})_1\left(\overline{x^2}\right)_2 \tag{3.33}$$

The above procedure was tested for a synthetic case: the modeled signal was computed for two fixed windows as the Rayleigh backscatter for a real profile of temperature and pressure, and then corrected to account for molecular absorption and range; the synthetic signal was derived as follows: (1) apply a gain and offset to the modeled signal; (2) for the upper window a correction was applied to simulate

the decrease in the signal due to transmittance through a cloud; (3) zero mean Gaussian white noise was applied to the resulting signal. The standard deviation level of noise was randomly varied for each synthetic lidar profile. In total 1440 profiles were simulated and the resulting values for gain, offset and transmission were determined. For comparison purposes, the old method was applied to yield values for the same parameters. The results from a simulated case in which the lower window was set between 5500 m and 9000 m, and the upper window between 11000 m and 16500 m, respectively, while the values used for a gain, offset and transmittance were set to be 100, 10 and 0.35 respectively, are shown in Figure 3.3. From the figure we see that the new proposed method is significantly more accurate than the old one, yielding reasonable values for all three parameters, with greatest accuracy for the gain (errors are less than 10 %, and the calculated values deviate from the actual values by less than 2 %), and poorer accuracy for the transmittance (errors are large, with calculated values within 20 % from the expected values). It is noted that there is a tendency for the old method to underestimate the gain and offset and overestimate the transmittance. For the new method, the transmittance is somewhat overestimated, otherwise the gain and offset are undisturbed. In the case when the windows intervals are reduced to 1500 m each (not shown here), the errors increase as one would expect, but the new method still gives reasonable results, while the old one yields parameter values that fail to give any physical values for transmittance, demonstrating the improvements made possible by the new method. The need for averaging several profiles and/or smoothing the signal is not necessary, thus errors associated with such procedures are eliminated [Ansmann et al. (1992a)]. Nevertheless, given the level of noise present in such an instrument, errors remain an issue, but based on tests done for synthetic cases, the values obtained for gain and offset can be considered reliable. These parameters are subsequently used for computing vertical profiles of the cloud backscatter coefficients, which are essential in inverting the lidar equation.

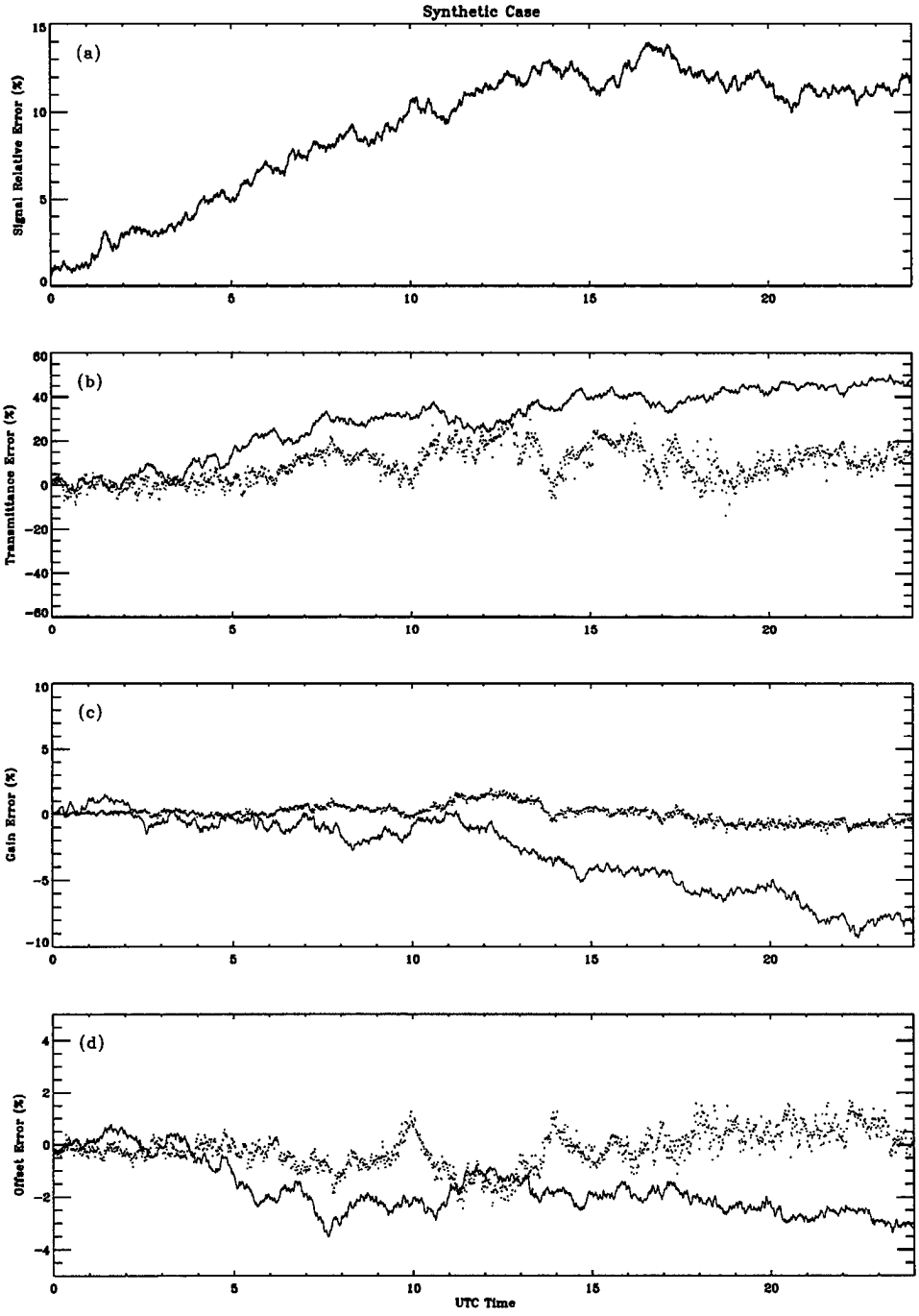

Figure 3.3: Synthetic Case: (a) Relative Error for the simulated signal; Errors in (b) Transmittance, (c) Gain and (d) Offset for the new method (dots) and old method (solid line). Shaded are the computed errors as explained in text for the new method.

3.3.3 Application to Experimental Data

To illustrate an application of the new method, we processed lidar profiles obtained from two lidars that are operational at the ARM site at Southern Great Plains (SGP). The Raman Lidar (RL) operates at 355 nm and has 39 m vertical resolution, while the Micropulse Lidar (MPL) operates at 523.5 nm and has 90 m vertical resolution. Both lidars have a temporal resolution of one-minute.

In Figure 3.4, the raw backscatter signal measured by the MPL as a function of height (solid line) along with the modeled signal fit (dashed line) for a particular time are plotted. The relatively strong returns between roughly 8.2 km and 9.8 km are due to a quasi-stable cirrus cloud.

In Figure 3.5 and Figure 3.6, the retrieved variables are plotted as function of time for the two instruments. The errors associated with each variable lie within the shaded region. We can see that the transmittance shows a relatively smooth behavior with respect to time. However, the gain exhibits some fluctuations around a mean value, which was reported before for these instruments. We also see that during the day time (roughly 0–1 and 13–24 UTC time), due to the solar radiation, the level of noise increases, and as expected, the errors for all variables increase. Related directly to the measured signal, the offset shows the largest variations. This feature, however, can be exploited to our advantage by filtering out profiles that display large variations for offset, or gain, or transmittance.

In order to further test our new method, we compared the transmittances deduced from these two different lidars. In Figure 3.7, the scattered plot of transmittance shows a good correlation between these two instruments especially during nighttime when solar radiation does not alter the received signal. The fitting slopes for the transmittance cases are 0.94 for the nighttime and 0.79 for the daytime case, respectively.

Because the present method is intended to be used as an operational method for processing the ARM lidar data, Figure 3.8, shows two days of processed data. We can see that the cloud boundaries are well determined, the values for transmittance show a relatively smooth variation with time, and noise is filtered out.

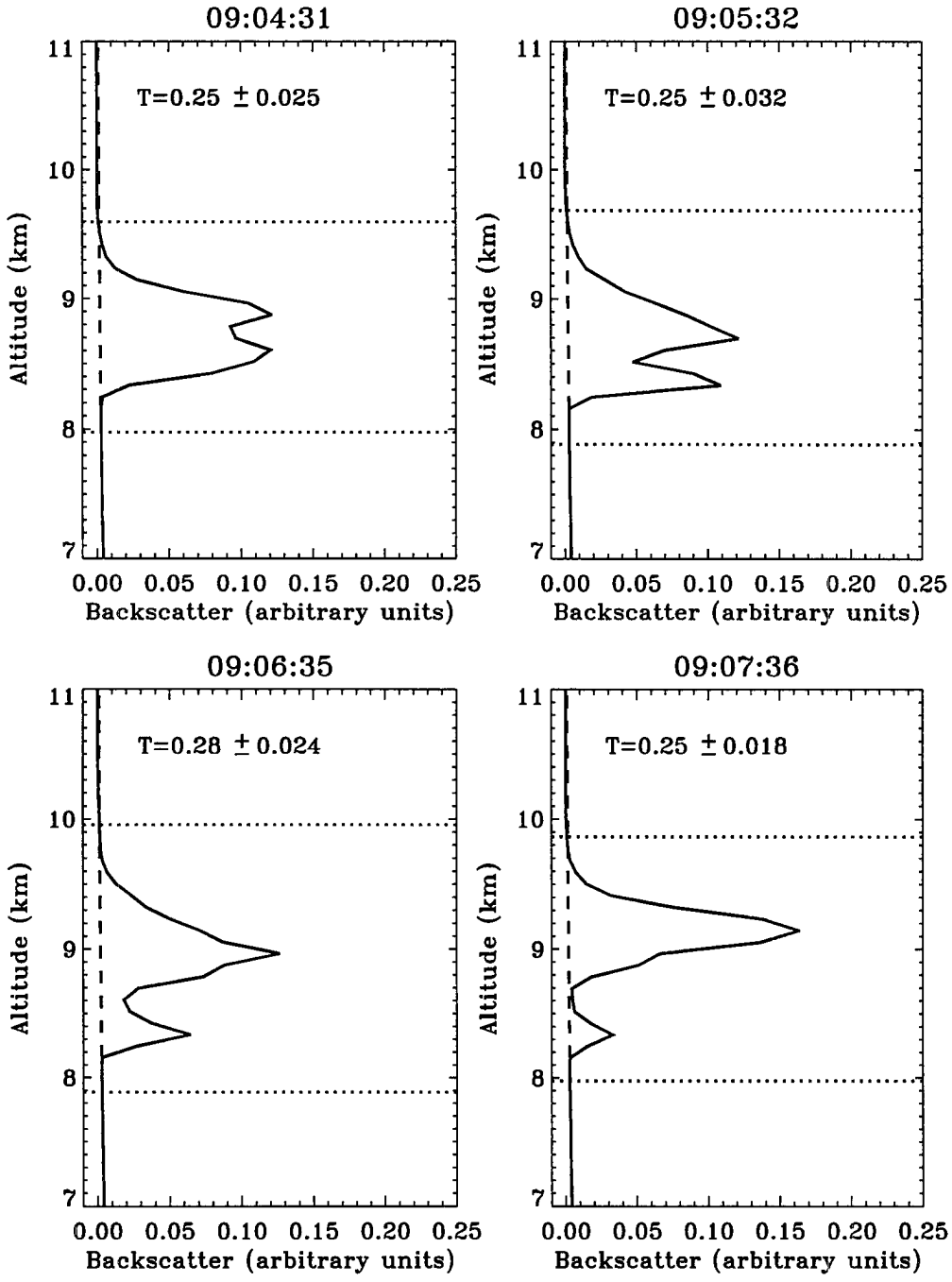

Figure 3.4: Raw backscatter signal (solid line), modeled signal (dashed line), and cloud boundaries (dotted line) at different times. Transmittance T for each profile is displayed. Nauru 1999/05/01.

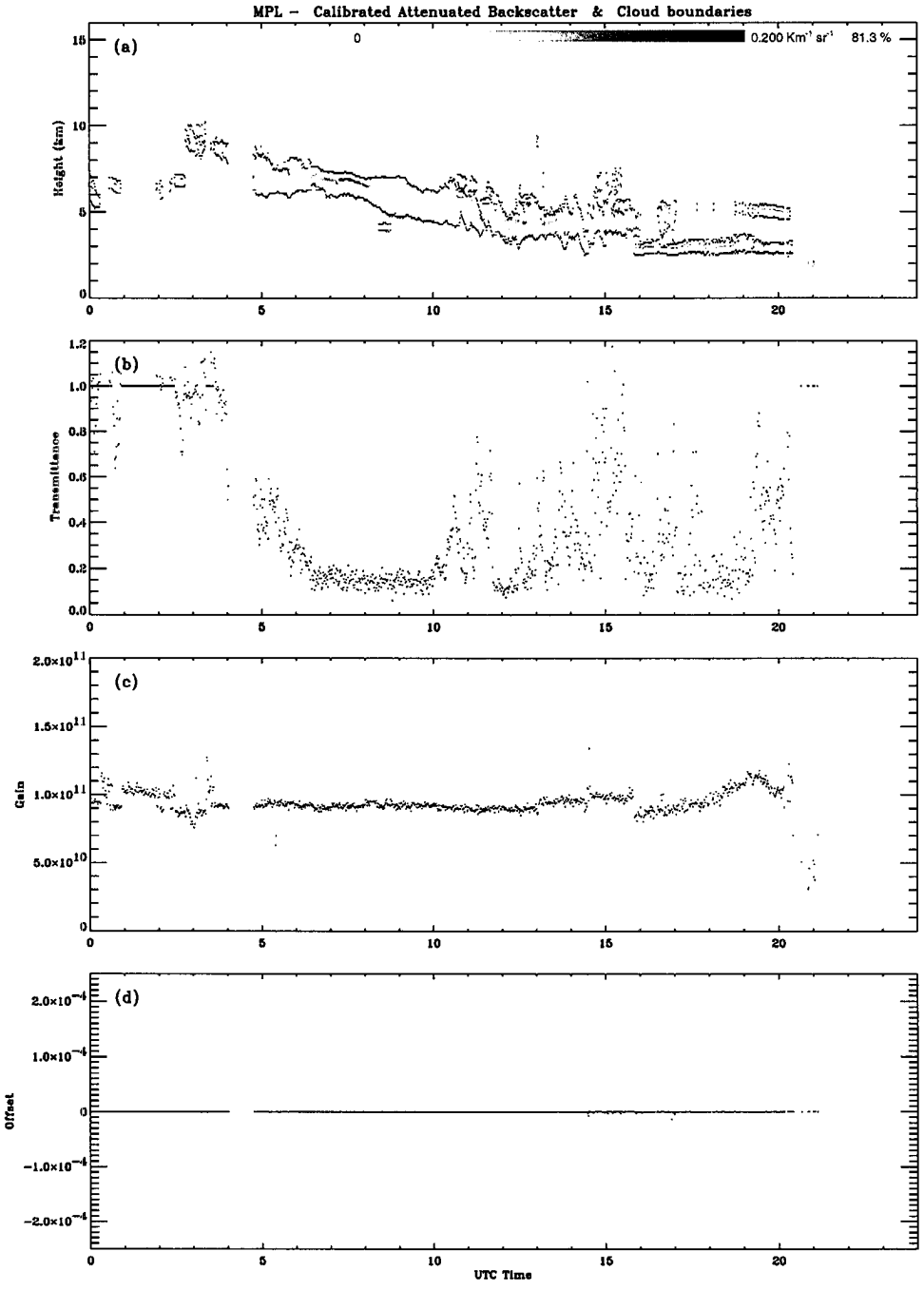

Figure 3.5: MPL: (a) Calibrated attenuated backscatter, (b) Transmittance, (c) Gain, and (d) Offset as function of time. SGP 2000/03/10.

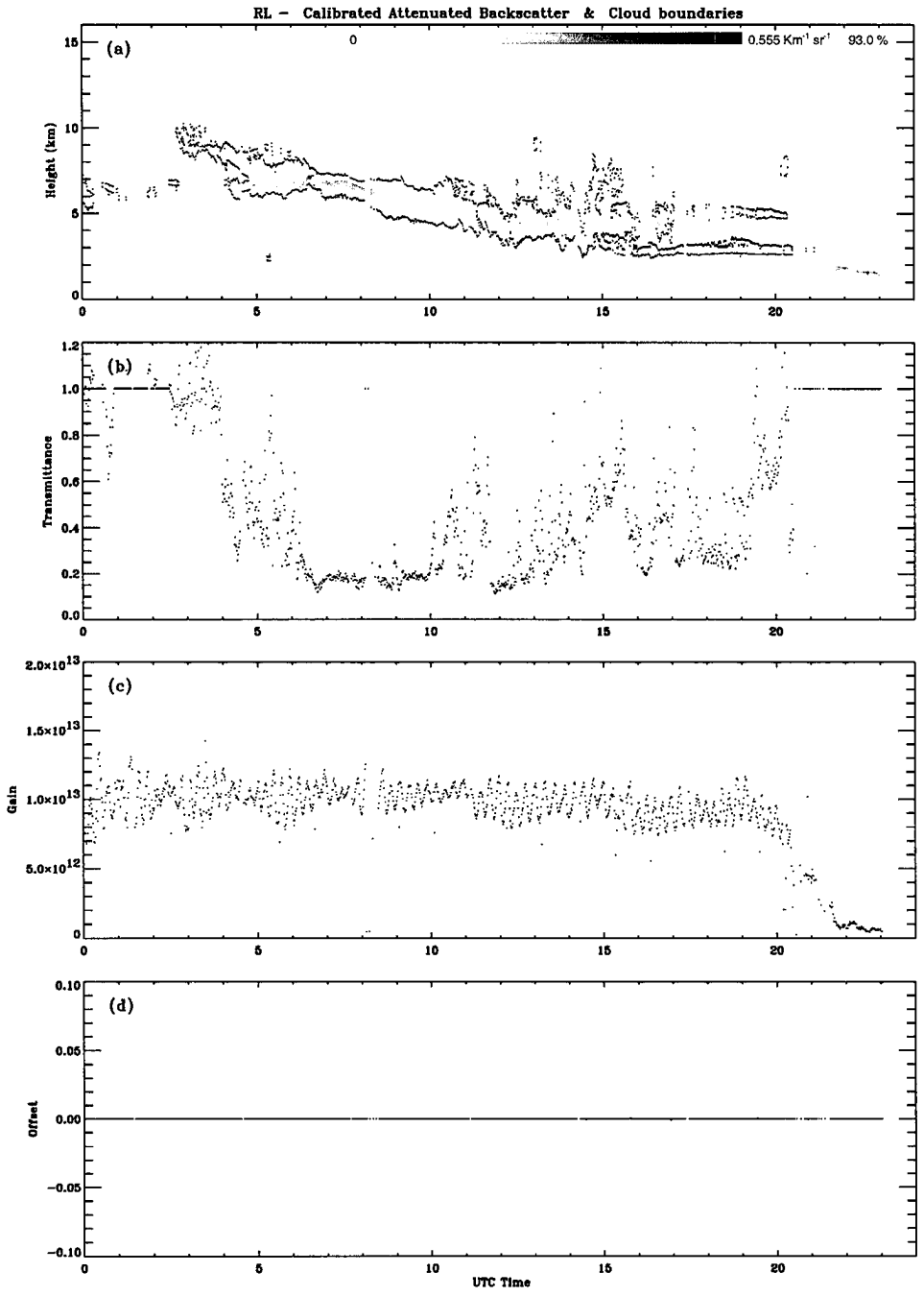

Figure 3.6: RL: (a) Calibrated attenuated backscatter, (b) Transmittance, (c) Gain, and (d) Offset as function of time. SGP 2000/03/10.

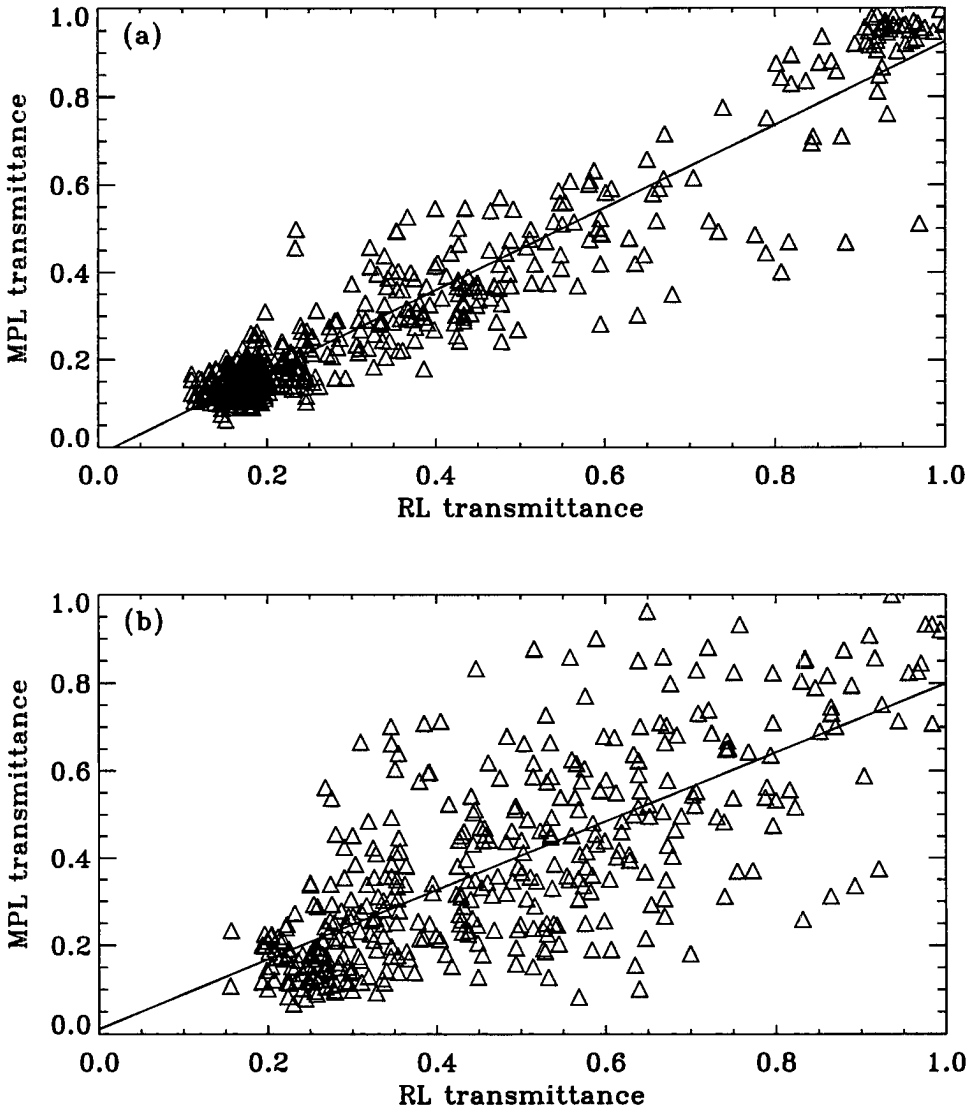

Figure 3.7: Correlations between transmittances deduced from RL and MPL (with triangles): (a) nighttime, (b) daytime. The linear fit for both cases is represented by the solid line.

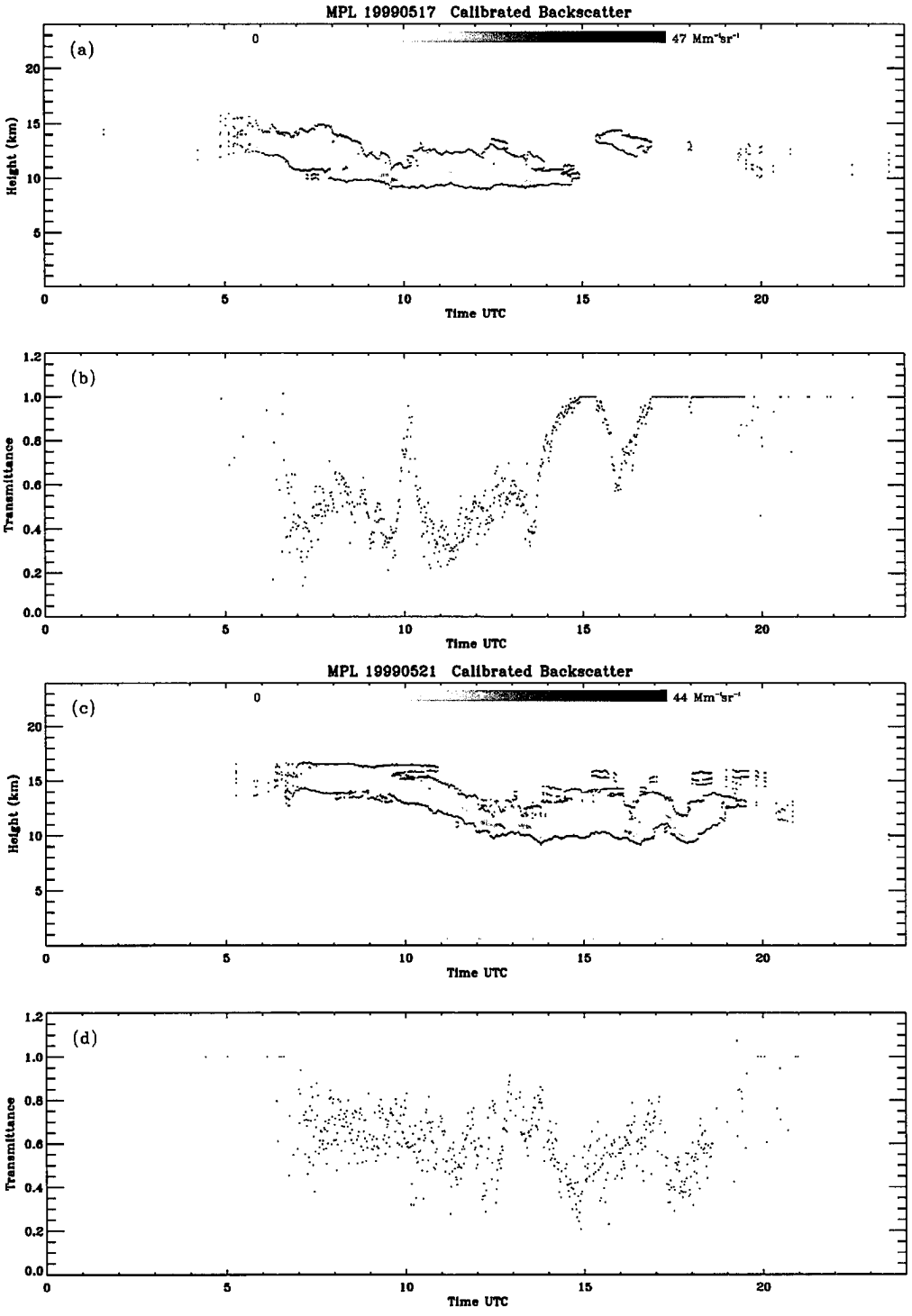

Figure 3.8: Time dependence of the MPL (a), (c) backscatter coefficient and (b), (d) transmittance for two days at Nauru: 1999/05/17 and 1999/05/21.

3.4 Efforts in Modeling Multiple Scattering (MS) Effects

By definition, the scattered radiance at angle θ is given by:

$$\delta I_{sca}(\theta,\phi) = \frac{\beta_{sca}}{4\pi} P(\theta,\phi) F_0 \delta r_0 \tag{3.34}$$

where β_{sca} is the volumic scattering coefficient, F_0 is the incident flux, $P(\theta,\phi)$ is the phase function and δr_0 is the length of the scattering element (see Figure 3.9). Here we assumed that the phase function is normalized to 4π:

$$\int_0^{2\pi} \int_0^{\pi} P(\theta,\phi)\, d\theta\, d\phi = 4\,\pi \quad .$$

It follows that the scattered power in the solid angle $d\Omega$ is:

$$\delta P_{sca}(\theta,\phi) = \delta I_{sca}(\theta,\phi) |\cos\theta| dA d\Omega \tag{3.35}$$

and that the incident flux on the surface dA' is given by:

$$F_0' = \frac{\delta P_{sca} e^{-\tau(r)}}{dA'} \quad . \tag{3.36}$$

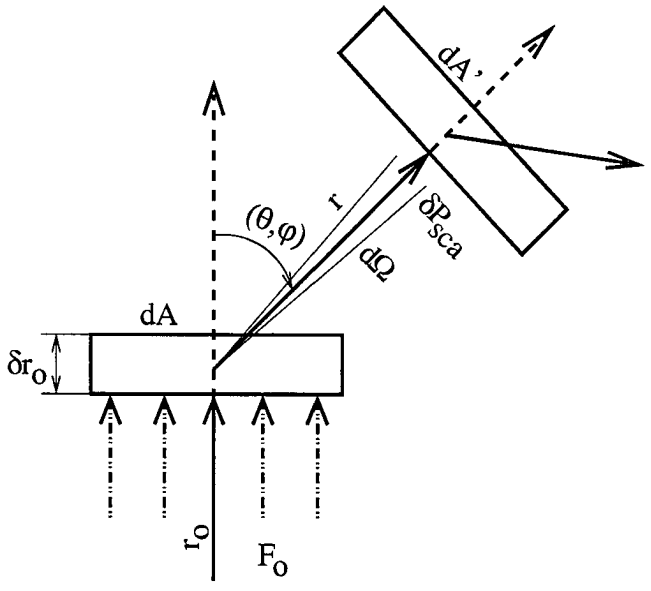

Figure 3.9: Scattering Geometry.

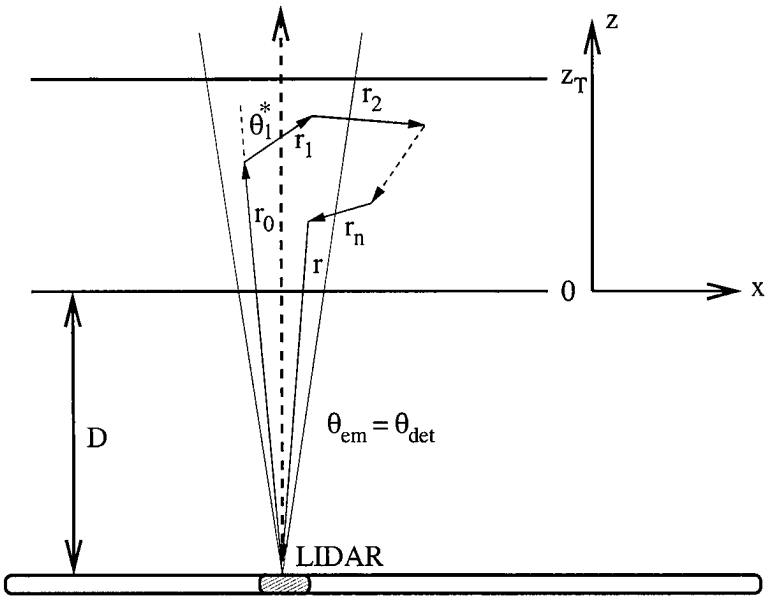

Figure 3.10: Multiple Scattering Geometry.

Using the definitions above we can show that the p-th order scattering contribution to the received power is given by the following expression (see Figure 3.10):

$$dP^{(p)} = \left(\frac{1}{4\pi}\right)^p I_0 \prod_{i=1}^{p} \left[\beta_{sca}(i) P(\theta_i^\star) |\cos\theta_i^\star| e^{-\tau(r_i)} dr_{i-1} d\Omega_{i-1}^\star\right] e^{-\tau(r)} \frac{\Delta S_d \cos\theta_d}{r^2} \tag{3.37}$$

where we introduced the intensity of the emitter $I_0 = \Delta P_{em}/\Delta\Omega_{em}$. For the particular case of LIDAR detection we must also introduce constraints which require that: (1) the total path of the photon after p scatters is the range of the signal; (2) any scattering process must occur within the clouds boundaries, and (3) the first/last scattering must occur within the emitter/detector field of view (FOV). These constraints can be expressed as:

$$2 \cdot (z + D) \leq \sum_{i=1}^{p} r_{i-1} + r < 2 \cdot (z + D) + \Delta z \tag{3.38}$$

$$D \leq \sum_{i=1}^{p} r_{i-1} \cos\theta_i^\star \leq z_T + D \tag{3.39}$$

$$\theta_o \leq \theta_{em} \tag{3.40}$$

$$|\sum_{i=1}^{p} r_{i-1}\sin\theta_{i-1}^{\star}| \leq r\sin\theta_{det} \tag{3.41}$$

where Δz is the lidar resolution. In the case of LIDAR detection, the FOV is very small (10^{-4} sr), and if we assume a homogeneous cloud, then the power detected due to single order scattering (backscatter) can be approximated by:

$$\Delta P_{sca}^{(1)}(z) \approx \frac{\beta_{sca}}{4\pi} I_0 T_{clr}^2 P(\pi)\cdot e^{-2\beta_{ext}z}\Delta\Omega_{em}\frac{\Delta S_d}{(z+D)^2}\Delta z \tag{3.42}$$

where T_{clr} is the clear sky transmission, ΔS_d is the detector area, $\Delta\Omega_{em}$ is the solid angle for the emitted radiation. From the geometrical constraints, we can see that the above expression is valid only within the cloud boundaries (i. e. $0 \leq z \leq z_T$). Also to be noticed is the inverse square range dependence and the two-way transmission due to cloud extinction:

$$\Delta P_{sca}^{(1)}(z) \sim e^{-2\beta_{ext}z}/(z+D)^2 \quad .$$

In a similar way, the power contributed by second order scattering can be approximated by:

$$\Delta P_{sca}^{(2)}(z) \approx \left(\frac{\beta_{sca}}{4\pi}\right)^2 I_0 T_{clr}^2 2\pi \int_0^z \int_{\mu_1(x)}^{\mu_2(x)} P(\mu)P(-\mu)\mu^2\, d\mu dx$$
$$\times\, e^{-2\beta_{ext}z}\Delta\Omega_{em}\frac{\Delta S_d}{(z+D)^2}\Delta z \tag{3.43}$$

where $\mu_{1,2}(x)$ are determined from the geometrical constraints (3.38– 3.41).

In the thin cloud limit, the dependence of second order scattering with z varies according to:

$$\Delta P_{sca}^{(2)}(z) \sim z\cdot e^{-2\beta_{ext}z}/(D+z)^2 \quad .$$

Beyond third order scattering, complexity rapidly escalates. For the third order scattering contributions, we can write:

$$\Delta P_{sca}^{(3)}(z) \approx \left(\frac{\beta_{sca}}{4\pi}\right)^3 I_0 T_{clr}^2\, e^{-2\beta_{ext}z}\Delta\Omega_{em}\frac{\Delta S_d}{(z+D)^2}\Delta z$$
$$\times\, 4\pi \int_0^{\min(z,z_T)} \int_{\mu_1(x)}^{\mu_2(x)} \int_0^{R(\mu)} \int_{\phi_1'}^{\phi_2'} \int_{\mu_1'}^{\mu_2'} P(\mu)P(\mu')P(\mu'')|\mu\cdot\mu'\cdot\mu''|d\mu' d\phi' dr d\mu dx \tag{3.44}$$

where the limits of integration must be computed from our geometrical constraints. In the thin cloud limit the above contribution to the detected power will be of the form:

$$\Delta P_{sca}^{(3)}(z) \sim z^2 \cdot e^{-2\beta_{ext}z}/(D+z)^2 \quad .$$

For the i^{th} order of scattering, we expect the range dependence to be in the form:

$$\Delta P_{sca}^{(i)}(z) \sim z^{i-1} \cdot e^{-2\beta_{ext}z}/(D+z)^2 \quad .$$

Figure 3.11 presents a plot of the individual contributions to the return power, calculated as explained above. The figure has features that are very similar to that computed by Platt (1981) using a Monte Carlo approach (see Figure 3.12). In this way, the total backscatter power is expressed as the sum of individual order of scattering:

$$\Delta P_{sca}(z) = \sum_{i=1}^{\infty} \Delta P_{sca}^{(i)}(z) \tag{3.45}$$

which for a thin, homogeneous cloud can be written as:

$$\Delta P_{sca}(z) \approx \sum_{i=1}^{\infty} \left[C_i \left(\frac{\beta_{sca}}{4\pi} \right)^i z^{i-1} \right] \cdot I_0 T_{clr}^2 \cdot e^{-2\beta_{ext}z} \Delta\Omega_{em} \frac{\Delta S_d}{(z+D)^2} \Delta z \tag{3.46}$$

where the coefficients C_i represent the integral terms and depend on both the phase function and the geometry of the cloud. Equation (3.46) is the lidar equation. From it, we see that multiple scattering (MS) effects can be neglected for thin clouds, or if the scattering coefficient is small ($\beta_{sca} \cdot z \ll 4\pi$). In this particular case, the only term left in the square brackets is that originating from single scatter, which can be expressed as:

$$P_{sca}(z) = \beta_\pi \cdot I_0 T_{clr}^2 \cdot e^{-2\beta_{ext}z} \Delta\Omega_{em} \frac{\Delta S_d}{(z+D)^2} \Delta z \ , \tag{3.47}$$

and is the limiting form of the lidar equation (3.1) for thin clouds. When the remaining terms in square brackets are not negligible, MS cannot be neglected.

Seeking a similar formulation to that postulated by equation (3.4), we may write the summation term in equation (3.46) in the following way:

$$\sum_{i=1}^{\infty} \left[C_i \left(\frac{\beta_{sca}}{4\pi} \right)^i z^{i-1} \right] = k \cdot \beta_{sca} \left[1 + \sum_{i=1}^{\infty} a_i \left(\frac{\beta_{sca}}{\beta_0} \right)^i \right] \tag{3.48}$$

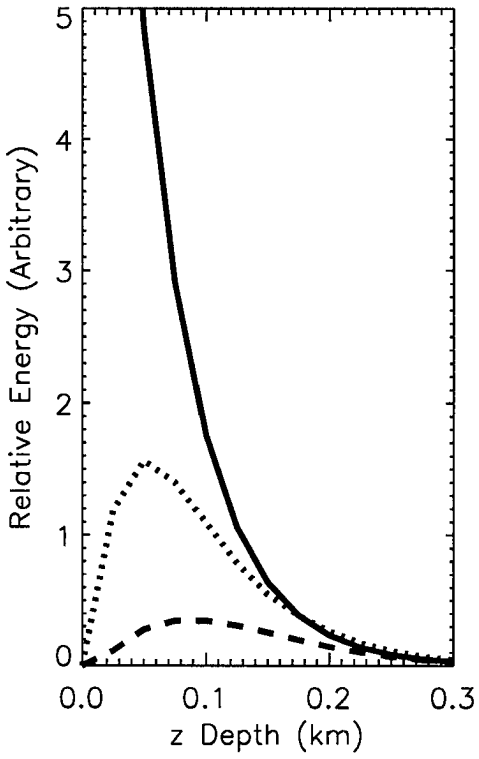

Figure 3.11: Relative energy from different orders of scattering for the "analytical" phase function: first order (solid line), second order (dotted line), third order (dashed line).

where k is a constant yet to be determined, and a_i's are coefficients that depend on cloud particles' phase function, penetration distance z and lidar characteristics (mainly FOV). These coefficients also depend on β_0, which is just some reference value for the scattering coefficient (can be set to 1 km^{-1} for example). Its introduction in the above expression is motivated by the fact that we want to have non-dimensional terms, and therefore to be able to use the property of scalability. This will be better understood later on. Note that contribution from higher order scattering must approach zero as a requirement that the backscatter signal does not become infinite; in other words the above expression describes a saturation effect for higher order scattering contributions.

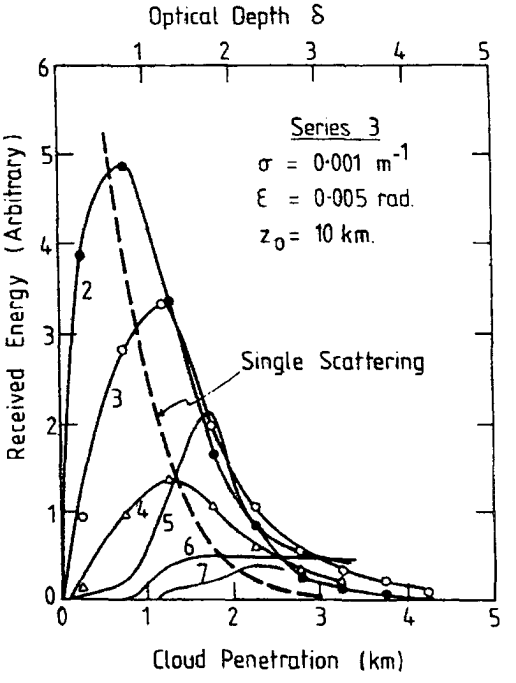

Figure 3.12: The relative received energies in different orders of scattering. (After Platt, 1981)

Moreover, the right hand side of the above expression may also be written as:

$$k \cdot \beta_{sca} \left[1 + \sum_{i=1}^{\infty} a_i \left(\frac{\beta_{sca}}{\beta_0} \right)^i \right] \approx k \cdot \beta_0 \left(\frac{\beta_{sca}}{\beta_0} \right)^n \tag{3.49}$$

where the exponent n is a non-constant parameter describing the MS effects and depends on the penetration distance z, ice crystals' phase function, geometry of the cloud, scattering coefficient and the reference value for scattering coefficient. Notice that the above equation is very similar to the expression postulated in the equation (3.4). One way of setting a value for our constant k is to assume that in the case of no MS then the exponent n is unity (see equations 3.42, 3.48 and 3.49) and thus we can determine that:

$$k = \frac{P(\pi)}{4\pi} \quad . \tag{3.50}$$

Summarizing, we propose that for describing MS effects, the backscatter coefficient that appears in the lidar equation be in the form:

$$\beta_\pi = k \cdot \beta_0 \left(\frac{\beta_{sca}}{\beta_0} \right)^n , \tag{3.51}$$

with k set as explained above, and the exponent n carrying information regarding MS effects. Then, for the purposes of solving the lidar equation, we use the definition of the single scatter albedo written in the form:

$$\beta_{sca} = \tilde{\omega}_0 \cdot \beta_{ext} \quad . \tag{3.52}$$

It is worth mentioning that at lidar wavelengths, the single scatter albedo is close to unity. From these two formulations we obtain an equation that is similar to the postulate expressed by equation (3.4):

$$\beta_\pi = F \cdot \beta_0 \left(\frac{\beta_{ext}}{\beta_0} \right)^n , \tag{3.53}$$

where the inverse of the lidar ratio is:

$$F = \frac{P(\pi)}{4\pi} \cdot (\tilde{\omega}_0)^n \quad . \tag{3.54}$$

Although similar, (3.51) and (3.52) describe two different properties of a cloud: first, (3.51) models the total backscatter coefficient in terms of the scattering coefficient; second, (3.52) expresses a linear relationship between the backscatter coefficient to the extinction coefficient as being defined by similar definition equations (see equation 3.3), and is the definition for the single scatter albedo. Later, when constructing the inverse model, we will show that the use of a nonlinear function for describing MS effects, as expressed by equation (3.53), is preferred over the linear one.

To assess MS effects, we compute the contributions to the backscatter from the first three scattering orders using various phase functions [Baran et al. (2001)], assuming an extinction coefficient of 10 km^{-1} for a homogeneous cloud at an altitude D=10 km having a 2 km thickness. Lidar FOV is set to 1 mrad. The results are presented in Figure 3.13, where only the contribution to the backscatter is

plotted, and the terms involving the inverse power law with range, the two-way transmission factor as well as other lidar parameters are left out. The first order backscattering (solid line) is constant throughout this homogeneous cloud as one would expect. The second order scatter (dotted line) increases linearly at the bottom of the cloud, reaches a maximum value and close to the top of the cloud starts decreasing linearly to zero. Depending on the phase function, the shape and maxima can vary. Note the close to symmetry shape with respect to the middle of the cloud. Looking at the third order backscatter (dashed line), we can see the quadratic dependence on the penetration distance, and as expected after reaching a maxima, the contribution rapidly starts decreasing to zero somewhere above the cloud top, but contrary to the previous two orders of scattering it has a non-zero value above the cloud top. Again the magnitude of this order of scattering depends on the phase function, but the general shape is similar for all phase functions. This is a result of the power law for the multiple scattering terms (second order and up); for various extinction/scattering coefficients, the amplitude of these terms will increase or decrease, but for a given phase function and lidar geometry the shape of the curves will remain the same, making them relatively easy to be parameterized and therefore useful in a forward and inverse model.

When adding these MS contributions we can use the following equation:

$$\beta_\pi = \frac{P(\pi)}{4\pi} \cdot \beta_{sca} \cdot \left[1 + a_1 \left(\frac{\beta_{sca}}{\beta_0} \right) + a_2 \left(\frac{\beta_{sca}}{\beta_0} \right)^2 \right] \tag{3.55}$$

where a_1 and a_2 are computed from our integral expressions (3.43) and (3.44) for a specific value β_0:

$$a_1 = \frac{\beta_0}{2P(\pi)} \int_0^z \int_{\mu_1(x)}^{\mu_2(x)} P(\mu)P(-\mu)\mu^2 \, d\mu dx \tag{3.56}$$

$$a_2 = \frac{\beta_0^2}{2\pi P(\pi)} \int_0^{\min(z,z_T)} \int_{\mu_1(x)}^{\mu_2(x)} \int_0^{R(\mu)} \int_{\phi_1'}^{\phi_2'} \int_{\mu_1'}^{\mu_2'} P(\mu)P(\mu')P(\mu'') \times |\mu \cdot \mu' \cdot \mu''| d\mu' d\phi' dr d\mu dx \quad . \tag{3.57}$$

We note that depending on the phase function, the contribution from the second and third order scattering differs, although the shape of this dependence with respect to cloud penetration depth is quite similar.

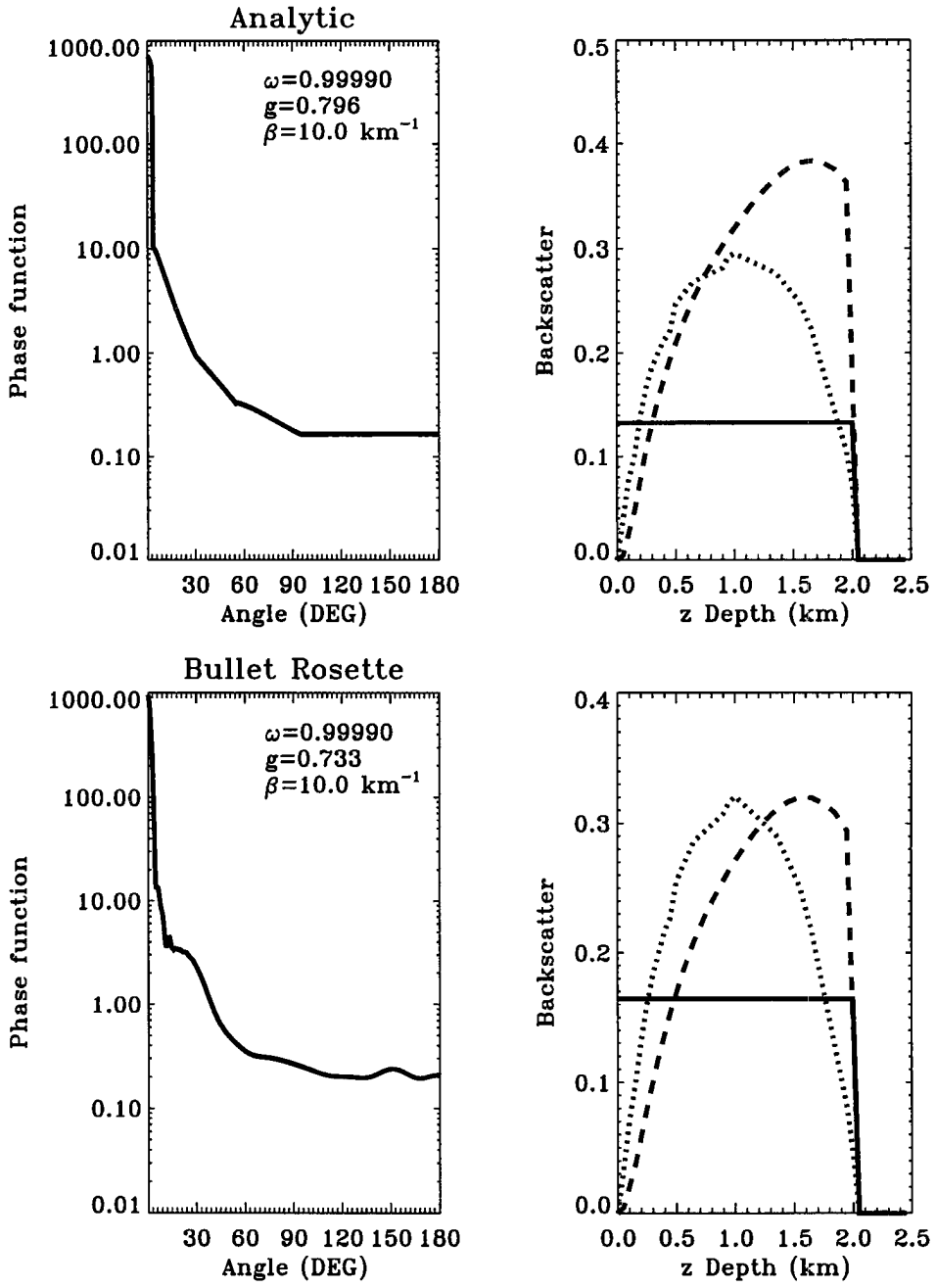

Figure 3.13: Multiple Scattering Contributions (right panels) to the Backscatter for a given Phase Function (left panels): first order (solid line), second order (dotted line), third order (dashed line).

The above formulation explains the apparent contradictory results reported by different authors regarding the magnitude of MS for various types of clouds. One school of thought proposes that these MS effects are very small compared with the first order backscatter. In a paper by Liou and Schotland (1971), the contribution from the second order backscatter is between 5 and 8 % of the first order, depending on the radius of the cloud particles that is considered (4 μm and 8 μm respectively) for a fixed number concentration. The third order is one order of magnitude lower than the second order. The conclusion is that the MS effects can be neglected [Liou (1971)]. At the other extreme, Miller (1997), using a Monte Carlo model for MS problem, pointed out that contributions from higher order scattering become important as both the optical depth and the penetration depth are increased. However, as seen from the explicit representation for the MS terms, the lidar FOV and the distance between cloud and lidar (D) are important in determining the magnitude of these terms. A simple analytical evaluation of their effects is not an easy job, especially for higher scattering orders. These complications contribute to apparently different results obtained by different authors.

The main advantage of the new approach presented here is its scalability with respect to the extinction coefficient, and to the best of our knowledge, it is the first time that a simple analytical expression is proposed for modeling the MS effects. It also gives a basis for the postulated expression given by equation (3.4). However, as in previous work, coefficients must be pre-computed or some empirical assumptions must be made. This implies knowledge of the phase functions associated with the cloud particles, FOV and D.

In the next section, we make use of the polynomial expression that describes the MS effects (equation 3.55) when we construct our inverse model for retrieving the vertical profile of the extinction coefficient. Along with this important cloud characteristic, and using some simplified assumptions we can determine the mean lidar ratio, particle number concentration and ice water content.

3.4.1 MS Effects on Cloud Transmittance

As radiation penetrates a cloud layer, it is scattered and absorbed. When there is no MS, the amount of radiation that is transmitted is linearly related to the amount of radiation that is absorbed and scattered. This is in fact the definition of transmittance. When MS effects are to be considered, some of the scattered radiation can in fact be interpreted as "transmitted" through the cloud, thus the "apparent" transmittance affected by the MS effects for this particular cloud layer decreases. In the literature, this effect is parameterized as the scattering coefficient η, which is positive and less that unity [Platt (1979)]:

$$T_{MS} = T^{\eta} \quad . \tag{3.58}$$

In other words, equation (3.58) implies that the extinction coefficient itself is reduced by the MS effects, and we can write the "apparent" extinction coefficient in the form:

$$\beta_{MS} = \eta\, \beta \quad . \tag{3.59}$$

However, we must remember that MS effects are only due to scattering and not to absorption; therefore the above equation fails for media that absorbs. Also, there is no evidence to convince us that the above equation has any physical meaning. In fact, MS is a nonlinear additive process and not a multiplicative one, as we showed in the previous section. Based on these developments, we can express the amount of detected power coming from the region above the cloud, due to molecular backscattering in the form:

$$\Delta P^{(1)}_{mol}(z) \approx \frac{\beta_R}{4\pi} I_0 T^2_{clr} P_R(\pi) \cdot e^{-2\beta_{ext} z_t} \Delta\Omega_{em} \frac{\Delta S_d}{(z+D)^2} \Delta z \tag{3.60}$$

where β_R is the molecular scattering coefficient, $P_R(\pi)$ is the backscatter molecular phase function and z_t is the thickness of the cloud. Since the FOV is very small, we can approximate the amount of radiation due to two extra scattering events in the cloud layer interpreted as coming from the same range z in the form:

$$\Delta P^{(2)}_{mol}(z) \approx 2 \left(\frac{\beta_{sca}}{4\pi}\right)^2 \frac{\beta_R}{4\pi} I_0 T^2_{clr} P_R(\pi)$$

$$\times 2\pi \int_0^{z_t} \int_0^{\delta(z,z_t)} \int_{\mu_1(x)}^{\mu_2(x)} [P(\mu)\mu]^2 e^{-\beta_{ext} x(1-\mu)}\, d\mu dx dz' \qquad (3.61)$$

$$\times e^{-2\beta_{ext} z_t} \Delta\Omega_{em} \frac{\Delta S_d}{(z+D)^2} \Delta z \quad .$$

Here the constraints that determine both the possible scattering angles μ_1 and μ_2 as well as the parameter δ are expressed as:

$$0 \leq \delta\mu + z \leq z_t \qquad (3.62)$$

$$\delta\sqrt{1-\mu^2} \leq (z+D)\sin\theta_{det} \qquad (3.63)$$

$$0 \leq \delta(1-\mu) \leq 2(z-z_t) \qquad (3.64)$$

and simply require that the two extra in-cloud scatterings take place in the lidars' FOV illuminated cloudy region, and that the total path be identical to the pure molecular backscattering one. The factor of two that appears in front of equation (3.61) is due to the two in-cloud scattering events that can take place either before or after the molecular scattering.

The ratio between the two above expressions for the measured power gives us the relative increase in observed backscatter power for the region above the cloud, due to MS effects (limited to the second order effect for this particular case):

$$R \approx \frac{\beta_{sca}^2}{4\pi} \int_0^{z_t} \int_0^{\delta(z,z_t)} \int_{\mu_1(x)}^{\mu_2(x)} [P(\mu)\mu]^2 e^{-\beta_{ext} x(1-\mu)}\, d\mu dx dz' \quad . \qquad (3.65)$$

A simple inspection of this ratio shows that it has a complicated form, depending on the square of the extinction coefficient, the phase function and geometry of the cloud. Since MS is additive, we expect this ratio to increase with cloud thickness. The variations of this ratio with respect to cloud extinction coefficient (β_{ext}) for four different phase functions for a 2 km cloud layer, are presented in Figure 3.14. The single scatter albedo for cloud particles is assumed unity. The molecular backscattering was assumed to take place anywhere within a 200 m distance range. Simulations showed that this value is not critical for our calculations since for the region above the cloud we are still in the lidar's small FOV, thus the propagation of light can be considered almost parallel. From this figure, we note the expected nonlinear

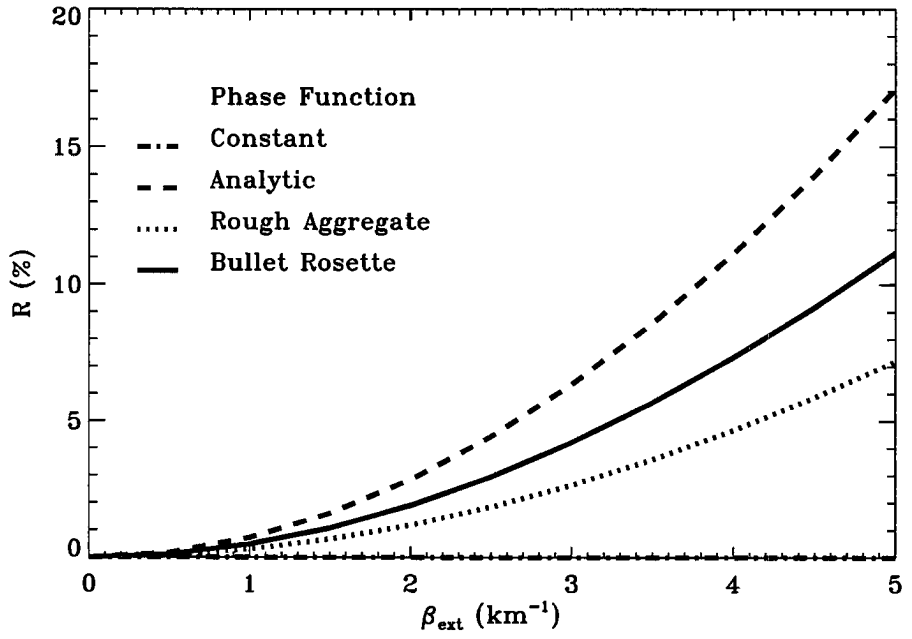

Figure 3.14: MS contributions to the received molecular backscatter signal from a region above the cloud as function of cloud extinction coefficient.

behavior with the extinction coefficient and the different response for various phase functions. However, for extinction coefficients less than 3 km^{-1} the MS influence on the signal above the cloud is less than 3 %. This means that the reference signal that enters into equation (3.14) must be corrected for the MS effects with the calculated value for R for the specified cloud thickness, phase function and extinction coefficient. In the end, this corrected reference signal will influence the gain and offset of the lidar as well as the transmittance of the cloud. However, transmittance will be most influenced by this correction. This is because in equation (3.14) it multiplies the reference signal for the region above the cloud. It can be concluded that the corrected transmittance T_{MS} should be in the form:

$$T_{MS} \approx T/\sqrt{1+R} \tag{3.66}$$

where T is the un-corrected transmittance. Based on our simulations, the correction factor R is less than about 3 % for the measured cirrus clouds. This value is less

than the errors in transmittance associated with errors in our lidar signal, and for this reason we choose not to make any MS corrections to the cloud transmittance.

3.5 Retrieving the Extinction Coefficient (Inverse Model)

The starting point for constructing our forward model is the lidar equation which also accounts for molecular backscatter (β_R):

$$\beta'(z) = (\beta_\pi + \beta_R) \exp\left[-2\int_0^z \beta_{ext} dz'\right] \tag{3.67}$$

where $\beta'(z)$ is the range corrected measured backscatter (also corrected for attenuation due to Rayleigh absorption), β_π is the cloud backscatter and the exponential term is the two-way attenuation factor due to cloud absorption. This last term can be approximated as follows:

$$\exp\left\{-2\int_0^z \beta_{ext} dz'\right\} \approx \exp\left\{-\frac{\Delta z}{\tilde{\omega}_0}\sum_{j=1}^{i}[\beta_{sca}(j) + \beta_{sca}(j-1)]\right\}$$

$$= T^2(z-\Delta z)\cdot \exp\left\{-\frac{\Delta z}{\tilde{\omega}_0}\beta_{sca}(z)\right\} ,$$

where we used equation (3.52) and the notation:

$$T(z) = \exp\left\{-\frac{\Delta z}{\tilde{\omega}_0}\sum_{j=1}^{i}\beta_{sca}(j)\right\} . \tag{3.68}$$

For a given level z $(= i \cdot \Delta z)$, the inverse model is simply the solution to the transcendental equation:

$$\beta_\pi = \beta'(z)\cdot T^{-2}(z-\Delta z)\cdot \exp\left[\frac{\Delta z}{\tilde{\omega}_0}\cdot\beta_{sca}\right] - \beta_R , \tag{3.69}$$

together with our postulate expressed by (3.55), which provides the relationship between scattering and backscattering coefficients. Then an iterative method for solving the above equations can be used:

$$\beta_{sca}^{(p+1)} = \frac{4\pi}{P(\pi)}\cdot\left[1 + a_1\left(\frac{\beta_{sca}^{(p)}}{\beta_0}\right) + a_2\left(\frac{\beta_{sca}^{(p)}}{\beta_0}\right)^2\right]^{-1}\beta_\pi(\beta_{sca}^{(p)}) \tag{3.70}$$

where p is the order of iteration. The iterative process continues until the convergence criteria is met:

$$\frac{\mid \beta'(z) - \beta'(i \cdot \Delta z) \mid}{\beta'(z)} \leq \epsilon_y \tag{3.71}$$

which states that the relative error between the measured attenuated backscatter $\beta'(z)$ and the calculated value $\beta'(i \cdot \Delta z)$ should be less than the inverse model relative error ϵ_y. Since we have no *a priori* knowledge about the phase function nor the single scattering albedo some assumptions must be made. We assume that the clouds are almost perfect scatterers which means that the single scattering albedo is close to unity and therefore this parameter is set to 0.999. The backscatter phase function $P(\pi)$ is determined such that the calculated transmittance matches the transmittance determined from the calibration procedure. However the coefficients a_1 and a_2 that describe the MS contribution are calculated using the "analytical" phase function. Therefore, the actual procedure involves two iterations: one that determines $P(\pi)$, while the other calculates the profiles for the scattering coefficient. In order to test the validity of such an approach several synthetic tests were performed and their results are presented later, in comparison with results from published lidar inversion methods.

A special note must be made in the particular case when MS effects are neglected. In this case, a necessary condition for the existence of a solution (β_{sca}) for our equation is (note that $\beta_R \ll \beta_\pi$):

$$\beta_{sca} \leq \frac{\tilde{\omega}_0}{\Delta z} \tag{3.72}$$

or in other words, the maximum value for the retrieved extinction coefficient is on the order of the inverse of the lidar vertical resolution:

$$\beta_{ext} \leq \frac{1}{\Delta z} \quad . \tag{3.73}$$

An important concept in radiative transfer theory is the mean free path, defined as the inverse of the extinction coefficient [Stephens (1994)]:

$$< L >= \frac{1}{\beta_{ext}} \quad .$$

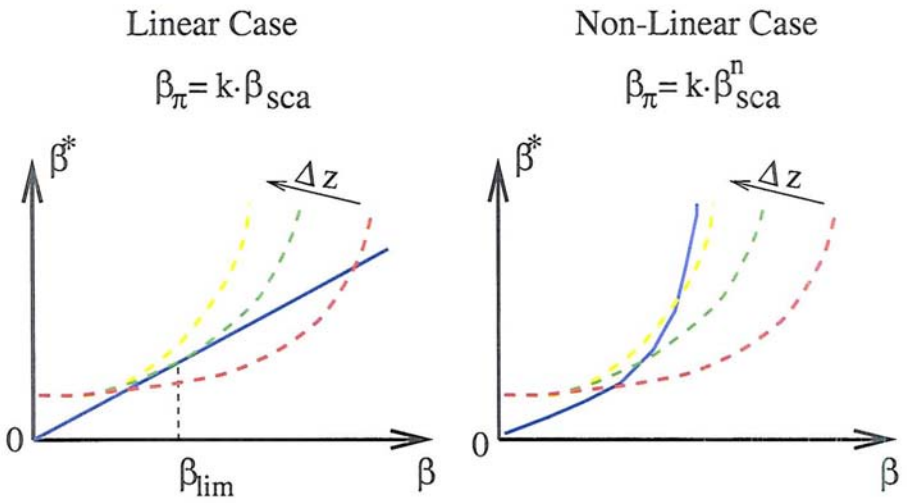

Figure 3.15: Inverse Method iteration procedure: Linear case: as the vertical resolution Δz increases, there is a limit in the retrieved scattering coefficient (β_{lim}). Non-linear case: a solution for the retrieved scattering coefficient exists for all possible vertical resolutions.

It is interpreted as the mean length that a photon can travel without interacting with matter (i. e. not being absorbed or scattered). From the above definition and equation (3.73), which expresses a necessary condition for solution in the case with no MS effects, we can conclude that the lidar resolution Δz is the minimum mean free path for such a lidar system. For the MPL lidar that is used, with a vertical resolution of 90 m, the maximum retrievable extinction coefficient without MS effects, is in the order of 11 km^{-1}. For clouds whose extinction coefficient exceeds this value, our scheme will not converge. Inclusion of the MS effects in the way presented above, increases the upper limit of our retrieval. This can be seen in Figure 3.15(b) where MS effects are taken into account, as opposed to Figure 3.15(a) where linear dependence is assumed. In Figure 3.15(b), we always have a solution for any values of the lidar resolution (Δz), while in Figure 3.15(a) as we decrease the resolution (i. e. increase Δz) the solutions cease to exist.

As mentioned above, the proposed retrieval procedure was tested on a few synthetic cases. First, a cloud with a specified profile for the scattering coefficient (β_{sca})

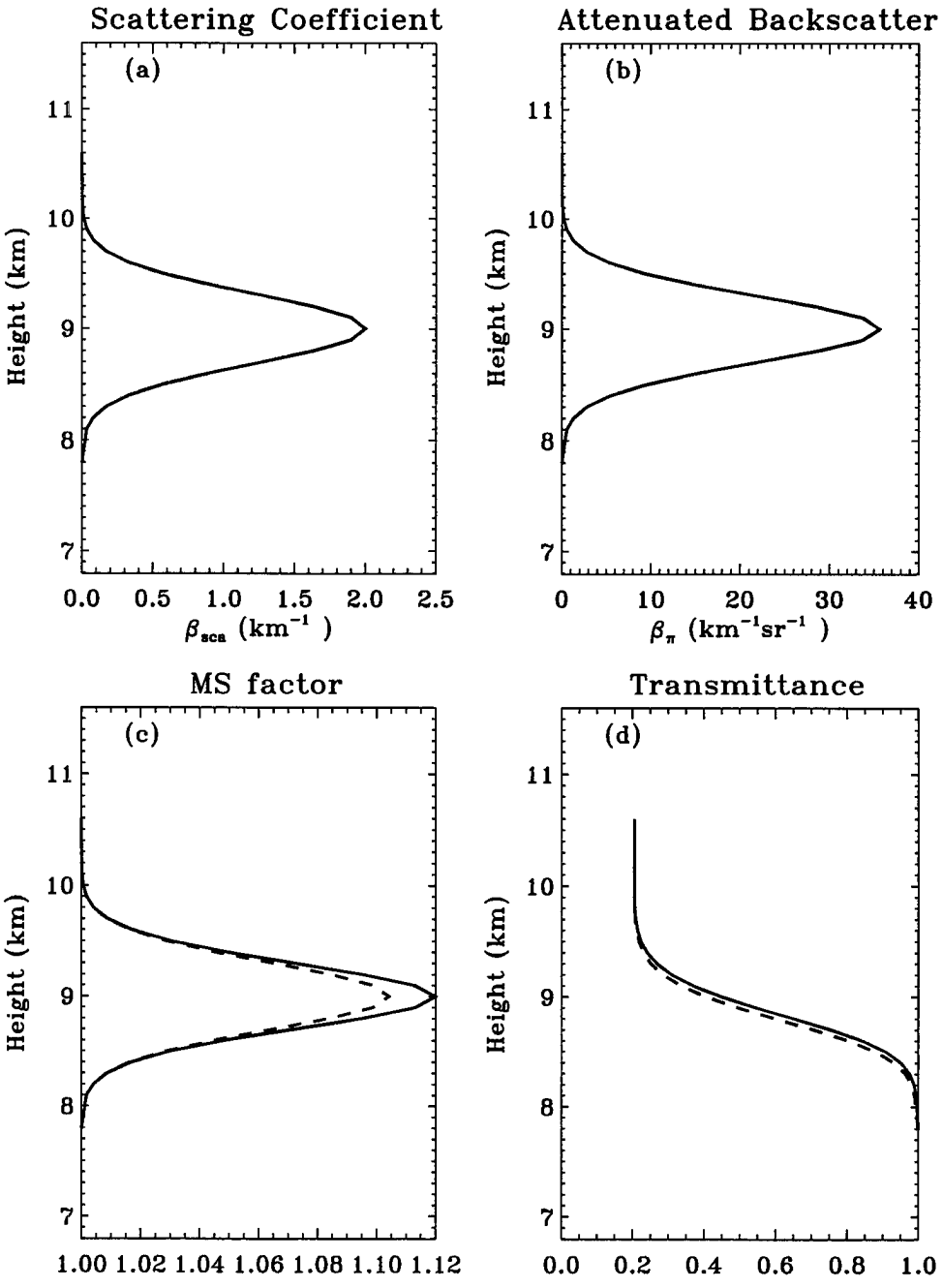

Figure 3.16: Synthetic case 1: (a) Scattering Coefficient; (b) Attenuated Backscatter; (c) MS contribution; (d) Transmittance. Input parameters – solid line; Retrieved quantities - dashed line.

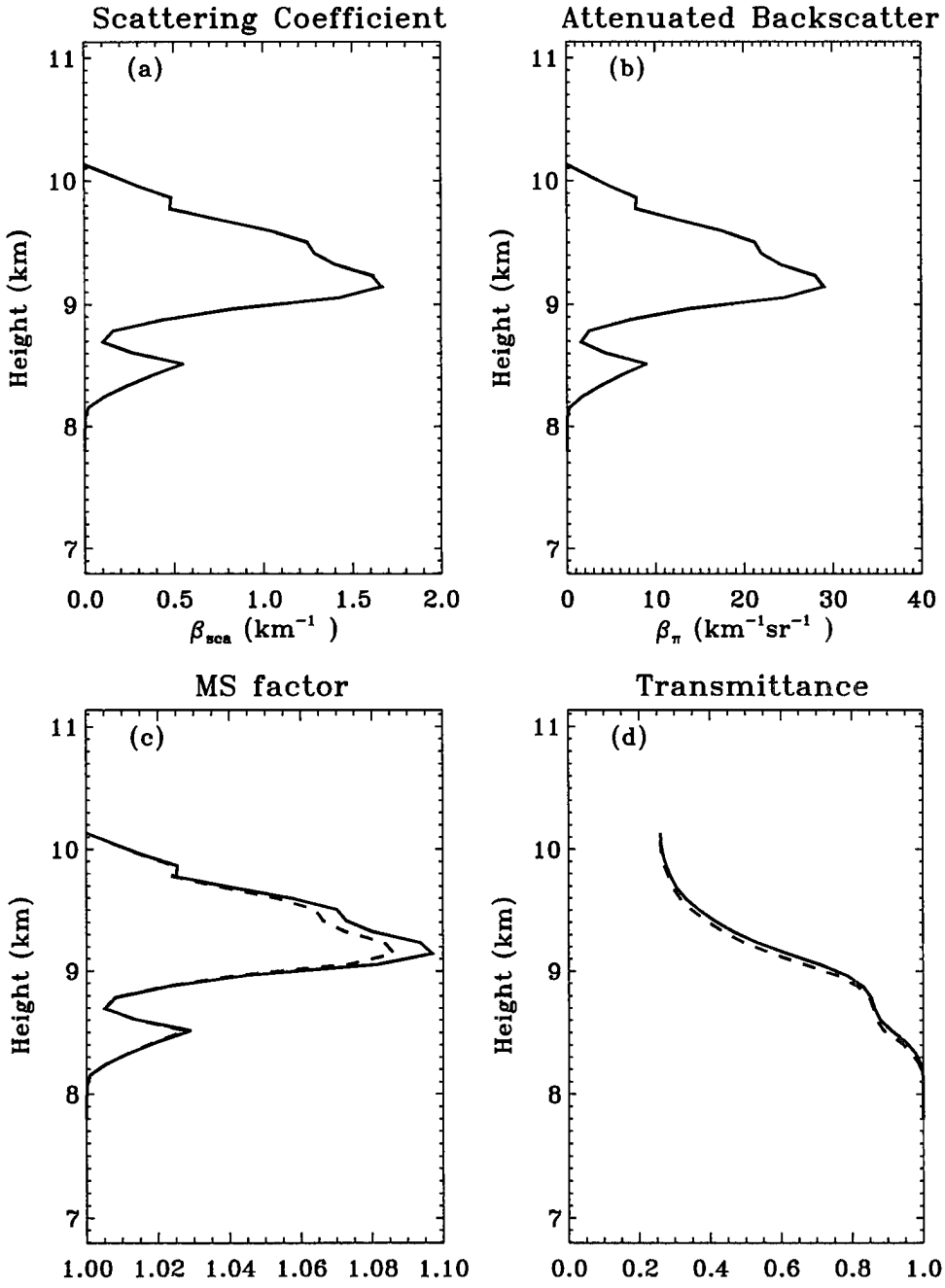

Figure 3.17: Synthetic case 2: As in Figure 3.16 but using MPL data at Nauru on 05/01/1999 09:00 UTC.

in the form:

$$\beta_{sca}(z) = \beta_{max} \cdot exp\left[-\frac{(z - z_0)^2}{(\Delta z)^2}\right]$$

where $z_0 = 9$ km, $\Delta z = 0.447$ km and $\beta_{max} = 2$ km^{-1}sr-1 was tested (see Figure 3.16). We specified values for the single scattering albedo ($\tilde{\omega}_0 = 0.999$) and phase function ($P(\pi) = 0.2$ sr^{-1}). For this "synthetic" cloud, the MPL attenuated backscatter coefficient was generated using equations (3.55) and (3.67). For simplicity, since the second order backscattering contribution has a very rapid variation with cloud penetration in the first few hundred meters, then becomes relatively constant, the coefficient a_1 was set to half. Since our clouds are relatively transparent, the contribution from the second order backscatter was assumed to be constant throughout the cloud and therefore we assumed $a_2 = 0.5$. The above parameters were determined from Figure 3.13(b) which was produced for the "analytic" phase function. In Figure 3.16, we present the initial and retrieved profiles for various cloud parameters. We see that the differences between the retrieved quantities and the synthetic ones are negligible as we imposed a relative error for our convergence criteria on the order of 10^{-7}. We also mention that the value of the backscatter phase function $P(\pi)$ was also correctly determined by the proposed algorithm. The main problem that may arise is when computing cloud transmittance. For very thick clouds, due to inherent errors that accumulate, the computed cloud transmittance is underestimated affecting the retrieved quantities, with errors increasing with the penetration depth. We tested the inverse algorithm for a variety of clouds and it performed very well provided that cloud transmittance was above 0.01.

A second round of tests were performed on MPL data using the inverse model to determine the extinction coefficient profile for a given $\tilde{\omega}_0$ and then using the direct model to recompute the profile for attenuated backscatter coefficient. Using this synthetic attenuated backscatter profile we retrieved the same cloud parameters as in previous cases. The results are presented in Figure 3.17, from which we can see that the retrieved quantities agree very well with the initial ones. Like in the first set of tests, the backscatter phase function was also correcly retrieved. In another series of tests we vary the value for the single scattering albedo and/or the MS

contribution by varying the values for a_1 and a_2. The extinction coefficient profile didn't change significantly, which is what we expected since the transmittance was kept unchanged. When we lowered the single scattering albedo (i. e. decreasing the scattering contribution and increasing the absorption), the retrieved value for $P(\pi)$ increased as the attenuated backscatter remained the same — more light must be first order backscattered and less scattered sideways; therefore MS effects decrease. When changing the MS contribution by varying a_1 and a_2 a similar effect was observed: lower values for a_1 and a_2 increased the first order backscatter contribution.

The results obtained from these synthetic cases suggest that the proposed algorithm for determining cloud properties is valid.

The relative errors in the scattering coefficient are due to errors in the attenuated backscatter coefficient, in transmittance, and forward model. Using equations (3.68), (3.69) and (3.70) we can write:

$$\left[1 + 2a_1\beta(j)/\beta_0 + 3a_2[\beta(j)/\beta_0]^2\right] \frac{\delta\beta(j)}{\beta(j)} = \frac{\delta y}{y} + \frac{\delta\beta'}{\beta'} + \frac{\delta T_0^2}{T_0^2} + \frac{\delta\Delta T_0}{\Delta T_0}$$

where δy is the convergence criteria absolute error, $\delta\Delta T_0$ is the absolute error associated with the exponential term in equation (3.61) and all other terms are self explanatory. Here we used the fact that the individual relative errors are not independent, along with the assumption that the Rayleigh backscattering is small relative to cloud backscattering. Employing the following notation for the relative error of a variable w as:

$$\epsilon_w = \frac{\delta w}{w}$$

we can write that the relative error of the retrieved scattering coefficient is:

$$\epsilon_{\beta(j)} = \frac{\epsilon_y + \epsilon_{\beta'(j)} + 2\epsilon_T}{1 - \beta(j)\Delta z/\tilde{\omega}_0 + 2a_1\beta(j)/\beta_0 + 3a_2[\beta(j)/\beta_0]^2} \tag{3.74}$$

where ϵ_y is convergence criteria error; $\epsilon_{\beta'(j)}$ is the attenuated backscatter coefficient error as determined from the calibration procedure at each level j, and ϵ_T is the transmittance error, evaluated by:

$$\epsilon_T = \frac{\Delta z}{\tilde{\omega}_0} \sum_{k=0}^{j-1} \beta(j)\epsilon_{\beta(j)} \quad .$$

A casual perusal of equation (3.74) reveals that we may expect larger errors when: (1) the cloud particles become more absorbing (i. e. $\tilde{\omega}_0$ becomes smaller), (2) the lidar vertical resolution decreases (Δz increases), and (3) the degree of confidence in the phase function degrades. Due to the transmittance error that increases with the penetration depth, the relative errors increase with height. To be noted here is the fact that our proposed model for MS effects helps in reducing the error levels for the retrieved scattering coefficient, and as expected, the reduction is more pronounced when the MS effect is more important. Moreover, the MS effects are more dominant in clouds composed of particles that have lower values for the backscatter phase functions $P(\pi)$ [Platt et al. (1999)].

So far, nothing was said about the lidar ratio defined from equation (3.4) with the exponent n set to unity. It can be computed as defined in the forward model (see equation 3.49). In cirrus clouds, the lidar ratio is not constant throughout the cloud and this is especially true if layers of falling crystals are present. During the fall, the highly anisotropic ice crystals are oriented with their longest axis parallel to the ground. In this case, few horizontally oriented ice crystals acting like small mirrors are able to produce large backscatter signal while the extinction coefficient is practically the same. As a consequence the lidar ratio can be very small — less than 3 sr according to Ansmann et al. (1992a). In the case of small numbers of small spherical particles the lidar ratio can be quite large (up to 80 sr).

In order to evaluate the profile for the lidar ratio, one must know the profiles for both the scattering coefficient and the extinction coefficient. This is not possible unless a Raman lidar is used. The technique involved in this case uses both the elastic and inelastic backscattered signal to independently calculate profiles for the two variables involved in the definition of the lidar ratio. However, the evaluation of the extinction coefficient also requires knowledge of the molecular number density profiles, computed from the perfect gas law using profiles for temperature and pressure as determined from radiosondes. The errors in the extinction coefficient introduced by the presence of temperature inversions can be as large as 10 to 20 %. The presence of noise in the weak Raman signal can also introduce relatively large errors for the estimates. Measurements using Raman data showed that the lidar

ratio varies quite significantly in the cloud. Since a Raman lidar is not available at the TWP locations, only MPL lidar data is used; for this reason, an averaged value for the lidar ratio is determined. It is understood that this mean value is representative only of clouds whose particle size distribution, hence phase functions are similar. The treatment for MS effects is dealt with separately in contrast to previous techniques where the MS effects were modeled by reducing the two-way transmittances. In these techniques, *a priori* knowledge of the lidar ratio must be provided. Any errors in this parameter will propagate into the magnitude for the MS effects. From our model, we can easily deduce that the errors in the determined lidar ratios are related to errors in the transmittances:

$$\left| \frac{\Delta F}{F} \right| = \left| \frac{1}{\ln T} \cdot \frac{\Delta T}{T} \right| \tag{3.75}$$

and we expect that the level of confidence in the assumed values for the lidar ratios to decrease for thiner clouds. Time series for the lidar ratios are presented in Figure 3.18. We note that in the case of thin cirrus the ratio is around 80 sr, while for more consistent ones the ratios is around 24 sr. Both these values are within the observed values determined with Raman lidar for cirrus clouds [Ansmann et al. (1992a)].

Using the above retrieved cloud optical properties, and some simple assumptions about the cloud particles, cloud microphysical properties can be derived. For example, the IWC profile can be deduced by using the retrieved extinction coefficient, assuming constant effective radius for the entire cloud [Stephens et al. (1990)]:

$$w(z) = \frac{2\rho}{3} r_{eff} \beta_{ext}(z) \tag{3.76}$$

with $\rho = 920$ kg/m^{-3} and $r_{eff} = 30$ μm. The particle concentration profile can be deduced from the definition of the extinction coefficient (equation 3.3) assuming that the distribution for the diameters of ice particles follows a gamma distribution, and the main body of this distribution is due to ice particles that are larger than 10 μm. In this case the extinction efficiency $Q_{ext}(D) \approx 2$ and therefore we can write:

$$N_t(z) = \frac{4 \cdot \beta_{ext}(z)}{3\pi r_{eff}^2} \quad . \tag{3.77}$$

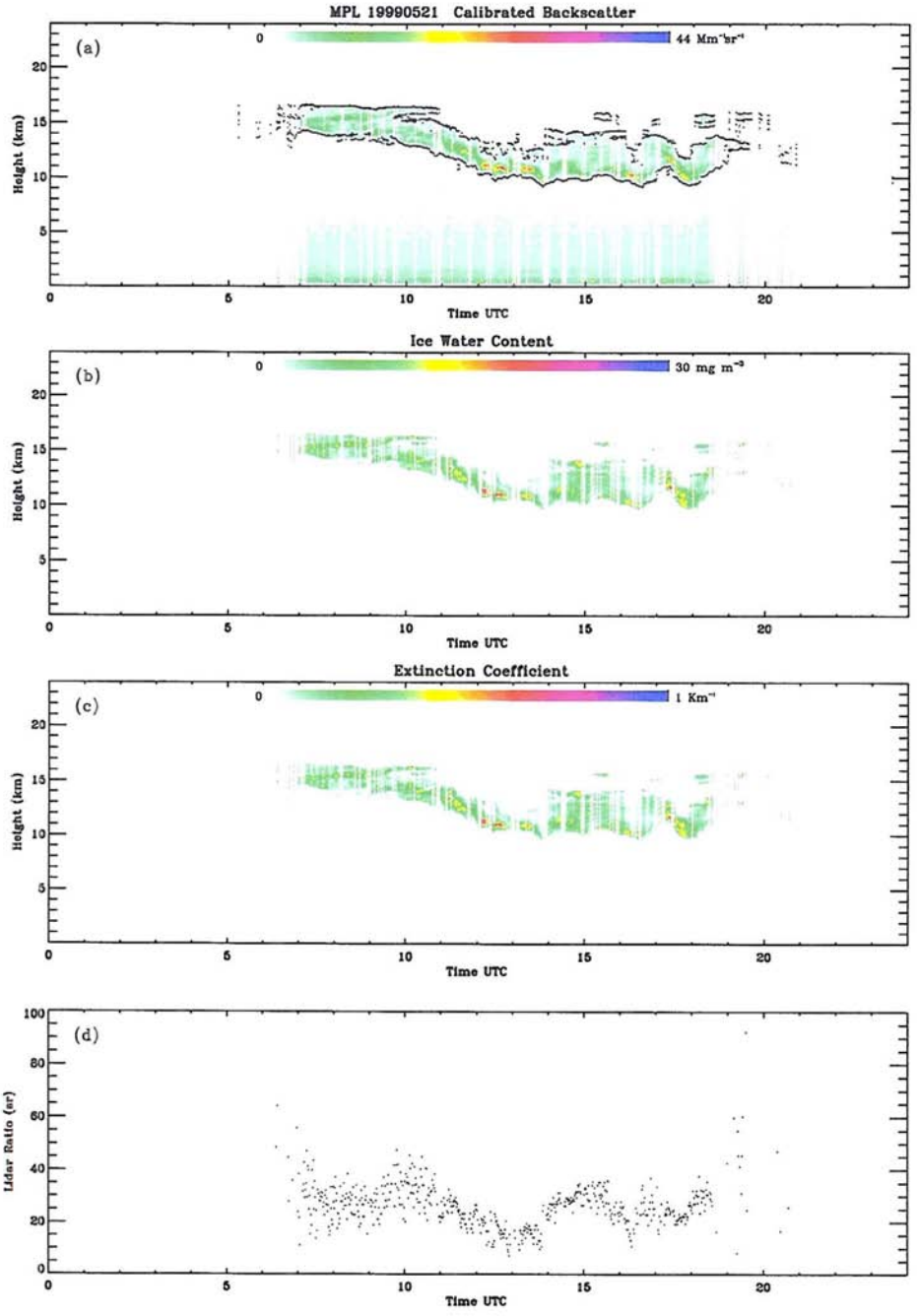

Figure 3.18: Time series for: (a) Backscatter coefficient (Cloud boundaries with dots); (b) Ice Water Content; (c) Extinction coefficient; (d) Lidar Ratio.

It is clear that both the IWC and N_t will follow the shape of the extinction coefficient. This is a result of the limited information that we have, namely one equation with more than one unknown. Inverting this equation will only give us at best some estimates about our retrieved quantities, which depend on one hand on the assumptions made when constructing the forward model and on the other, on the parameters that we use in this forward model. Errors associated with the inverse model only increase the level of uncertainty in our retrieved quantities. However, we expect that integrated or mean values of these retrieved quantities to be within the measured ones. In our particular case we can estimate both the Liquid Water Path (LWP):

$$LWP = \int_0^{Z_t} w(z')dz' \tag{3.78}$$

and the mean number concentration ($< N_t >$):

$$< N_t >= \int_0^{Z_t} N_t(z)dz' / \int_0^{Z_t} dz' \tag{3.79}$$

but we can easily understand that both these quantities are in fact related to the cloud optical depth. In Figure 3.19 cloud optical and microphysical properties for a particular lidar profile are presented.

The vertical profile for the retrieved IWC can be used for determining the effects of clouds on radiation. We can also estimate the magnitude of these effects due to uncertainties (errors) in our retrievals. In a following chapter (Chapter 6) we use retrieved IWC profiles to compute fluxes and heating rates using a radiative transfer model, and compare these values to the observed fluxes.

3.6 LIDAR derived tropical cirrus statistical properties

MPL data collected at Nauru during a three month period starting May and ending July 1999 were processed using the lidar algorithm described above. The results are presented in Figures 3.20 and 3.21 in the form of probability distribution functions (PDFs) for various cloud characteristics in terms of mean cloud temperature, as shown in Figure 3.20(c). In Figure 3.20 PDFs for cloud base, cloud top, cloud thickness and mean extinction coefficient are presented. Since other cloud characteristics

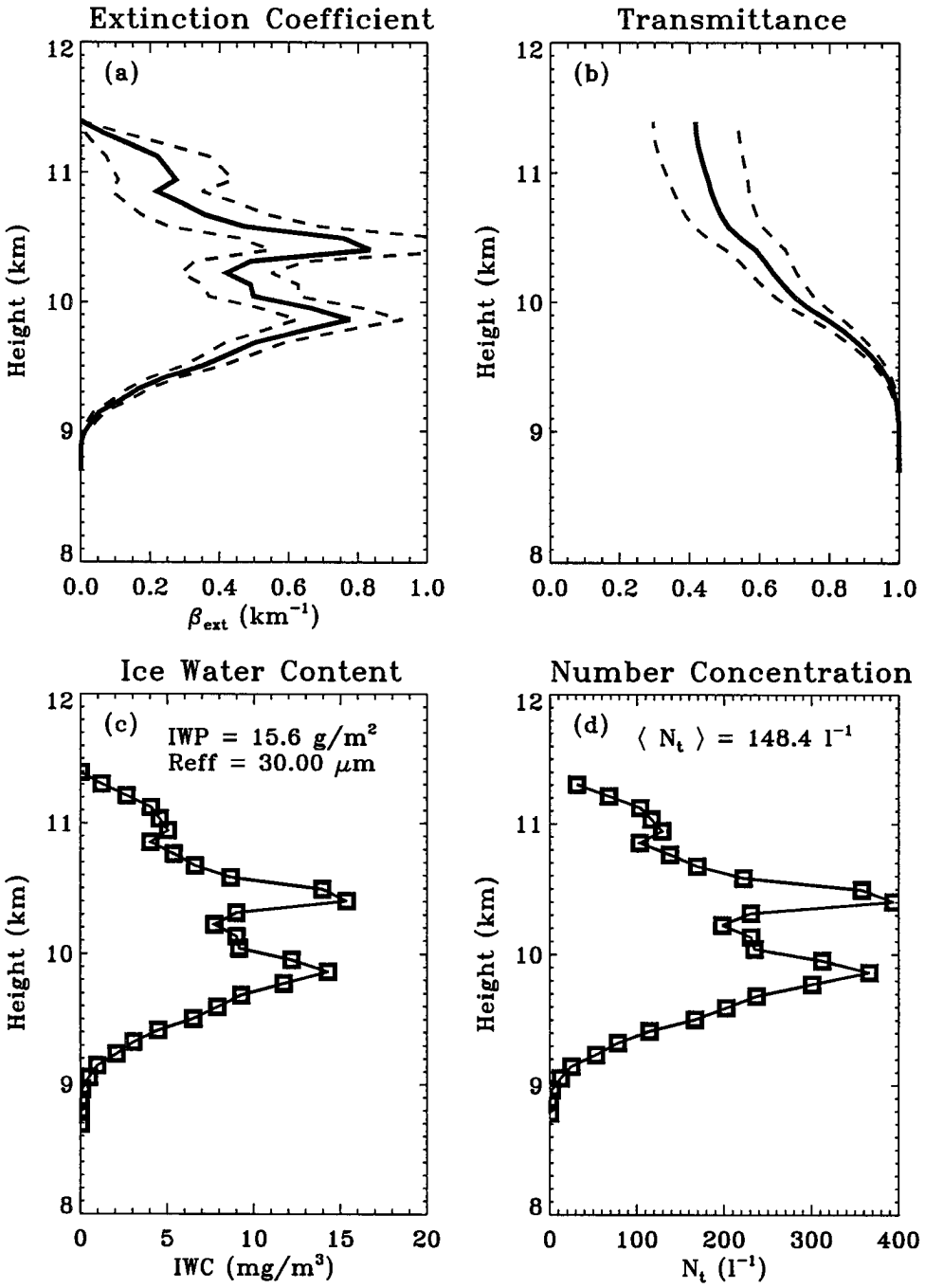

Figure 3.19: Retrieved quantities: (a) Extinction Coefficient (errors shown by dashed lines); (b) Transmittance (errors shown by dashed lines); (c) Ice Water Content; (d) Number Concentration. Nauru, 01/05/99 08:22:08 UTC.

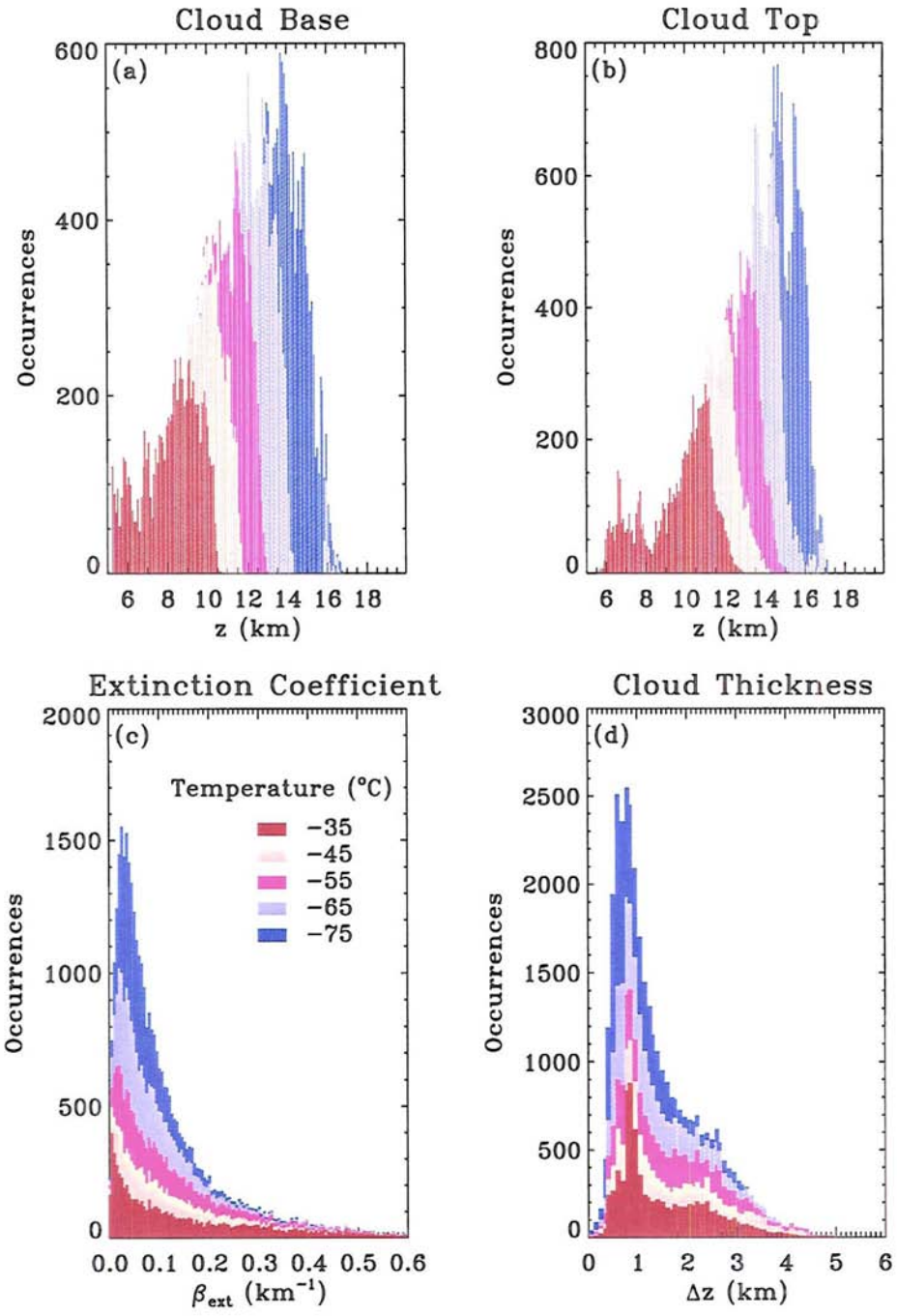

Figure 3.20: PDF for (a) Cloud base; (b) Cloud top; (c) Mean extinction coefficient; (d) Cloud thickness.

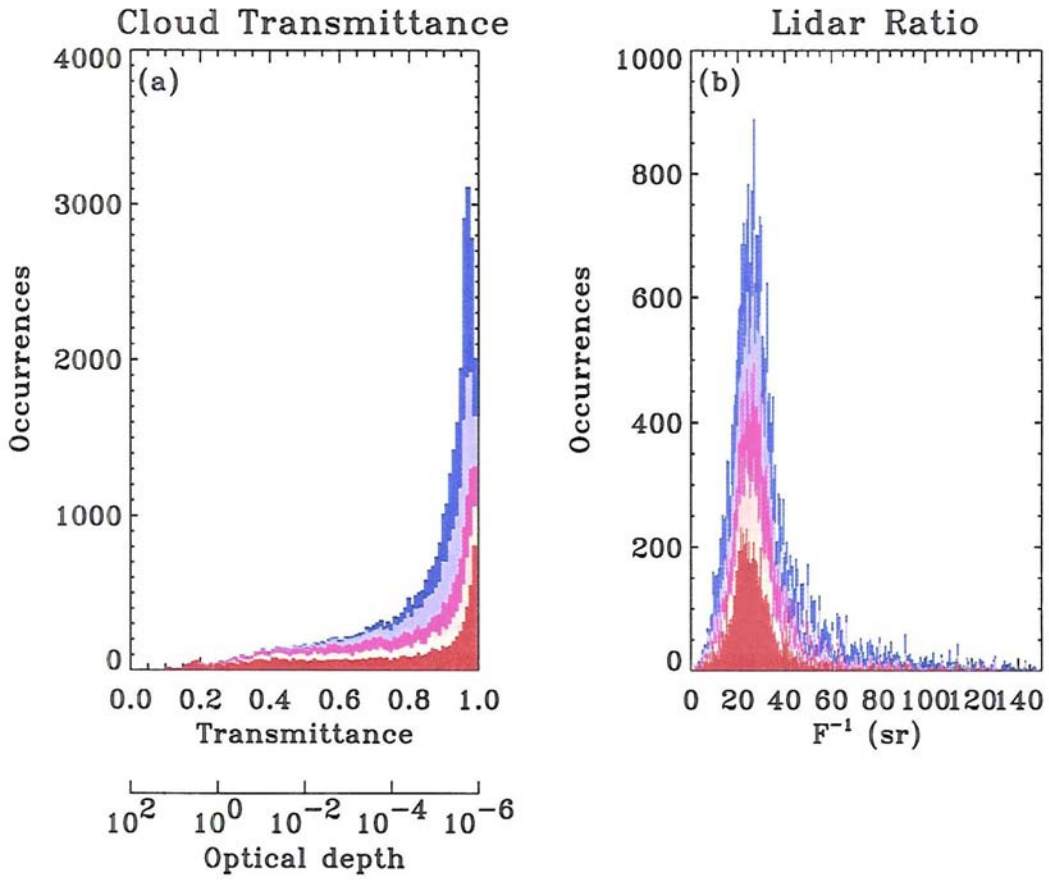

Figure 3.21: PDF for (a) Cloud Transmittance; (b) Cloud Lidar ratio.

such as IWC and number concentration are derived from the extinction profile, it follows that their PDFs will match that for the extinction coefficient. Cloud events were counted only for those clouds whose bases were higher than 5 km. From the plots we see that during this period, cloud bases span a large range: starting from our imposed lower boundary of 5 km up to nearly 17 km, having a distinct maximum probability at 13.75 km. Other local maxima appear at 6, 11, 12 and 16 km. The PDF for cloud top is more relevant. There is a maxima in probability for clouds to have their tops at around 14.5 km with a mean cloud temperature of around -70°C, but two other altitudes are likely: 13.5 km and 15.5 km. This parameter shows a better distinction between lower clouds (with tops between 6 and 8.5 km) and

higher clouds (with tops above 8.5 km) but having approximately the same mean temperature. Cloud geometrical thickness ranges from 100 m (which is roughly the lidar resolution) up to 5 km. The most probable thickness is around 0.8 km, but secondary maxima are found for thicknesses of 0.6 km and 2.8 km. The general distribution is due to warmer clouds (temperatures around -40°C). For colder clouds the distribution is more uniform, but still with a weak maximum around 0.8 km. As expected, the mean extinction coefficient is less than 0.6 km^{-1} but on occasions can be as large as 3 km^{-1}. The most probable value is around 0.03 km^{-1} signifying that optically thin cirrus are the dominant feature. The mean value is found to be around 0.8 km^{-1}. Figure 3.21 shows PDFs for cloud transmittance and cloud lidar ratio using the same color coded representation as explained above. The transmittance ranges from around 0.15 to 1.0 with a maximum at 0.95 and a mean value of 0.85, with warmer clouds dominating the general features. The mean values for lidar ratios are greater than 5 sr and less than 150 sr. For the period considered in this analysis, the most probable value was around 25 sr with another weak maxima at 50 sr. We see that for warmer clouds the values are concentrated around the value of 25 sr, while for higher clouds the determined values ranges mostly from 10 to 80 sr. These values are also consistent with the ranges determined by others using lidar data [Platt et al. (1999), Ansmann et al. (1992b), Ansmann et al. (1992a)]. Most of the processed data came from nighttime measurements when the level of noise is at its minimum (i. e. solar radiation does not alter the measured signal) and therefore the retrieved quantities have the highest level of confidence.

We mentioned before that the life-cycle of high cirrus clouds in the tropics is influenced by the stratospheric waves. Following a paper by Boehm and Verlinde (2000) we tested this hypothesis by using the MPL data. In Figure 3.22 (a) the time dependence of the cirrus clouds as detected by the MPL system at Nauru during an intense observation period (June 17–July 15, 1999) is presented. We can clearly see cirrus clouds as high as 16 km and expect the greatest influence on these high clouds form stratospheric waves. From the balloon soundings available for the same period, we computed temperature perturbations associated with these eastward propagating Kelvin waves. They have periods of 9.5 days and 5 days for

zonal numbers 2 and 4, respectively and vertical wavelengths of about 4 km. They appear very clear in figure (b), where the contours were plotted for -3, -1, 1 and 3 K intervals. It can be seen that most of the highest cirrus events are correlated with negative temperature perturbations. Figures (c) and (d) are the mathematical confirmation of the aforementioned statement, captured by the PDF functions for the correlations coefficients between high cirrus clouds events (having altitudes of 12.5 km or higher) and temperature perturbations. For the cloudy sky case, we see that the most probable temperature perturbation is -1 K, while for the clear sky case the most probable temperature perturbation is 0 K. In general, cloudy sky events are associated with negative temperature perturbations, whereas clear sky events are associated with positive temperature perturbations. These observations suggest that high thin tropical cirrus cannot be studied in isolation from large scale forcing.

3.7 Summary

This chapter focused on ways of improving methods for processing the lidar data. As mentioned above, the lidar system proved its importance in providing useful information about high altitude thin cirrus clouds. Due the growing importance of the effects exerted by these clouds on the climate system, accurate information of their optical properties is essential. This chapter was dedicated to improving the methods concerning processing the lidar data for determining cloud optical properties. Below we summarize the main improvements and developments of this chapter:

1. We have developed a new calibration and cloud detection technique. For any individual lidar profile, our technique determines gain and offset as well as cloud transmittance with better accuracy, eliminating the inherent ambiguities due to the previous methods. At the same time, cloud boundaries are determined and used for establishing the lower and upper windows regions. This new development is important as it provides us with the means to obtain transmission measurements and thus cloud optical depth using the MPL. This optical depth information is further discussed in the next chapter.

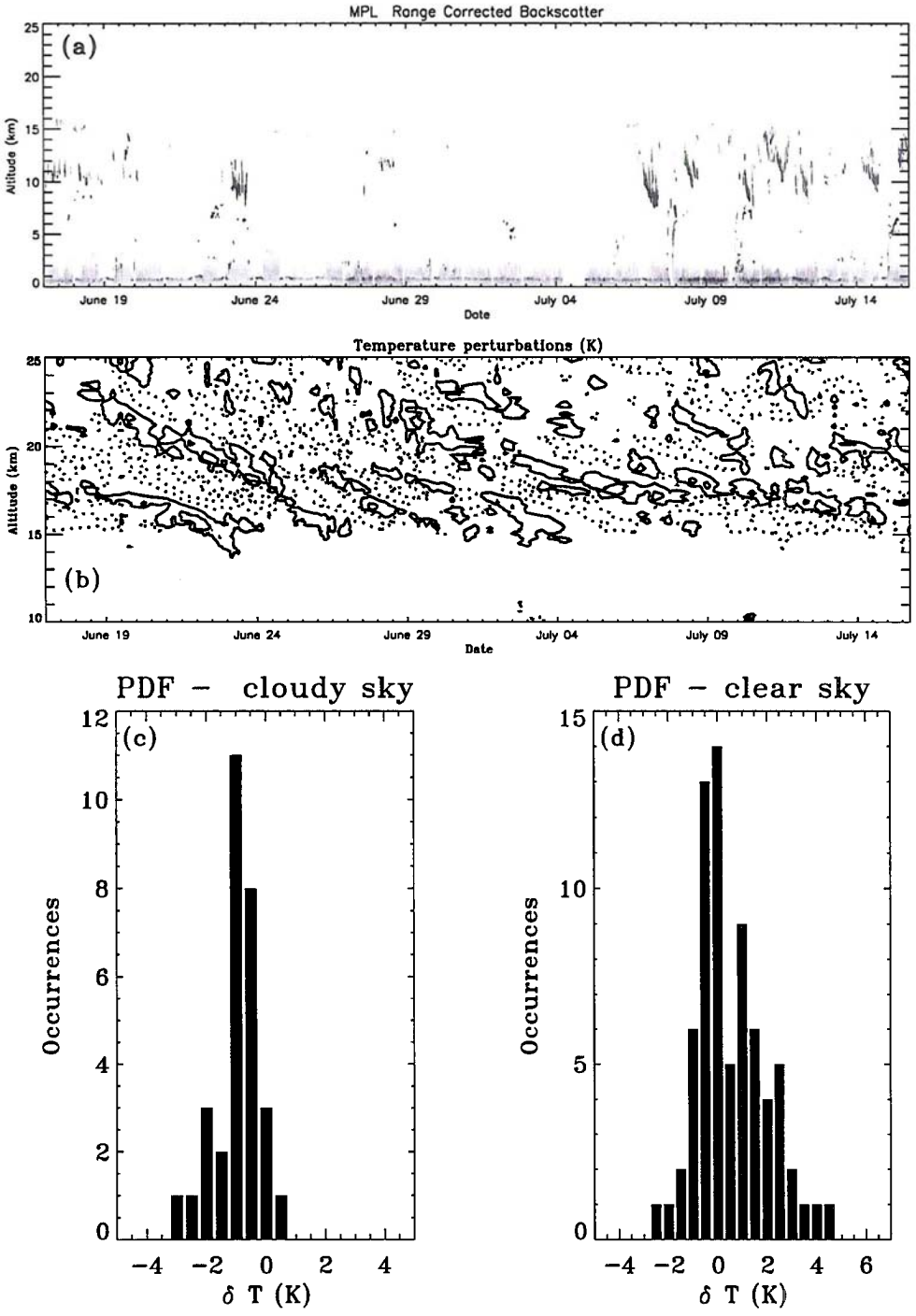

Figure 3.22: Waves interacting with cirrus clouds: (a) MPL time variation; (b) Temperature perturbations (2 K contours) time variation; (c) PDF: cloudy sky events vs. Temperature perturbations; (d) PDF: clear sky events vs. Temperature perturbations.

2. Starting from basic principles of radiative transfer, a solution to the problem of MS is proposed. The final results show that the lidar equation in the case of a homogeneous cloud is similar to that proposed before. We offer a simple method of determining the MS effects in cloud, expressed by a polynomial function of the scattering coefficient. In regard to the MS effects on the cloud transmittance, we establish that for the cirrus clouds, this effect is minimal. We have to mention that our approach is different from the conventional study which assumes that the MS effect can be assessed by modifying the two-way transmission function. We show theoretically that this more convenient approach is incorrect.

3. Based on the new model above, cloud optical properties are derived. The proposed inverse model is based on two iterative procedures: one iterative procedure solves the new transcendental lidar equation that accounts for MS effects; the other iterative procedure determines the value for the lidar ratio such that the extinction profile matches the predetermined cloud transmittance. The proposed equation for MS effects is an essential factor in retrieving high values of the extinction coefficient for optically thick clouds. Methods that don't account for MS in such a way cannot converge in these cases.

4. The above new methods were tested first on synthetic cases, then used to infer various cloud optical properties. The methods are however limited since we still lack knowledge about some important parameters like phase functions, single scatter albedos, lidar ratios. For this reason they can only apply when above parameters don't vary significantly within the cloud.

5. Direct application of the proposed methods was performed on data collected by the MPL system at Nauru, TWP. These cirrus clouds form at various altitudes ranging from 6 to 17 km, and with thicknesses up to 5 km. The average thickness is around 0.8 km, with low optical depth. Another key optical parameter is the lidar ratio, which was found to vary within the range of values that were previously reported.

6. By using lidar as a detection tool for high cirrus clouds in combination with sounding data, evidence that the very high cirrus clouds are influenced by stratospheric waves, that influence the temperature of the tropopause, is also presented. The existence of such high cirrus clouds is correlated with negative perturbations of temperature in the tropopause, while the reverse is likely to be true: positive temperature perturbation of the tropopause are correlated with the non-existence of high cirrus clouds.

Chapter 4

Active-Active Methods

4.1 Introduction

Among the remote sensing systems used to investigate the atmosphere, active remote sensing instruments have the ability to discern incoming radiation with respect to range. Since active remote sensing systems measure the response of a target to a controlled beam of energy, these systems are more efficient in the spectral ranges where the natural emitted/scattered radiation is minimal. However, active systems are essentially monochromatic and unable to provide a broad spectral picture of the radiative properties of the atmosphere.

Combinations of two or more active remote sensing systems provide a way of inferring profiles of two or more atmospheric characteristics, thus creating a more detailed picture of the atmosphere. In this chapter, a method for retrieving cirrus cloud properties using two active systems (RADAR and LIDAR) is described. This is based on simple radiative transfer calculations that link key microphysical properties to the measurements from these sensors. The method is then applied to synthetic data to prove the validity of the approach. Finally, the method is applied to data collected at the ARM Nauru site. These results are presented and discussed.

4.2 The RADAR System

As in the case of lidar, radar remote sensing of cloud properties is a two step process. First, the measured power recorded by the radar must be related to cloud physical properties. Second, methods that use radar-derived quantities to estimate cloud properties must be developed and tested. The first step is, in many ways, a solved

problem; there are several accurate techniques that yield reflectivity, mean Doppler velocity and mean Doppler width fields. The second step is by no means a solved problem and much effort is dedicated to the development and improvement of various algorithms that use radar reflectivities as inputs for determining cloud properties.

The return power P_{rad} measured by a radar can be written as follows (see Appendix C):

$$P_{rad}(z) = \frac{C}{z^2} \cdot \eta \cdot \exp\left(-2\int_0^z \beta_{ext} dz'\right) \tag{4.1}$$

where C is the radar constant (transmission power, gain, etc.), z is the range from radar to the backscattering target, η is the radar backscatter, and β_{ext} is the extinction coefficient accounting for the two-way attenuation of the beam due to the atmospheric constituents.

In the Rayleigh regime, the radar backscatter can be expressed in terms of the radar reflectivity:

$$\eta = \frac{\pi^5 \mid K \mid^2_{i,w}}{\lambda^4} \cdot Z_e \tag{4.2}$$

where $K_{i,w}$ is the dielectric factor for ice or water cloud particles, λ is the radar wavelength and Z_e is the equivalent radar reflectivity factor ($\mathrm{mm^6 m^{-3}}$). Under this assumption, Z_e is approximated by the radar reflectivity factor Z, which in the case of spherical particles is expressed as the sixth moment of the cloud droplet size distribution:

$$Z_{ice} = \int_0^\infty D^6 \, n(D) \, dD \quad . \tag{4.3}$$

In the case considered here, when the particle size distribution is approximated by a modified gamma size distribution, the above expression becomes (see Appendix A):

$$Z = N_t \, D_n^6 \, \frac{\Gamma(\nu+6)}{\Gamma(\nu)} \quad . \tag{4.4}$$

The above expression simply states that the return power (in terms of the radar reflectivity), in the case when the particle size distribution can be approximated by a modified gamma size distribution, is proportional to the particle number concentration N_t and the sixth power of the characteristic diameter of the distribution D_n. It also depends on the distribution width ν. Since the gamma distribution depends

on these three parameters and so far we only have one measurement (radar reflectivity), it is only possible to solve for one of the three parameters, by imposing some constraints on the other two parameters. Lidar works on similar physical principles as radar, and like radar, profiles the returns of an incident beam of light. Since the same atmospheric target can be illuminated by these two instruments simultaneously, we can use lidar- and radar-derived profiles to infer information about two of the three parameters involved in the definition of the gamma distribution. The following paragraph presents a simple model for the radar-lidar system.

4.3 A Radar-Lidar Microphysical Retrieval Scheme

As presented in Chapter 3, lidar operates in the visible region of the spectrum, by profiling the atmospheric returns via pulses of a laser light. At lidar wavelengths, the gamma distribution yields an extinction coefficient given by ($Q_{ext} = 2$):

$$\beta_{ext} = \frac{\pi}{2} N_t D_n^2 \frac{\Gamma(\nu+2)}{\Gamma(\nu)} \quad . \tag{4.5}$$

From equations (4.4) and (4.5) we can solve for the characteristic diameter and the particle concentration, provided that the distribution width ν is known. In most applications, this parameter is usually set to two. A theoretical discussion regarding the implications of such a hypothesis is presented later on. Assuming that this hypothesis is correct, the expression for the characteristic diameter takes the form:

$$D_n = \left[\frac{\pi}{1680} \cdot \frac{Z}{\beta_{ext}} \right]^{1/4} , \tag{4.6}$$

which can be re-arranged into the more useful expression:

$$D_n = 6.57597 \cdot \left[\frac{Z\ (mm^6 m^{-3})}{\beta_{ext}\ (m^{-1})} \right]^{1/4} \quad (\mu m) \quad . \tag{4.7}$$

Use of the above equation results in the expression for particle concentration:

$$N_t = \frac{10^9}{3\pi} \cdot \frac{\beta_{ext}\ (m^{-1})}{D_n^2\ (\mu m)} \quad (l^{-1}) \quad . \tag{4.8}$$

The above equations (4.7 and 4.8) constitute a radar-lidar based method for retrieving characteristic diameter and particle concentration. From equation (4.7) we

can infer that errors in both reflectivity and extinction coefficient have the same influence on values of characteristic diameter. However, more important is the actual value for the extinction coefficient since it appears in the denominator. For equation (4.8) however, it is the radar reflectivity that is the crucial variable. It becomes clear now that these two quantities (radar reflectivity and lidar extinction coefficient) must be measured at the same points throughout the cloud. If one field is not measured then the above radar-model cannot be applied.

When lidar profiles alone are used to infer particle concentration N_t and characteristic diameter D_n, the introduction of spurious correlations between these quantities is unavoidable. However, retrievals that are based on the use of both radar and lidar data demonstrate that these quantities are uncorrelated. But as in the case of lidar alone, these estimates should be treated with caution since errors in either profile (Z or β_{ext}) can lead to large errors in the retrieved quantities.

Like in the previous chapter, in order to estimate the errors associated with these quantities we calculate their variances. It follows that the variances are:

$$\sigma_{D_n} = \frac{D_n}{4} \sqrt{\left(\frac{\sigma_Z}{Z}\right)^2 + \left(\frac{\sigma_{\beta_{ext}}}{\beta_{ext}}\right)^2} \tag{4.9}$$

and

$$\sigma_{N_t} = \frac{N_t}{2} \sqrt{\left(\frac{\sigma_Z}{Z}\right)^2 + \left(3\,\frac{\sigma_{\beta_{ext}}}{\beta_{ext}}\right)^2} \quad . \tag{4.10}$$

Another microphysical parameter that can be calculated is the IWC, defined as:

$$IWC = \rho_{ice} \int_0^\infty V(D)\, n(D)\, dD \tag{4.11}$$

where ρ_{ice} is the density for ice particles and is assumed constant. Assuming that all particles are spherical, then the volume $V(D)$ for a single particle is:

$$V(D) = \frac{\pi}{6}\, D^3 \tag{4.12}$$

and under the same assumption of a gamma size distribution, the IWC can be calculated using the following expression:

$$IWC = 4\pi\, \rho_{ice}\, N_t\, D_n^3 \quad . \tag{4.13}$$

As before, the variance for the IWC is given by:

$$\sigma_{IWC} = \frac{IWC}{4} \sqrt{\left(\frac{\sigma_Z}{Z}\right)^2 + \left(3\,\frac{\sigma_{\beta_{ext}}}{\beta_{ext}}\right)^2} \quad . \tag{4.14}$$

In cirrus, ice particles are mainly non-spherical, hence the expression for the volume can become complex. In the case of a hexagonal plate geometry, the volume of the particle is:

$$V(D) = \frac{3\sqrt{3}}{8}\, d\, D^2 \,, \tag{4.15}$$

where D is the major diameter and d is the minor diameter. Using the above expression for the individual volume, the IWC for non-spherical plate-like particles described above is in the form:

$$IWC = 7.55503 \times 10^{-9}\, \rho_{ice}\, N_t\, D_n^{5/2} \quad (mg/m^3) \tag{4.16}$$

where N_t is in m^{-3}, ρ_{ice} in $\mathrm{g/cm}^3$ and D_n in μm.

Variations of Retrieved Variables with the Distribution Width ν

As mentioned before, in general, the value for the distribution width parameter (ν) is unknown, and therefore set to a prescribed value. Most of the experimental studies found this parameter to be two [Dowling and Radke (1990)]. However, in special cases this is not necessarily true. Since we assumed that the particle size distribution is described by a gamma size distribution, which has some nice mathematical properties (see Appendix A), it is easy to determine correction coefficients to be applied to all retrieved microphysical variables, when changes in the distribution width parameter are made. These coefficients, calculated for various values of ν, are presented in Table 4.1. From the table we notice that when the distribution width is less than two (the value used in the radar-lidar model), the values for all retrieved variables (D_n, N_t, and IWC) must be corrected by factors greater than unity. The reverse is true: when using a larger distribution width than the initial one, then the correction coefficients are less than unity. In all cases, the largest correction is applied to IWC, while the smallest to D_n. For all retrieved variables, the level of correction when changing ν, is relatively large and nonlinear with respect to the

Table 4.1: Correction coefficients for the retrieved variables

Retrieved variable	ν=0	ν=1	ν=2	ν=3	ν=4
D_n	1.6266	1.2359	1	0.8409	0.7260
N_t	2.2678	1.9640	1	0.7071	0.5692
IWC	3.2663	2.3031	1	0.6209	0.4477

direction of variation for ν. An increase (decrease) in ν by one is accompanied by a decrease (increase) of more than 15% in values for D_n. For IWC, the change is greater than 38 % when increasing ν by one, or larger that 130 % when decreasing ν by one. Since sensitivity to ν is large, better knowledge about the distribution width is desirable. Variations in the retrieved parameters (D_n, N_t, and IWC) are expected when other distributions describing the particle size distribution are used. It is possible that even larger uncertainties in the retrieved variables exist when bi-modal distributions are used instead of uni-modal ones (like the one used in our case).

4.3.1 A RADAR-Optical Depth Based Retrieval Method

Based on the model presented in the preceding paragraph, we can develop a less sophisticated model that uses only radar reflectivity profiles and visible optical depth. It is based on the same assumption that the particles follow a gamma size distribution, but since less information describing the system is available (i. e. total optical depth instead of profiles for the extinction coefficient), more constrains must be imposed. In such a simplified model we must assume that another parameter describing the distribution is invariant throughout the cloud. It is customary to assume that parameter to be the particle concentration (N_t), although there is no physical reason against choosing the characteristic diameter (D_n) to be the invariant one. We start by defining the cloud optical depth as:

$$\tau = \int_0^H \beta_{ext}(z)\, dz \quad . \tag{4.17}$$

By using (4.4) we can solve for the characteristic diameter (D_n) at a given level, as function of reflectivity (Z) and particle concentration (N_t). Then the above equation can be rewritten as:

$$\tau = \frac{\pi}{2}\,\Gamma^{-2/3}(\nu)\,\Gamma(\nu+2)\,\Gamma^{-1/3}(\nu+6)\,\frac{H}{L}\sum_{i}^{L} Z_i^{1/3}\,N_t^{2/3} \tag{4.18}$$

where H is the thickness of the cloud and L is the number of radar vertical bins. Then the particle concentration can be calculated using the following expression:

$$N_t = \left[\frac{2}{\pi}\,\Gamma^{2/3}(\nu)\,\Gamma^{-1}(\nu+2)\,\Gamma^{1/3}(\nu+6)\,\frac{L}{H}\left(\sum_{i}^{L} Z_i^{1/3}\right)^{-1}\tau\right]^{3/2} \tag{4.19}$$

while the vertical profile for the characteristic diameter is given by:

$$D_n(i) = \left[\Gamma(\nu)\,\Gamma^{-1}(\nu+6)\,N_t^{-1}Z_i\right]^{1/6} \quad . \tag{4.20}$$

The above set of equations (4.19 and 4.20) represents the radar-optical depth retrieving method. It should be noted here that the above model can be further improved if the functional dependence of the optical depth is known or at least assumed. In this way, this method can be upgraded to the original radar-lidar retrieving method. One must keep in mind that these estimates are as good as our assumptions describing the cloud are. In other words, if one wishes to accurately determine cloud microphysical parameters, an accurate model describing the physics of the cloud must be used. Otherwise, our retrieved quantities will only partially reflect the reality and the results will be influenced by errors in formulating the forward model. This model should be used when less knowledge about cloud vertical structure is available. It is also an alternative method based on direct analytical calculations as opposed to other methods that use an optimal estimation approach to retrieve the same physical parameters.

4.4 Application to Modeled Data

We tested our model using synthetic radar and lidar data fields from a two-dimensional cirrus cloud model [Wang and Sassen (2001)]. Employing our proposed radar-lidar

model, we used both lidar and radar fields to infer the microphysical properties of the cirrus clouds simulated by this particular model. As explained above, our "inverse model" is based on the assumption that all ice crystals are spherical, have the same ice density ($\rho_{ice} = 0.92$ g/cm^3) and are described by a gamma distribution with $\nu = 2$.

Figure 4.1 presents the temporal and vertical structure of the radar reflectivity and the lidar extinction coefficient as input variables. We can see the evolution of a relatively deep cirrus cloud (base at approximately 5 km, top at 10 km) having a weak radar signal (reflectivity ranges between -47 dBZ and -30 dBZ) and lidar extinction coefficient (values below 1 km^{-1}). It is worth noting that these two fields are not strongly correlated, suggesting that the microphysical properties of the cirrus cloud are not stationary. This is evident in Figures 4.2(a) and 4.3(a) that show the time evolution of the vertical profiles in the control model. The performance of our proposed radar-lidar model can be seen in panel (b) of the same figures. For both the IWC and effective radius, the general appearance is that there are no significant differences between the control fields and those produced by the present radar-lidar model. For the IWC, the values for the mean difference between the control and the model fields is 0.1 mg/m^3 with a standard deviation of 0.14 mg/m^3, while for the effective radius these differences are 1.6 μm and 1.5 μm respectively. The conclusion that follows is that our basic assumption of characterizing the ice crystals in a cirrus cloud by a gamma size distribution with a distribution width parameter set to two is a good choice for the purpose of retrieving vertical profiles of number concentration and characteristic diameter given the profiles for radar reflectivity and extinction coefficient.

At this point, we can make use of equations (3.76) and (3.78) and test the validity of our assumption made back in Chapter 3 when we introduced a constant effective radius for all cirrus clouds. Following the above mentioned equations we can deduce a relationship between the visible cloud optical depth, IWP and mean characteristic diameter in the form:

$$\tau = \frac{3}{4} \frac{IWP}{\rho < D_n >} \tag{4.21}$$

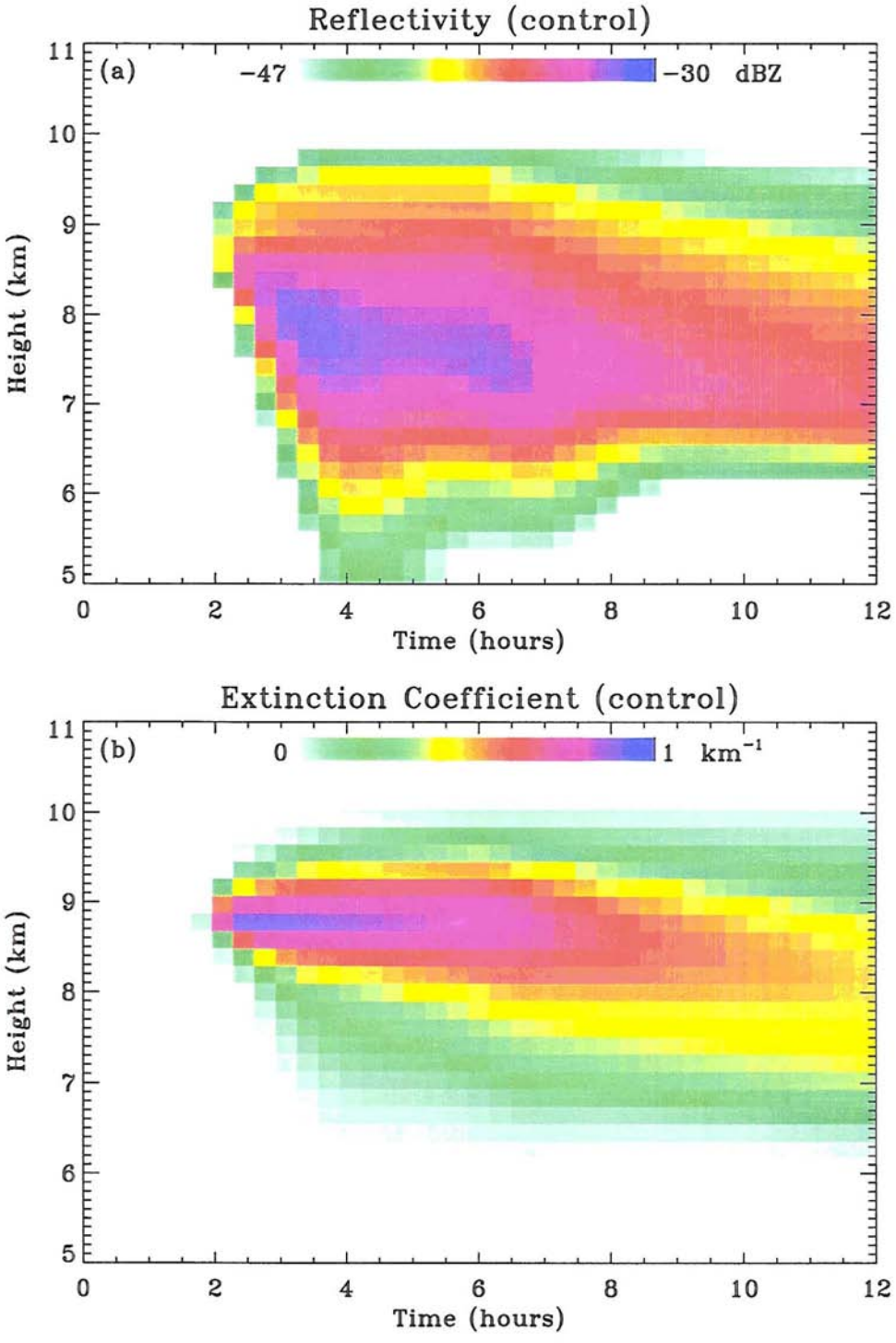

Figure 4.1: Input fields: (a) Radar Reflectivity; (b) Lidar Extinction Coefficient.

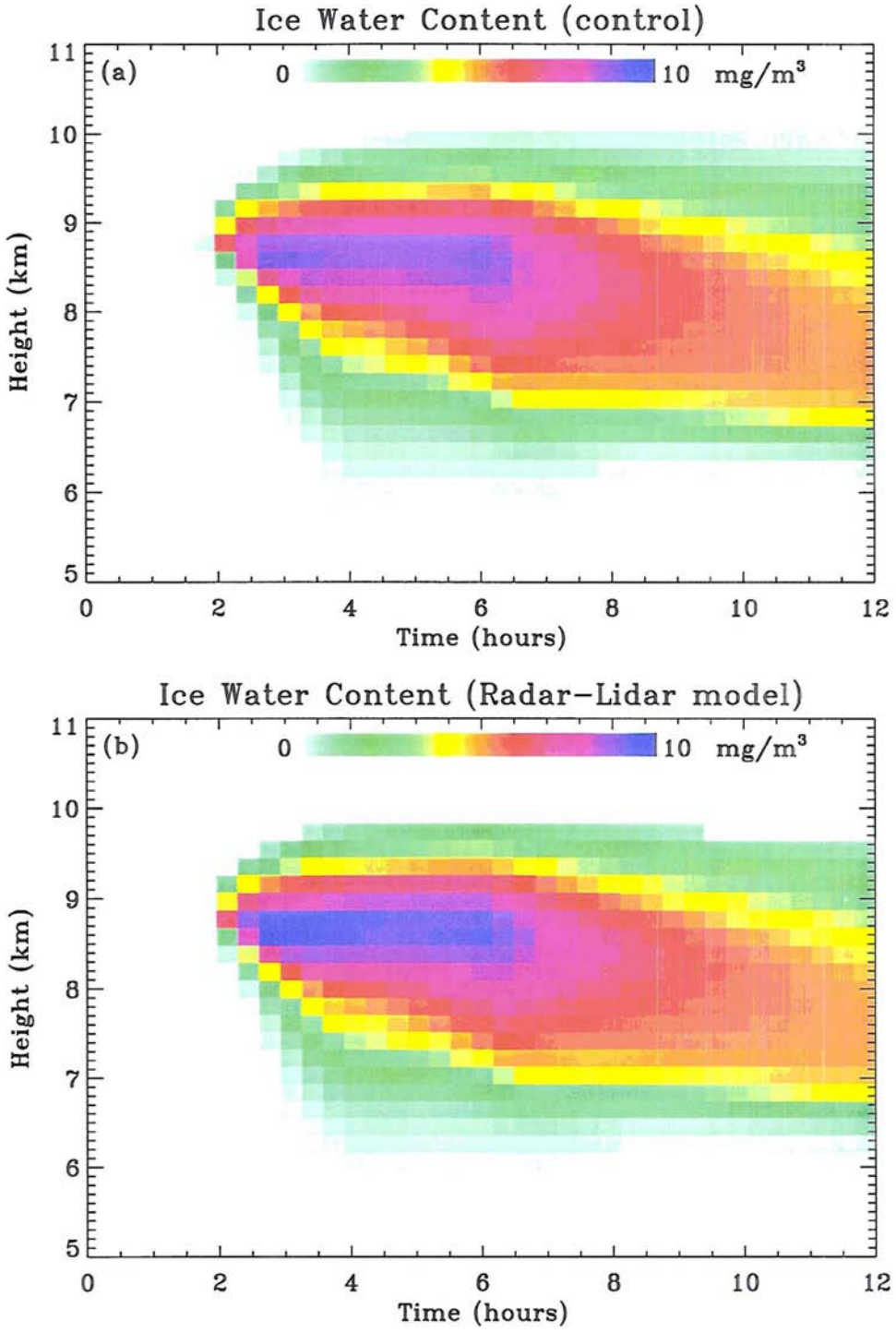

Figure 4.2: Comparison between (a) Control Ice Water Content and (b) Retrieved Ice Water Content.

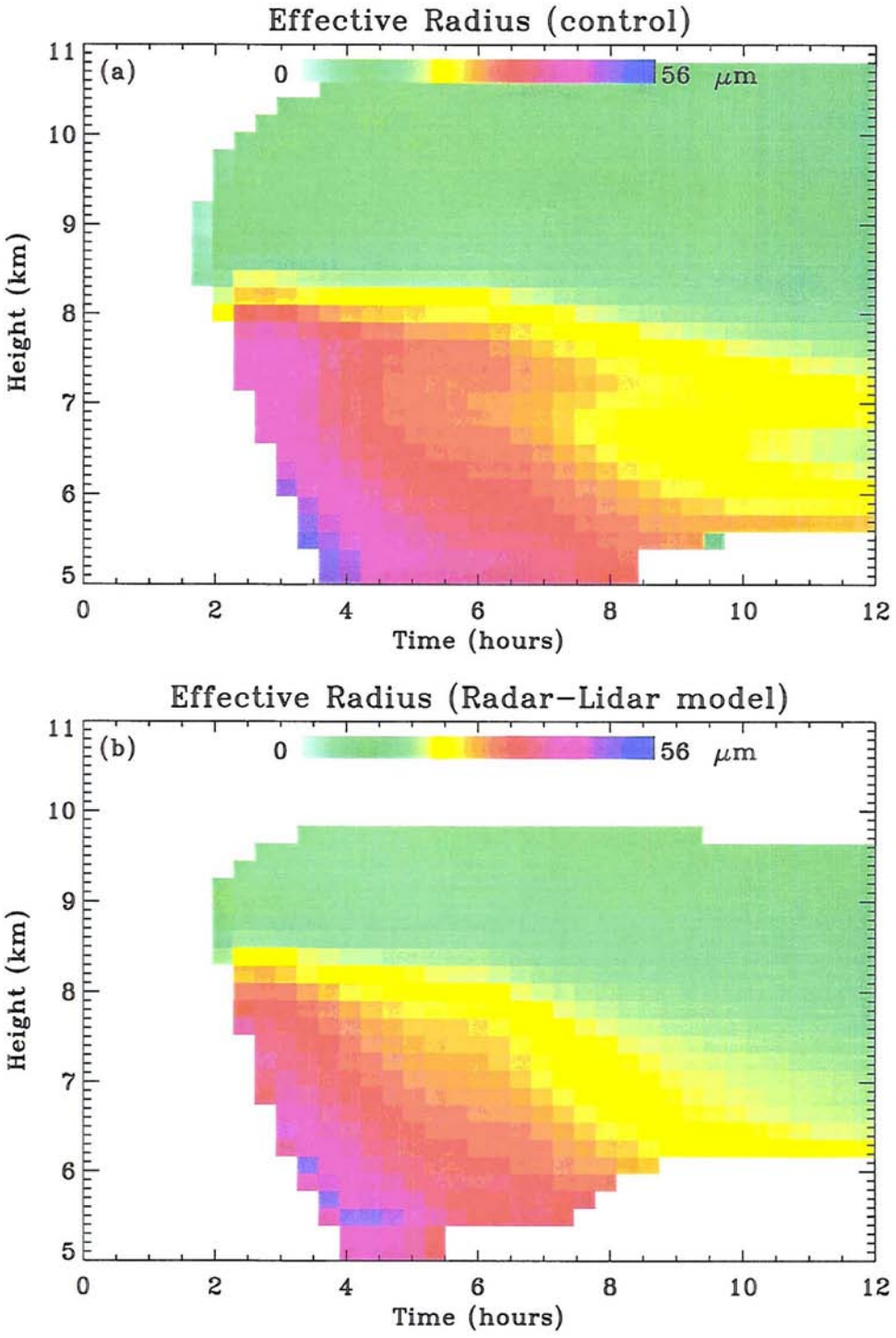

Figure 4.3: Comparison between (a) Control Effective Radius and (b) Retrieved Effective Radius.

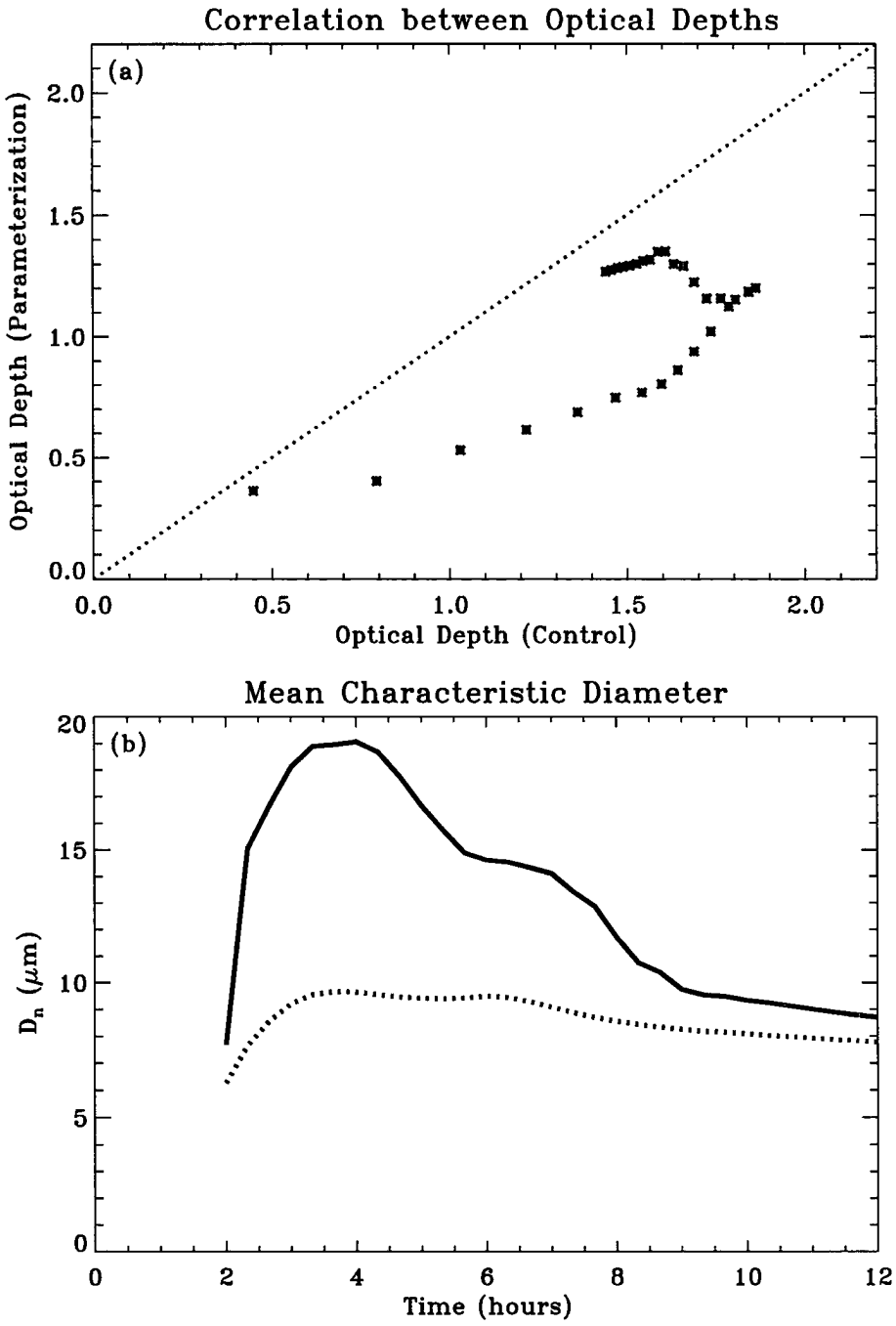

Figure 4.4: (a) Comparison between Control Optical Depth and Parameterized Optical Depth (with stars). Dotted line is the one-to-one relationship; (b) Time variation for Model Mean Characteristic Diameter (solid line) and Control Mean Characteristic Diameter (dotted line)

By using the inferred profiles for characteristic diameter and particle concentration both IWP and $< D_n >$ can be determined. Here $< D_n >$ is the mean value of the profiles of characteristic diameters calculated at each level by our radar-lidar model, which in fact is equivalent to the assumption that number concentration is constant for a given profile. We then can compare this parameterization against the "true" optical depth:

$$\tau = \int_0^H \beta_{ext} dz' \quad . \tag{4.22}$$

The purpose of this exercise is to test the above simple parameterization (equation 4.21) against the "true" values and to assess and correct the problems. Figure 4.4 (a) shows the scattered plot of the computed and true optical depths (represented by stars). Figure 4.4 (b) holds the answer for interpreting the above correlation. Represented with solid line is the layer mean characteristic diameter used in our parameterization, while the true layer mean characteristic diameter is represented with dots. We see that at the beginning and ending of the simulation these two quantities are close, and, as expected, the value for the parameterized optical depth approaches the true optical depth. The difference between the two column-mean particle sizes is a result of the assumption that the number concentration is constant. Better correlation is expected when the vertical structure of the cloud can be considered homogeneous with respect to the number concentration.

These results indicate that our proposed radar-lidar model is capable of retrieving both IWC and effective diameter with good accuracy, but also indicates that the retrieved column constant particle concentration is questionable. We further tested our radar-lidar model using radar and lidar data obtained by the MMCR and the MPL at Nauru.

4.5 Application to Measurements

4.5.1 Selected Case Studies

In Figure 4.5, time series of MPL and MMCR data for two different days at Nauru are presented. Superimposed on each pair of images are the cloud boundaries as

determined by the MPL. We note that on occasion, the MMCR data are absent while the MPL detects cirrus cloud. The reverse is also true. Sometimes, the MMCR penetrates deeper into the cirrus cloud while the MPL clearly does not "see" the top of the cloud. For such events our radar-lidar model will not work and therefore the retrieved quantities (IWC, effective diameter and particle concentration) will not be produced.

We start by analyzing a particular case that occurred on 05/01/1991. Vertical profiles of the retrieved quantities are presented in Figures 4.6, 4.7, and 4.8 respectively. For this particular case, a two-layer cloud is apparent with base at about 9 km and top at 11.5 km. The calculated transmittance for this profile is 0.42 with a maximum extinction coefficient of 0.8 km^{-1}. The radar reflectivity has a maximum value of -5 dBZ at about 10 km. The particle sizes for this particular case range from about 17 μm to less than 34 μm with larger particles at the base and top. The mean characteristic diameter was determined to be around 24 μm. The number concentration presents a pronounced maxima (235 particles per liter) correlated with a minima in the characteristic diameter. Two additional local maxima are also visible, suggesting a three layer cloud structure. The mean number concentration is 68 particles per liter. Another microphysical characteristic is the IWC. It clearly shows the layered structure of the cloud, having larger IWC values in the lower layer (a maxima of 28 mg/m^3) than in the upper layer (a maxima of 20 mg/m^3). The inferred IWP for this particular profile is around 26 g/m^2. All these retrievals are based on the hypothesis that the particles are perfect spheres and the size distribution is described by a gamma distribution. We can compare these results with those obtained from the lidar-model (see Figure 3.19). The differences in number concentration, IWC and IWP are quite significant. The radar-lidar model gives values for IWC and IWP that are almost double the values retrieved with the lidar-model, while the reverse is almost true for the number concentration (N_t). For comparison purposes, in Figure 4.9 we present the retrieved vertical profile for the characteristic diameter as deduced from the radar-optical depth retrieval method. In this case, the mean particle concentration is close to that computed from the radar-lidar model, while the profile for the characteristic diameter resembles the vertical profile for the

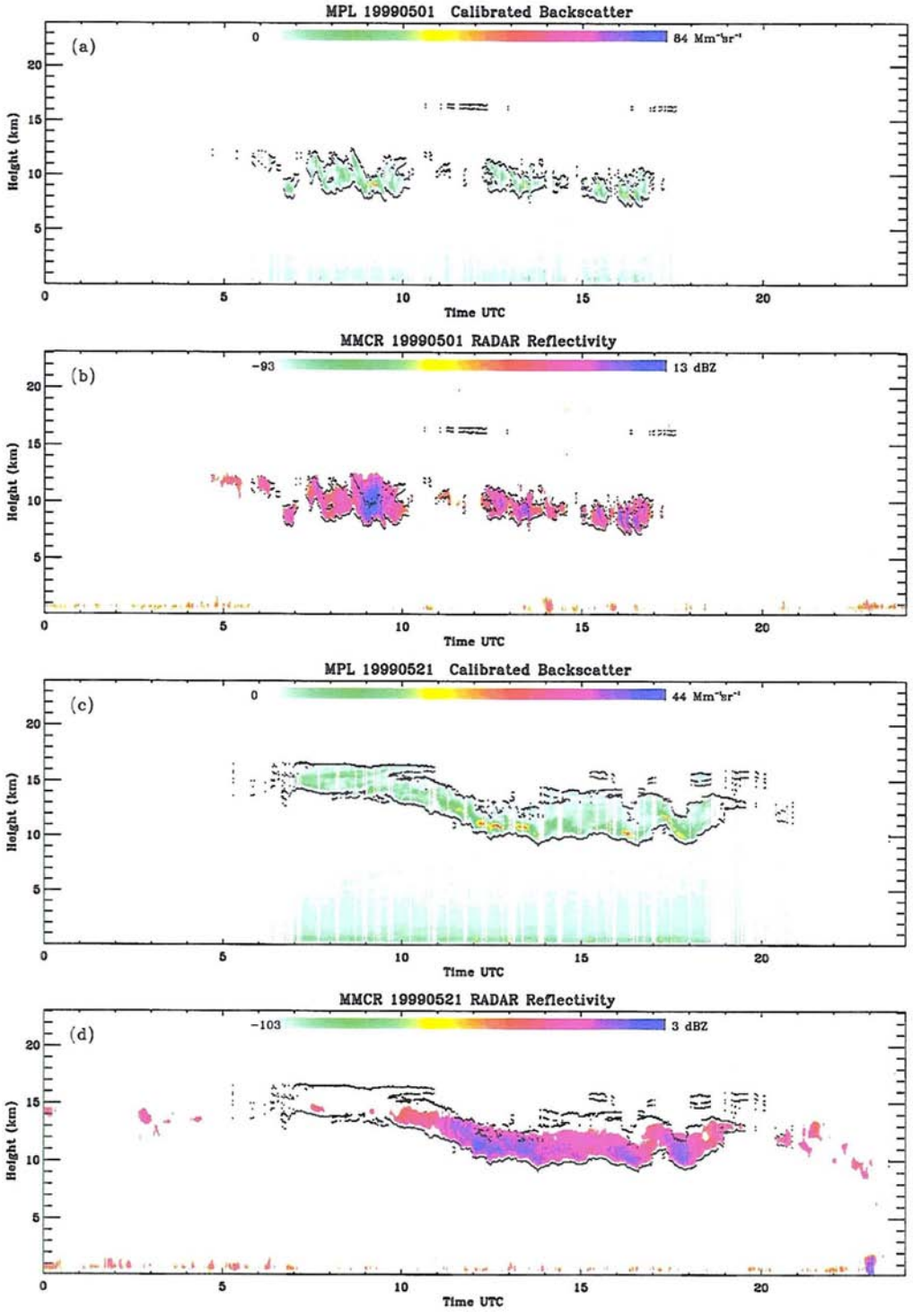

Figure 4.5: Time series of MPL and MMCR data at Nauru: (a), (b) 1999/05/01, (c), (d) 1999/05/21. Cloud boundaries shown by dots.

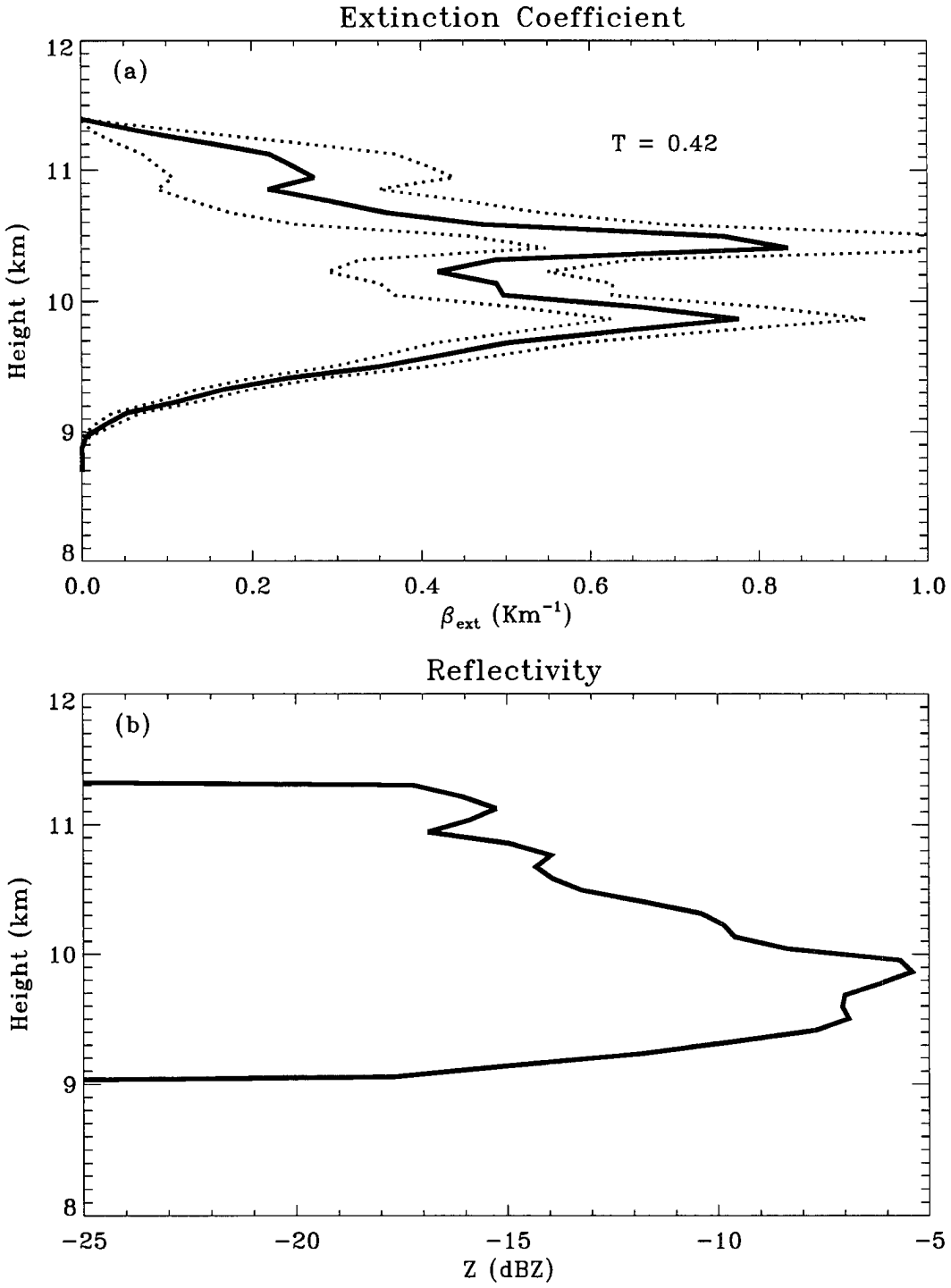

Figure 4.6: Profiles of (a) MPL Extinction Coefficient (transmittance of 0.42), and (b) MMCR Reflectivity. Uncertainties in profiles are shown by dots. Nauru 1999/05/21 08:22:09 UTC.

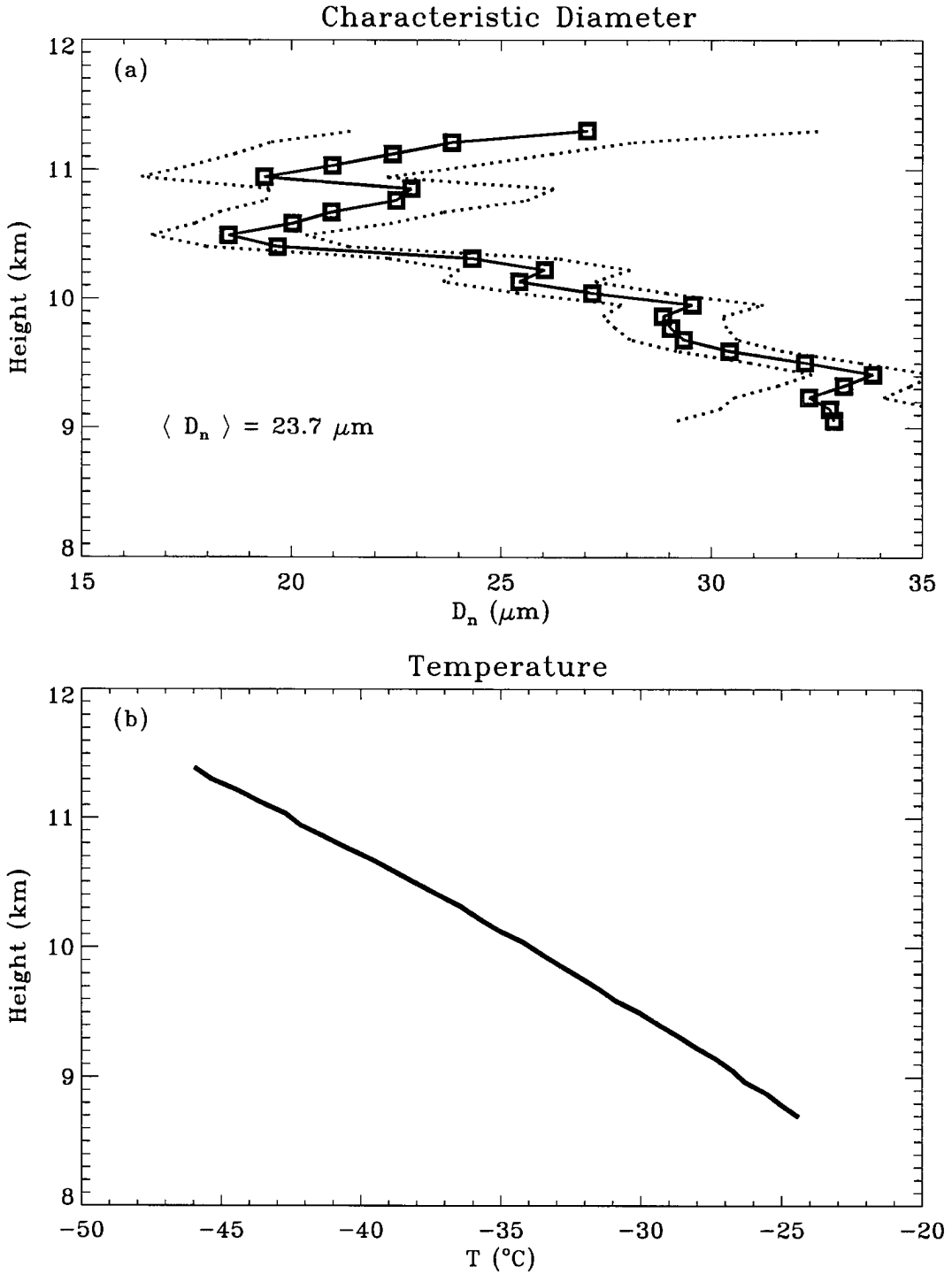

Figure 4.7: Profiles of (a) Characteristic Diameter (D_n), and (b) Temperature. Errors associated with the retrieval are shown by dots. Nauru 1999/05/21 08:22:09 UTC.

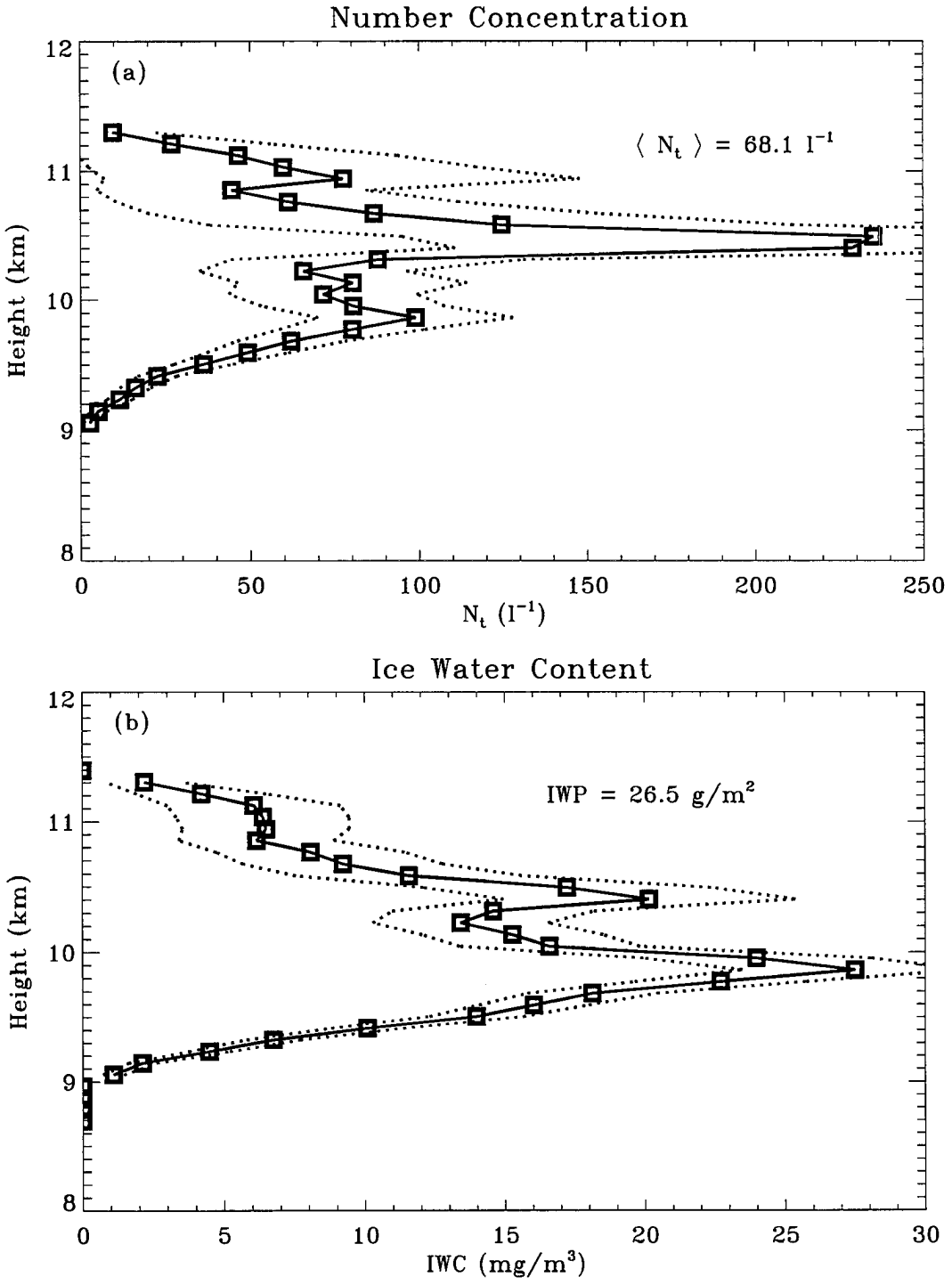

Figure 4.8: Profiles of (a) Number Concentration, and (b) Ice Water Content. Errors associated with the retrieval are shown by dots. Nauru 1999/05/21 08:22:09 UTC.

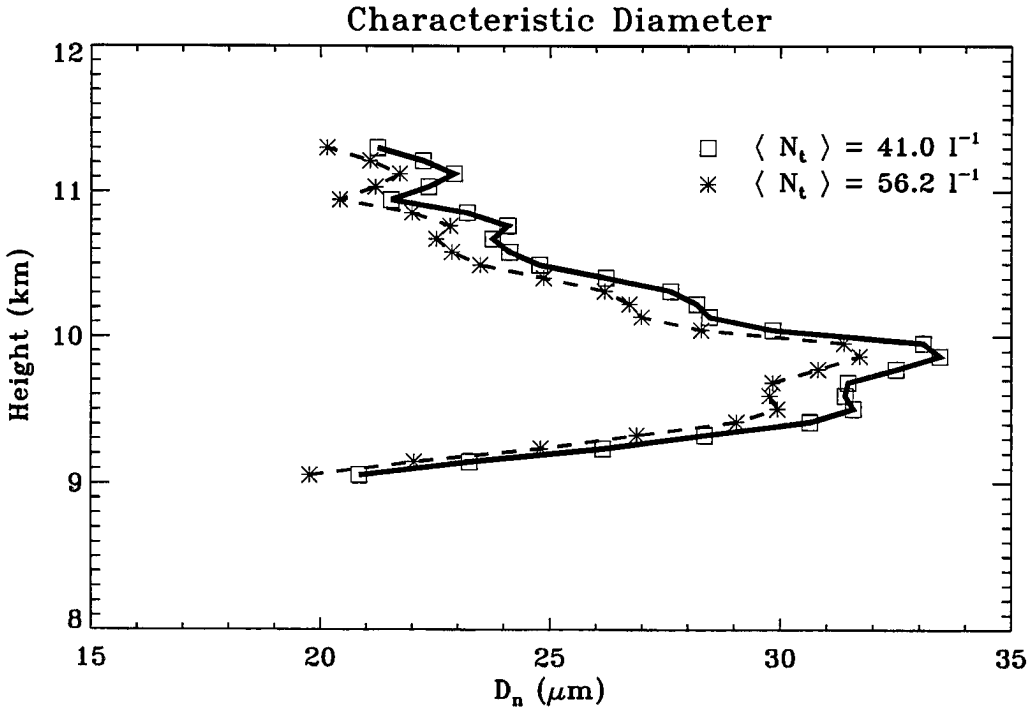

Figure 4.9: Profiles of Characteristic Diameter (D_n) using two radar-optical depth methods: optimal estimation approach (solid line and squares) compared with the present analytical method (dashed line and stars). Nauru 1999/05/21 08:22:09 UTC.

radar reflectivity. The results from using the optimal estimation approach (courtesy of J. Haynes) are also presented. As expected, in this case the number concentration is slightly underestimated (41 per liter compared with 56.2 per liter with the proposed analytical method). As a result, the characteristic diameter profile for the optimal estimation method is slightly larger than that produced with the present analytical method.

4.6 Composite Analysis

We can test again the validity of our approximations by comparing the lidar-derived optical depth (equation 4.22) to the one deduced from the proposed parameterization (equation 4.21). The scatter plot obtained from processing three months of

MPL and MMCR data is presented in Figure 4.10(a). We see that there is a strong correlation between these two quantities, with a trend for our proposed relationship to underestimate the optical depth, although many points show a one-to-one correlation. As mentioned before, this underestimation is most probably due to the overestimation of the layer mean characteristic diameter. However, other possible explanations can be investigated. The underestimation of the optical depth by applying this parameterization may be due to the fact that larger particles have lower density, thus lowering the IWP, and/or due to our assumption of spherical particles, thus affecting both the IWP and the layer mean characteristic diameter D_n. We tested the first possibility by computing a particle density using an expression given by Brown and Francis (1995), which is applied for particles having diameters larger than 0.1 mm:

$$\rho(g/cm^3) = 0.07\ D(mm)^{-1.1}\ . \tag{4.23}$$

Because the above correction is valid only for larger particles, it does not influence our results too much. Therefore, this correction is arguably not the main reason for underestimating the optical depth.

The second option for explaining the reduced values for the parameterized optical depth relies on the fact that non-spherical particles have smaller volumes than spherical particles for the same characteristic diameter, but at the same time their cross-sectional area is smaller. This implies that when computing the relationship between the IWP and the optical depth we underestimate the latter. From the plot, we estimate this decrease to be of the order of approximately 0.87 on average (see dashed line). By applying this correction factor to the spherical volume given by equation (4.12) that we used instead of the non-spherical one (in this case we chose the one given by equation 4.15), we can deduce the expression for the minor diameter of a hexagonal plate:

$$d = 0.58\ D\quad . \tag{4.24}$$

The above value is also close to those inferred from measurements of cirrus clouds [Heymsfield (1972)]. However this is only one possible explanation, since a variety of causes can contribute to such an effect.

Figure 4.10 (b) shows the correlations between the mean extinction coefficient and mean cloud temperature. The mean cloud temperature for the great majority of the cases analyzed during the three month period spans from -20° to -75°C, with only a few having larger, but still negative mean cloud temperatures. Unlike other studies [e. g. Platt and Dilley (1981)], we cannot infer any functional relationship between these two quantities, but we can observe that there is a tendency for very cold clouds (temperatures less than -60°C) and relatively warmer clouds (temperatures around -20°C) to have on average smaller values for the cloud mean extinction coefficient. Higher values are possible for clouds with temperatures between -60°C and -30°C.

In Figure 4.11, correlations between cloud optical depth and IWP, and characteristic diameter and IWP respectively are presented. The temperature dependence is detailed into three distinct regions as shown in the temperature legend. We note the correlation between the cloud optical depth and the IWP, which seems to have different slopes according to the temperature range: as the temperature decreases, we expect an increase in optical depth for the same IWP. This is consistent with our parameterization between the optical depth, IWP and characteristic diameter, if we accept that the latter decreases when temperature decreases. It is also consistent with the assumption that the number concentration can be considered invariant in the cloud layer. The parameterization proposed by Heymsfield (2002) following a study of cirrus clouds is also represented and it shows good agreement with our retrieved quantities. The analytical formulation for this parameterization is in the form:

$$\tau = 0.028 \cdot IWP^{1.06} \quad , \tag{4.25}$$

where IWP is expressed in g/m^2. We conclude that on average, this proposed parameterization between IWC and optical depth is valid for tropical cirrus clouds.

From Figure 4.11(b), we can only conclude that IWP is not directly related to characteristic diameter since for a given IWP, a range of characteristic diameters is possible. A probable explanation for such a behavior resides in the highly irregular shapes displayed by the ice crystals. However, as the IWP increases, the ranges in characteristic diameters decrease too.

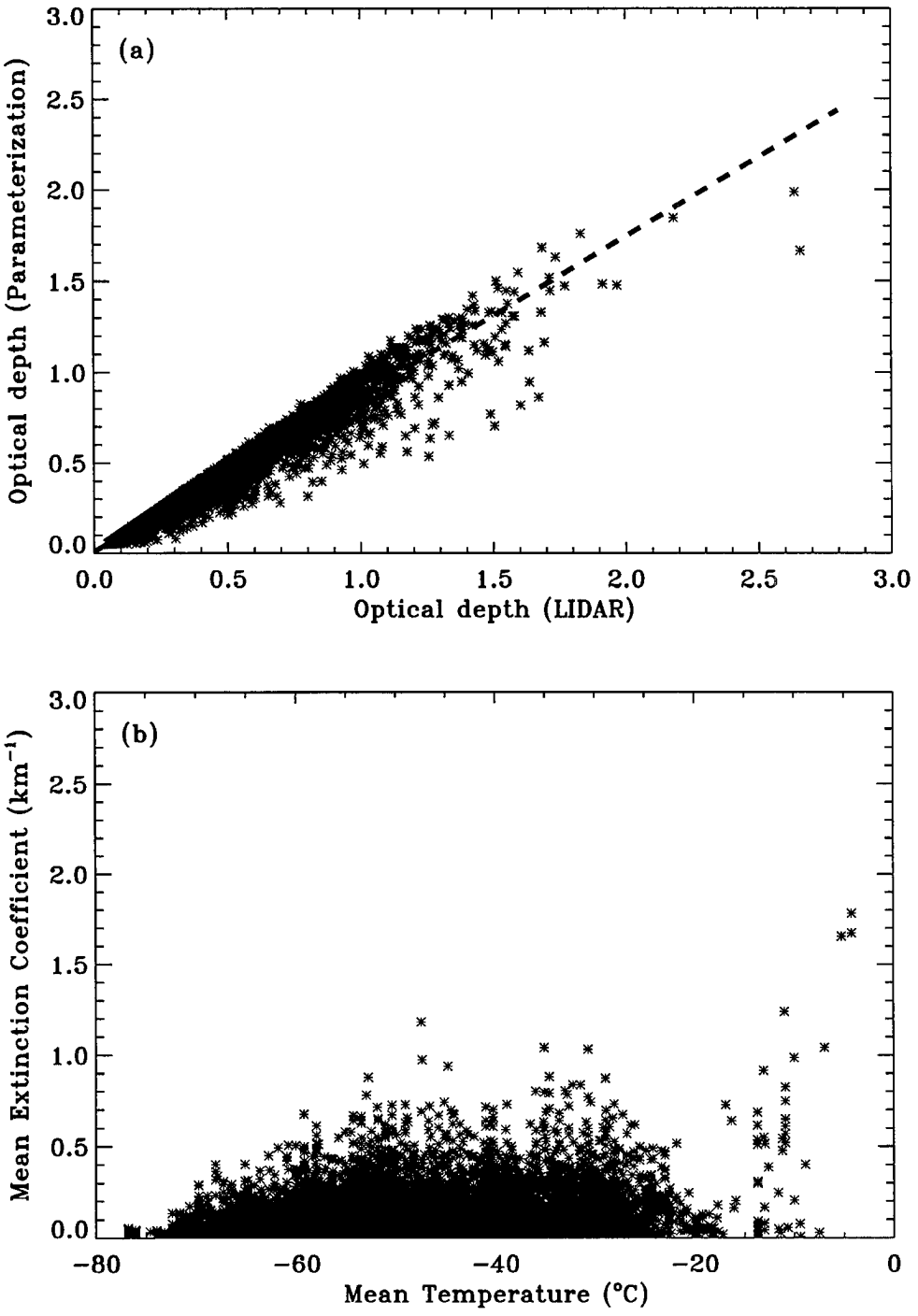

Figure 4.10: (a) Correlations between Optical Depths (stars). The slope for the linear correlation (dashed line) is 0.87; (b) Mean Extinction Coefficient vs. Layer mean Temperature. Nauru May-July 1999.

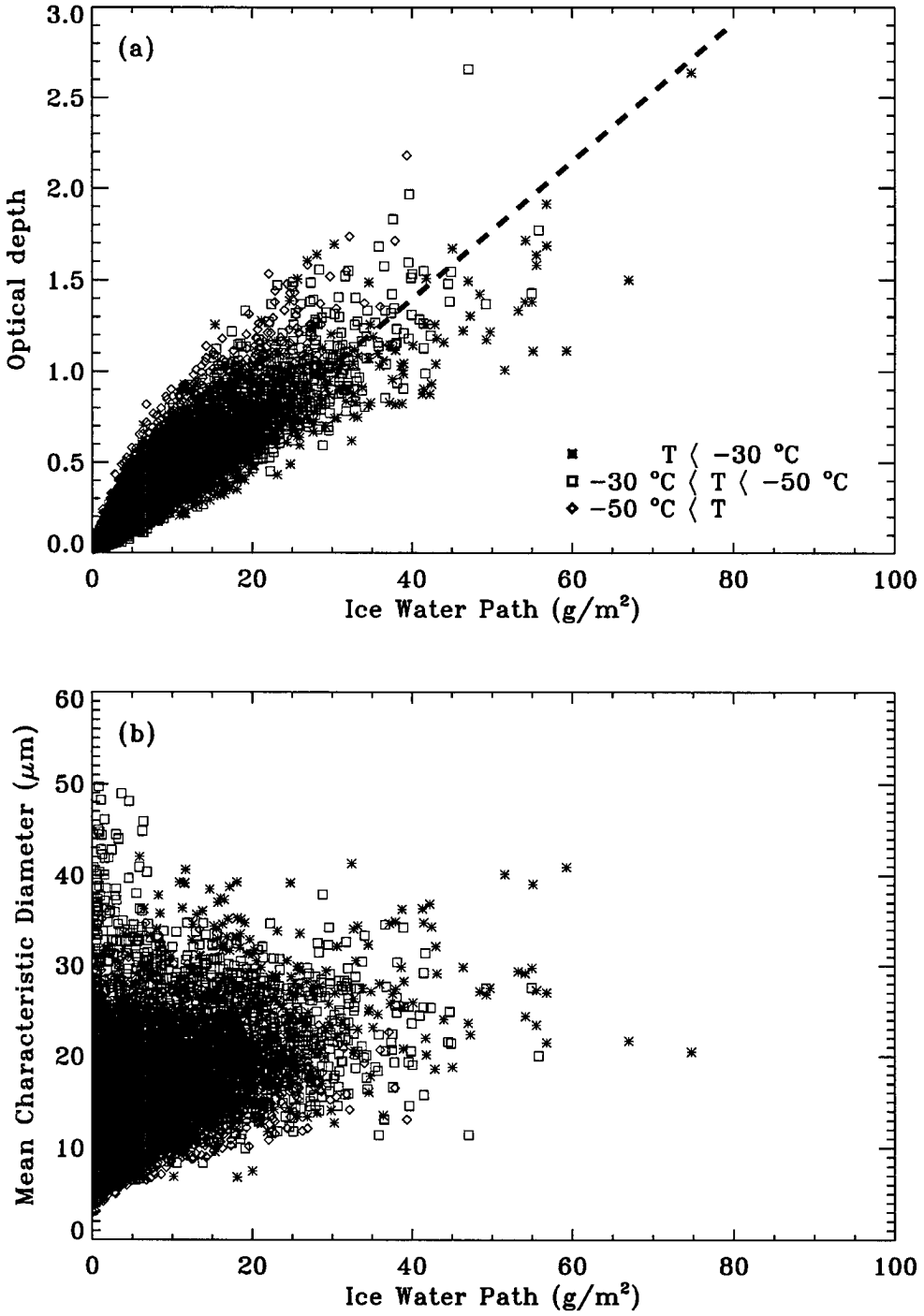

Figure 4.11: (a) Optical depth vs. Ice Water Path. With dashed line is the proposed parameterization (see text); (b) Mean Characteristic Diameter vs. Ice Water Path. Temperature dependence is according to Legend. Nauru 1999 May-July.

Figure 4.12 shows correlations with temperature for two cloud parameters: mean radar reflectivity and mean characteristic diameter respectively. Both parameters have a tendency to increase in value as the temperature increases. In particular, the values for the characteristic diameter range from 5 to 50 μm, with lower values at lower temperatures.

In Figure 4.13 a two-dimensional histogram between the cloud optical depth and the layer mean reflectivity is presented. This study shows that from 14317 cases, a total of 1135 cases have reflectivities less than -30 dBZ. Out of these, 706 have optical depth less than 0.2 while 429 with optical depths greater than 0.2. Below, a probability distribution function of the cases that are missed by radar, with a minimum detectability signal of -30 dBZ (such as the spaceborne cloud radar proposed for CloudSat), but for which we were able to detect and calibrate, shows that mostly very thin cirrus with optical depths less than 0.2, will be undetected by such a radar. This is a limitation of the radar-lidar retrieval model.

4.7 Summary

Defined as an active-active remote sensing system, the radar-lidar combination is a powerful tool in investigating radiative properties of the atmosphere, in particular those of cirrus clouds. Although the principle of operation for these two remote sensing instruments is very similar, they differ on the spectral region used for detecting atmospheric targets. It is due to this nonlinear response that we are able to successfully profile key microphysical characteristics of clouds. This chapter develops a retrieval method using data from a combination between MMCR and MPL systems located at Nauru. The following summarizes principal aspects introduced in this chapter:

1. The key assumption made is that the ice particles are characterized in terms of a gamma size distribution with fixed distribution width. The measured quantities (radar reflectivity and lidar extinction coefficient) can be expressed in terms of the remaining two parameters of the distribution (N_t and D_n); therefore these two parameters can be determined at each level using (4.7)

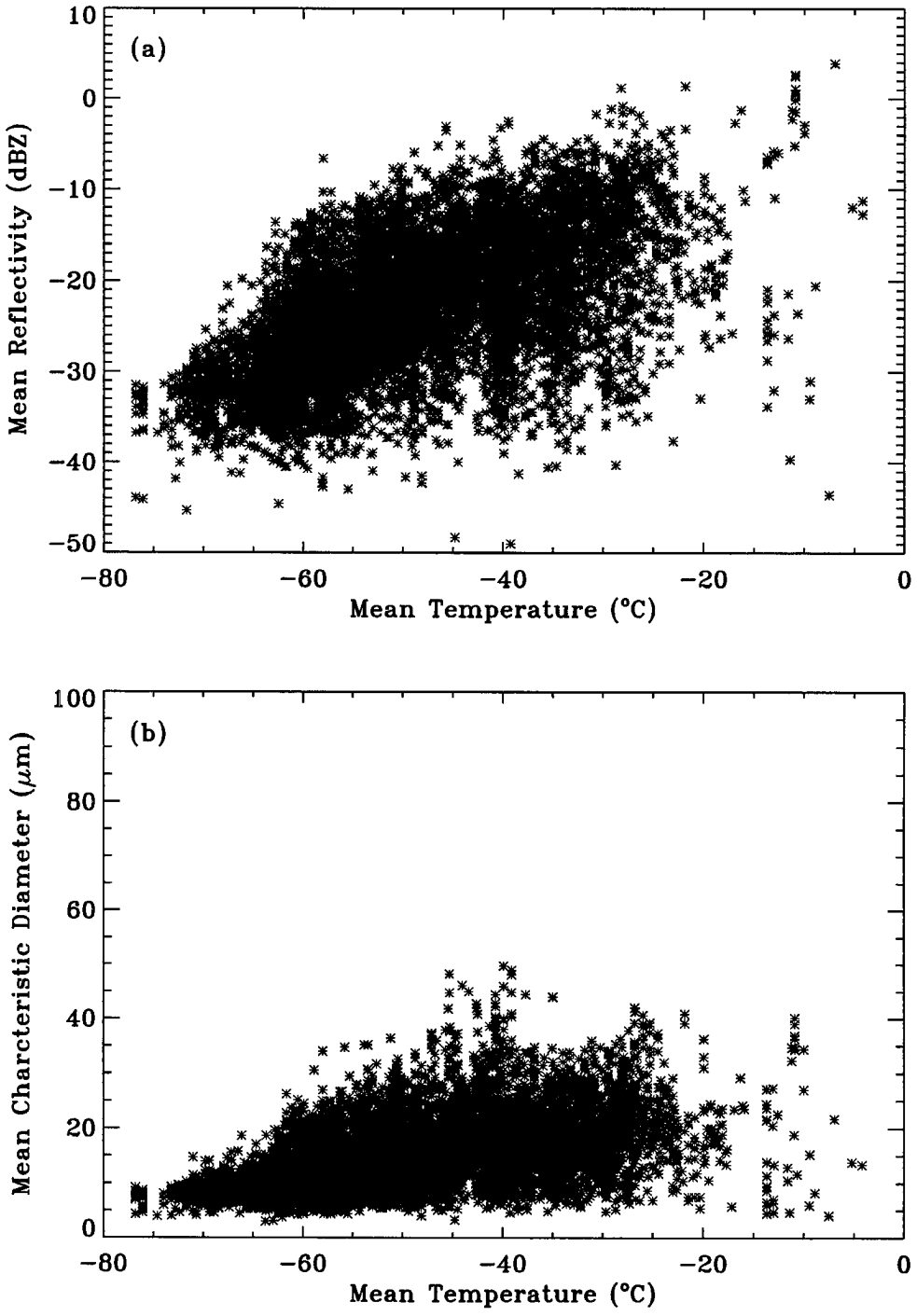

Figure 4.12: (a) Mean Radar Reflectivity vs. Temperature; (b) Mean Characteristic Diameter vs. Temperature. Nauru 1999 May-July.

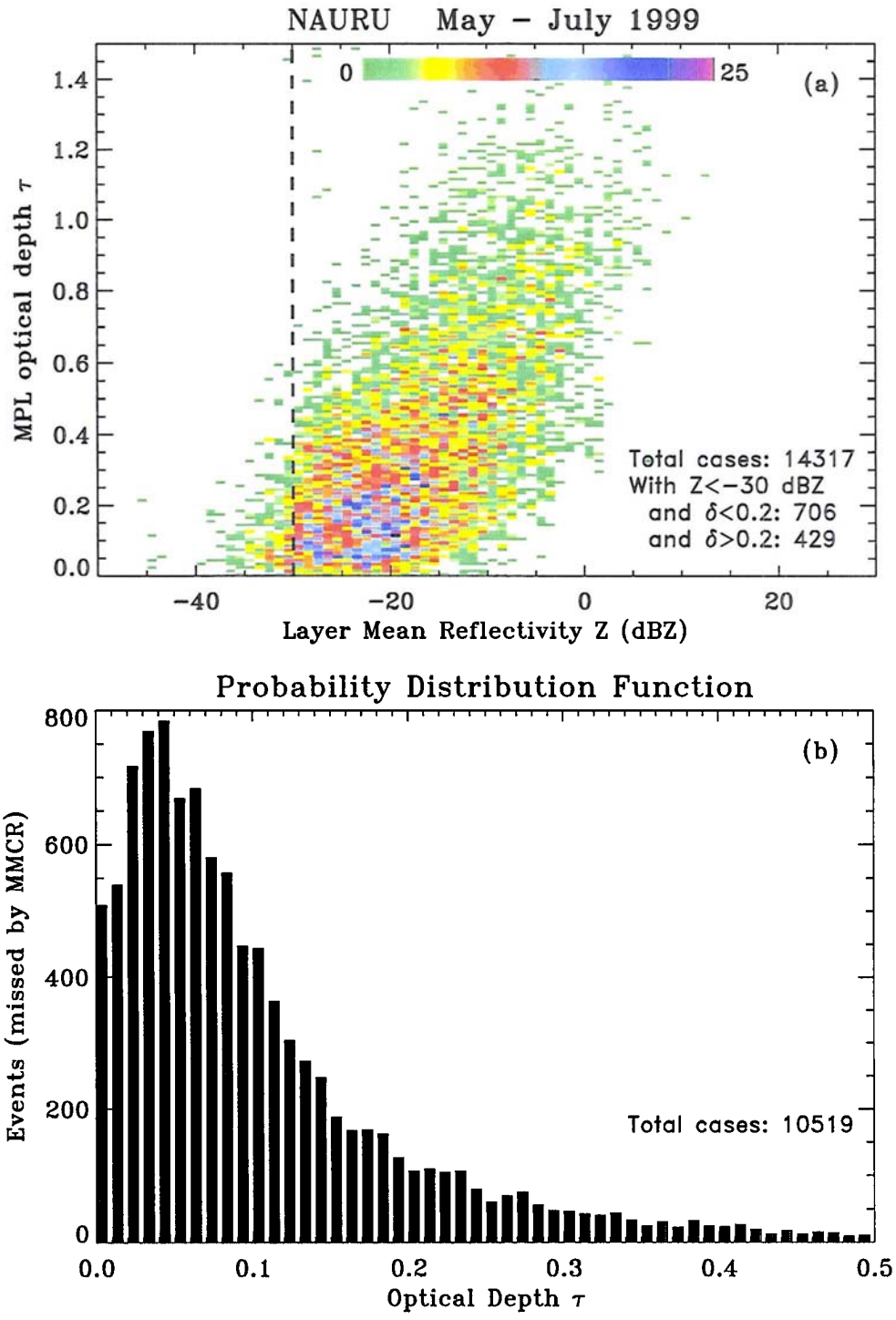

Figure 4.13: (a) Scatter plot of Layer Mean Reflectivity vs. MPL Optical Depth; (b) PDF of events missed by MMCR.

and (4.8). From these two parameters, the vertical profile for the IWC as well as the value for the IWP can be estimated.

2. Uncertainties in the value for the distribution width however, can lead to large errors for the retrieved variables; the need for methods determining its value are imperative. The level of errors are larger for IWC and smaller for D_n.

3. The proposed method was tested on a complex cirrus model. The results showed very good agreement between the retrieved and control variables, proving that our assumption regarding the use of a gamma function with a fixed value for the distribution width characterizing particle size distribution is valid for this case.

4. For the case when only radar reflectivity and cloud optical depth is available, another retrieval method is proposed. In this case however, since reduced information is available, we expect that the quality of our retrieval to worsen compared to the radar-lidar method. However, when the clouds are vertically homogeneous with respect to particle concentration the proposed method produces reliable results.

5. Application of this active-active instrument system on data collected at Nauru, shows agreement with other studies regarding cirrus clouds. We refer here to the parameterized relationship between the cloud optical depth and the IWP. The other retrieved cloud property, the characteristic diameter, varies within the previously reported ranges.

6. Unlike past studies that observed and proposed functional dependencies with temperature for various cloud parameters, the present study only finds evidence in favor of a trend, implying that cloud characteristics (particle size, IWC, for instance) increase with increasing temperature.

7. We can conclude that the radar-lidar combination is a reliable way of determining vertical profiles of cirrus cloud microphysical properties, provided that both sets of measurements (radar and lidar) overlap. For thin cirrus (with

optical depth less than 0.2) however, such a probability is small, indicating that the methods proposed here are best suited for clouds of optical depth in the range between 0.2 to 3.0, where the upper limit is established by the attenuation of lidars in cirrus.

Chapter 5

Active-Passive Methods

5.1 Introduction

The primary source of energy for the climate system is the sun. The radiation emitted by the sun interacts first with the superior part of our atmosphere. On its way down to the Earth's surface, it is absorbed and scattered by the atmospheric constituents in a complex way depending on its wavelength and on the composition of the atmosphere. As a result, the radiative field is "transformed" and contains information about all the complex radiative interactions that took place.

Basic physical laws are used to describe these complex interactions. Sensors that measure the natural levels of radiation emitted/scattered by the atmosphere are called passive sensors. They measure radiation coming from a FOV without influencing it in any way. Since atmospheric matter is more or less transparent to radiation, these instruments measure the integrated response of the atmosphere, thus lacking the range property that active sensors have. But because they don't use an artificial source of energy for investigating the atmosphere, they are smaller and cheaper to build and operate. As we are interested in profiling the properties of the atmosphere, and also in taking advantage of the passive sensors, measurements from both passive and active sensors are desirable. This chapter addresses this problem by studying combinations between an active and a passive sensor. As the active sensor we choose LIDAR, while for the passive sensor we choose either an IR or MAS sensor. The theory for combining active-passive sensors is described in this chapter, with applications on measured and synthetic data. The inevitable limitations of these systems are also addressed.

Since the focus of this work is on cloud properties, we start by developing a cirrus cloud model to be used in RT calculations that serve as a way of simulating passive observations and as a way of analyzing active-passive combinations of observations.

5.2 The Cirrus Cloud Model

One of the primary uses of the lidar instruments was to determine cloud boundaries accurately. In parallel, classic balloon atmospheric soundings provide information about the thermodynamic and dynamic properties of the cloud or environment. Based on *in-situ* measurements of cloud microphysical properties, various parameterizations relating microphysical properties to thermodynamical properties have been proposed and applied in cloud-climate models. Based on the above information, we propose a simple cirrus cloud model to be used in conjunction with our RT model to compute radiances as seen by the MAS sensor. Later, using a retrieval technique we examine the validity of our model and its effect on the retrieval of cloud optical depth.

Figure 5.1 depicts our cirrus cloud model. It is basically a one-layer cloud composed of various ice crystals (habits) having different concentrations. The habits and concentrations are set within some limits. A look-up table for the phase functions associated with a particular ice crystal habit and a mean diameter is used to compute the mean phase function for the cloud. In a similar way the single scatter albedo and the optical depth of the cloud are also computed. The mathematical formulation for computing the mean optical parameters to be used in our RT model is presented below:

$$\overline{\tau} = \frac{\pi}{4}\,\Delta Z\; N_0 \sum_{i=1}^{h} W_i \int_0^{\infty} n_i(D)\; Q_{ext}(i)\; D^2\; dD \tag{5.1}$$

$$\overline{\tilde{\omega}_0} = \left[\frac{\pi}{4}\,\Delta Z\; N_0 \sum_{i=1}^{h} W_i \int_0^{\infty} \tilde{\omega}_0(D,i)\; n_i(D)\; Q_{ext}(i)\; D^2\; dD\right] / \overline{\tau} \tag{5.2}$$

$$\overline{P(\theta)} = \left[\frac{\pi}{4}\,\Delta Z\; N_0 \sum_{i=1}^{h} W_i\right.$$

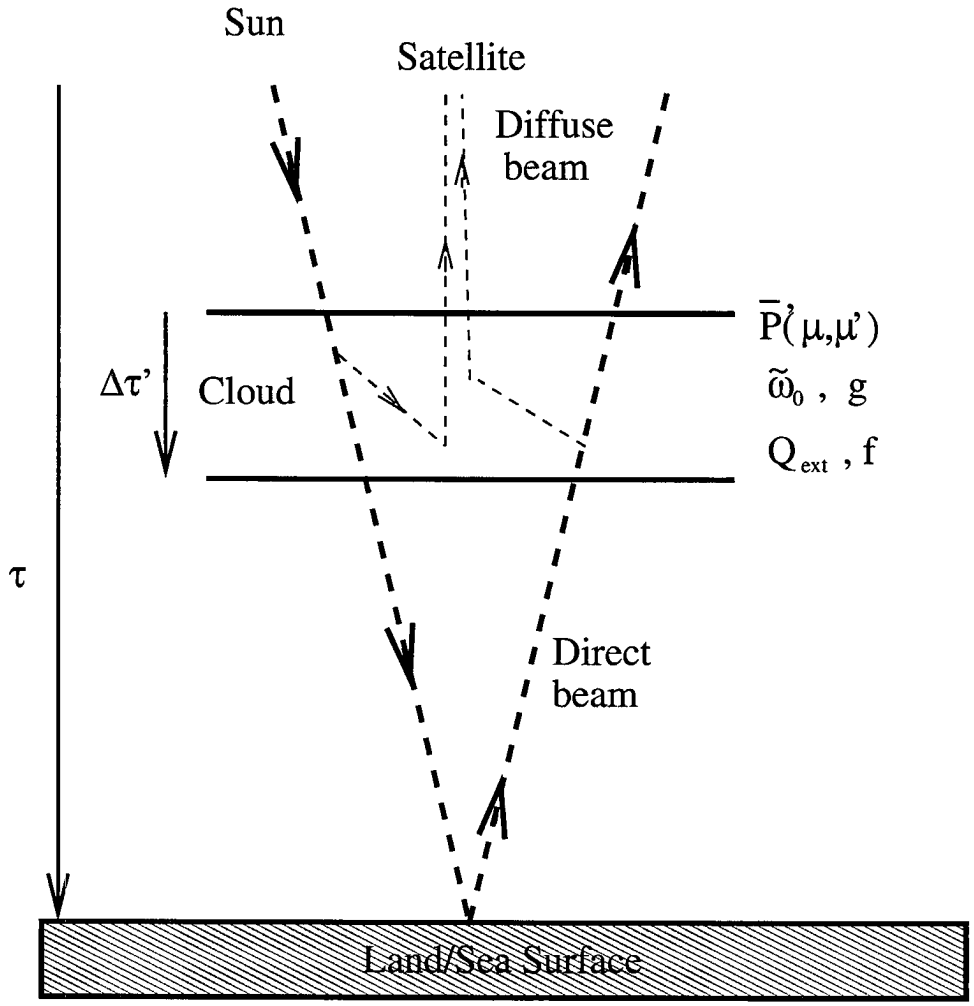

Figure 5.1: A Simple Cloud Model for RT Calculations

$$\times \int_0^\infty P_i(\theta, D)\, \tilde{\omega}_0(D, i)\, n_i(D)\, Q_{ext}(i)\, D^2\, dD \Big] \Big/ \left[\overline{\tau}\, \overline{\tilde{\omega}_0}\right] \tag{5.3}$$

where the summation is performed over all particular habits (from $i = 1$ to $i = h$) having various concentrations W_i. N_0 is the particle concentration and ΔZ is the thickness of our cloud. The particle size distribution $n_i(D)$ is assumed to be a Gamma size distribution and each of the habits have a predetermined characteristic diameter. The width parameter is set to two for all distributions after Dowling and Radke (1990). Based on previous measurements for cirrus clouds we assume that our cloud is composed of columns, plates and aggregates [Lynch et al. (2002)]. The habit concentrations are fixed to 50 %, 40 % and 10 % respectively, while the total particle number concentration must be adjusted to the value of the cloud optical depth. Using the above layer-mean quantities, we can determine the reflection and transsmition matrices for the cloud layer, which are later used to compute the diffuse and direct radiances at this level. We will also examine the sensitivity of our retrievals to the assumptions of this model.

5.3 LIDAR-IR Radiometer: LIRAD Technique

In this section we examine a popular procedure for evaluating optical properties of cirrus clouds using a combination of lidar and IR radiance data.

5.3.1 Background

Platt (1979) combined the LIDAR's integrated attenuated backscatter with the emissivity of the cloud as determined from using the Infrared Radiometer (IRT). This dual instrument procedure is referred to as the LIRAD technique. In the derivation below, we follow Platt (1979), but introduce an alternative equation to deal with multiple scattering effects. These effects are parameterized via the exponent n in equation (3.4).

We begin by introducing the ratio of the VIS extinction coefficient to the IR absorption coefficient, and assume it constant with height:

$$\alpha = \frac{\beta_{ext}(z)}{\sigma_{abs}(z)}\,. \tag{5.4}$$

When cloud particles become large, α asymptotically approaches two. Larger values of α indicates smaller cloud particles [Platt et al. (2002)]. We define the absorption optical depth as:

$$\tau_{abs}(z) = \int_{z_0}^{z} \sigma_{abs}(z')\, dz' \ . \tag{5.5}$$

The grey body emissivity associated with this optical depth is:

$$\epsilon(z) = 1 - e^{-\tau_{abs}(z)} \tag{5.6}$$

so that when $z = z_0$, $\tau_{abs}(z_0) = 0$ or $\epsilon = 0$ signifying the absence of clouds.

The information regarding IR spectral radiance is treated separately and an IR model is used to compute contributions from both the clear column and cloudy column as described in detail in a paper by Platt et al. (1984). Since water vapor is the main absorber/emitter in this spectral range (10–12 μm), profiles of this element need to be known. In the present study, the data collected by the MWR sensor at Nauru was used to accomplish that. A first guess for the emissivity coefficient is obtained from the ratio between the inferred IR radiance at cloud base and the IR blackbody radiance computed using the mid-cloud temperature. These parameters (cloud base and mid-cloud temperature) are determined from the lidar data and matched to an atmospheric sounding. An important limitation of using this technique is the requirement of clear sky IR data, which for some days is very hard to obtain.

From (5.5) and (5.6) we have:

$$\sigma_{abs}(z) = \frac{d}{dz}[\tau_{abs}(z)] = \frac{d}{dz}\{-ln[1 - \epsilon(z)]\} \ . \tag{5.7}$$

Accounting for the two way transmission factor, the (range corrected) measured cloud backscatter is thus:

$$\beta'(z) = \beta_{\pi}(z) \cdot \exp\left(-2 \int_{z_0}^{z} \beta_{ext}(z')dz'\right) \quad . \tag{5.8}$$

We now discuss two ways to account for the MS effects:

1. The first follows Platt (1979) and is widely used in the lidar community. The approach introduces a parameter (η) that lowers the transmittance, and assumes that the exponent n entering equation (3.4) is set to unity. In this way

we can now write (5.8) as:

$$\beta'(z) = F \cdot \beta_{ext}(z) \cdot \exp\left(-2\int_{z_0}^{z} \eta\beta_{ext}(z')dz'\right) \tag{5.9}$$

2. The second approach is the method introduced in Chapter 3. Using equation (3.53), (5.7) becomes:

$$\beta'(z) = F \cdot \beta_0 \left(\frac{\beta_{ext}}{\beta_0}\right)^n \cdot \exp\left(-2\int_{z_0}^{z} \beta_{ext}(z')dz'\right) . \tag{5.10}$$

With the introduction of the apparent integrated backscatter [Platt (1979)]:

$$\gamma'(z) = \int_{z_o}^{z} \beta'(z')\, dz' \tag{5.11}$$

then, for the first approach, using equations (5.4) and (5.7), we can deduce that:

$$\gamma'(z) = \frac{F}{2 \cdot \overline{\eta}} \left[1 - (1-\epsilon)^{2\eta\alpha}\right] \tag{5.12}$$

while using the second approach (equation 5.10) we obtain:

$$\gamma'(z) = \overline{(\beta'/\beta_0)^{\frac{n-1}{n}}}\ \frac{n \cdot F^{1/n}}{2} \left[1 - (1-\epsilon)^{2\alpha/n}\right] \quad . \tag{5.13}$$

Since β' is proportional to β_{ext}, we can write the above equation as:

$$\gamma'(z) \approx \overline{(\beta_{ext}/\beta_0)^{(n-1)}}\ \frac{n \cdot F}{2} \left[1 - (1-\epsilon)^{2\alpha/n}\right] \quad . \tag{5.14}$$

From the above equation (5.14) we see that the integrated backscatter depends on the power n. Note also how the extinction coefficient appears as a mean over the layer. The above expression is very similar to that proposed by Platt and Dilley (1981) and expressed by equation (5.12). The difference is that the MS effects (η) are now replaced by the nonlinear relationship between the backscatter and absorption coefficients (n), accompanied by a non-constant term which in the previous approach is unity due to the fact that the exponent n was set to unity. Since the first term in equation (5.12) involves a complicated averaging procedure for a given power $(n-1)$, we approximate it with its average value at the same power. In such a way we approximate equation (5.14) by the following expression:

$$\gamma'(z) \approx \overline{(\beta_{ext}/\beta_0)}^{(n-1)}\ \frac{n \cdot F}{2} \left[1 - (1-\epsilon)^{2\alpha/n}\right] \quad . \tag{5.15}$$

Some of the mathematical properties for the above expression can be summarized below:

1. it is continuous for any real n, including negative values for n.
2. it becomes linear with the product $\overline{\beta_{ext}/\beta_0}^{(n-1)}\ F\ \alpha\ \epsilon$ as $\epsilon \to 0$;
3. approaches a constant value of $1/2\ \overline{(\beta_{ext}/\beta_0)}^{(n-1)}\ F\ n$ as $\epsilon \to 1$;
4. it has an extremum when the exponent n is proportional to $-1/\ln(\beta_{ext})$

5.3.2 Application to Data

In order to test our new formulation of the LIRAD method, both simulated and measured data were used. Data collected by the MPL, IRT, and MWR system at Nauru on May 21, 1999, was processed according to the procedure proposed by Platt et al. (1984). Since in this particular procedure the inverse of the lidar ratio F is slightly different from our definition, we use that introduced by these authors. This difference in defining F, arising from the particular value assigned to the exponent n, is unimportant for the discussion below. The results of interest in our discussion are shown in Figure 5.2. Using the properties inferred for the attenuated integrated backscatter, we correlate γ' with the product $F\alpha\epsilon$ in the scatter plot presented in Figure 5.2(a). The factor $F\alpha\epsilon$ derives from the newly proposed relationship (5.15) for $\epsilon \to 0$. This is in direct contrast to the assumption in the Platt (1979) formulation that γ' is directly related to ϵ (see Figure 5.2 (b)).

The color coded dots are chosen according to some threshold values as follows: if the slope of the curve (γ') vs. ($F\alpha\epsilon$) is greater than 0.85 we chose either light blue (if $n < 0$) or blue (otherwise), while if less than 0.85 we chose either red (if $\alpha\epsilon\eta < 0.9$) or green (otherwise).

With the help of the color coding, the new proposed representation clearly shows an identifiable structure in the measured data, while the conventional representation, fails to do so. According to Figure 5.2(a), three distinct regimes can be identified:

1. a *low linear regime*, with small values for the apparent integrated backscatter (less than 0.05) and small values for the product $F\alpha\epsilon$ (less than 0.05);

2. a *high linear regime*, with large values for the apparent integrated backscatter (greater than 0.05) and small values for the product $F\alpha\epsilon$ (less than 0.05);

3. a *saturation regime*, with relatively constant values for the apparent integrated backscatter (around 0.12), and large values for the product $F\alpha\epsilon$ (greater than 0.2).

Surprisingly, all the cloud events studied fit into one or more of these characteristic regimes, suggesting that such a behavior is universal. Also, these regimes seem correlated with temperature. This is illustrated in Figure 5.2 (bottom panels), where mid-cloud temperature correlations between γ' and ϵ respectively are shown. Clouds colder than - 65 °C are most likely associated with type (1) and (3) regimes, while clouds warmer than - 65 °C, are most likely associated to type (2) regime. A trend in increasing values for γ' with increasing cloud temperature is also observed. When we choose to study the dependencies with respect to cloud emissivity (ϵ) alone, no clear distinction or dependence can be inferred (see Figures 5.2 (c) and (d)). A solid physical interpretation for such behavior is not yet available. However, synthetic data, based on the new proposed formulation, supports this type of behavior.

The synthetic data was produced by using the expression for the integrated backscatter given in equation (5.15). Consequently a Monte Carlo approach was used. Synthetic integrated backscatter coefficients were calculated for random values of the quasi-independent variables ϵ, β_{ext}, and α. The limits of variation for each variables were set as follows: (1) ϵ between 0 and 1; (2) β_{ext} between 0.2 and 1.4; (3) α between 2 and 5. These imposed limits are within the observed ranges for each variable. We chose the exponent n to be proportional to $-1.4/\ln(\beta_{ext})$ for reasons explained above. We further filter the output as well: we only represent the simulated values for which γ' is less than 0.3, and $F\alpha\epsilon$ is less than 0.6. In Figure 5.3 (a), and (b), the simulation mimics those presented in Figures 5.2 (a), and (b) respectively. The very close agreement between plot Figure 5.2 (a), which is the measured data, with Figure 5.3 (a), which is the synthetic data, supports our assumption regarding the nonlinearity effects in the MS problem. Agreement between Figures 5.2 (b) and 5.3 (b) also supports our hypothesis. Figure 5.3 (c) and

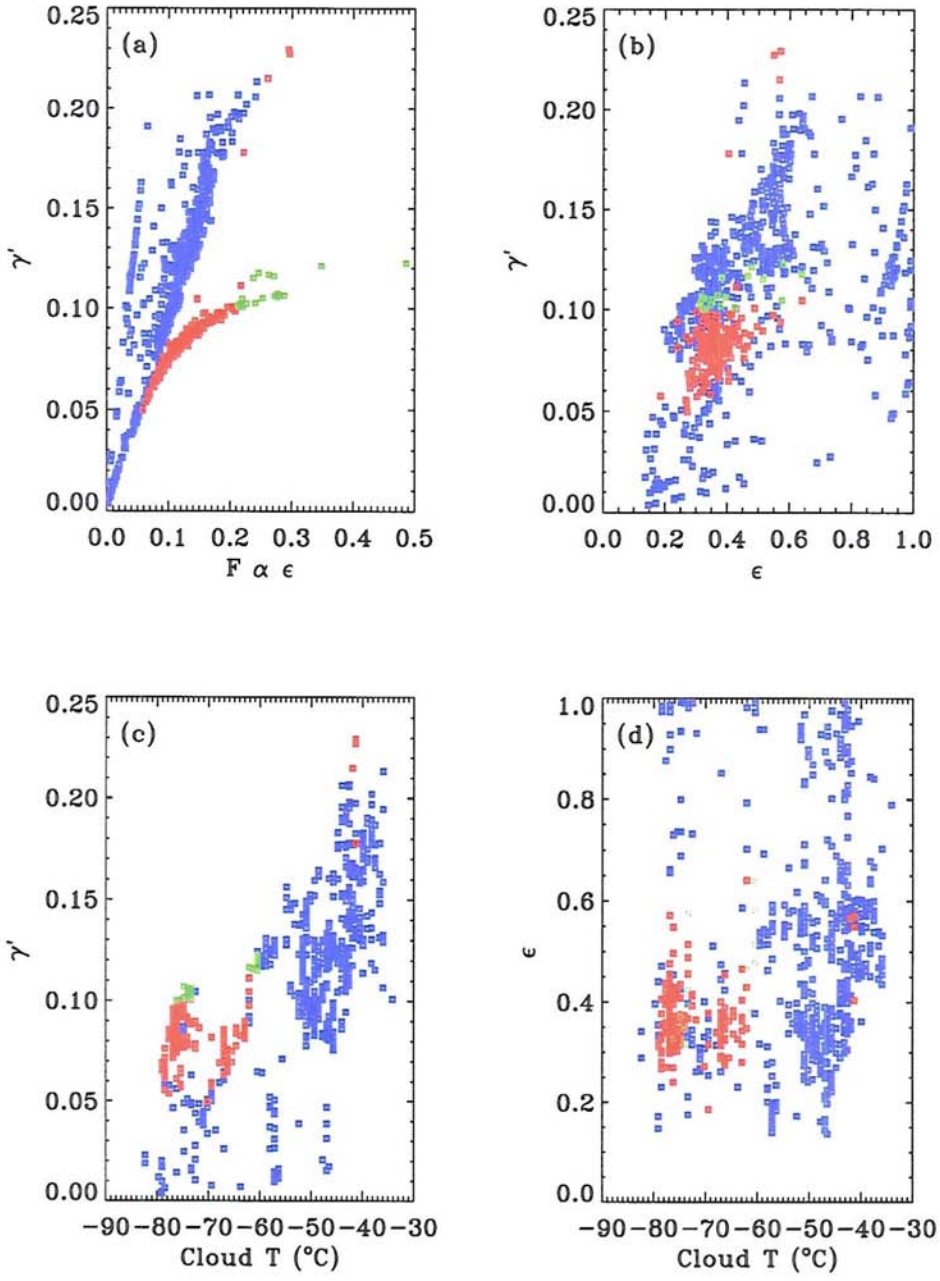

Figure 5.2: Observed data. (a) New representation; (b) Old representation; (c), (d) Variation of cloud properties with Mid-cloud Temperature. Color coding as explained in text. Nauru 1999/05/21

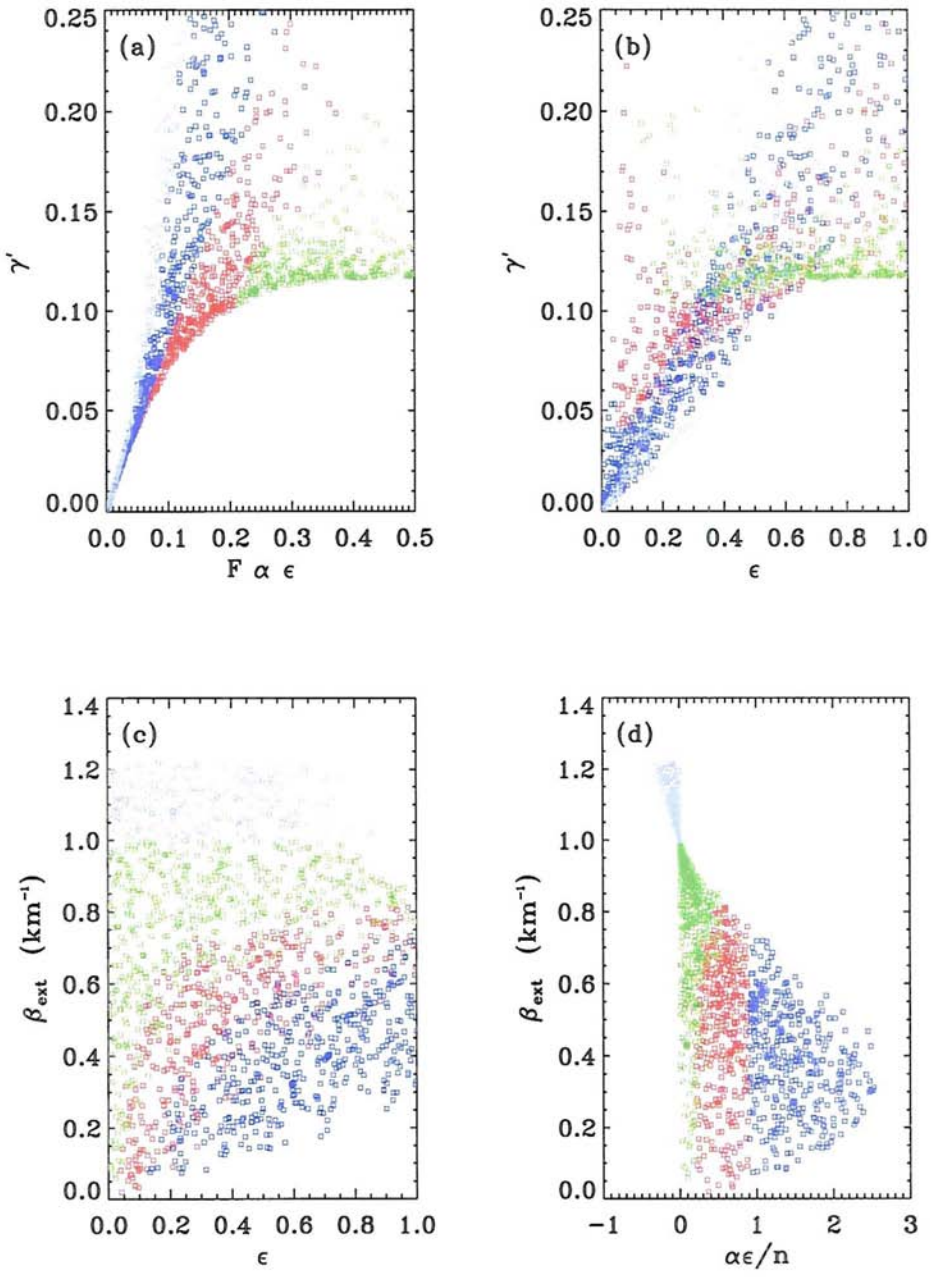

Figure 5.3: Synthetic data. (a), (b) Same as in figure 5.2 (a), (b). (c), (d) Domains of variations for the VIS extinction coefficient. Color coding as explained in text.

(d) shows possible domains of variations for the extinction coefficient with respect to emissivity and the product $\alpha\epsilon/n$ respectively. We note the well-defined boundaries for these domains, perhaps supporting specific regimes, as those identified above. Note the effect that a negative value for the exponent n has on the synthetic data: it produces high values for γ', regardless of the value for the emission coefficient ϵ. Such large values were observed and reported as "anomalous" backscatter by Platt and Dilley (1981), since they could not be explained. Larger values for γ' are also favored by smaller ratios between β_{ext} and ϵ.

What is interesting is that we are able to simulate the observed behavior closely without referring to the phase functions associated with cloud particles. The phase function governs both the backscatter signal and MS effects. It seems that regardless of the complexity of the phase function, the response is very similar. But we have to remember that information about phase function, as well as cloud geometry is contained in both the exponent n and the inverse of the lidar ratio F. Also, the attenuated integrated backscatter contains such information. But all these parameters are some sort of a mean for the cloud layer. Additionally, this information comes from the properties of the cloud in the visible spectra. The connection with the infrared properties is still unclear. A parameter that directly "connects" visible and infrared properties is alpha (α). Emissivity coefficient ϵ only characterizes the infrared properties of the cloud.

In conclusion, this simulation for the integrated backscatter coefficient supports our earlier hypothesis that the exponent n not is necessarily fixed to unity. More theoretical and experimental work is needed to further investigate this technique.

5.4 LIDAR-MODIS System

In this section, we investigate the basis for another active-passive system: a combination between lidar and solar spectral radiances as measured by a radiometer. The objective is to develop and test a model for retrieving cloud optical properties from combined measurements. The approach to this objective is to first analyze the problem, assess possible limitations, develop a theory, perform sensitivity studies,

test the model, and finally process the data and interpret the results. This is not an easy task given the variability of the unknown parameters and the lack of coincidental lidar and reflected radiance data. The results and interpretations of such an effort are presented below. An attempt to test the proposed method using SAFARI data was not successful for reasons described below.

5.4.1 Background

The Terra satellite carries a new-generation instrument for the observation of cirrus clouds and provides data from which optical thickness and average size of ice crystals can be retrieved. This instrument, The Moderate Resolution Imaging Spectroradiometer (MODIS) surpasses the capabilities of previous instruments with its 36 bands for studies of land, ocean, and the atmosphere. These channels include a 1.38 μm band for cloud detection and correction, 0.65, 1.66, and 2.11 μm bands for cloud microphysical and optical property retrievals, and bands centered at 8.5, 11 and 12 μm for infrared cloud property retrieval. The data collected via the three bands for infrared retrievals is processed using a trispectral algorithm based on that developed by Nakajima and King (1990) to retrieve the optical thickness and average particle size for water clouds. However, despite the increased spectral combinations provided by these channels, the models used to invert the data are still deficient as shown below. Currently, most algorithms for retrieving cirrus optical thickness and particle size make the assumption that the cloud ice crystals have the same shape such as spheres, hexagonal plates, hexagonal columns, or fractal polycrystals, and make use of a single size distribution. This however is incorrect as aircraft- and balloon-borne measurements have shown that ice crystals come in a wide range of shapes including solid and hollow columns, bullet rosettes, plates, aggregates, and irregular particles, and also that they are heterogeneously distributed. An example of the vertical heterogeneity of cirrus is the vertical profile obtained from replicator images of cloud ice crystals collected on November 25 and December 5, 1991 during the FIRE-11 program [Yang et al. (2001)]. The clouds appear to have three layers (see Figure 5.4). The top layer contains mostly small "quasi-spheres", the middle

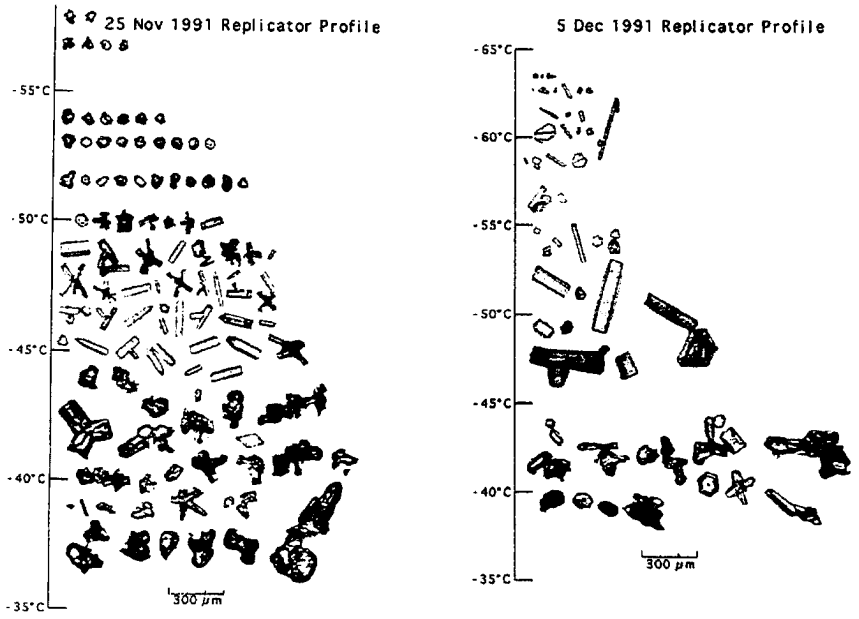

Figure 5.4: Replicator images of ice crystals for two different cirrus clouds: 25 November 1991 and 5 December 1991. After Yang et al. (2001)

one is composed primarily of pristine ice crystals with well-defined hexagonal shapes or bullet rosettes, while the bottom layer contains irregular particles and aggregates with rounded edges.

It is thus necessary to understand how this natural heterogeneity affects the retrieval of optical depths. We do this by assessing the effect of the vertical heterogeneity of the ice crystal sizes and shapes on the radiative transfer calculations. Consequently, reliable tables of bidirectional reflectances for cirrus clouds over a series of sizes, optical thicknesses, and viewing geometries (i.e., solar zenith angle, viewing zenith angle, and relative azimuth angle) need to be generated.

For the purpose of estimating cloud optical properties for cirrus clouds, the well known Doubling and Adding radiative model, described in Appendix D, is used. This model is chosen because it computes radiances that are accurate enough for our purposes. This represents nothing more than a test for both forward and

inverse models. It can also be used to test the sensitivity of the measured radiances to various parameters with a special attention to the mean phase function of the cloud. The mean phase function is dependent on ice crystal habit, distribution and concentration and from this it follows that the measured radiances will also be influenced by these factors. This is also true for any other optical properties that we may be able to retrieve using these measurements. The following paragraphs describe our findings using the above RT model applied to an idealized cirrus cloud.

5.4.2 The Radiative Transfer Model

As mentioned above, the RT model used for our calculations is the Doubling and Adding method. This technique is robust, and has proven useful in many radiative problem calculations. However, one major problem needs to be resolved. Because ice crystals are characterized by a strongly asymmetric phase function with a narrow but intense forward lobe, computational difficulties can arise. An example of such a phase function with strong forward scattering values is presented in Figure 5.5(a). It represents the computed phase functions for plate ice crystals at a particular diameter [Yang et al. (2001)]. Also computed are the extinction factor Q_{ext} and the single scatter albedo $\tilde{\omega}_0$ which can be used to determine averaged optical properties for a particular cirrus cloud layer. As the diameter of the ice crystals increases, the forward values for the phase function increase dramatically reaching values around 10^4 - 10^6. This creates a serious numerical problem when computing the coefficients χ_l that appear in the expansion of the phase function with respect to the Legendre polynomials (see equation D.8). To achieve an accurate representation for such a strongly asymmetric phase function, the number of χ_l terms that need to be considered increases accordingly. Unfortunately,the computational burden increases as the square of the number of terms in this expansion. A solution to making this problem more tractable is the well known and used treatment for the phase function: the "Delta-M" method proposed by Wiscombe (1977). It simply decomposes the phase function in two parts: one that is representative of the forward direction and behaves like a δ-function, the other describing the phase function for angles other

than the forward direction. Mathematically the above statements can be written as follows:

$$P(\cos\theta) = 2f\delta(1-\cos\theta) + (1-f)P'(\cos\theta) \quad . \tag{5.16}$$

However, given the large magnitude of the forward peak in the phase function, this method doesn't work well, since it still requires the computation of many χ_l coefficients for the original phase function. Further, the value for the fraction f of incident energy scattered in the forward direction, is arbitrarily set to the value of the coefficient χ_l that follows the last term in our truncated representation for the phase function. This particular value is presented in Table 5.1 for reasonable numbers of streams.

An alternative to the above method was proposed by Hu et al. (2000). This method determines the values of χ_l coefficients from the requirement of minimizing the errors between the original phase function and its truncated representation. However, for the purposes of solving the RT equation with a strongly asymmetric phase function, we propose another method which in fact is a combination of the above methods, yet different in the way we define and compute the value for f, as explained in the following subsection.

5.4.3 Similarity as a Consequence of the Radiative Transfer Equation

An important concept in the RT field is the concept of *similarity*. It simply states that different radiative transfer problems, determined by different phase functions, can be made equivalent using different pairs of optical depth and single scatter albedo. In other words, the radiative field is not uniquely determined by a given set of the above parameters. We present a simple demonstration of this below. We start from the RT equation valid for the visible part of the spectra:

$$\mu\frac{dI(\mu)}{d\tau} = I(\mu) - \frac{\tilde{\omega}_0}{2}\int_{-1}^{1} P(\mu')\, I(\mu')\, d\mu' \tag{5.17}$$

where I is the radiance field, τ is the optical depth of the layer, $\tilde{\omega}_0$ is the single scatter albedo and $P(\mu')$ is the azimuthally averaged phase function. In this equation, by "forward" direction we understand the direction defined by angle μ. The integration

angle μ' is defined with respect to the "forward" direction. Using the normalization requirement for the phase function, the above equation can be rewritten as:

$$\mu \frac{dI(\mu)}{d\tau} = (1-\tilde{\omega}_0)I(\mu) + \frac{\tilde{\omega}_0}{2} I(\mu) \int_{-1}^{1} P(\mu')\, d\mu' - \frac{\tilde{\omega}_0}{2} \int_{-1}^{1} P(\mu')\, I(\mu')\, d\mu' \quad . \quad (5.18)$$

A simple inspection of the above form shows that if the radiance in the "forward" direction does not change much within a small angular cone around this direction, then we can write the above equation as:

$$\mu \frac{dI(\mu)}{d\tau} = (1-\tilde{\omega}_0)I(\mu) + \frac{\tilde{\omega}_0}{2} I(\mu) \int_{-1}^{\alpha} P(\mu')\, d\mu' - \frac{\tilde{\omega}_0}{2} \int_{-1}^{\alpha} P(\mu')\, I(\mu')\, d\mu' \quad (5.19)$$

where α characterizes the small angular cone we defined above. The advantage of this formulation is evident in the case of strongly asymmetric phase functions. But the drawback is that the quantity α is not precisely defined; therefore the limits of integration are not defined. Moreover, for the purposes of evaluating the integral terms, a quadrature formula is usually employed. Since equations (5.17) and (5.19) are equivalent (within the limit explained above), we can manipulate the latter by redefining the phase function for the "forward" direction, such that its asymmetric structure is diminished. That is, we can use an equation that is *similar* to the starting one (i. e. 5.17) but with a more symmetric phase function. In other words, in equation (5.17), we can add and subtract a term of the form:

$$\frac{\tilde{\omega}_0}{2} I(\mu) \int_{\alpha}^{1} P''(\mu')\, d\mu' \approx \frac{\tilde{\omega}_0}{2} \int_{\alpha}^{1} P''(\mu')\, I(\mu')\, d\mu' \quad (5.20)$$

where $P''(\mu')$ is yet to be defined, and we use our hypothesis that the radiative field does not vary much within the "forward" direction. By inspecting equations (5.19) and (5.21), we can define the fraction of the incident energy that is scattered in the forward direction as:

$$f = \frac{1}{2} \int_{\alpha}^{1} [P(\mu) - P''(\mu)]\, d\mu \quad . \quad (5.21)$$

The above definition for the fraction of energy that is scattered in the forward direction constitutes the difference between the present method and the "Delta-M" method. In our numerical simulations we set $\alpha = \cos(2°)$, but there is no limitation on this value, except when our hypothesis concerning the scattered radiative field

is violated, which is expressed by equation (5.20). From it, we can also infer the optimal number of streams that should be used. This number should not be too large to oversample nor too small to under-sample the dependence of the radiative field with respect to scattering angle. An estimated value for N is given by the ratio between 180, which is the angular range for our phase function and the value chosen for the forward angle. At this point, it should also be noted that $P''(\mu)$ can be any function we choose; therefore the definition for f is not unique. Using the above definition, we can rewrite equation (5.19) in the form:

$$\mu \frac{dI(\mu)}{d\tau} = (1-\tilde{\omega}_0)I(\mu) + (1-f)\,\tilde{\omega}_0 I(\mu)$$

$$-\frac{\tilde{\omega}_0}{2}\int_{\alpha}^{1} P''(\mu')\,I(\mu')\,d\mu' - \frac{\tilde{\omega}_0}{2}\int_{-1}^{\alpha} P'(\mu')\,I(\mu')\,d\mu' \qquad (5.22)$$

which can be rewritten in the desired form (as equation 5.17) by defining a "truncated" phase function of the form:

$$P'(\cos\theta) = \begin{cases} P(\cos 2^\circ)/(1-f) & ,\ 0^\circ \le \theta < 2^\circ \\ P(\cos\theta)/(1-f) & ,\ 2^\circ \le \theta < 180^\circ \end{cases} . \qquad (5.23)$$

Here we already apply the definition for the "forward" angular cone and set $P''(\cos\theta) = P(\cos 2^\circ)/(1-f)$. In such a way, $P'(\mu)$ is a continuous function, which is helpful when expanding it in terms of the Legendre polynomials. It is easy to demonstrate that the above definition ensures normalization for our "truncated" phase function. We also solve for the non-uniqueness for the f parameter and ensure that the representation in terms of Legendre polynomials of the truncated function does not yield negative values since the continuity requirement for the truncated phase function is satisfied. An example of the truncated phase function is given in Figure 5.5(b) where we also use the representation in terms of Legendre polynomials for two different number of streams: $N = 32$ and $N = 64$ respectively. We expect that by increasing the number of terms, the representation for the truncated phase function becomes more accurate. This is true up to the point when both the oversampling and the computational errors become more important and the representation for the phase function becomes worse.

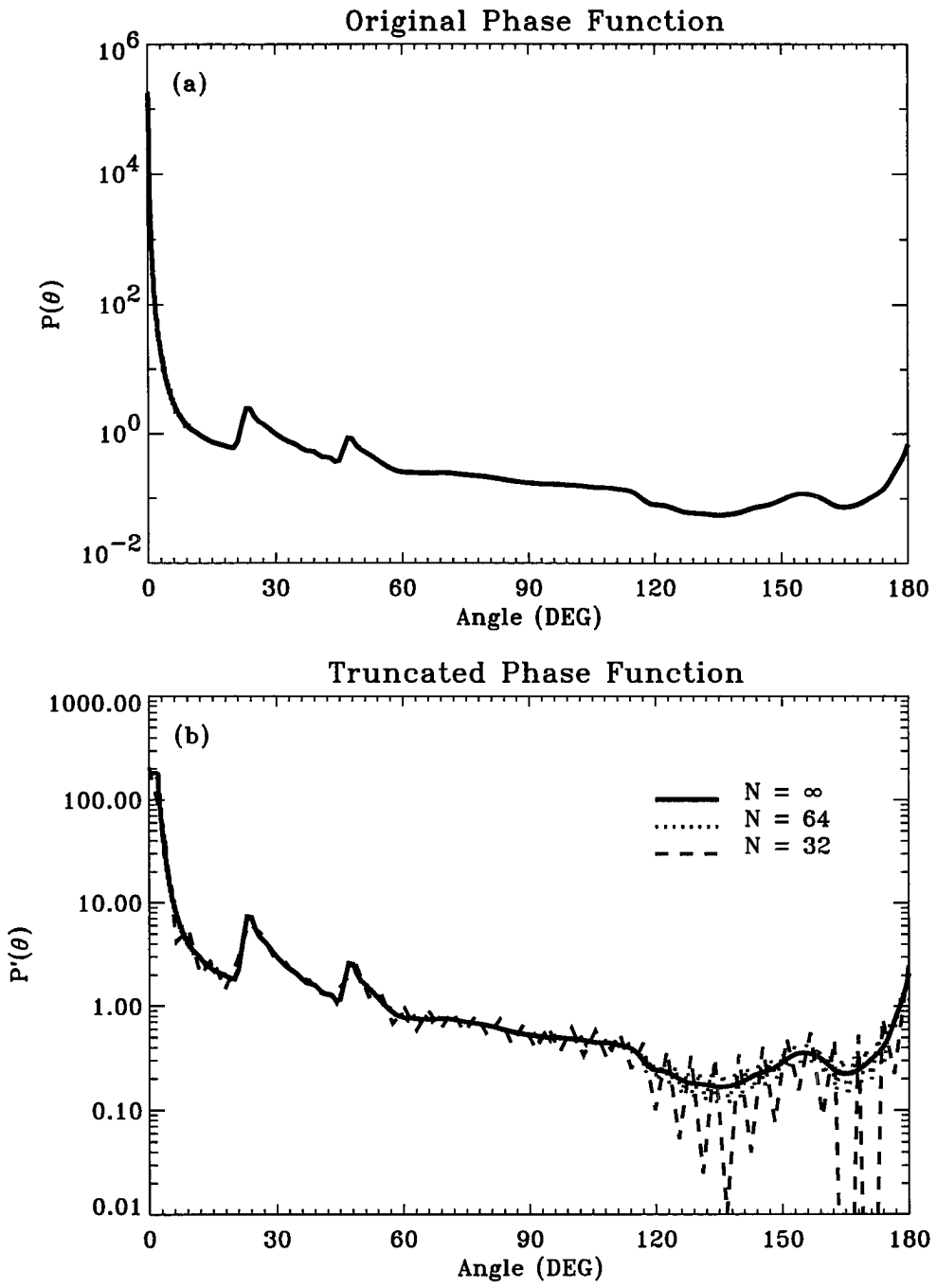

Figure 5.5: (a) Original Phase Function; (b) Truncated Phase Function (solid line). Approximation using Legendre Polynomials: dotted line for N=64; dashed line for N=32.

By substituting (5.23) into (5.22) we obtain the expression for the RT equation in the form:

$$\mu \frac{dI(\mu)}{d\tau} = (1 - f\ \tilde{\omega}_0) I(\mu) - (1 - f)\ \frac{\tilde{\omega}_0}{2} \int_{-1}^{1} P'(\mu')\ I(\mu')\ d\mu' \qquad (5.24)$$

which we can reduce to equation (5.17) by introducing the new variables [Wiscombe (1977)]:

$$\tau' = (1 - f\tilde{\omega}_0)\tau \qquad (5.25)$$

$$\tilde{\omega}_0' = \frac{1 - f}{1 - f\tilde{\omega}_0}\ \tilde{\omega}_0 \quad . \qquad (5.26)$$

If the thermal emission term is added to the original RT equation, then the emissivity coefficient must be scaled as well, leading to the following expression:

$$\epsilon' = \frac{\epsilon}{1 - f\tilde{\omega}_0} \quad . \qquad (5.27)$$

The above definitions (equations 5.25 and 5.26) represent the *similarity relations* introduced by van de Hulst (1980). It simply states that the solution for complex phase functions can be approximated in terms of solutions for simpler phase functions [Goody and Yung (1989)]. In other words we can solve a RT equation that has *scaled* values for the single scatter albedo and the optical depth, using a simpler (i. e. more symmetric) phase function. It should also be noted here that this new representation is a property of the RT equation and not of the phase function, and is simply a consequence of our hypothesis that by "forward" direction we actually understand a small angular cone, defined by the setting of the "forward angle". The only contribution of the phase function is in the value of parameter f. An asymmetric phase function produces a larger value for f than a symmetric one for the same "forward" angle. There is no loss in radiation (energy), just a "redistribution" of radiation in the "forward" direction. There are two factors contributing to this. The first one concerns the scaled optical depth. According to (5.20) the scaled optical depth is less than the non-scaled optical depth. But one must keep in mind that the actual radiative field increases, hence these two effects tend to compensate. The other factor is the reduction in the single scatter albedo (equation 5.26). This reduced scaled single scatter albedo implies that there is an apparent absorption

in the radiative field. But as mentioned above the scaled optical depth is reduced, and it compensates for this apparent sink of energy. Figure 5.6 shows the diffuse radiative fields (upward and downwards) as function of scattering angle, calculated for a particular cloud type for two different values of the "forward angle". The radiative fields coincides for angles that are not on the direction of the direct solar beam (defined here as 40°). The differences at this particular angle are compensated by the direct field, such that the total fluxes are (within computational errors) identical. It is worth noting that the figure shows two symmetrically distributed local maxima which are more accentuated for the downward radiative fields. They are due to the local maxima in the phase function at around 30°. It easy to observe that the radiative field becomes more isotropic as the "forward" angle cone, and thus f, is increased (compare dots with lines). We must also mention that equation (5.27) states that the scaled emissivity coefficient is larger that the un-scaled emissivity coefficient, with values greater than unity being possible.

We use the above scaled quantities in our RT model for each atmospheric layer to calculate the radiances at the top of the atmosphere, as seen by a radiometer satellite. At the same time, other optical properties for each layer, like the mean single scatter albedo or the transmission and the reflection coefficients can be inferred. These quantities give us some idea about the cloud microphysical structure. By adjusting various parameters in our idealized cloud model we shed some light about the accuracy and sensitivities that one can expect when retrieving cloud properties from satellite measurements and in such a way adjustments and/or assessments can be made.

5.4.4 Tests on Synthetic Data

In a first set of experiments we tested sensitivities of the forward model to both the values of the "forward angle" (θ) and the numbers of streams (N). The atmosphere was considered to be a layer of Rayleigh scattering with a 2 km thick cloud with base at 10 km. The cirrus cloud ice crystal composition for this particular test was assigned to be 50 % plates and 50 % columns having a total number concentration

of 50 particles per liter. The computed asymmetry factor and the single scatter albedo for the cloud layer were 0.791 and 0.99999 respectively. The surface albedo was assumed to be 0.3 and the solar zenith angle was set to 40°. The results are summarized in Table 5.1. In the table, F_d^+ is the upward diffuse flux at the top of the cloud and F_d^- is the downward diffuse flux at the base of the cloud (in arbitrary units). Indicated in parenthesis, are the values for the total upward and downward fluxes. I is the upward radiance at the top of the atmosphere. The units for fluxes and radiances are arbitrary. $\Delta\tau'$ is the "scaled" cloud optical depth and f is the fraction of energy that is scattered in the forward direction.

As expected, $\Delta\tau'$ decreases when θ increases, since f increases. As a result, the total optical depth decreases as well. The upward and downward diffuse and total fluxes are practically invariant to the number of streams used. However, discrepancies between calculated diffuse fluxes for various values of f are observed. This was expected since by varying the values for f we vary the partition between direct and diffuse fluxes. For example, the differences in the diffuse fluxes, from using a forward angle θ of 2° instead of 1° are as follows: around 5 % for the downward diffuse flux at cloud base, and around 3 % for the upward diffuse flux at cloud top respectively. The values for the total upward and downward fluxes are practically unchanged to the number of streams or to the value of the forward angle. However, the upward radiances at top of the atmosphere are sensitive to these parameters. But that is because for smaller and larger numbers of streams we violate our basic assumption in developing the similarity relationship (equation 5.20). We can only apply the scaled variables for a given forward angle θ, within a range of streams N. We also expect that our hypothesis to be violated around the forward direction, where the angular resolution is increased. It is therefore necessary to average the radiance field around these angles. In order to demonstrate that our proposed method is superior to the δ-M method, we apply this latter method as well. Since the phase function has a strong asymmetry, the number of streams to be used is well beyond those listed. It is for this reason that the values for f are unrealistic. From our interpretation f should be positive and less than unity. Because of this, optical depths as well as radiances are negative and therefore unrealistic.

Table 5.1: Sensitivity to the "forward angle" (θ)

θ	Variables	Number of Streams (N)				
		16	32	64	128	256
1°	F_d^+ (F_t^+)	0.1728 (0.2619)				
	F_d^- (F_t^-)	0.2390 (0.7190)				
	I	3.906	4.180	4.180	3.843	3.856
	$\Delta\tau'$	0.348				
	f	0.540				
2°	F_d^+ (F_t^+)	0.1679 (0.2620)				
	F_d^- (F_t^-)	0.2256 (0.7188)				
	I	3.797	3.831	3.761	3.745	3.754
	$\Delta\tau'$	0.327				
	f	0.567				
3°	F_d^+ (F_t^+)	0.1662 (0.2621)				
	F_d^- (F_t^-)	0.2209 (0.7188)				
	I	3.755	3.757	3.725	3.708	3.717
	$\Delta\tau'$	0.320				
	f	0.577				
δ-M Method	F_d^+ (F_t^+)	4.45 (15.24)	-NaN	-NaN	-NaN	-NaN
	F_d^- (F_t^-)	1.31 (8.25)	NaN	NaN	-NaN	-NaN
	I	-66.9	-131.2	-246.8	-426.5	-613.2
	$\Delta\tau'$	-66.9	-131.2	-246.8	-426.5	-613.2
	$f = \chi_{2N-1}$	44.6	86.5	161.8	279.0	400.6

In Figure 5.6, we plot the upward diffuse radiance field at the top of the cloud and the downward diffuse radiance field at the base of the cloud for two choices of the "forward angle" used in the definition of the truncated phase function. It can

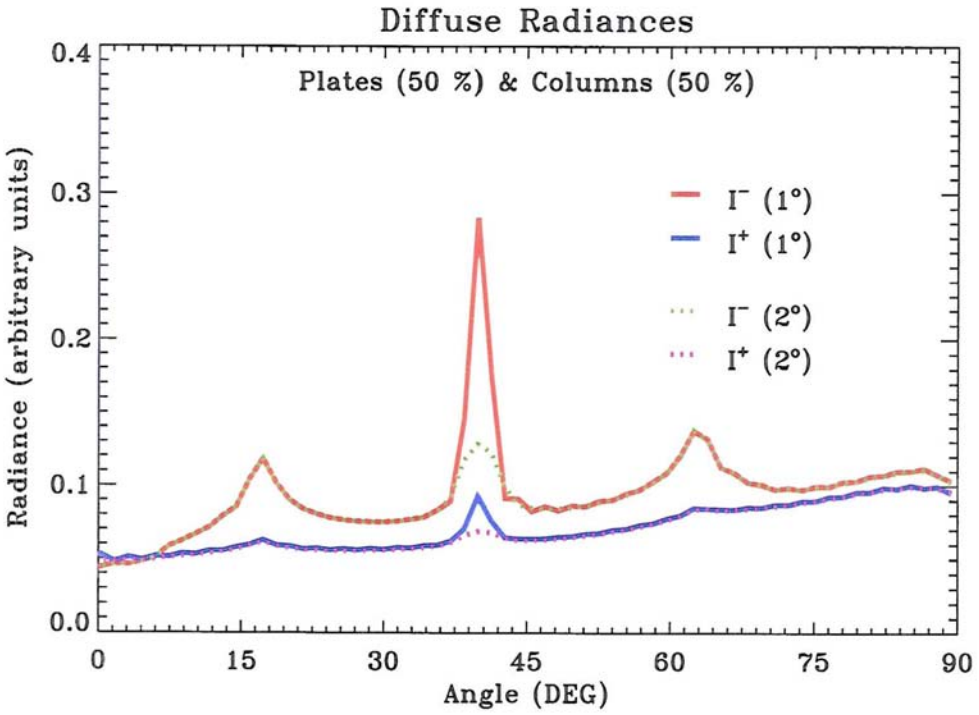

Figure 5.6: Diffuse radiances at top (I^+) and base (I^-) of the cloud layer for two forward angles: $\theta = 1°$ and $\theta = 2°$ respectively.

be inferred that the use of a larger "forward angle" has the effect of "smoothing" the angular dependence of the diffuse radiance field. The "smoothing" effect only takes place around angles close to the solar zenith angles (in this case set to 40°), leaving the rest of the dependence unchanged. As expected, the values for radiances at and around the solar zenith angles are reduced due to the use of the scaled cloud optical depth. The energy is still conserved however, since more energy is now in the direct beam. It follows that the radiances calculated using a relatively large "forward angle" are reliable, while keeping the computational costs low. Also to be noted here is the fact that the diffuse hemispherical fluxes for the two cases, for both the top and base of the cloud, are within few percent from each other, thus cloud effects and properties are reliably calculated. Evident from Figure 5.6 is the fact that the radiance field (upward and downward) has some of the characteristics of the cloud mean phase function. Note also the relatively large values for diffuse

radiances that are "trapped" within cloud boundaries (i. e. at 90° scattered angle) — a reason of concern when discussing 3D cloud effects. Last, the "smoothing" in the radiance field supports our claims that the diffuse term in the RT equation can be calculated using less terms, since the radiance field looks more isotropic. It is for this reason that the scattering term in the RT equation can be computed using less terms.

Another set of experiments were performed by assuming a cirrus cloud composed of various ice crystals of varying number concentration, but keeping the total number concentration fixed to 50 particles per liter. In these cases (see Figures 5.7 (a,b) and 5.8) we only vary the weighting functions for different habits and notice the variations in the synthetic radiance at the top of the atmosphere. In the legend, values for the weighting coefficients $W_{1,2,3}$ used to describe our cirrus cloud are presented. Combinations of Plates and Dendrites, Plates and Columns, and Plates and Columns and Aggregates were tested. The calculated values for the parameter f, cloud optical depth $\Delta\tau$, scaled cloud optical depth $\Delta\tau'$, asymmetry parameter g and TOA radiance I (in arbitrary units) for each combination are displayed. The key aspect to be noted here is the fact that even when the cloud optical depths for clouds composed of different ice crystals are identical, the synthetic radiances are not the same. However, when the scaled cloud optical depths are identical, the synthetic reflected radiances are close in values. This is shown in Figure 5.9 where synthetic reflected radiances I for all these cases are plotted with respect to the scaled cloud optical depth $\Delta\tau'$, and cloud optical depth $\Delta\tau$ respectively. These results are consistent with Yang et al. (2001) when the bidirectional reflectance was insensitive to the number of cloud layers used. We see that the radiances are not sensitive to the details of the cloud model when expressed in terms of $\Delta\tau'$. This property of the radiant field seems valid regardless of the mean phase function, or the value of the mean asymmetry parameter. However, we note that the general characteristic of the phase function is very similar in all cases, and we must also remember that "contribution" from the phase function is contained in the parameter f, which in turn is used in the definition for $\Delta\tau'$. Moreover, $\Delta\tau$ itself contributes to the value of $\Delta\tau'$. We also note that the asymmetry parameters differ, leading to the

conclusion that this is not the parameter controlling the radiative properties of the clouds — for fixed solar zenith angles, but instead it only plays a minor role since for our simulations we cannot distinguish a clear relationship between its variations and the variations in the radiance field. This is supported by the fact that the asymmetry parameter can only affect the magnitude of the solar term, as explained earlier.

In Table 5.2 we present the magnitude of the phase function at two different scattering angles: one representing the "backscatter" contribution of the direct (solar) beam, characterized by an angle defined as complementary to the solar zenith angle; another one representing the "forward" scatter of the reflected direct (solar) beam, characterized by an angle equal to the solar zenith angle. In this particular experiment, the phase function was calculated using either our cirrus cloud model (see Figure 5.8) or by imposing a Henyey-Greenstein function (see Figure 5.10) generated by choosing a specific value for the asymmetry parameter. The solar zenith angle was set to 40°. It can be observed that when we consider that cloud particles are described by a Henyey-Greenstein function, the values of the phase function at the above particular scattering angles varies significantly when we change the asymmetry parameter. The change in this particular case is about 33 % for the "backscatter" term and 40 % for the "forward" term respectively. These changes are responsible for large changes in the radiative field, concluding that the asymmetry parameter is the leading factor. If we look now at the same variations for the phase functions as calculated using our cirrus model (and we must keep in mind that these variations must be corrected to account for the scaling argument that we used in generating them), we see that these variations are much smaller than those from the Henyey-Greenstein representation (6% and respectively 28%), supporting our conclusion that the asymmetry parameter only plays a secondary role in influencing the radiative field. It is the phase function itself influencing the radiative field.

In the last series of tests, we studied sensitivities of the radiative field with respect to a two-layer cloud. For this, we assumed one layer as a thin cirrus cloud, composed only of small ice crystal plates ($D_n = 10$ μm), with a fixed optical depth of 0.5. The second layer was composed only of ice crystal aggregates ($D_n = 50$ μm),

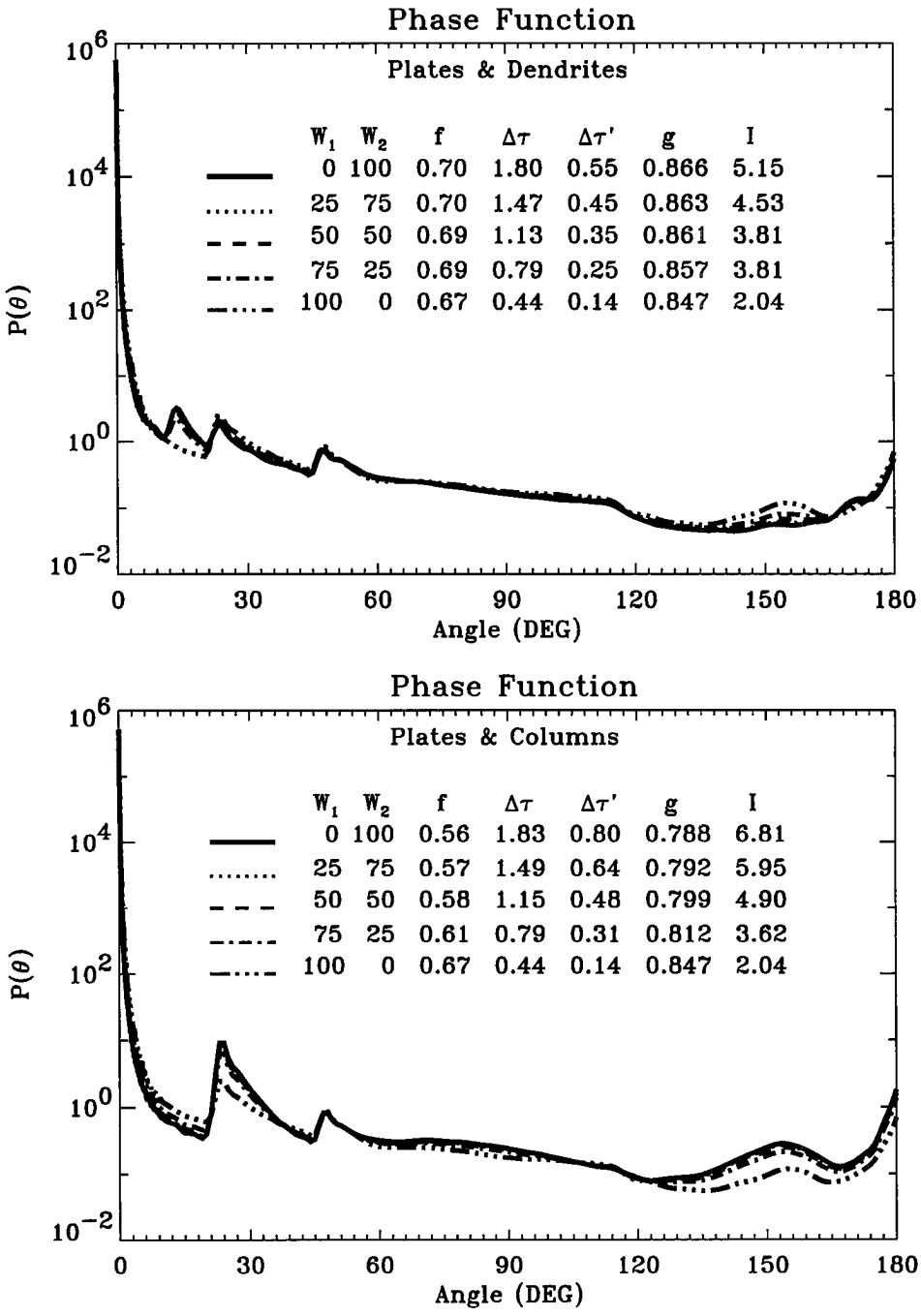

Figure 5.7: Sensitivity to particle habit and concentration: (a) Plates (W_1) and Dendrites (W_2); (b) Plates (W_1) and Columns (W_2). See text for explanations.

Table 5.2: Sensitivities to the phase functions.

Phase function	g	P(40°)	P(140°)
50 (Column) 40 (Plate) 10 (Aggregate)	0.837	1.23	0.25
60 (Column) 40 (Plate) 0 (Aggregate)	0.855	1.21	0.22
40 (Column) 40 (Plate) 20 (Aggregate)	0.819	1.24	0.26
40 (Column) 50 (Plate) 10 (Aggregate)	0.830	1.26	0.23
50 (Column) 30 (Plate) 20 (Aggregate)	0.846	1.21	0.27
50 (Column) 50 (Plate) 0 (Aggregate)	0.823	1.25	0.21
60 (Column) 30 (Plate) 10 (Aggregate)	0.847	1.19	0.25
Henyey-Greenstein	0.800	1.36	0.074
Henyey-Greenstein	0.850	1.02	0.053

with a variable optical depth between zero and 4. One layer was between 10.5 and 12 km while the other between 8.5 and 10 km. Two sets of runs were performed, such that each layer can be either at top or base. The results of these runs, for two solar zenith angles (10 °, and 40 °) are presented in Figure 5.11. The figure shows that the radiance field depends on both the solar zenith angle and the cloud optical depth. However, it is also dependent on the configuration of the two-cloud system. Although the differences are small, they are still detectable, especially when the cloud optical depth differences between the two cloud layers increase. The sign of the difference in radiances between these two configurations, depends on the solar zenith angle, its magnitude on both the solar zenith angle and the cloud optical depth. We conclude that large vertical inhomogeneities in clouds can be important and thus cannot be neglected. The vertical structure of the cloud must be properly accounted for in RT calculations.

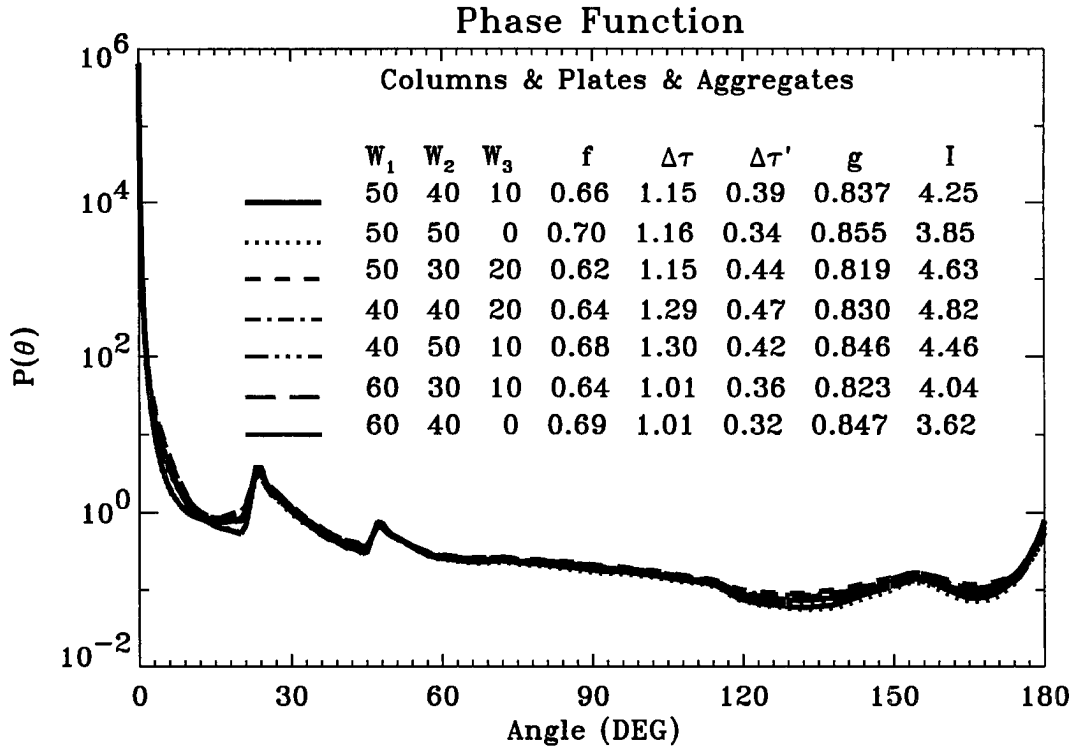

Figure 5.8: Sensitivity to particle habit and concentrations: Columns (W_1), Plates (W_2) and Aggregates (W_3). See text for explanations.

5.4.5 The Inverse Model

The objective of the inverse model is to determine mean optical properties of the clouds given measured radiances. While we focus on retrieval of cloud optical depth, other atmospheric properties can be retrieved. In fact, when applied to experimental data, we use the following method for deriving the surface albedo, since cloud optical depth was determined from CPL data.

Due to the relative complexity of the RT model, the inverse model cannot be constructed by simply inverting the forward model. For this reason, the solution is based on the optimal estimation approach [Austin and Stephens (2001)], which uses a Newtonian iteration involving the knowledge of a reference and *a-priori* values for our retrieved field. The measured radiance field can be expressed in terms of a

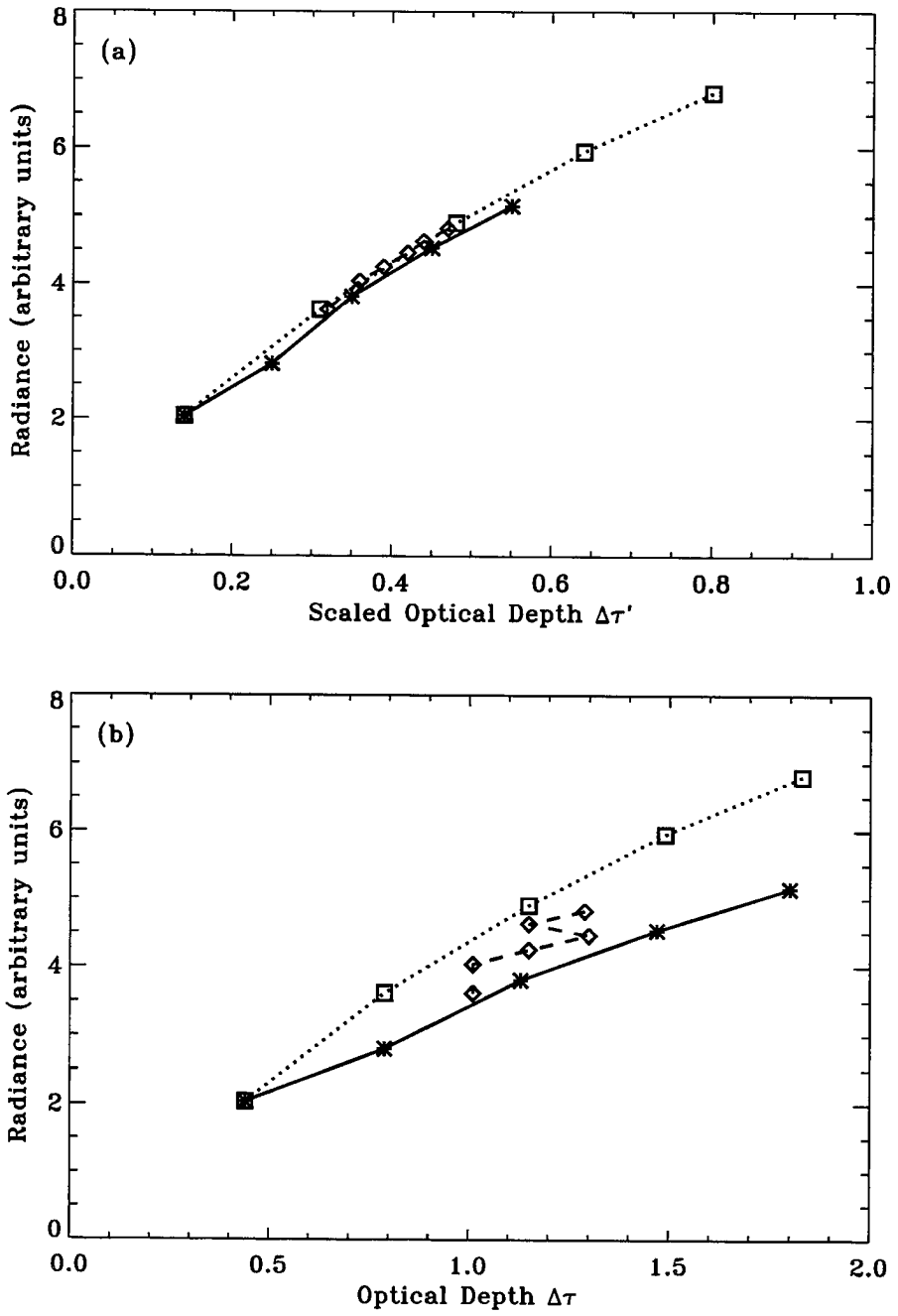

Figure 5.9: Radiances vs. (a) scaled optical depth or (b) optical depth for various ice crystals. Plates & Dendrites (solid line), Plates & Columns (dashed line), Plates & Columns & Aggregate (dotted line)

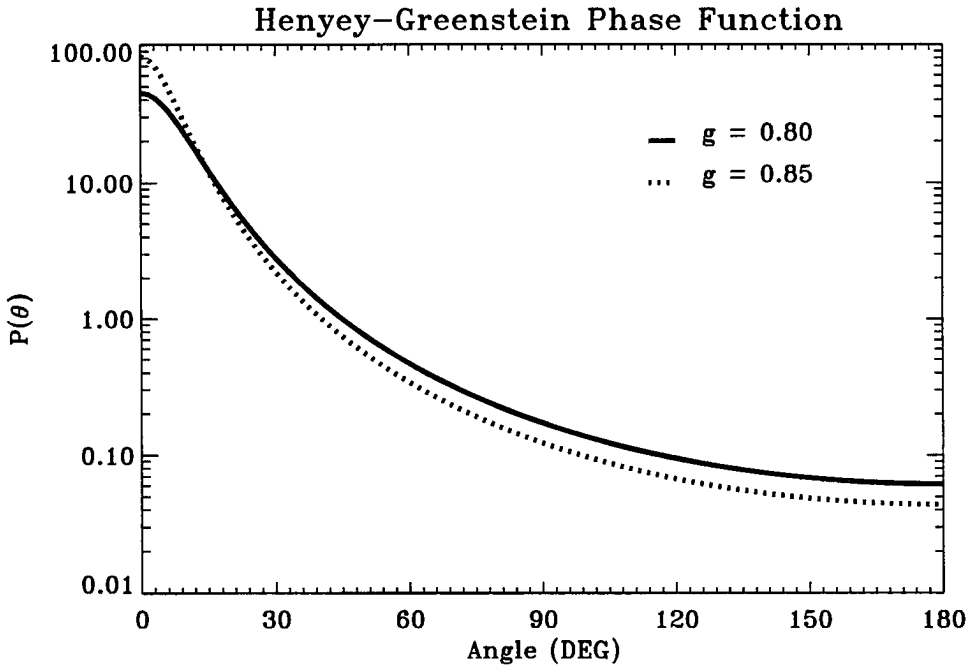

Figure 5.10: Henyey-Greenstein phase function for two asymmetry parameters: g=0.8 (solid line) and g=0.85 (dotted line).

forward model F:

$$y = F(\tau, \mathbf{b}) + \epsilon_y \tag{5.28}$$

where τ is the cloud optical depth that we wish to retrieve, $\mathbf{b}$ represents the forward model parameters (like phase function, single scatter albedo, surface albedo, particle concentration, crystal habits, "free atmosphere" optical depth, etc.) and ϵ_y represents the measured and forward model error. The retrieval algorithm is designed based on minimization of the scalar cost function:

$$S = S_a^{-1}(\tau - \tau_a)^2 + S_y^{-1}(y - F(\tau, \mathbf{b}))^2 \tag{5.29}$$

where S_a is the *a-priori* covariance, S_y is the forward model plus observational error covariance and τ_a is the *a-priori* value for our retrieved quantity. Omitting many of the details, the iteration procedure can be expressed as:

$$\tau_{i+1} = \tau_i + \mathbf{A}\mathbf{K}_i^{-1}(y - F(\tau_i, \mathbf{b})) + (\mathbf{I} - \mathbf{A})(\tau_a - \tau_i) \tag{5.30}$$

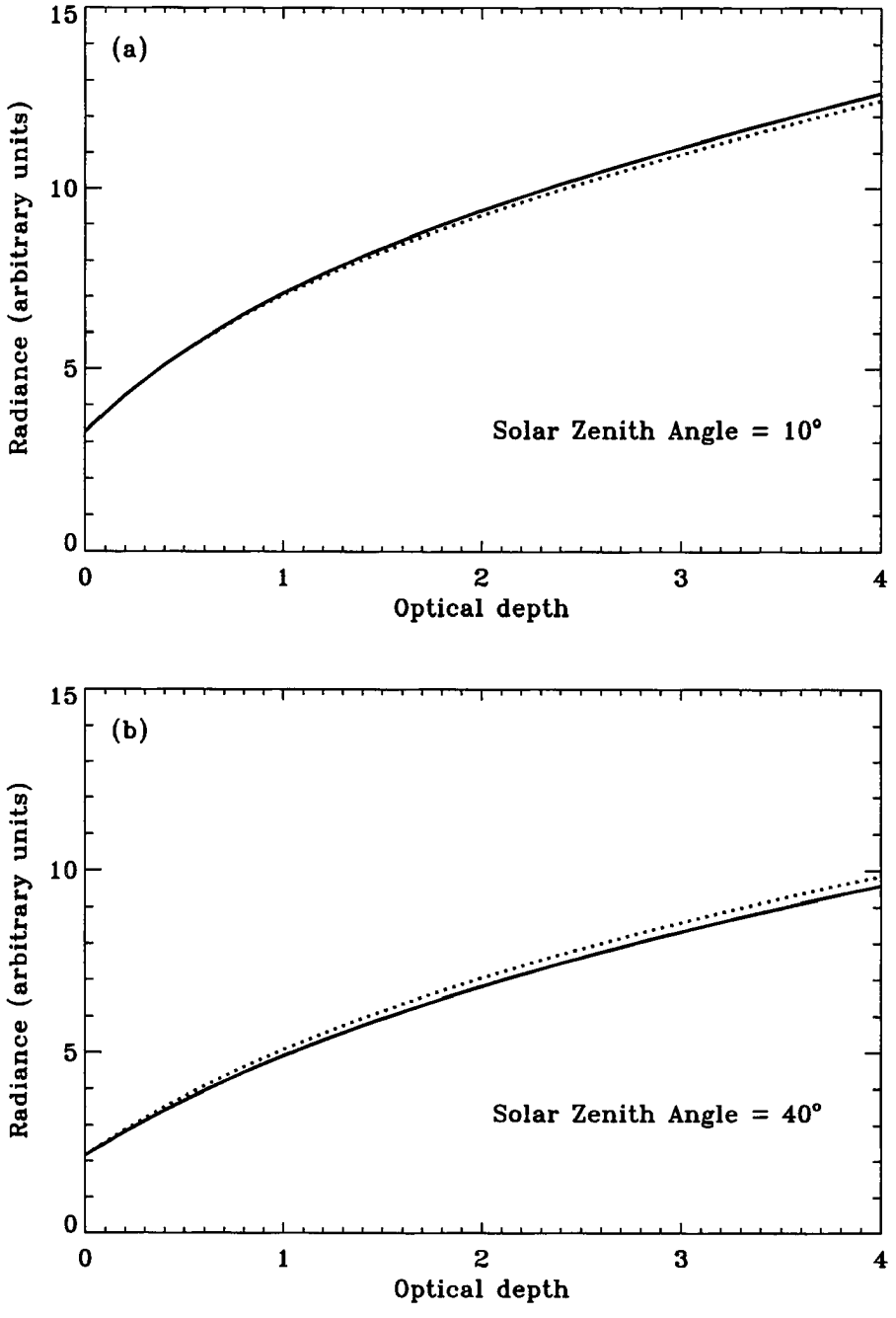

Figure 5.11: Two-layer cloud sensitivities for two solar zenith angles and two configurations: variable layer at base (solid line), and variable layer at top (dashed line). Optical depth for fixed layer is 0.5.

with

$$\mathbf{A} = (S_a^{-1} + \mathbf{K}^T S_y^{-1}\mathbf{K})(\mathbf{K}_i^T S_y^{-1}\mathbf{K}_i) \quad . \tag{5.31}$$

Here, K is the Jacobian of the forward model with respect to τ. The solution is achieved when the convergence criteria is satisfied:

$$(S_a^{-1} + \mathbf{K}^T S_y \mathbf{K}^{-1})^{-1} \, (\tau_{i+1} - \tau_i)^2 \ll 1 \quad . \tag{5.32}$$

In the next section we make use of this inverse model to retrieve various atmospheric characteristics using data from two sensors flown in the SAFARI 2000 Experiment.

5.4.6 Results from SAFARI Experiment

The intent of the analysis of SAFARI data is to use lidar and reflected radiance data in the retrieval of cloud optical depth. As mentioned in Chapter 2, the ER-2 research aircraft included the CPL and the MAS as part of its payload. Unfortunately, this was not possible using SAFARI data directly for two reasons: (1) the optical depth of the cirrus clouds was generally small (less than 0.1); (2) the underlying surface was also bright (albedo varying between 0.2 – 0.3), making it practically impossible to identify cirrus in the radiance data.

Presented in Figure 5.12 is the time series of the backscattered signal as measured by the CPL instrument flown on the ER-2 on September 04, 2000. From the figure we can clearly identify the planetary boundary layer (PBL) with a top at about 6.5 km, which is occasionally accompanied by low level clouds and apparently significant levels of aerosol. We focus our interest on cirrus clouds that were detected almost throughout the whole flight, with boundaries between 12.5 and 14 km. The altitude scale in the figure is relative to the sea level, therefore the topography of the terrain is also visible. Worth noting is the fact that the lidar return at the ground level exhibits high values, which is an indicator of a relatively high surface albedo, with possible large variations from point to point. Accompanying the CPL instrument was the MAS radiometer with its high spectral and angular resolution capabilities.

Our initial goal was to test how well measurements from the visible MAS sensor can be used to infer thin cloud optical depths given typical errors in the other

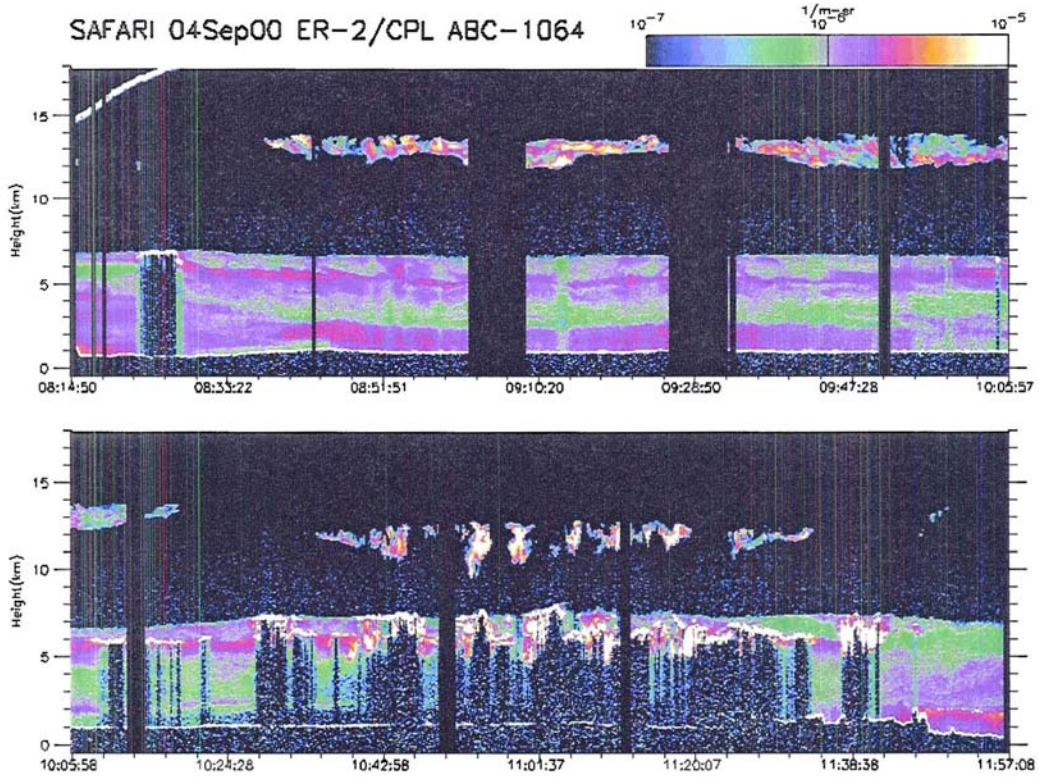

Figure 5.12: SAFARI 04 September 2000: CPL Data.

forward model's parameters. Since we were unable to derive optical depths from the MAS data, we produce an analysis of optical depth errors as function of optical depth and the surface albedo. We also use the SAFARI data to retrieve the albedo of the underlying surface.

First we present our analysis of errors in the retrieved cloud optical depth due to uncertainties in the surface albedo. These errors are calculated using estimates of variances (see equation 3.18). The results are presented in Figures 5.13 (a) and (b). In Figure 5.13(a) we assume that there is no aerosol layer below the cloud, while the results of Figure 5.13(b) assume an aerosol layer with an optical depth of 0.8, with a variance of 0.1 and the single scatter albedo set to 0.95. The aerosol layer has its top at 5.8 km and base at the surface, broadly mimicking the SAFARI data. The cirrus cloud in both cases has an optical depth of 0.5 and its upper and

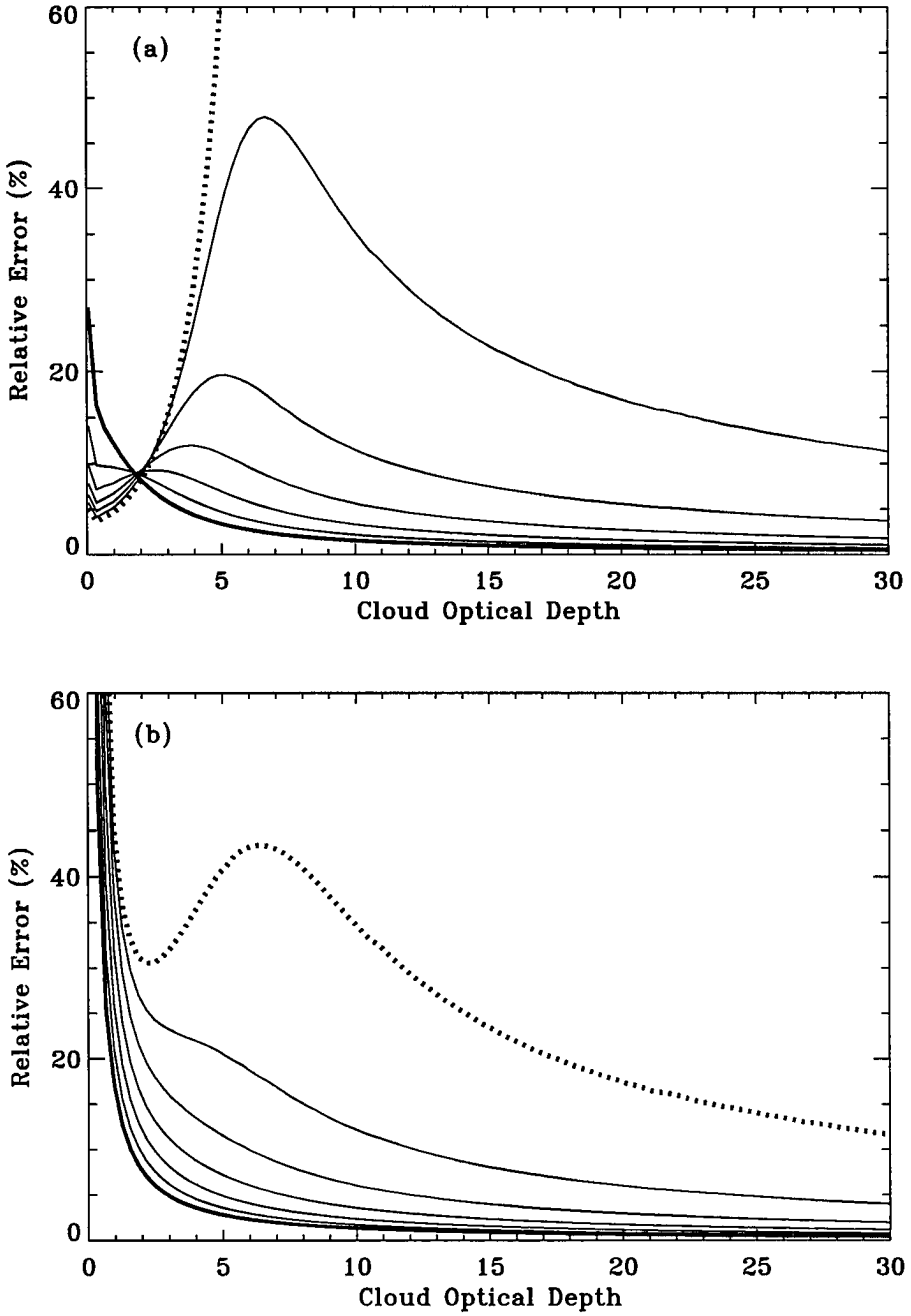

Figure 5.13: Best relative errors for retrieved cloud optical depth as function of albedo (5 % (thick solid line), 95 % (thick dotted line) in 15 % increments) in the presence of aerosol (b) or without aerosol (a). Aerosol optical depth was set to 0.8

lower boundaries are set to 12 and 10 km respectively. Surface albedo is varied between 0.05 and 0.95 with a 0.15 increment and a variance of 0.05 is assumed. The solar zenith angle is set to 35°. In both cases we notice that errors in retrieved optical depth associated with errors in both surface albedo and aerosol optical depth, generally decrease when cloud optical depth increases and surface albedo decreases. The opposite trend appears in the case when PBL is ignored, but only for optical depths below 6. In both cases however, for cirrus clouds having optical depth below 0.1, the errors are extremely large, but decrease as the cloud optical depth increases. It is for this reason that it is almost impossible to correctly retrieve optical depth for very thin cirrus, given reasonable errors in albedo. In order to reduce the errors in the retrieved optical depth, errors in albedo must be lowered to a degree impractical over land and other bright surfaces.

Since we were unable to use MAS for retrieving optical depth, we produce an alternative retrieval of surface albedo. As mentioned above, processing the CPL data provided us with information about the vertical profile for optical depth, and we used the cloud model to infer the other optical properties of the cloud required to simulate MAS data. Using the same idea, the aerosol and/or PBL layer was modeled assuming a Henyey-Greenstein phase function with g=0.7 and $\tilde{\omega}_0 = 0.95$. The value of solar zenith angle as well as the incident solar radiation was that prevalent at the time of the flight. The only unknown parameter was the surface albedo (which was assumed to be equal to the diffusive surface albedo). The time variation of the retrieved surface albedo is presented in Figure 5.14(a). From this figure, we notice that the retrieved surface albedo presents a rapid variation with time. The mean value for the retrieved surface albedo is 0.221 with a variance of 0.094. There are two distinct features associated with this variation, which can be interpreted using figure 5.14(b), where the temporal variation of the measured radiance is plotted. The first one is that the retrieved albedo increases very rapidly to values above 0.4 when the measured radiance increases to values above 90 W/m^2/sr/μm. This behavior can be attributed to rapid changes in the roll angle of the airplane. The second type of variation in the values of the surface albedo, between 0.2 and 0.3, is less dramatic and is probably associated with a combination of natural variations

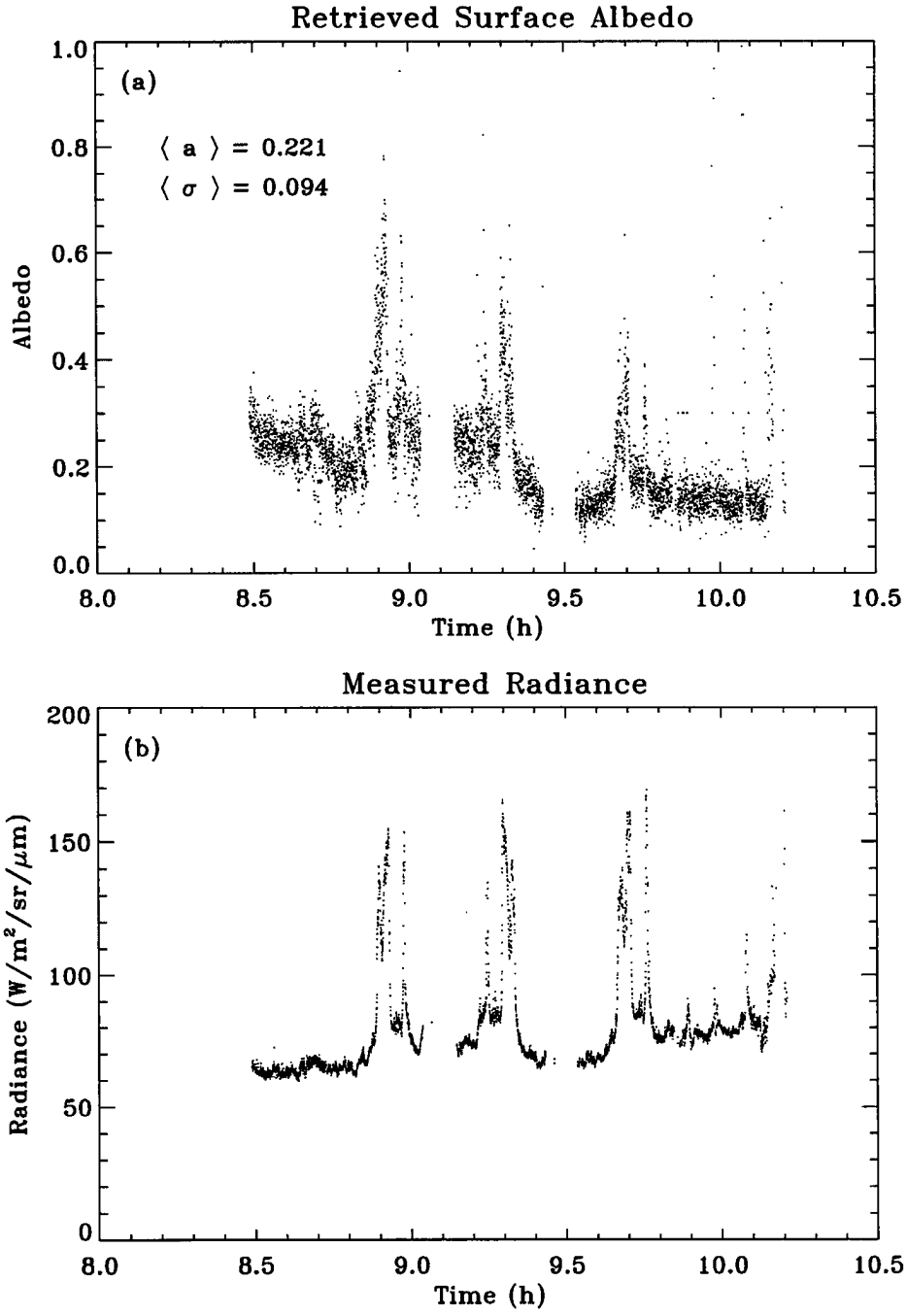

Figure 5.14: SAFARI 2000. Time series of (a) retrieved surface albedo and (b) MAS channel 2 measured radiance (8:29 - 10:12 UTC). Mean albedo is 0.221 with a variance of 0.094.

Table 5.3: Sensitivities to model parameters in determining albedo (clear sky).

Parameter					Retrieved
g	$\tilde{\omega}_0$	τ_{PBL}	$\cos\theta$	I	albedo
0.7	1.0	0.296	0.749	65.1	0.302
5 %	-	-	-	-	+3 %
-	-5 %	-	-	-	+9 %
-	-	10 %	-	-	+7 %
-	-	-	5 %	-	+7 %
-	-	-	-	5 %	+6 %

in surface albedo, minor airplane roll and uncertainties in the atmospheric optical properties as deduced from CPL data and/or from our cloud model. This variation was expected from inspecting the CPL data as mentioned before. In order to have a measure of the influences of these parameters on our retrieved albedo, we performed sensitivities to the retrieved albedo.

We summarize our findings in Table 5.3. The first three parameters in the table are associated with describing the PBL and/or the aerosol layer. The fourth is the solar zenith angle, while the fifth is the measured radiance. We see that the retrieved albedo is most sensitive to errors in the single scattering albedo and least sensitive to the errors in the asymmetry parameter and the PBL optical depth. Of equal importance are errors in the remaining two other parameters: solar zenith angle and measured radiance. When all these errors are combined, the errors in retrieved albedo can increase considerably. However, the uncertainties in both solar zenith angle and measured radiance are very low, therefore the resulting errors in the retrieved albedo remain at about 20 %, which for our particular case translates into absolute errors of about 0.05.

5.5 Summary

In this chapter we focused on developing, testing, and interpreting measurements from a combination of active-passive sensors. Methods for processing such combinations of data are desirable given the multitude of passive sensors in use, the profiling capabilities of active sensors, and given that the active sensors to be flown on satellites will have supporting radiometric data. Even the combination of lidar-radiometer data requires other information such as that available from conventional data and/or *a priori* knowledge about key cloud microphysical parameters.

An outline of key findings of this chapter follows:

1. A widely used technique for investigating the cloud properties is the LIRAD technique. It combines information from lidar — as the active component, with IR radiometer — as the passive component. We use this technique as a way to demonstrate that the treatment introduced in Chapter 3 for describing MS effects in clouds is valid. The theoretical development of that earlier chapter leads to a new way for representing key cloud optical properties. The use of such a representation suggests some universal properties for cirrus clouds in terms of the product of parameters $F\alpha\epsilon$. Simulated data also supports these findings. Correlations with cloud temperatures are also implied. However no solid physical explanation is proposed, probably due to the nonlinear effects that are invoked.

2. A second approach is also introduced. This approach proposes to combine lidar with reflected radiance data as acquired from MODIS or similar sensors. A radiative transfer model was developed to simulated radiances measured by these instruments. A serious problem in a multi-stream RT model, however, is the treatment for strongly asymmetric phase functions that characterize (relatively large) ice crystals. Throughout the years, various techniques were proposed and applied, and the concepts of similarity and scaling were introduced. However the definition for the key scaling parameter f was ambiguous in these studies and this ambiguity negatively influenced the value of the

method. In this chapter, we propose a robust theoretical approach for defining f and discuss its implications. Synthetic tests shows the validity of the method.

3. A key question that was addressed concerns the extent to which the details of the crystal microphysics affect radiances and eventually optical depth retrievals.

   Since the scaling factor f depends on cloud microphysics, we examine the sensitivity of our model against the parameter f and the number of streams used. As anticipated, the diffuse radiance field, away from the solar aureole scales directly with the scaled optical depth. This analysis was performed with respect to ice crystal concentration and habit. Sensitivity to the phase function is imbeded into the definition of f. The phase function characteristics are evident at angles where specific features are more pronounced or when measuring at angles close to the solar zenith angles. We also identify the importance of the cloud vertical structure in RT calculations. Ice crystal habit becomes important especially when the cloud is highly inhomogeneous.

4. Data from the SAFARI experiment was processed with the intent to compare MAS derived optical depth to the CPL derived optical depth. However this was not possible for the cases available due to the lack of contrast between the cloud and the surface below.

This page intentionally blank.

Chapter 6

Radiative Effects of Cirrus Clouds over TWP

6.1 Introduction

To understand the role clouds play in climate, one needs to know, among other properties, the time evolution of the three-dimensional structure of cloud radiative forcing. Clouds strongly influence atmospheric circulation through cloud radiative forcing, affecting surface energy fluxes and atmospheric heating rates and thus the ocean circulations. The atmospheric feedback to diabatic heating is a function of the time evolution of both the vertical and horizontal structure of that heating. Cloud radiative forcing can be calculated from averages of top of the atmosphere and surface values of radiative heating. However, the vertical structure of longwave (LW) atmospheric heating depends on the distribution of atmospheric factors, such as humidity and cloud water content. The shortwave (SW) element of cloud radiative forcing in the atmosphere is mostly ignored because it is small when integrated over the atmospheric column. Still, a small integral can be produced from the cancellation of positive values above the cloud layer and negative values below the cloud layer, leading to the conclusion that in fact, SW cloud radiative forcing is important in atmospheric circulations.

It must be acknowledged that radiative fluxes depend non-linearly on atmospheric state variables and, therefore, high-frequency variability which is not accounted for in monthly calculations contributes to inaccuracies in the calculated fluxes. For certain cloud conditions, the plane-parallel radiative transfer calculations, which presume the atmosphere to be horizontally homogeneous, are not valid. Cloud effects on radiative fluxes make those fluxes non-linear functions of cloud properties.

An example of such a non-linear effect can be seen in Figure 6.1 (a), where the effective emissivity and cloud albedo are shown as functions of the IWP. From this figure, we can infer that for the range of the observed IWP for thin cirrus clouds, emissivity increases with increasing IWP in a non-linear manner, as opposed to the cloud albedo that for a fixed solar zenith angle varies almost linearly with the IWP. However, cloud albedo too, exhibits a non-linear variation with respect to the solar zenith angle for small values in the IWP, as can be seen from Figure 6.1 (b).

As mentioned previously, the process of absorbing and/or emitting radiation represents a sink or a source of energy in the atmosphere. These sources/sinks directly influence the temperature field distribution which in turn affects the dynamics of the atmosphere.

The purpose of this chapter is to evaluate the fluxes and heating rates associated with tropical cirrus clouds, and relate these quantities to the cloud physical parameters derived in the previous chapter. The flux calculations are performed using a RT model that takes into account all atmospheric constituents (air molecules, aerosols, clouds). Cloud effects are estimated by comparing fluxes and heating rates in *simulated* clear sky conditions against cloudy sky conditions. This terminology will be explained later in this chapter along with a brief description of the RT model that was used.

The key result of this portion of the research is the relationship between the cloud radiative forcing and the ice water path of the studied thin cirrus.

6.2 Radiative Heating Rate Equation

The use of the first thermodynamic law enables us to directly relate the net radiative flux to the local heating/cooling rate. We start by identifying the heat source/sink (dQ/dt) as the radiative field $(\vec{F}_{net})$:

$$\rho \frac{dQ}{dt} \Delta V = \oint \vec{F}_{net} d\vec{S} \tag{6.1}$$

which can be rewritten using the definition of div operator:

$$div(\vec{F}_{net}) = \lim_{dV \to 0} \left[\frac{1}{\Delta V} \oint \vec{F}_{net} d\vec{S} \right] \tag{6.2}$$

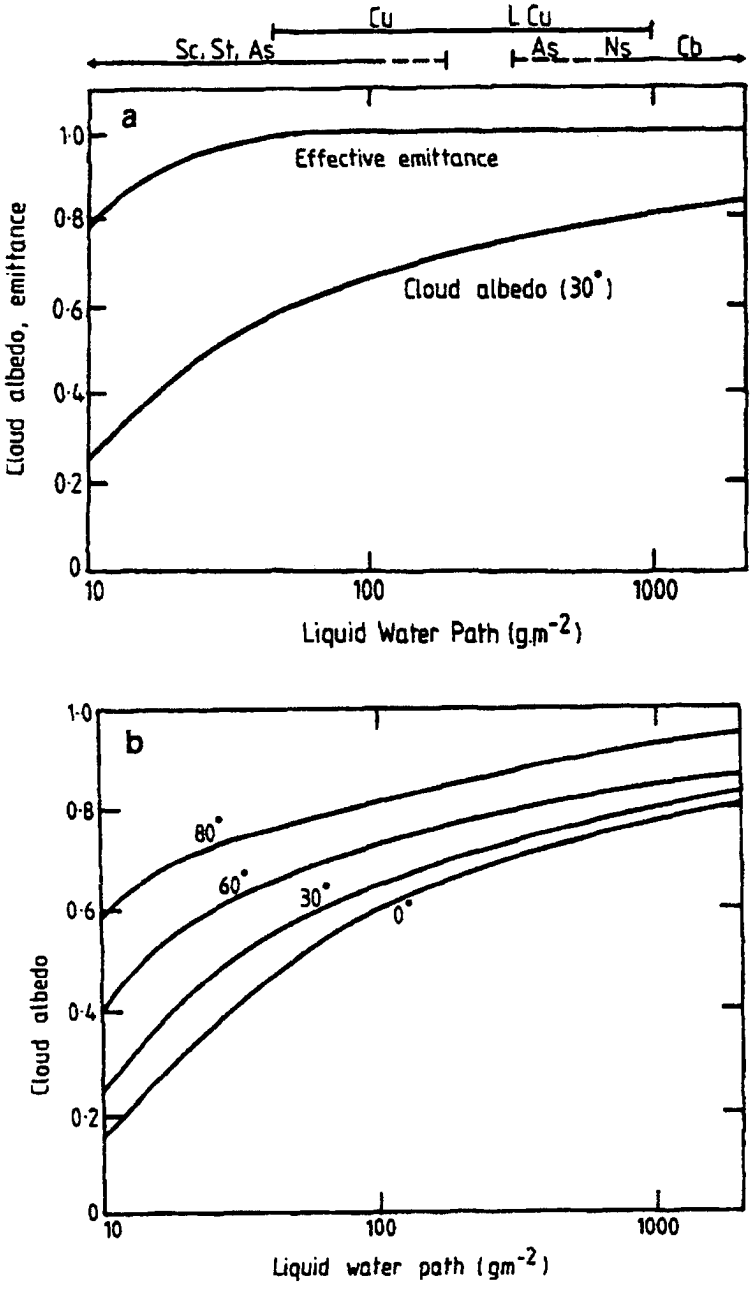

Figure 6.1: (a) Cloud Albedo and Emissivity as function of IWP for a zenith angle of 30 °. (b) Cloud Albedo as function of IWP for various zenith angles. From Stephens and Webster (1981).

in the form:

$$\rho \frac{dQ}{dt} = div(\vec{F}_{net}) \tag{6.3}$$

where ρ is the mean air density over the volume ΔV.

We apply the above form of the heating source/sink in the expression of the first law of thermodynamics applied to atmosphere:

$$c_p \frac{dT}{dt} - \alpha \frac{dp}{dt} = \frac{dQ}{dt} \tag{6.4}$$

Here c_p is the specific heating coefficient at constant pressure, α is the specific volume, T is the temperature, and p is the pressure of the atmosphere. It is customary to assume that pressure does not vary with time and that the net flux is mainly due to the hemispheric flux, which is defined as:

$$F^{\uparrow,\downarrow} = \int_0^{2\pi} \int_0^1 I(\pm\mu, \phi)\ \mu\ d\Omega \tag{6.5}$$

where $I(\pm\mu, \phi)$ is the spectral intensity (or radiance). By combining 6.3, 6.4 and 6.5, we get the expression for the atmospheric heating rate as:

$$c_p \frac{dT}{dt} = -\frac{1}{\rho} \left[\frac{\partial (F^{\uparrow} - F^{\downarrow})}{\partial z} \right] \tag{6.6}$$

The calculation of fluxes implies solving for the radiative transfer equation:

$$\frac{dI}{ds} = -\sigma_{ext}(I - J) \tag{6.7}$$

where J is the source term and σ_{ext} is the extinction coefficient for the specified spectral range. In order to perform these calculations, profiles for the extinction coefficient must be known. Among various atmospheric constituents, clouds can induce important effects in the intensity fields, thus affecting both fluxes and heating rates.

Having the IWC profile for our cloud field, along with profiles of the other significant atmospheric constituents, fluxes and heating rates can be computed using RT models. For our calculations we choose the state-of-the-art CSU BUGSrad RT model, which is briefly explained in the next section.

6.3 BUGS Radiation Code

Part of the BeaUtiful General circulation modeling System (BUGS), the radiation code computes the influence that various atmospheric constituents have on radiative fields. BUGS-Rad covers the entire radiative spectra, by separating it into 6 SW bands and 12 LW bands, respectively (see Table 6.1). This is helpful since atmospheric optical properties vary with the wavelength, but in the same time computational costs are kept at reasonable levels.

In Figure 6.2 the flow-chart for the BUGS-Rad code is presented, while in Table 6.2 the action of each subroutine is presented. The table indicates that the RT model takes into account various gases and the water vapor continuum along with the cloud LWC/IWC profiles. In this model, the phase functions describing ice/water particles are assumed to be characterized by a fixed value of the asymmetry parameter. Although this is a limitation of the model, the effects of this simplification on broadband fluxes are small [Stephens et al. (2001)]. Also, the effective radius for such particles are parameterized to 10 μm for water clouds and 30 μm for ice clouds respectively, and all particles are assumed spherical. This is a crude approximation in the case of cirrus clouds, composed mostly of non-spherical particles with a very large range of possible diameters. This assumption influences the values of IWC that clouds contain, thus influencing the results. However, based on the findings presented in Chapter 4, on average, 30 μm radius is characteristic of the thin cirrus clouds observed at Nauru. Other parameters, like the single scatter albedo or the emissivity may also play a role in influencing the final results. For this reason, when calculating the radiative fluxes, we assume that the IWC for the clouds has a relative error of 40 %. This relative large error is thought to include all the above mentioned uncertainties and limitations, and provide us with a realistic value for errors that one might expect from modeling effects that cirrus clouds induce on the radiative field. In the following paragraphs, we focus on these effects.

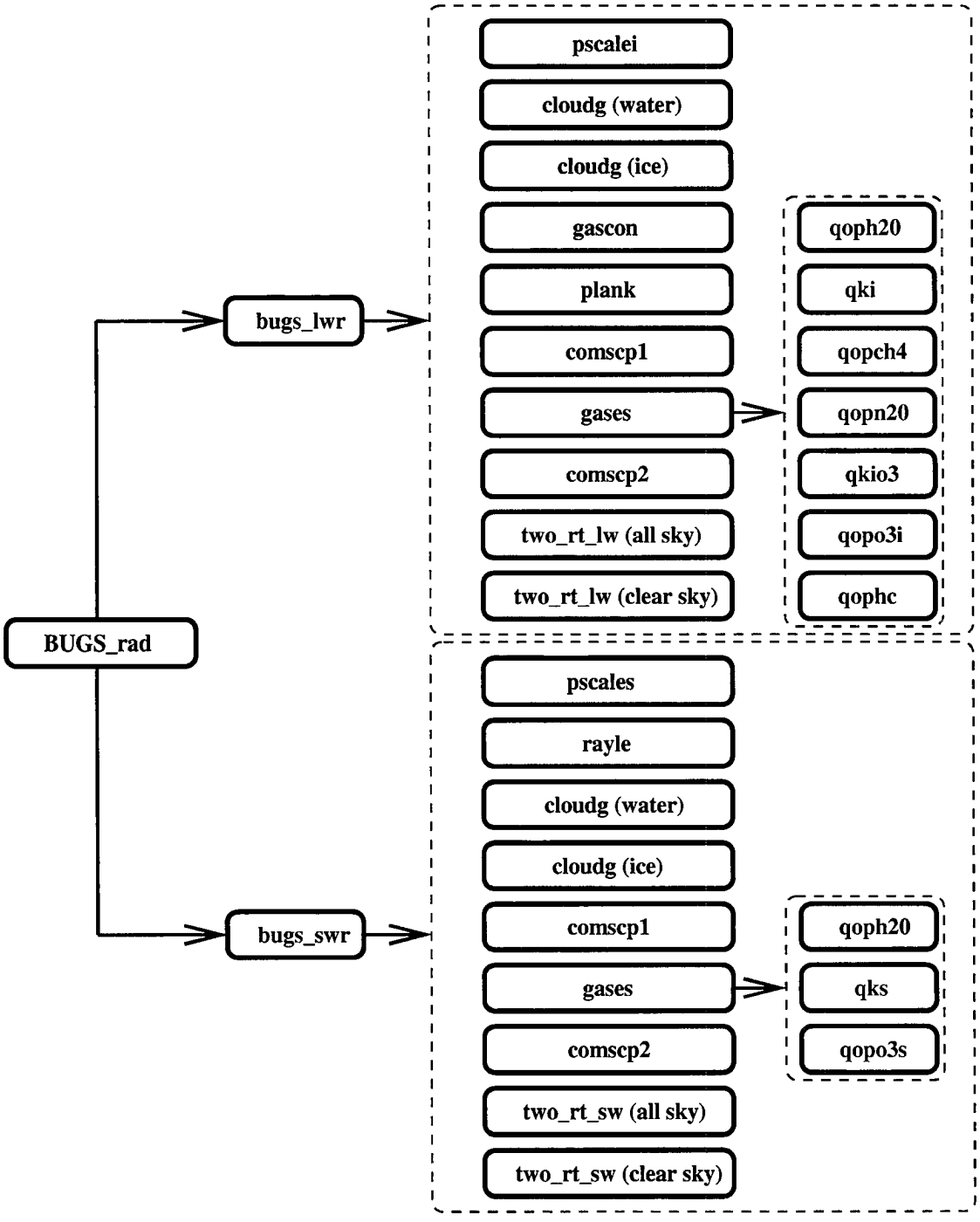

Figure 6.2: BUGS-Rad flow chart.

et al. (2001), the first type is attributed to *in situ* formation, while the second type is associated with convective systems. Since the thinner cirrus layers were frequently not observed by the cloud radar, only the lidar-derived cloud information was used for characterizing these cloud layers.

We mentioned in Chapter 3 that determining cirrus cloud properties during daytime was difficult due to the significant amount of noise that was present in the MPL data. In this case, when only night-time cases of cirrus clouds are available, the solar term in our RT model is turned off. In an abstract sense, we cannot assess the influences that cirrus clouds have on the solar spectrum. However, based on the fact that apparently cirrus clouds do not show significant changes with time (unless major atmospheric activity is present), we calculate an equivalent solar contribution to fluxes and heating rates using the night-time data as input into BUGSRad. By setting the solar zenith angle to unity, we obtain an upper limit of the effect of clouds on the solar fluxes. Another artifact in the data was needed to assess changes in radiative fields for contrasting between the cloudy case and the clear case. For one location at one particular time we cannot have both clear and cloudy sky. In order to "simulate" clear sky conditions to compare against cloudy sky ones, we simply assumed that the cloud does not exist when computing radiative fluxes. We therefore assigned to zero the cloud LWC and/or IWC and performed the radiative calculations using the same atmospheric environment. In this way, both the SW and LW and clear and cloudy sky radiative effects can be computed and discussed. We stress the fact that this is done only for this purpose.

6.4.1 Sensitivity Analysis

We start our analysis by studying the effects that uncertainties in the IWC profiles have on the radiative fluxes. Two cases are considered: one of a relatively thick cirrus cloud and one of a thin cirrus that could only be detected by lidar. For this reason, these sensitivities are developed using only lidar cloud information. We performed radiative calculations for three different IWC profiles that were set to 140, 100, and 60 % of the IWC profile as determined from the MPL data. The

results are presented in Figures 6.3–6.8. All cases are from the TWP site at Nauru, taken on 05/01/1999 at 09:00:23, and 10:00:18 UTC respectively. In the first case, a thick cirrus cloud with an optical depth of 1.56 was present, while in the second case, a two-layer, thin cirrus cloud with an optical depth of 0.09 was detected.

We discuss first the case at 09:00:23 UTC. As mentioned before this is a nighttime case but we pretend that it is a daytime one. By using the lidar retrieval algorithm, the vertical profile for mixing ratio for this cloud is presented in Figure 6.4(a). From it we see that in fact it is a two layer cloud, with the main layer above, and a total vertical thickness of 2338 m. The mixing ratio varies almost linearly within cloud layer with a maximum value of about 65 mg/kg. With green we present the assumed relative errors of $\pm$ 40 % that we use to determine the errors induced in the radiative fields (δSW or δLW).

In Figure 6.3(a) and (b) the vertical profiles of the SW and LW radiative fluxes are presented. The cloud influence on both upward and downward components of these fluxes is evident. In the SW region, the cloud clearly diminishes the downward SW component by either absorbing or reflecting it. The reflected component however, becomes part of the upward SW component for the region above the cloud. In the LW region, the upward component is reduced, while the downward LW component is increased. This is due to the cloud emission, which is close to that of blackbody at mean-cloud temperature. Shaded in blue are the variations in the SW fluxes associated with variations in cloud IWC as explained above. The magnitude of these variations is shown again in Figure 6.3(c). For this particular case, the magnitude of the variations is relatively large: 25 W/m^2 for the downward SW flux and 15 W/m^2 for the upward SW flux. We also notice that both these variations are almost symmetrical with respect to the sign of the variation in the IWC. This suggests that for this particular cloud, the cloud albedo effect is still in the linear range as suggested by Stephens and Webster (1981).

The LW variations with respect to IWC uncertainties shown in Figure 6.3(d), suggest that the emissivity effect is in the non-linear regime. An increase in the IWC by 40 % translates into a 19 W/m^2 decrease of the upward LW flux for the region above the cloud, while a 40 % decrease in the IWC is associated with a 12

Table 6.1: BUGS-Rad: Two-stream spectral band limits

Band	No.	wavenumber (cm^{-1})	wavelength (μm)
SW (BUGSswr)	1	50000–14500	0.20–0.69
	2	14500–7700	0.69–1.23
	3	7700–5250	1.23–1.90
	4	5250–4000	1.90–2.50
	5	4000–2850	2.50–3.51
	6	2850–2500	3.51–4.00
LW (BUGSlwr)	7	2200–1900	4.55–5.26
	8	1900–1700	5.26–5.88
	9	1700–1400	5.88–7.14
	10	1400–1250	7.14–8.00
	11	1250–1100	8.00–9.09
	12	1100–980	9.09–10.20
	13	980–800	10.20–12.50
	14	800–670	12.50–14.92
	15	670–540	14.92–18.51
	16	540–400	18.51–25.00
	17	400–280	25.00–35.71
	18	280–0	35.71–∞

6.4 Calculated Fluxes and Heating Rates

The data collected during the three month period (May – July 1999) at Nauru suggests that two distinct types of cirrus clouds are present. The first type is composed of very high, thin, laminar cirrus clouds. The second type resides at lower altitudes, is thicker and shows more structure in the layer. The optical depths associated with the latter type exhibits a larger variation than the first type. According to Pfister

Table 6.2: BUGS-Rad: Subroutines in the model

Subroutine	Action
BUGSrad	drives the longwave and shortwave code
BUGSlwr	the longwave code
BUGSswr	the shortwave code
pscalei	pressure scaling for correlated-k in the longwave
pscales	pressure scaling for correlated-k in the shortwave
cloudg	cloud optical properties
gascon	water vapor continuum
rayle	Rayleigh optical depth
planck	Planck emission
gases	gaseous optical depth calculation
qks	shortwave gas absorption coefficients
qki	longwave gas absorption coefficients
qkio3	longwave O_3 absorption coefficients
qopo3i	longwave O_3 optical depth
qopo3s	shortwave O_3 optical depth
qoph2o	longwave and shortwave H_2O optical depth
qopn2o	longwave N_2O optical depth
qopch4	longwave CH_4 gas optical depth
qophc	longwave overlapping H_2O and CO_2 optical depth
comscp1	combines scattering properties for spectral interval
comscp2	combines scattering properties for cumulative prob. interval
two_rt_lw	longwave radiative transfer
two_rt_sw	shortwave radiative transfer

W/m^2 increase in the upward LW flux for the region above the cloud. Thus the OLR field can be influenced by both cloud altitude and microphysical characteristics. For the downward LW flux we expect the same behavior: an increase in the IWC is only perceived as a 12 W/m^2 increase in the downward flux, while the decrease in IWC influences by approximatively 20 W/m^2 the downward flux. The large influence on both SW and LW fluxes is also noticeable on the heating rates presented in Figure 6.4(b) (c) and (d). The SW heating effect (due to absorption) of the cloud layer is about 8 K/day. LW heating occurs at the base of the cloud due to the warmer surfaces below (2 K/day), while the upper cloud regions are dominated by a cooling to space (- 11 K/day). The total heating is the superposition of both SW and LW heating, and is dominated by an averaged heating effect, although it should be remarked that the solar contribution is a maximum. The variation of heating rates due to variations in IWC can be appreciable (up to $\pm$ 3 K/day), but does not affect the shape of the heating profile. In order to better see the cloud effects on the radiative field, the idealized clear sky case is presented in Figure 6.5(a) and (b). With dots, the profile of the fluxes for the cloudy case is presented for comparison purposes. This particular cirrus cloud induces large variations in both SW and LW fluxes. At the cloud level, the cloud LW forcing effect is at maximum with a value of around 80 W/m^2. The emission from cloud acts to warm the surface by increasing the downward flux with 10 W/m^2. Similar large variations are observed in the SW downward flux (55 W/m^2) and SW upward flux respectively (30 W/m^2 for the region above the cloud). It must be remembered that these variations are instantaneous since the vertical temperature profile did not change from the cloudy to the clear case. In reality, a temperature adjustment will take place, thus influencing the LW fluxes profiles.

As mentioned above, the cloud detected at 10:00:18 UTC is a two-layer, thin cirrus cloud with a mixing ratio of about 4 mg/kg. Since it is such a thin cloud (optical thickness 0.09), the influence that it has on the upward and downward SW and LW fluxes are minimal (see Figure 6.6). We employ the same sensitivity to the IWC content study as above. Both the albedo and emissivity effects are now in the linear regime, thus variations in the SW and LW fluxes are symmetrical. In

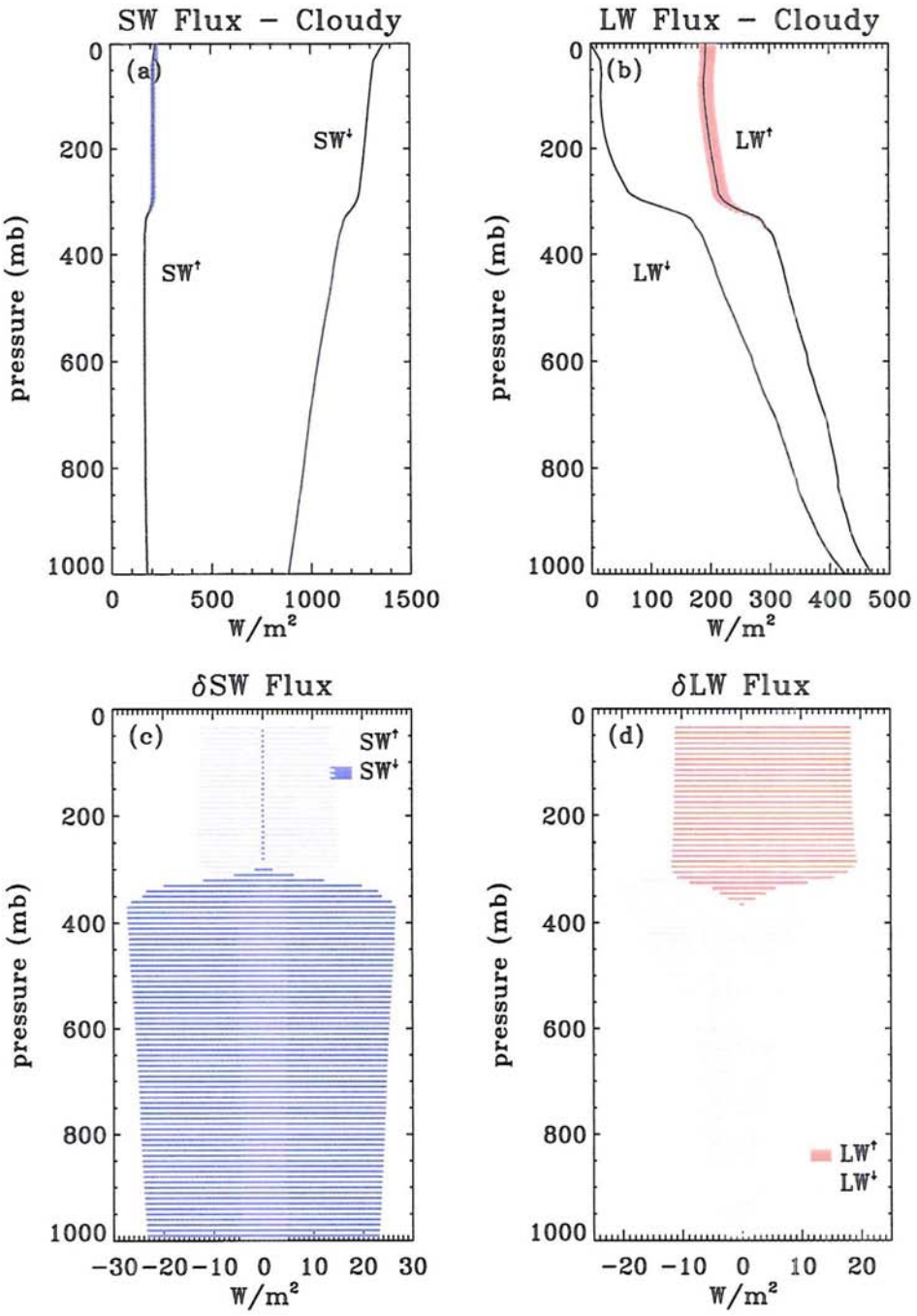

Figure 6.3: Cloudy sky computed fluxes and variations due to errors in mixing ratio: (a) SW fluxes; (b) LW fluxes; (c) δSW fluxes; (d) δLW fluxes. Nauru 1999/05/01 – 09:00 UTC.

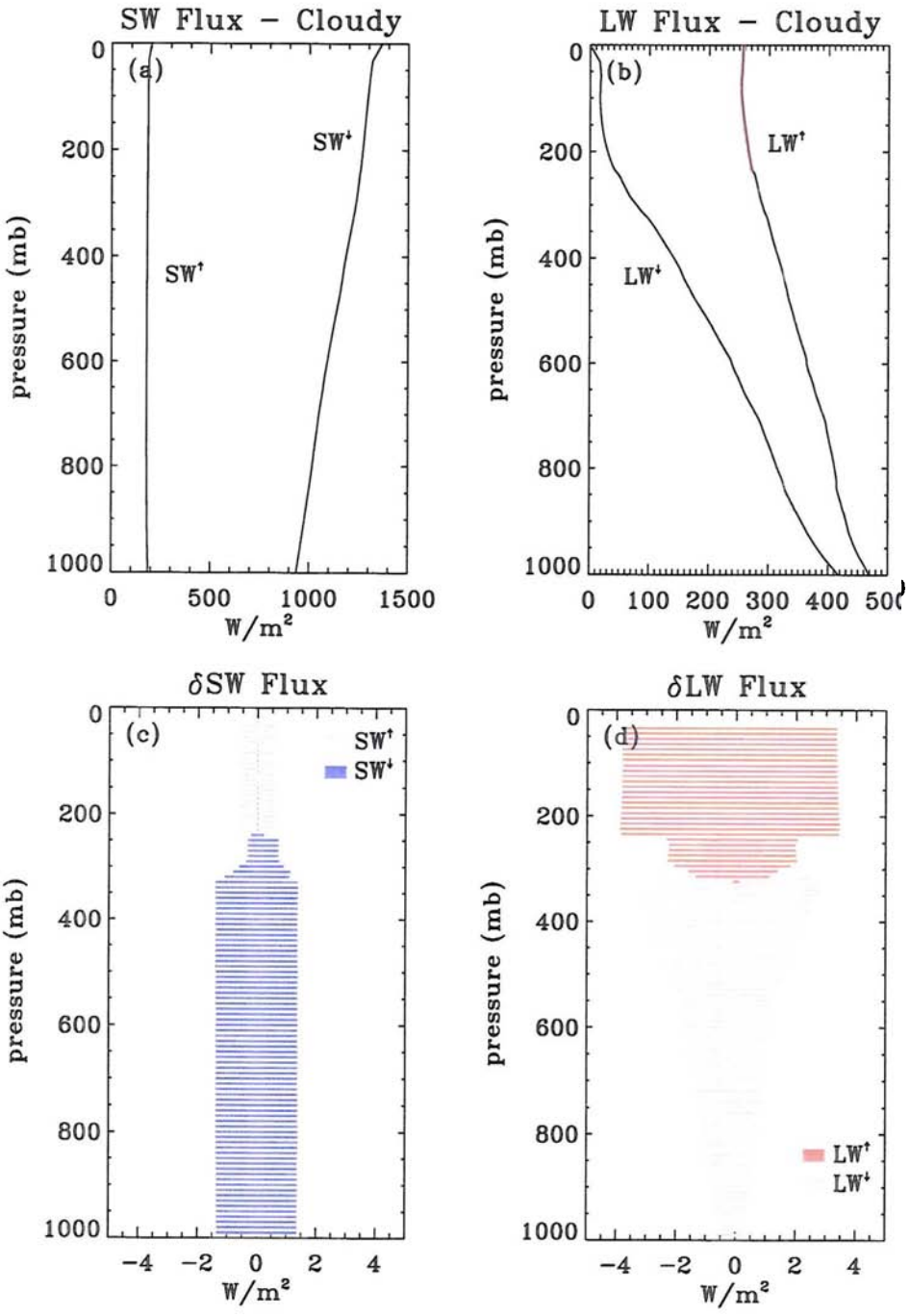

Figure 6.6: Cloudy sky computed fluxes and variations due to errors in mixing ratio: (a) SW fluxes; (b) LW fluxes; (c) δSW fluxes; (d) δLW fluxes. Nauru 1999/05/01 — 10:00 UTC.

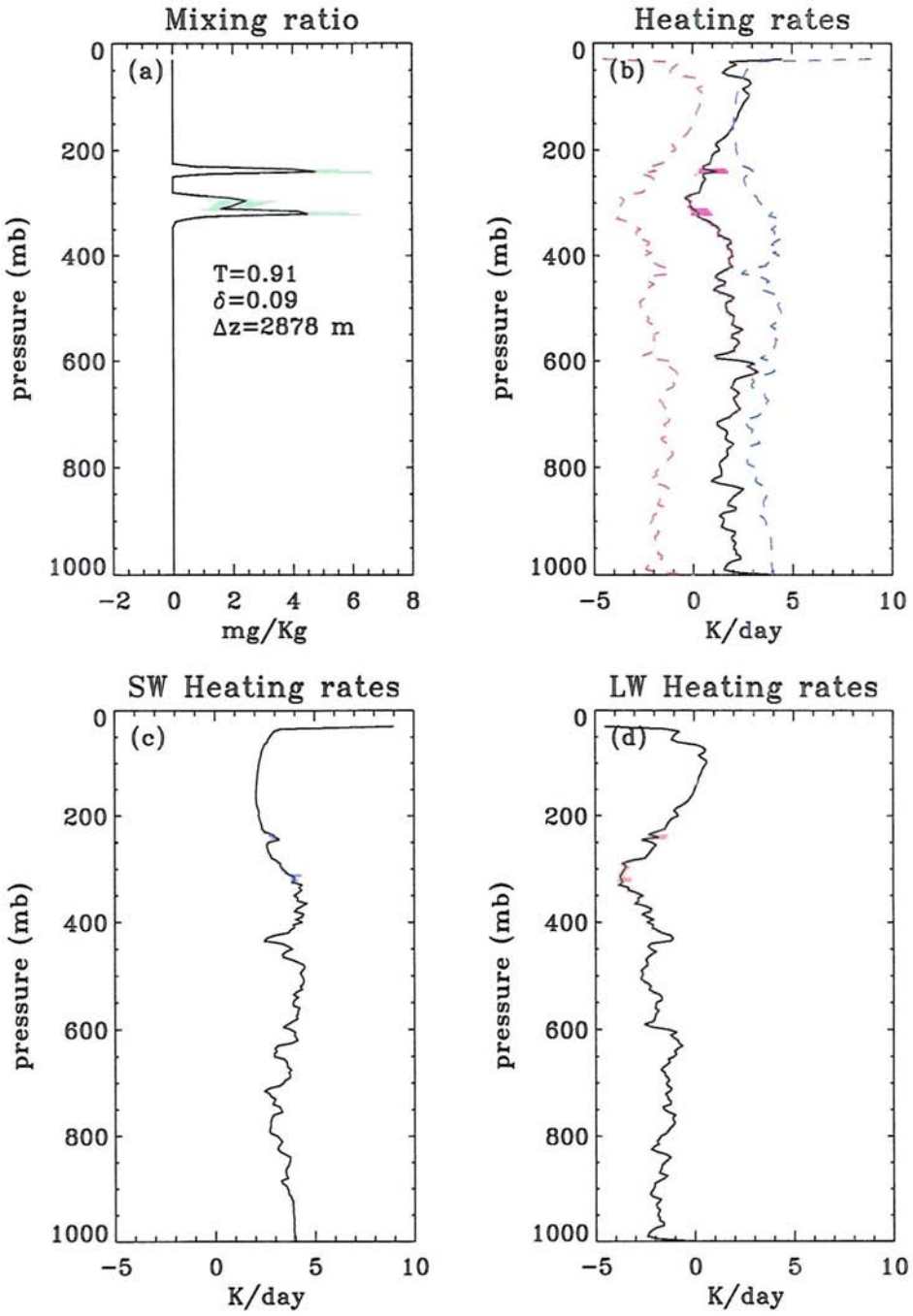

Figure 6.7: Cloudy sky heating rates and variations due to errors in mixing ratio: (a) Mixing ratio; (b) Total heating rate; (c) SW heating rate; (d) LW heating rate. In (a), cloud transmittance, optical depth and thickness are displayed. Nauru 1999/05/01 — 10:00 UTC.

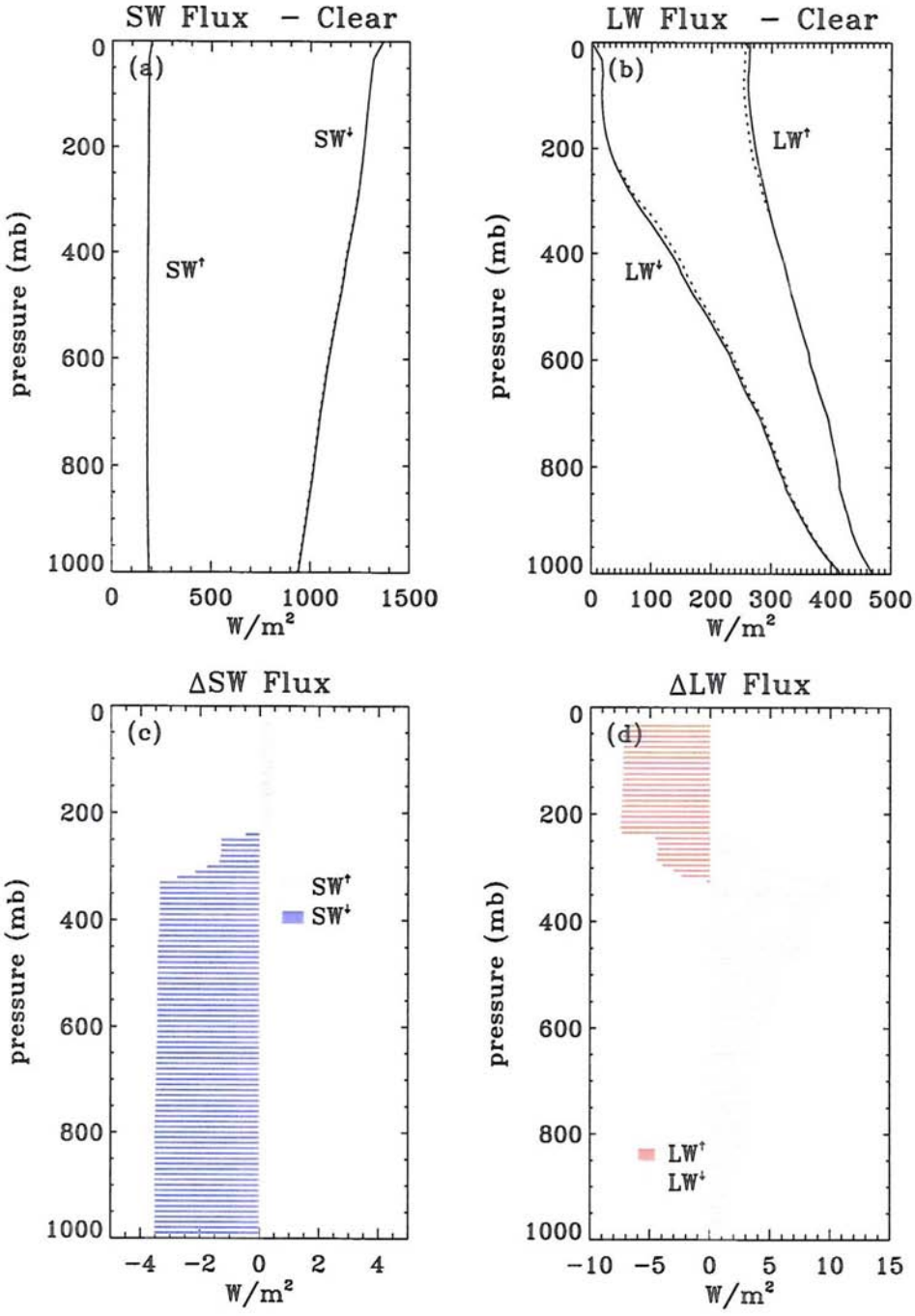

Figure 6.8: (Simulated) Clear sky computed fluxes and variations between cloudy and (simulated) clear sky: (a) SW fluxes; (b) LW fluxes; (c) ΔSW fluxes; (d) ΔLW fluxes. Nauru 1999/05/01 — 10:00 UTC.

this case however, for the regions close to the cloud, the LW variations are slightly larger than SW variations; therefore the emissivity effects are slightly larger than the albedo effects. The variations are in the range of 1 W/m^2 for SW and 0.5 W/m^2 for LW at the surface level. Following these small values in the fluxes, the heating rates are almost negligible, although a SW heating of about 0.5 K/day can be perceived. In LW, due to the two-layer structure, the radiative cooling at the top is diminished. However, the LW heating rate is still sensitive to variations in IWC value, and an increase in IWC can lead to heating within the top layer associated with emission from the lower layer. This potentially leads to an increase in the temperature of the upper layer which could eventually increase the water vapor partial pressure and vertical velocities in these regions of the atmosphere. We note also that the radiative heating of the upper thin layer is influenced by the emission from the lower layer. According to Rosenfield et al. (1998), an increased radiative heating of 0.4 K/day resulted in an increase of 1 ppmv in water vapor and an increase in the vertical velocity field of 0.1 mm/s.

The comparison to the clear sky fluxes, presented in Figure 6.8, show that this cloud induces a negligible effect on the SW flux and a large effect on the LW flux.

In the next section we focus more on the effects that clouds induce on the surrounding atmosphere and surface by studying the differences between radiative properties for cloudy and clear sky fluxes and heating rates. However the results should be treated in a statistical manner since the clear events were simulated, by imposing again that the IWC profile be zero.

6.5 Clear/Cloudy Sky Effects

The effect of clouds on solar radiation depends mostly on the optical thickness, particle size and phase function, while the thermal effect depends mostly on cloud temperature, vertical structure, and emissivity. The solar radiation effect and the thermal emission effect oppose one another, with a tendency to compensate each other. Although the effect on each flux is quite large, the net radiation effect can be relatively small. It is dependent on cloud parameters (height, thickness, effective

radius, IWC, IWP, etc.) and state of the system (temperature, humidity, aerosols, etc.).

6.5.1 Effects on LW Heating Rates

In order to asses the effects of thin, high cirrus clouds on the radiative budget of the surrounding atmosphere, we start by defining three regions: (1) *above the cloud*; (2) *in-cloud* and (3) *below the cloud*. These regions are defined with respect to the MPL cloud boundaries. Only in some special cases involving very thick clouds, the upper boundaries detected by the lidar are not the true cloud boundaries. Since we only consider clouds that are higher than 9 km, which from our previous analysis are very thin cirrus clouds, we expect that the majority of cloud characteristics that are inferred by our retrieval method to be close to reality. Also, since the clouds were detected mostly during nighttime, only LW heating rates are examined.

Figures 6.9 and 6.10 present the heating rates as a function of cloud base location, for various regions of the atmosphere, computed for both cloudy (right panel) and (simulated) clear skies (left panel). In order to better assess cloud radiative properties, for the cloudy sky cases, the differences between the cloudy and (simulated) clear heating rates are represented. We use color coded squares to indicate the mean IWC for the layer (units of mg/kg) as shown in the legend of Figure 6.9(c).

For the region *above the cloud*, for the (simulated) clear sky there is a net cooling to space at a rate of about - 1.5 K/day (see Figure 6.9(a)). The addition of clouds increases the cooling effect but no specific dependence on IWC can be inferred.

The *in-cloud* region exhibits the following trend: for the (simulated) clear sky, there is net cooling for the region below 180 mb and net heating above this level. The cooling rate increases with decreasing height due to the effects of local temperature curvature on the heating profile. By adding clouds, heat is added to this region, the degree of heating depending mostly on the cloud microphysical properties (IWC); clouds with higher IWC adding more heat than those with lower IWC. It is also evident that cloud altitude is important: on average, higher clouds contribute more to the heating rate as expected [Stephens (1980)]. The degree of additional heating

rate ranges from zero for clouds with low IWC up to 8 K/day for high altitude clouds having large values for the IWC.

The region *below the cloud*, exhibits a more or less constant cooling rate of about - 2 K/day for clear sky; the addition of clouds increases the heating rates for this region, but for these high, thin cirrus clouds, the net effect is still a cooling, as the clouds do not add more than 1 K/day to the net heating rate. As expected, thicker clouds with larger values of IWC have a greater effect than thinner clouds. It is also apparent that lower clouds heat more in this region of the atmosphere than higher clouds with the same IWC, which is in contrast to the radiative heating of the cloud layer itself. By adding all of the above columns, we obtain the heating rates for the column between 50 and 1000 mb. Its characteristics follow closely the same features as the region below clouds. This behavior is expected, since most of the atmospheric mass is concentrated here.

We also represented the heating rates with respect to the differences between surface temperature (T_s) and base of the cloud temperature (T_b). From these plots (see Figures 6.11 and 6.12) we deduce that the heating rates for very thin cirrus clouds (having IWC less than 2 mg/kg) vary almost linearly with the above temperature difference. Since we encounter these thin clouds over a broad temperature differences, we can also conclude that their presence is not influenced by surface induced processes. An increase in the IWC seems to be somewhat correlated with a decrease in the temperature difference.

6.5.2 Cloud Radiative Forcing

Other quantities that usefully describe cloud effects are the LW and the SW cloud forcing respectively:

$$C_{LW} = LW^{\uparrow}_{\infty}(clear) - LW^{\uparrow}_{\infty}(cloudy) \tag{6.8}$$

$$C_{SW} = SW^{\uparrow}_{\infty}(cloudy) - SW^{\uparrow}_{\infty}(clear) \tag{6.9}$$

where all upward fluxes are those measured at the top of the atmosphere. Although clear sky conditions were recorded, we did not use this data in our analysis, since

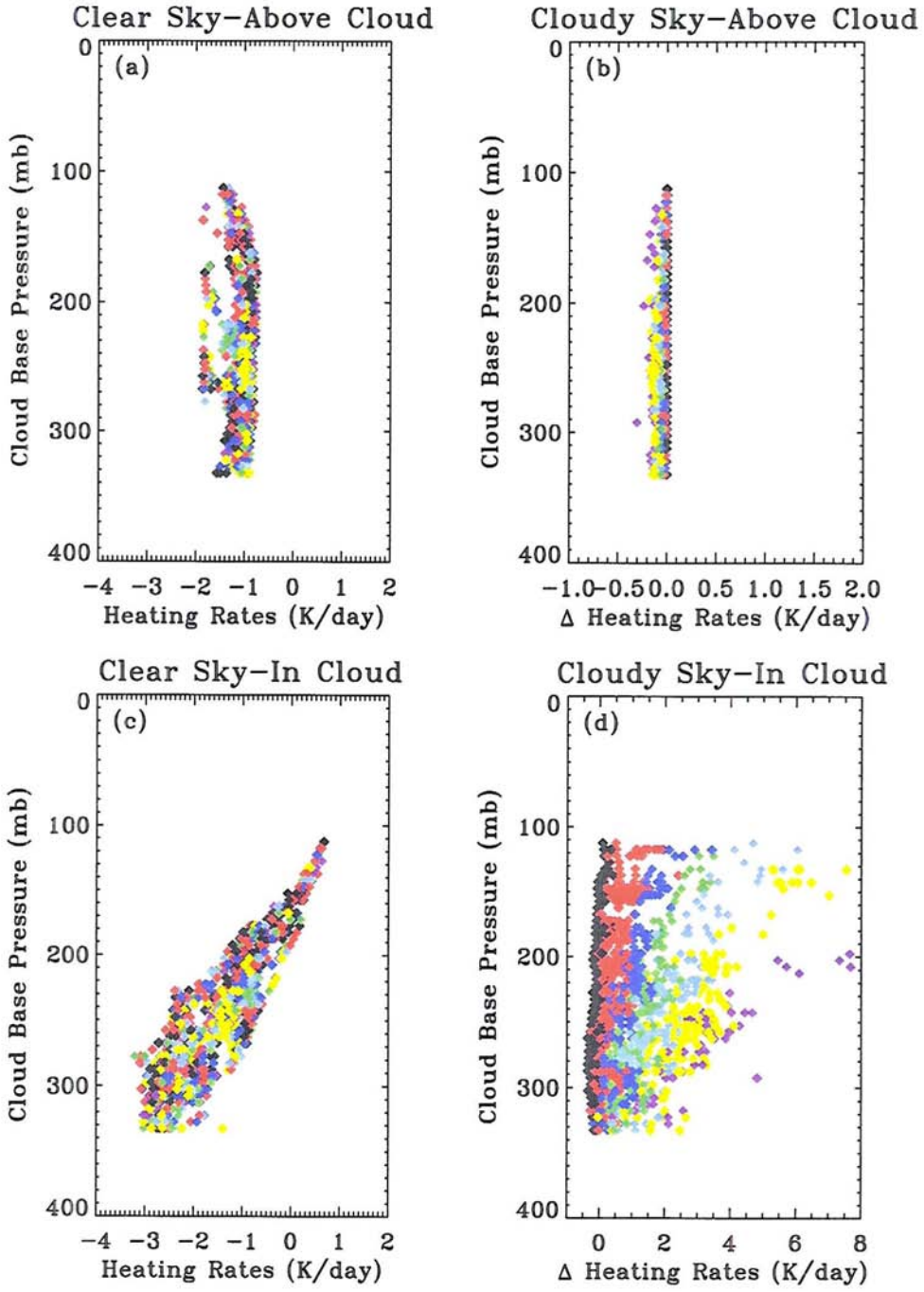

Figure 6.9: LW Heating rates for different atmospheric regions. Simulated clear sky (left panels); Differences between cloudy and clear sky (right panels). Colors represent mean IWC values as in figure 6.10. Nauru 1999/06/18–1999/07/15.

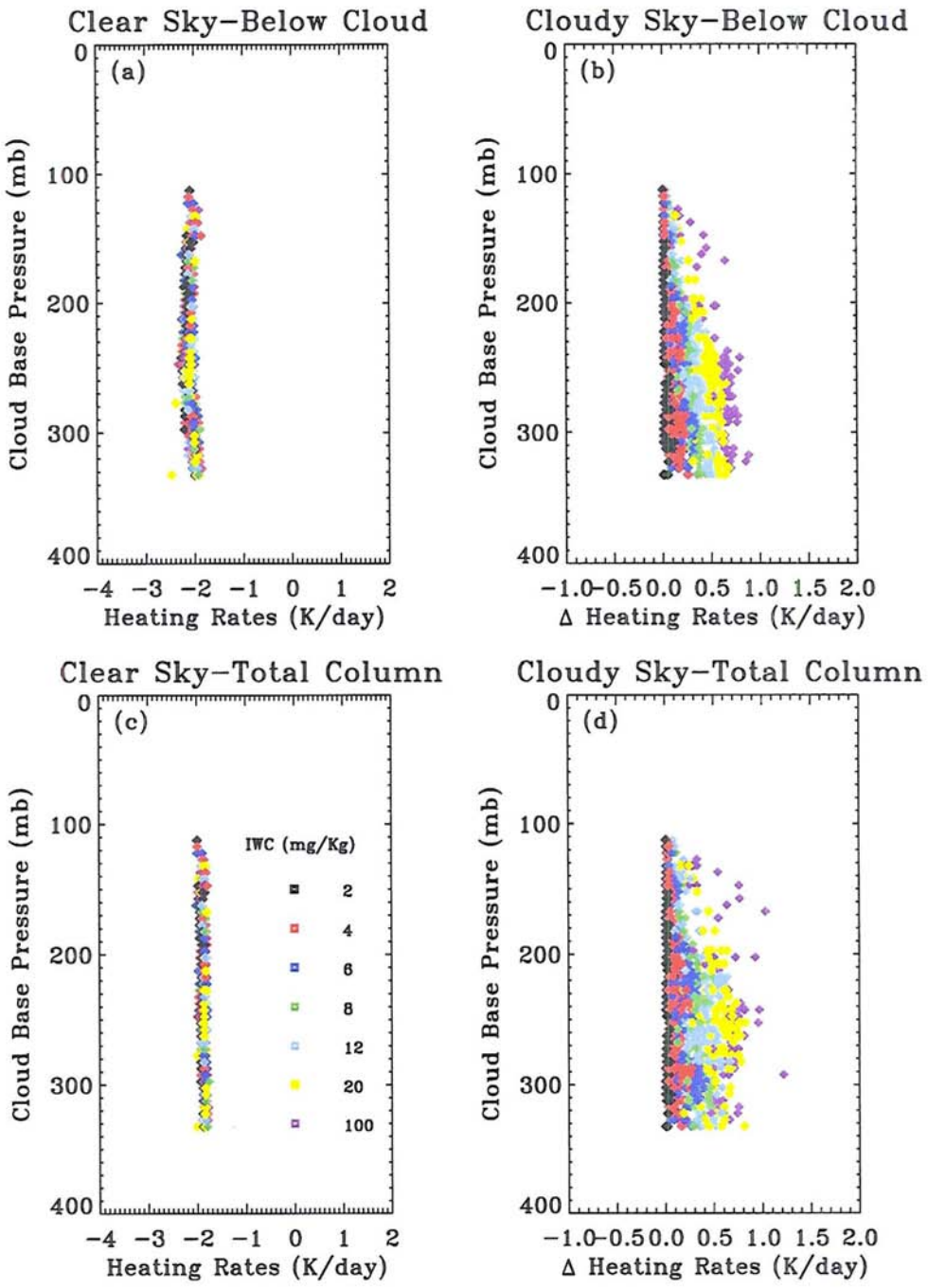

Figure 6.10: LW Heating rates for different atmospheric regions. Simulated clear sky (left panels); Differences between cloudy and clear sky (right panels). Colors represent mean IWC values. Nauru 1999/06/18–1999/07/15.

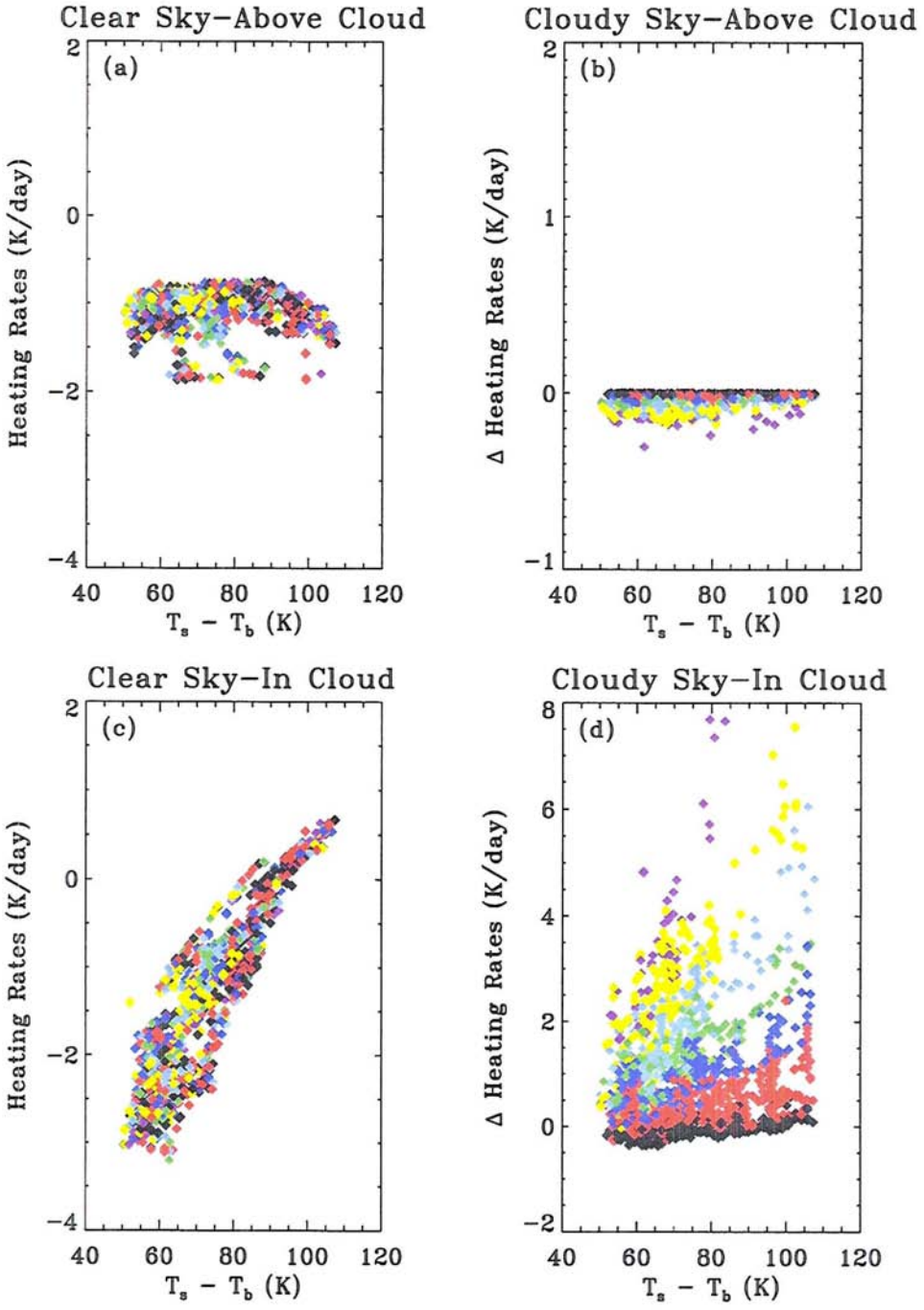

Figure 6.11: LW Heating rates vs. Temperature difference (surface - cloud) for different atmospheric regions. Simulated clear sky (left panels); Differences between cloudy and clear sky (right panels). Colors represent mean IWC values as in figure 6.10. Nauru 1999/06/18–1999/07/15.

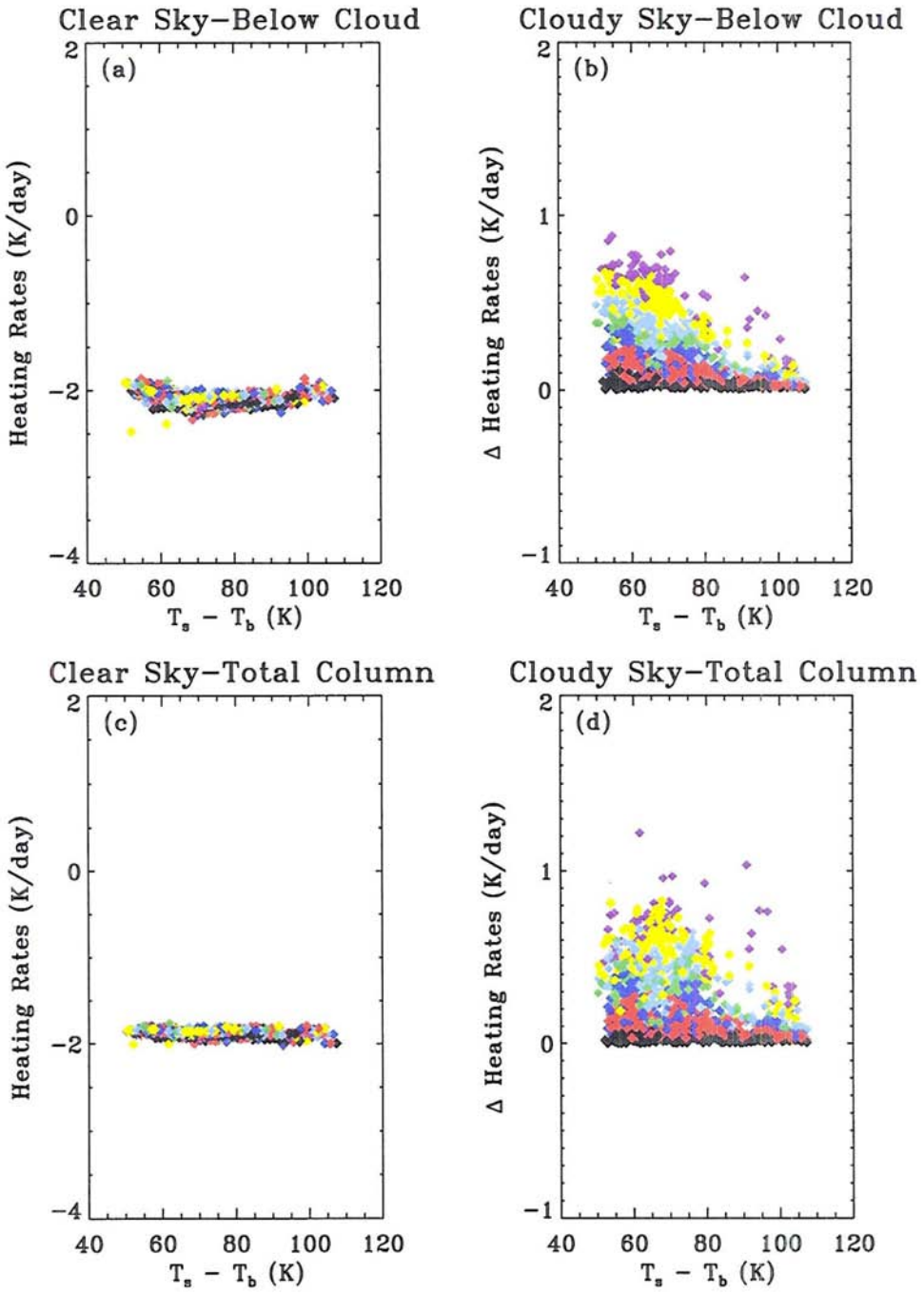

Figure 6.12: LW Heating rates vs. Temperature difference (surface - cloud) for different atmospheric regions. Simulated clear sky (left panels); Differences between cloudy and clear sky (right panels). Colors represent mean IWC values as in figure 6.10. Nauru 1999/06/18–1999/07/15.

they were recorded at various moments of the day and mostly during night-time. As explained in the previous paragraph, we simulate clear sky conditions by setting the IWC to zero. The cloud influence on the SW spectral band was also simulated by setting the solar zenith angle to a fixed value, such that all cases are uniform with respect to this parameter.

Parameterization of Cloud Radiative Forcing

The scope of this paragraph is to apply our knowledge about cirrus clouds and interpret the effects that clouds have on radiative fields. More precisely, we are interested in developing and testing expressions for the magnitude of the cloud radiative forcing as function of the IWP. We start with the definition for the upward component of the LW flux for a cloudy region, by identifying the cloud emittance coefficient as the main parameter driving the magnitude of this term:

$$LW_{\infty}^{\uparrow}(cloudy) \approx (1-\epsilon) \cdot LW_{\infty}^{\uparrow}(clear) + \epsilon \sigma T_c^4 \tag{6.10}$$

The first term is the radiation from below transmitted through the cloud, while the second term is that emitted by the cloud at temperature T_c. Here we approximate that the atmosphere above the cloud level does not contribute much to the outgoing longwave radiation (OLR) field. The expression for a clear region is verified too, as we simply set the emission coefficient ϵ to zero.

In Chapter 4 we established a relationship between the visible optical depth and the IWP (equation 4.21). As was shown in the previous chapter, a relationship between the VIS extinction coefficient and the IR absorption coefficient also exists and was introduced in terms of the quantity α. Therefore a relationship between the emission coefficient and the IWP can also be proposed in the form:

$$\epsilon = 1 - e^{a \cdot IWP} \tag{6.11}$$

where a is considered a fixed parameter. It incorporates knowledge about particle size and the above mentioned relationship between VIS extinction coefficient and IR absorption coefficient. From equations (6.8), (6.10), and (6.11) we deduce that

for the case of the thin cirrus clouds that we study, the LW cloud forcing is in the following form:

$$C_{LW} = (1 - e^{a \cdot IWP}) \cdot \left[LW^{\uparrow}_{\infty}(clear) - \sigma T_c^4 \right] \quad . \tag{6.12}$$

The above form of the equation tells us to expect a linear relationship between LW cloud forcing and the IWC for small values of the IWC. For larger values of the IWC, a saturation effect for the C_{LW} will appear. This particular behavior in the LW regime is due to the non-linear emissivity effect, that was mentioned before in this chapter. As an exercise, we can calculate the value for parameter a using the proposed parameterization between VIS optical depth and IWP (see equation 4.25) and assuming that the ratio between VIS extinction coefficient and the IR absorption coefficient is set to two. From these we deduce $a = 0.056$ [m^2/g], which is consistent with values reported in the literature [Stephens (1984)]. Using a cloud temperature of T_c = - 55 °C and a mean value for the OLR flux $LW^{\uparrow}_{\infty}(clear)$ = 260 W/m^2, the parameterization for the LW cloud forcing C_{LW} [W/m^2] with respect to the cloud IWP [g/m^2] is in the form:

$$C_{LW} = 132 \cdot (1 - e^{0.056 \cdot IWP}) \quad . \tag{6.13}$$

However, the above parameterization is deduced for a fixed cloud temperature. In fact, for *in-situ* generated cirrus, IWP roughly depends on temperature, thus the mean cloud temperature itself can be parameterized in terms of the cloud IWP. It is therefore possible that a more complex relationship between the LW cloud radiative forcing and the cloud microphysical parameter IWP to be obtained.

For SW fluxes, the contribution from a cloudy region, can be written as follows:

$$SW^{\uparrow}_{\infty}(cloudy) \approx R \cdot SW^{\downarrow}_{\infty} + \frac{T^2_{cloud} \cdot T^2_{atm} \cdot \alpha}{1 - R \cdot T^2_a \cdot \alpha} \cdot SW^{\downarrow}_{\infty} \tag{6.14}$$

where R is the VIS cloud reflection coefficient, T_{cloud} is the VIS cloud transmission, T_{atm} is the VIS atmospheric transmission, α is the VIS surface-atmosphere albedo and $SW^{\downarrow}_{\infty}$ is the incident solar flux at top of the atmosphere. Here we accounted for the MS effects between the surface and cloud. As above, the clear case is obtained by simply setting cloud effects to zero, that is, by setting R to zero and T_{cloud} to

unity. The reflection coefficient for thin cirrus can be expressed in terms of its VIS optical depth in the form:

$$R \approx \frac{(1-g)\tau}{2+(1-g)\tau} \tag{6.15}$$

where g is the asymmetry parameter, and τ is the VIS cloud optical depth. For the VIS cloud transmission, since this is for the case of thin cirrus clouds, and we neglect absorption effects, we can approximate it as follows:

$$T_{cloud} \approx 1 - R \quad . \tag{6.16}$$

For small values of the VIS cloud optical depth and for small solar zenith angles, we can approximate the SW cloud radiative forcing as follows:

$$C_{SW} \approx R \cdot (1 - T_{atm}^2 \cdot \alpha)^2 \cdot \left[1 + T_{atm}^2 \cdot \alpha \cdot R\right] \cdot SW_{\infty}^{\downarrow} \quad . \tag{6.17}$$

Using the relationship between τ and IWP introduced in Chapter 4, we deduce that SW cloud forcing, in the case when VIS optical depth and solar zenith angle are small, can be parameterized as follows:

$$C_{SW} = 1.3 \cdot IWP + 0.0006 \cdot IWP^2 \tag{6.18}$$

where the units for C_{SW} are in W/m^2, while those for IWP are in g/m^2. Here we have assumed a value of 0.87 for the asymmetry parameter g, 0.3 for the product $T_{atm}^2 \cdot \alpha$, and 1367 W/m^2 for the incoming solar radiation $SW_{\infty}^{\downarrow}$. However, in the case when the solar zenith angle is not close to zero, then the VIS optical depth must be corrected for such an effect. Such a correction increases the VIS optical depth and thus the reflection coefficient. In that case, the coefficients in the above parameterization will be different (expecting an increase in their values), and for the term describing the quadratic behavior a change in sign will appear. We see that the dependence for the SW cloud forcing is quadratic in IWP. SW cloud forcing increases when IWP increases. As for the LW fluxes, this increase becomes saturated and cannot exceed a maximum value. Unlike the LW case, the SW cloud radiative forcing is also dependent on the solar zenith angle, as explained above. We thus establish a relationship between IWP as a microphysical cloud parameter

and both LW and SW cloud radiative forcing as radiative cloud parameters. The relationship so developed will serve as an important way of testing parameterization schemes used in global models.

Next, application on measured data from Nauru, for the same three month period as before, is described. We use the same color representation to indicate the mean IWC of the cloud. From Figure 6.13(a) we see that the magnitude of the cloud forcing can be as high as 115 W/m^2 for thicker clouds (with ice water path around 20 g/m^2) and only around 30 W/m^2 for thinner clouds (IWP around 5 g/m^2). As the clouds get thicker, it appears that they have a saturation effect on the amount of cloud forcing, as the difference between the clear sky and cloudy sky fluxes reaches its maxima. The dotted line in the figure is based on (6.13) which is the parameterization of LW cloud radiative forcing with respect to IWP. It shows a good agreement with the simulated data.

In panel (b) of the same figure, the SW cloud radiative forcing, with sun at nadir, is represented using the same color representation as above. Again, the dotted line is our theoretical fit for the SW cloud radiative forcing (see equation 6.18). The quadratic effect is clearly seen in the figure. Although the level of agreement between our SW parameterization and simulated data is poor, by adjusting the values for some parameters — like the cloud reflection coefficient, or the surface albedo, the degree of correlation between the parameterization and simulated data can be improved considerably.

From these plots, it is clear that the LW cloud forcing exceeds the SW forcing, implying that these clouds produce a more dominant greenhouse effect. This supports past studies that have proposed the influence of tropical thin cirrus on the climate system.

6.6 Summary

In this chapter, we determine the effects of thin cirrus clouds on the radiative heating of the atmosphere. We approximate the atmosphere and clouds as plane-parallel and

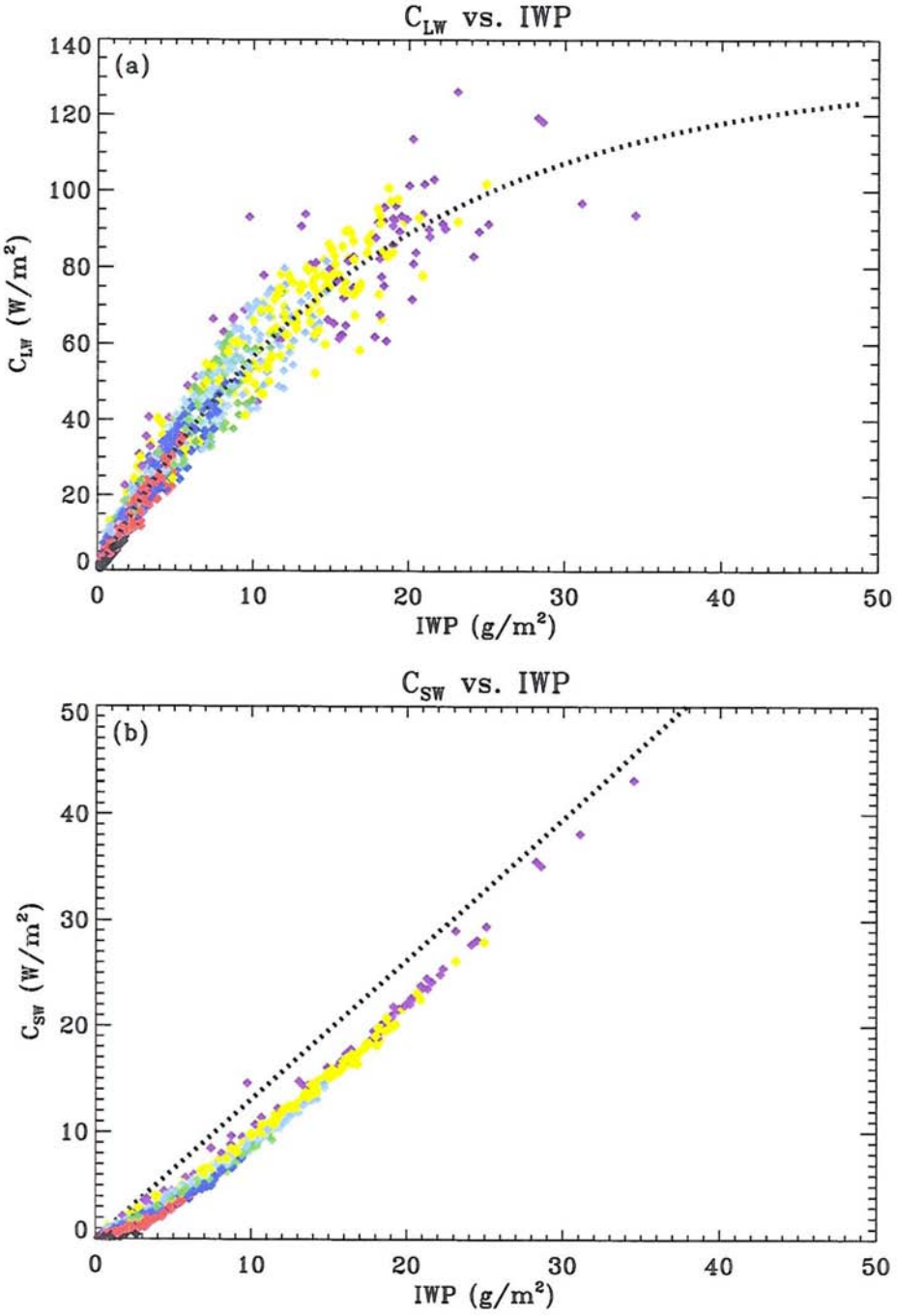

Figure 6.13: (a) LW and (b) SW cloud radiative forcing as function of IWC. Colors represent mean IWC values as in figure 6.10. With dotted lines are the proposed parameterizations as explained in text. Nauru 1999/06/18–1999/07/15.

neglect effects of 3D geometry. This is probably reasonable since these clouds are thin and layered in nature. For the calculations of the fluxes and the associated heating, we use a two-stream RT model, that accounts for a variety of absorbing gases over a wide range of spectral bands. The main findings of this chapter are summarized below.

1. Sensitivity tests with respect to uncertainties in the cloud IWC profile show that this microphysical parameter has a substantial impact on both LW and SW fluxes. There is a direct proportionality between the IWC and its level of uncertainty, and the fluxes. Like previous studies, we identified a linear relation between cloud albedo and IWP, and a non-linear relation between cloud emissivity and IWP.

2. By absorbing and emitting radiation, clouds either warm or cool, thus being influenced by and influencing the thermodynamics of their surroundings. Changes in the thermodynamic field are followed by changes in the dynamical field, thus changing the clouds themselves. From both simulated clear sky and cloudy sky conditions, we can deduce the influence that thin high cirrus clouds have on the radiative heating rate, both on the cloud itself and on the surrounding atmosphere. As in previous studies of thin high cirrus clouds, a heating effect due to the presence of clouds is observed. The heating rates depend on both cloud location (altitude) and ice water content. The presence of thin cirrus clouds is also associated with a heating of the layer below the cloud as well as that of the cloud. The amount of additional heating is dependent on the IWC and cloud altitude, higher clouds with larger values of IWC heating more. The layer above the cloud is less influenced by the presence of thin cirrus clouds.

3. Based on previous knowledge about the relationship between the visible cloud optical depth and the ice water path, parameterizations for the LW and SW cloud radiative forcing were developed using Nauru data. For the LW thin cirrus cloud forcing, the relationship is nearly linear for small values of the IWP, but saturates for larger values. The SW cloud forcing for these clouds

however is more complicated due to the well known albedo effect arising from variations of the solar zenith angles. However, for all zenith angles a quadratic relationship between the SW cloud forcing and the IWP is proposed and tested only for zero solar zenith angles. The sign of the non-linear term is positive for small zenith angles, but becomes negative for larger values of the zenith angle. Such a behavior suggests that a saturation effect also occurs for the SW fluxes.

4. This study, as previous ones, finds that for thin cirrus clouds over the TWP, LW dominates over SW effect, thus a net warming occurs.

This page intentionally blank.

Chapter 7

Summary and Conclusions

The aim of this thesis is to document the optical, radiative and microphysical properties for tropical thin cirrus clouds and thus establish their role in the climate system. It is well established that these high-altitude clouds, with their unique placement over the Tropical West Pacific, have the potential of influencing the climate system on multiple spatial and temporal scales. An analysis of these complex interactions requires the development of models capable of simulating the observed behavior and characteristics of the climate system. Use of remote sensing instruments makes this kind of analysis more feasible due to the well recognized coverage capabilities that these remote sensing techniques offer. Also, due to the diverse nature of clouds, and especially cirrus clouds, their optical properties, as inferred from remote sensing observations, serve as the best means of classifying clouds globally.

7.1 Summary

This work focuses on developing better methods for analyzing measurements obtained for thin cirrus clouds. The measurement approach that forms the core of this research is in inversion of remote sensing data. This inversion starts by proposing a better "forward" model, based on more physical description and less on parameterization. Such an improved model will help with the development of a superior "inverse" model — the tool used in retrieving the optical properties of a medium using remote sensing. Later on, these retrieved optical properties along with suitable parameterizations for cloud optical properties, can be used in a CRM or/and GCM model to study cloud influences and feedbacks (both quantitative and qualitative) on local and/or global climate.

In Chapter 3 we develop new algorithms for processing lidar data. We start by calibrating the lidar data — a necessary step for any retrieval method. For this procedure, the well-known molecular Rayleigh backscatter signal is used against the measured backscatter in regions where no cloud or aerosol particles are present. From the minima requirements imposed on the proposed metric, three parameters of interest can be solved: gain, offset and transmittance. This treatment not only resolves the ambiguity in the offset that old techniques were subject to, but also is less sensitive to the level of noise in the signal, demonstrated by tests against synthetic signals.

An important disadvantage of any remote system is its inability to discern between first order scattering (i.e. backscatter) and multiple scatter orders that may be measured for the same range, having the potential of complicating the analysis of the return signal. An analytical equation for describing MS effects is introduced, which contrasts with previous studies that proposed MS corrections based on empirical parameterizations. Our formulation also provides a theoretical explanation for the nonlinear relationship between the backscatter coefficient and the extinction coefficient. For simplicity the calculations were made for a homogeneous cloud, which is a good approximation for the case of a relatively thin cirrus clouds.

This method is applied to three months of data collected by the ARM micropulse lidar system at Nauru. It was determined that these cirrus clouds form at various altitudes ranging from 6 to 17 km, and with thicknesses of up to 5 km. The average thickness is around 0.8 km, with low optical depth (0.5). With the use of lidars, the only remote sensing system capable of detecting thin cirrus near the tropopause, we were able to show the influence of stratospheric waves on their life cycle.

As mentioned above, use of data collected from a multitude of remote sensing instruments is desirable for improving both the quantity and the quality of our retrievals. In this work, information from two distinct combinations of remote sensing instruments are used: active-active and active-passive remote sensing systems.

An example of an active-active remote system is the combination of RADAR-LIDAR system, which is introduced in Chapter 4. A simple and reliable analytical method based on the assumption that the cloud particle size distribution can be

characterized by a gamma size distribution is used for determining key microphysical cloud parameters such as vertical profiles for the characteristic diameter and the particle concentration. However, variations in the width parameter can lead to important variations in the retrieved parameters, thus *a priori* knowledge about this parameter must be available. We introduce a retrieval method for the case when only information about radar reflectivities and cloud visible optical depth is available.

Application of the radar-lidar retrieval method on data collected by the MMCR and MPL system at Nauru, shows that the values for retrieved variables are within those previously measured; on average, ice crystals are characterized by a mean value of 30 μm. Data analysis also confirmed the reported trend for all cloud microphysical properties to increase with increasing cloud temperature. A key parameterization between cloud optical depth and IWP was inferred from processing the data.

A well known technique for determining key visible and infrared cloud parameters along with some microphysical parameters is the LIRAD method. It is an example of an active-passive method using visible lidar data and infrared radiometric data. This technique is presented in Chapter 5. We show that the use of a nonlinear parameterization for describing multiple scattering effect leads to a different interpretation for the expression of attenuated integrated backscatter. This different approach proves useful for identifying three key backscatter regimes for cirrus clouds. However, no solid physical explanation can be offered for such a behavior. We also examine the use of CPL and MAS data as another example of an active-passive remote sensing system. Because ice crystals in cirrus clouds exhibit strongly asymmetric phase functions, computational problems for the RT equation arise. A way of addressing this problem is through the use of the similarity theory. In contrast with past studies that use this theory, the present work demonstrates that similarity is a property of the RT equation regardless of the phase function. The definition for the forward energy fraction f which provides a means for scaling the radiative transfer problem, is related to the value chosen for the forward angle and the phase function. This parameter controls the magnitude of scaling for both cloud optical depth and cloud single scatter albedo. The former is identified as

the key cloud optical parameter, since in the visible region absorption is negligible. Sensitivity studies with respect to the ice crystal composition found evidence that for radiative measurements, cloud internal structure becomes important only when highly inhomogeneous, thus, like previous studies showed, it can be considered single layered and homogeneous. Application of the RT model as developed in this chapter was applied for retrieving surface albedo during the SAFARI2000 experiment. In this section of the thesis, it is also demonstrated the impossibility of detecting very this cirrus over varying surface albedos.

In Chapter 6, we address the problem regarding the influence that cirrus clouds have on the radiative budget of the atmosphere. Use of a RT model provides the answer to these questions. Present findings confirm past studies that these effects depend on the IWC of the cloud and the height of the cloud: thicker clouds heat more than thinner clouds and higher clouds are warmer (in the sense that their heating rates is slightly higher) than lower clouds. Cirrus clouds tend to increase the temperature contrast between the troposphere and tropopause, by cooling the upper region and heating below the clouds.

7.2 Conclusions

The main conclusions drawn from results of this research are summarized below:

- Use of a new formulation for the metric describing the calibration procedure for the lidar system improves the stability and accuracy of the gain, offset and cloud transmittance.

- However, on average, for clouds with optical depths larger than 1.5, the reduction in the backscatter signal with penetration depth leads to considerable errors in detecting the top of the cloud. The reduction in the value for cloud thickness that follows from underestimating the cloud top, increases the estimated values for the extinction coefficient and ice water content. Moreover, estimations of cloud ice water content and ice water path are relative since an arbitrary mean effective radius is used. For a given 30 μm effective radius, the

above upper limit for the optical depth corresponds to an upper limit of 27 g/m^2 for the ice water path.

- In regards to multiple scattering effects, a new theoretical development shows the validity of the nonlinear relationship between the backscatter coefficient and the extinction coefficient. Use of this approach when applied to LIRAD data suggests some general properties for cirrus clouds in terms of the product $F\alpha\epsilon$.

- Use of a simple model connecting cloud microphysical properties with radar-lidar echoes yields accurate profiles for number concentration, characteristic diameter and ice water content, provided the width of the particle size distribution is known. Uncertainties in this parameter lead to large errors in the retrieved microphysical parameters. Application of this model to data led to development of a key relationship between the optical depth and ice water content.

- A more thorough study of the radiative transfer equation led to the removal of the ambiguity in defining both similarity and scaling by defining the key parameter f, that accounts for the fraction of forward scattering, and the truncated phase function. This finding is important since the inverse radiative problem is sensitive to the value of f which enters into the definition of the scaled optical depth. The scaled cloud optical depth is the key parameter influencing the radiative properties.

- By using the improved methods developed in this thesis, key cloud optical and microphysical properties were inferred. The results showed consistency with other studies, validating the methodology.

7.3 Future Work

We started our quest for knowledge about our climate system at the dawn of civilization. Man needed a tool in predicting the apparent erratic changes in the weather

and its implications: droughts or floods, warm or cold, as well as changes in the flora and fauna of a region. The early scientist was also the shaman - combining empirical knowledge with mystical powers — and he was highly respected in his society. But all his privileges could turn deadly should a forecast go wrong. Gradually mystical interpretation gave way to real science. However one common element is and should continue to be in place — imagination — that which is more important than knowledge, according to Albert Einstein. In order to describe nature, we use models. Models are based on our knowledge, experience and imagination. They also provide a way of measuring nature. We define important notions as energy or momentum, pressure or vorticity to mention a few. Instruments based on various sensors describe the state of the climate in an analytical way. We started with simple, mechanical devices for detecting changes in various physical parameters, and finally arrived at the use of sophisticated sensors on various platforms, recording a collection of physical parameters at a multitude of length and time scales, in wide spectral ranges. This hyper-data space is used by the modeling community to improve both the input data used as initialization data set, as well as the model itself by including new parameters, constants or constraints. In turn, results and interpretations of model output can help in identifying and improving the acquisition of specific climatic parameters.

For our specific research we should note that despite efforts to better characterize our climate, modeling cloud optical and microphysical properties is still a sector under construction. In this work we approach some of the specific problems in the RT field. One major problem in most RT models is the lack of description for the 3D radiative effects of clouds. A starting point would be to address the variability of ice crystals phase functions with respect to both incident and scattering angles. Further on, Monte Carlo RT models should be used for determining values and/or parameterizations describing vital cloud optical quantities. Use of such descriptions into CRMs and GCMs, will lead to a improved knowledge about effects and feedbacks of atmospheric particles on the climate. High quality and quantity experimental data can now be checked against synthetic data and adjustments for our parameterizations can be made.

Another improvement can be made by developing "forward" models for processing multi-sensor data fields. A RADAR-LIDAR-IRT-MWR model seems feasible based on our experience on LIRAD and RADAR-LIDAR models. Still, both measured data and theoretical developments are needed in order to better characterize the varying properties of the medium within this large spectral domain. It is also important to better characterize and/or parameterize the synthetic output of such a model, and check the validity of these formulations.

Research should also focus on theoretical aspects of the governing equations. Key aspects can still be deduced from manipulating them and particular solutions or conservation relationships can help our efforts in understanding our climate system. Thus both experimental and modeling efforts can be linked together into a coherent scientific research approach, that can only lead to improvements in gathering relevant specific data from field experiments and to superior atmospheric models used for simulating and predicting the complex structure of the climate.

This page intentionally blank.

Bibliography

Ansmann, A., M. Riebesell, U. Wadinger, C. Weitkamp, E. Voss, W. Lahmann, and W. Michaelis: 1992a, Combined Raman Elastic-Backscatter LIDAR for Vertical Profiling of Moisture, Aerosol Extinction, Backsctter, and LIDAR Ratio. *Appl. Phys.*, **B55**, 18–28.

Ansmann, A., U. Wadinger, M. Riebesell, C. Weitkamp, and W. Michaelis: 1992b, Independent Measurement of Extinction and Backscatter Profiles in Cirrus Clouds by Using a Combined Raman Elastic-Backscatter Lidar. *Appl. Opt.*, **31**, 7113–7131.

Arkin, A. and D. Ziskin: 1994, Relationship between Clouds and Sea Surface Temperatures in the Western Tropical Pacific. *J. Climate*, **7**, 988–1000.

Austin, R. T. and G. L. Stephens: 2001, Retrieval of Stratus Cloud Microphysical Parameters using Millimeter-Wave Radar and Visible Optical Depth in Preparation for CloudSat: Part i. Algorithm formulation. *J. Geophys. Res.*, **106**, 28233–28242.

Baran, A. J., P. N. Francis, L. C. Labonnote, and M. Doutriaux-Boucher: 2001, A Scattering Phase Function for Ice Cloud: Tests of Applicability Using Aircraft and Satellite Multi-Angle Multi-Wavelength Radiance Measurements of Cirrus. *J. R. Meteorol Soc.*, **127**, 2395–2416.

Boehm, M. T. and J. Verlinde: 2000, Stratospheric Influence on Upper Tropospheric Tropical Cirrus. *Geophys. Res. Let.*, **27**, 3209–3217.

Brown, P. R. A. and P. N. Francis: 1995, Improved Measurements of the Ice Water Content in Cirrus using a Total-Water Probe. *J. Atmos. Oceanic. Technol.*, **12**, 410–414.

Cess, R. D., G. L. Potter, J. P. Blanchet, G. J. Boer, A. D. D. Genio, M. D. M, V. D. V, V. G. V, W. L. Gates, S. J. Ghan, J. T. Kiehl, A. A. Lacis, H. L. Treut, Z.-X. Li, X.-Z. Liang, B. J. M. V. P, Meleshko, J. F. B. Mitchell, J.-J. Morcrette, D. A. Randall, L. Rikus, E. E. Roeckner, J. F. Royer, U. Schlese, D. A. Sheinin, A. Slingo, A. P. Sokolov, K. E. Taylor, W. M. Washington, R. T. Wetherald, I. Yagai, and M.-H. Zhang: 1990, Intercomparison and Interpretation of Climate Feedback Processes in 19 Atmospheric General Circulation Models. *J. Geophys. Res.*, **95**, 16601–16615.

Cess, R. D., M. H. Zhang, G. L. Potter, V. Alekseev, H. W. Barker, E. Cohen-Solal, R. A. Colman, D. A. Dazlich, A. D. DelGenio, M. R. Dix, V. Dymnikov, M. Esch, L. D. Fowler, J. R. Fraser, V. Galin, W. L. Gates, J. J. Hack, W. J. Ingram, J. T. Kiehl, H. L. Trent, K. K.-W. Lo, B. J. McAvaney, V. P. Meleshko, J.-J. Morcrette, D. A. Randall, E. Roeckner, J. F. Royer, M. E. Schlesinger, P. V. Sporyshev, B. Timbal, E. M. Volodin, K. E. Taylor, W. Wang, and R. T. Wetherald: 1996, Cloud Feedbacks in Atmospheric General Circulation Models: An Update. *J. Geophys. Res.*, **101**, 12791–12794.

Cotton, W. R. and R. A. Anthes: 1989, *Storm and Cloud Dynamics*. Academic Press, 883 pp.

Danielsen, E. F.: 1982, A Dehydratation Mechanism for the Stratosphere. *Geophys. Res. Lett.*, **9**, 605–608.

DelGenio, A. D.: 1996, *Observational Requirements for Modeling of Global and Regional Climate Change*. Springer, 614 pp.

Dowling, D. R. and L. F. Radke: 1990, A Summary of the Physical Properties of Cirrus Clouds. *J. Appl. Meteor.*, **29**, 970–978.

Goody, R. M. and Y. L. Yung: 1989, *Atmospheric Radiation*. Oxford, University Press, 519 pp.

Hartmann, D. L.: 1994, *Global Physical Climatology*. Academic, 411 pp.

Heymsfield, A. J.: 1972, Ice Crystals Terminal Velocities. *J. Atmos. Sci.*, **29**, 1348–1357.

Hu, Y. X., B. Wielicki, B. Lin, G. Gibson, S. C. Tsay, K. Stamnes, and T. Wong: 2000, δ-Fit: A Fast and Accurate Treatment of Particle Scattering Phase Functions with Weighted Singular Value Decomposition Least-Square Fitting. *J. Quant. Spectrosc. Radiat. Transfer*, **65**, 681–690.

Khairoutdinov, M. F. and D. A. Randall: 2001, A Cloud Resolving Model as Cumulus Parameterization in the NCAR Community Climate System Model: Preliminary Results. *Geophys. Res. Lett.*.

King, M. D., Y. J. Kaufman, W. P. Menzel, and D. Tanre: 1992, Remote Sensing of Cloud, Aerosol, and Water Vapor Properties from the Moderate Resolution Imaging Spectrometer (MODIS). *IEEE Trans., Geosci. Remote. Sens.*, **30**, 2–27.

Klett, J. D.: 1981, Stable Analytical Inversion Solutions for Processing Lidar Returns. *Appl. Optics*, **20**, 211–220.

Kristjansson, J. E., J. M. Edwards, and D. L. Mitchell: 2000, Impact of a New Scheme for Optical Properties of Ice Crystals on Climates of Two GCMs. *J. Geophys. Res.*, **105**, 10063–10079.

Lilly, D. K.: 1988, Cirrus Outflow Dynamics. *J. Atmos. Sci.*, **45**, 1594–1605.

Liou, K. N.: 1971, Time Dependent Multiple Backscattering. *J. Atmos. Sci.*, **28**, 824–827.

Liou, K. N. and R. M. Schotland: 1971, Multiple Backscattering and Depolarization from Water Clouds for a Pulsed Lidar System. *J. Atmos. Sci.*, **28**, 772–784.

Lynch, D. K., K. Sassen, D. O. Starr, and G. L. Stephens: 2002, *Cirrus*. Oxford, University Press, 480 pp.

Matveev, L. T.: 1984, *Cloud Dynamics*. Reidel, Dordrecht, 345 pp.

McCartney, E. L.: 1976, *Optics of the Atmosphere. Scattering by Molecules and Particles*. John Wiley & Sons, New York / London / Sydney / Toronto, 425 pp.

Miller, S. D.: 1997, *Multiple Scattering Effects in the LIDAR Pulse Stretching Problem*. Colorado State University, Paper No. 642, 156 pp.

Miller, S. D., G. L. Stephens, C. Drummond, A. Heidinger, and P. Partain: 2000, A Multisensor Diagnostic Satellite Cloud Property Retrieval Scheme. *J. Geophys. Res.*, **105**, 19,955–19,971.

Nakajima, T. and M. D. King: 1990, Determination of the Optical Thickness and Effective Particle Radius of Clouds from Reflected Solar Radiation Measurements, I, Theory. *J. Atmos. Sci.*, **47**, 1878–1893.

Peixoto, J. P. and A. H. Oort: 1995, *Physics of Climate*. American Institute of Physics, 520 pp.

Pfister, L., H. B. Selkirk, E. J. Jensen, M. R. Schoebel, O. B. T. E. V. Browell, W. B. Grant, B. Gary, M. J. Mahoney, T. V. Bui, and E. Hintsa: 2001, Aircraft Observations of Thin Cirrus Clouds near the Tropical Tropopause. *J. Geophys. Res.*, **106**, 9765–9786.

Platt, C. M. R.: 1981, Remote Sounding of High Clouds. III: Monte Carlo Calculations of Multiple-Scattered Lidar Returns. *J. Atmos. Sci.*, **38**, 156–167.

Platt, C. M. R. and A. C. Dilley: 1981, Remote Sounding of High Clouds: IV: Observed Temperature Variations in Cirrus Optical Properties. *J. Atmos. Sci.*, **38**, 1069–1082.

Platt, C. M. R., A. C. Dilley, J. C. Scott, I. J. Barton, and G. L. Stephens: 1984, Remote Sounding of High Clouds: V: Infrared Properties and Structures of Tropical Thunderstorm Anvils. *J. Climate and Appl. Meteor.*, **23**, 1296–1308.

Platt, C. M. R., D. M. Winker, M. A. Vaughan, and S. D. Miler: 1999, Backscatter-to-Extinction Ratios in the Top Layers of Tropical Mesoscale Convective Systems and in Isolated Cirrus from LITE Observations. *J. Appl. Meteor.*, **38**, 1330–1345.

Platt, C. M. R., S. A. Young, R. T. Austin, G. R. Patterson, D. L. Mitchell, and S. D. Miller: 2002, LIRAD Observations of Tropical Cirrus Clouds in MCTEX. Part I: Optical Properties and Detection of Small Particles in Cold Cirrus. *J. Atmos. Sci.*.

Platt, C. R. M.: 1979, Remote Sounding of High Clouds: I. Calculation of Visible and Infrared Optical Properties from Lidar and Radiometer Measurements. *J. Appl. Meteor.*, **13**, 1130–1143.

Ramanathan, V. and W. Collins: 1991, Thermodynamic Regulation of Ocean Warming by Cirrus Clouds Deduced from the el Niño. *Nature*, **351**, 27–32.

Ramaswamy, V. and V. Ramanathan: 1989, Solar Absorption by Cirrus Clouds and the Maintenance of the Tropical Upper Troposphere Thermal Structure. *J. Atmos. Sci.*, **46**, 2293–2310.

Randall, D. A., R. D. Cess, J. P. Blanchet, G. J. Boer, D. A. Dazlich, A. D. D. Genio, M. D. V. Dymnikov, V. Galin, S. J. Ghan, A. A. Lacis, H. L. Treut, Z.-X. Li, X.-Z. Liang, B. J. McAvaney, V. P. Meleshko, J. F. B. Mitchell, J.-J. Morcrette, G. L. Potter, L. Rikus, E. Roeckner, J. F. Royer, U. Schlese, D. A. Sheinen, J. Slingo, A. P. Sokolov, K. E. Taylor, W. M. Washington, R. T. Wetherald, I. Yagai, and M.-H. Zhang: 1992, Intercomparison and Interpretation of Surface Energy Fluxes in Atmospheric General Circulation Models. *J. Geophys. Res.*, **97**, 3711–3724.

Rosenfield, J. E., D. B. Considine, M. R. Scheberl, and E. V. Browel: 1998, The Impact of Subvisible Cirrus Clouds near the Tropical Tropopause on Stratospheric Water Vapor. *Geophys. Res. Lett.*, **25**, 1883–1886.

Rossow, W. B. and R. A. Schiffer: 1991, ISCCP Cloud Data Products. *Bull. Amer. Meteor. Soc.*, **72**, 2–20.

Stephens, G. L.: 1980, Radiative Properties of Cirrus Clouds in the Infrared Region. *J. Atmos. Sci.*, **37**, 435–446.

—— 1984, The Parameterization of Radiation for Numerical Weather Prediction and Climate Models. *Mon. Wea. Rev.*, **112**, 826–867.

—— 1994, *Remote Sensing of the Lower Atmosphere*. Oxford University Press, 523 pp.

Stephens, G. L., P. M. Gabriel, and P. T. Partain: 2001, Parameterization of Atmospheric Radiative Transfer. Part I: Validity of Simple Models. **58**, 3391–3409.

Stephens, G. L. and T. J. Greenwald: 1991, The Earth's Radiation Budget and Its Relation to Atmospheric Hydrology 2. Observation of Cloud Effects. *J. Geophy. Res.*, **96**, 15,325–15,340.

Stephens, G. L., S.-C. Tsay, P. W. Stackhouse, and P. J. Flatau: 1990, The Relevance of the Microphysical and Radiative Properties of Cirrus Clouds to Climate and Climatic Feedback. *J. Atmos. Sci.*, **47**, 1742–1753.

Stephens, G. L. and P. J. Webster: 1981, Clouds and Climate: Sensitivity of Simple Systems. *J. Atmos. Sci.*, **38**, 235–247.

van de Hulst, H. C.: 1980, *Multiple Light Scattering*. Academic Press, New York, 321 pp.

Wang, Z. and K. Sassen: 2001, Cirrus Cloud Microphysical Property Retrieval using Lidar and Radar Measurements: I Algorithm Description and Comparison with in situ Data. *J. Appl. Meteor.*.

Weitkamp, C.: 1996, *Lidar Measurements: Atmospheric Constituents, Clouds, and Ground Reflectance*. Springer, 614 pp.

Wielicki, B. A., R. D. Cess, M. D. King, D. A. Randall, and E. F. Harrison: 1995, Mission to Planet Earth: Role of Clouds and Radiation in Climate. *Bull. Am. Meteo. Soc.*, **76**, 2125–2153.

Wiscombe, W. J.: 1977, The Delta-M Method: Rapid Yet Accurate Radiative Flux Calculations for Strongly Asymmetric Phase Functions. *J. Atmos. Sci.*, **34**, 1408–1422.

Yang, P., B.-C. Gao, B. A. Baum, W. J. Wiscombe, Y. X. Hu, S. L. Nasiri, P. F. Soulen, A. J. Heymsfjeld, G. M. McFarquhar, and L. M. Miloshevich: 2001, Sensitivity of Cirrus Bidirectional Reflectance to Vertical Inhomogeneity of Ice Crystal Habits and Size Distributions for two Moderate-Resolution Imaging Spectroradiometer (MODIS) Bands. *J. Geophys. Res.*, **106**, 17,267–17,291.

Young, S. A.: 1995, Analysis of Lidar Backscatter Profiles in Optically Thin Clouds. *Appl. Opt.*, **34**, 7019–7031.

;

Appendix A

Particle Size Distribution

Consider a particle size distribution $n(D)$, where D is the particle diameter. By definition, the size distribution function is:

$$n(D) = \frac{\text{number of particles per m}^3 \text{ with diameters in the range } D, D + dD}{dD}. \tag{A.1}$$

The total number concentration of particles of all sizes is just:

$$N_t = \int_0^\infty n(D)\, dD \tag{A.2}$$

Using the above definition for the particle size distribution, we can determine some important characteristics of the distribution such as:

- Mean Diameter ($\overline{D}$):

$$\overline{D} = \frac{1}{N_t} \int_0^\infty D\, n(D)\, dD \tag{A.3}$$

- Mode (D_m):

$$\frac{dN(D_m)}{dD} = 0 \tag{A.4}$$

- p-th moment ($\overline{D^p}$):

$$\overline{D^p} = \frac{1}{N_t} \int_0^\infty D^p\, n(D)\, dD \tag{A.5}$$

- Standard deviation (σ):

$$\sigma = \sqrt{\overline{D^2} - \overline{D}^2} \tag{A.6}$$

One of the most commonly used distribution in atmospheric science is the so-called Gamma size distribution which is defined as:

$$n(D) = N_t \frac{1}{\Gamma(\nu)} \left(\frac{D}{D_n}\right)^{\nu-1} \frac{1}{D_n}\, exp\left(-\frac{D}{D_n}\right) \tag{A.7}$$

where N_t is the total number concentration, D_n is the characteristic diameter, ν is the distribution width, and $\Gamma(\nu)$ is the normalization factor, defined as:

$$\Gamma(\nu) = \int_0^\infty x^{\nu-1} e^{-x} dx \tag{A.8}$$

The above equation is the definition of the Gamma function, which has some nice properties:

$$\begin{cases} \Gamma(n+1) = n \cdot \Gamma(n) \\ \Gamma(1) = 1 \\ \Gamma(1/2) = \sqrt{\pi} \end{cases} \tag{A.9}$$

Using the above properties we can compute the p-th moment:

$$\overline{D^p} = D_n^p \frac{\Gamma(\nu+p)}{\Gamma(\nu)} \tag{A.10}$$

Note that it is proportional to the p power of the characteristic diameter and depends on the distribution width.

Since for the remote sensing applications, when computing various cloud characteristics (as reflectivity, extinction coefficient, ice water content, etc.) the power p is usually an integer, the calculations can be easily performed. In fact, *in situ* measurements showed that most of the particle populations follow such a distribution.

Appendix B

Rayleigh Scattering

Scattering is a physical process in which light interacts with matter. It occurs at all wavelengths of the electromagnetic spectrum. As the name suggests, an electromagnetic wave consists of two interacting waves: one electric and one magnetic. When such a wave passes through matter, its electric and magnetic fields interact with the basic constituents of the matter. As a result of such an interaction, energy from the incident wave is absorbed and then re–emitted in all directions. The relative intensity of the scattered energy depends strongly on the size parameter, or the ratio of particle size to wavelength of incident wave. When the size parameter is much less than unity, scattering is almost isotropic. For larger size parameters, the scattered energy is concentrated in the forward direction. The first case is called Rayleigh scattering, the latter is referred to as Mie scattering.

Rayleigh scattering expresses the interaction between the electric field component of the electromagnetic wave and the dipoles which constitute the scatterer. The oscillating dipole produces a plane polarized electromagnetic wave: the scattered wave. The intensity of this wave can be computed using classical electrodynamics. The angular distribution of the scattering energy is expressed in terms of the phase function, which can be determined from the differential scattering (volumic) coefficient [McCartney (1976)].

The differential scattering volumic coefficient for the Rayleigh scattering is given by:

$$\frac{d\beta_m(\theta)}{d\Omega} = \frac{9\pi^2}{2N\lambda^4}\left(\frac{n^2-1}{n^2+2}\right)^2(1+\cos^2\theta) \tag{B.1}$$

where n is the index of refraction for air, λ is the laser wavelength, N is the number of dipole oscillators per unit volume, and θ is the angle of scattering. We can identify

the phase function associated with the above (isotropic) scattering as:

$$P(\theta) = \frac{3}{4}(1 + \cos^2\theta) \tag{B.2}$$

Taking into account the anisotropy effects by introducing the following parameter:

$$p_n = \frac{I_2(\pi/2)}{I_1(\pi/2)} , \tag{B.3}$$

the anisotropic differential volumic scattering coefficient is:

$$\frac{d\beta_m(\theta)}{d\Omega} = \frac{9\pi^2}{2N\lambda^4}\left(\frac{n^2-1}{n^2+2}\right)^2 \frac{6+3p_n}{6-7p_n}(1+\cos^2\theta) . \tag{B.4}$$

Using Chandrasekhar's phase function that includes the anisotropic effects:

$$P(\theta) = \frac{3(1+p_n)}{2(2+p_n)}\left(1 + \frac{1-p_n}{1+p_n}\cos^2\theta\right) \tag{B.5}$$

we can calculate the anisotropic differential volumic scattering coefficient as:

$$\frac{d\beta_m(\theta)}{d\Omega} = \frac{2\pi^2}{3N\lambda^4} \cdot \left(\frac{n^2-1}{n^2+2}\right)^2 \cdot \frac{6+3p_n}{6-7p_n} \cdot P(\theta) . \tag{B.6}$$

The above formulation is valid only for standard pressure and temperature (1013.25 mb, 288.15 K). A correction for variable pressure and temperature must be made. Since the index of refraction for air is close to unity, the final expression for the Rayleigh backscatter coefficient has the form:

$$\beta_{(Ray)}(\pi) = \frac{\pi^2(n^2-1)^2}{N\lambda^4} \cdot \frac{2(6+3p_n)}{(6-7p_n)(2+p_n)} \cdot \frac{p}{p_0} \cdot \frac{T_0}{T} , \tag{B.7}$$

while the associated molecular extinction coefficient is:

$$\beta_{(Ray)ext} = \int_{4\pi} \frac{d\beta_m(\theta)}{d\Omega} d\Omega = \frac{8\pi^3(n^2-1)^2}{3N\lambda^4} \cdot \frac{6+3p_n}{6-7p_n} \cdot \frac{p}{p_0} \cdot \frac{T_0}{T} . \tag{B.8}$$

Given the molecular extinction coefficient, the molecular transmittance can be computed:

$$T_m(z) = exp\left[-\int_0^z \beta_{(Ray)ext}\, dz\right] \tag{B.9}$$

The above expressions are used in the calibration procedure of the lidar signal against Rayleigh backscatter, by computing the loss in signal strength due to molecular absorption and in fitting the measured signal in the cloud-free region to the molecular signal.

Appendix C

Active Sensing

A powerful way of observing the atmosphere, active sensing systems such as lidar and radar, are based on the interactions between electromagnetic energy emitted by a transmitter and the atmospheric constituents that absorb and scatter it. Active sensing instruments are capable of ranging the scattering volume of interest. In such a way, a two- or even tri-dimensional picture of the scatterers/absorbers can be obtained. Radars operate at microwave frequencies, while lidars use UV, VIS or IR radiation. Although radars and lidars differ in design and operation, they share a common principle of operation. These active systems are capable of measuring both the intensity and the phase of the scattered radiation (coherent systems) or just the intensity of the scattered radiation (incoherent systems).

Radars and lidar systems operate in either a constant wave mode or in a pulsed mode. In the pulse mode, a short pulse of radiation (10^{-6} to 10^{-10} s) is emitted. By measuring the time of return of the pulse, the distance between the scattering element and the emitter/receiver can be calculated. If we measure the echo at selected time intervals (referred to as range gates), the echo received at any range gate is received from an volume which is spread in range, and the magnitude of this spread is called resolution [Stephens (1994)]:

$$\Delta z = \frac{c\,\Delta t}{2} \tag{C.1}$$

Another parameter for these systems is the pulse repetition frequency, which is the rate at which pulses are transmitted. In order to ensure that echoes from successive pulses do not overlap, the time between pulses must be at least as long as the time required for the pulse to travel back and forth from the highest predetermined

maximum range (Z_{max}). In other words:

$$\delta t \geq \frac{2(Z_{max} + \Delta z)}{c} \tag{C.2}$$

As mentioned previously, a pulse of energy is emitted to a target and the received return power is analyzed for useful information. By introducing the concept of an antenna gain, defined as the ratio of the intensity at the peak of the transmission pattern (I_p) to an isotropic intensity corresponding to the emitted power (P_t):

$$G = \frac{I_p}{P_t/4\pi d^2} , \tag{C.3}$$

the incident power at a target of cross-sectional area A_t and range d can be written as:

$$P_{target} = \frac{P_t G A_t}{4\pi d^2} . \tag{C.4}$$

From here, radiation can be scattered at an angle θ at a distance z with an intensity given by:

$$I_{sca} = \frac{|S(\theta)|^2}{k^2 z^2} \frac{P_{target}}{A_t} \tag{C.5}$$

where $S(\theta)$ is the amplitude function while k is the wavenumber. It is customary to express the scattering properties through the definition of the cross-section:

$$C_b(\theta) = 4\pi \frac{|S(\theta)|^2}{k^2} \tag{C.6}$$

Since scattering occurs within a finite volume, all the constituent particles contribute to the total return. Assuming that the individual scattered radiation is incoherent, then the total scattered radiation is simply the sum of individual scattering processes:

$$P_r = \frac{P_t\, G^2 \lambda^2}{(4\pi)^3 z^2} \Delta\Omega \int_0^\infty C_b(r) n(r) dr \tag{C.7}$$

where $\Delta\Omega$ is the solid angle under which the radiation is emitted. Here we used the relationship between the receiver area and gain:

$$A_r = G \frac{\lambda^2}{4\pi} \tag{C.8}$$

But for radar wavelengths, the cross-section for an individual particle with diameter D, is proportional to:

$$C_b(r) = \frac{\pi^5}{\lambda^4} \left| \frac{m^2 - 1}{m^2 + 2} \right|^2 D^6 \tag{C.9}$$

where m is the complex index of refraction for the atmospheric particles. It follows that the relationship between the return power and atmospheric constituents is due to the factor:

$$Z = \int_0^\infty n(D)D^6 dD \tag{C.10}$$

which is called the radar reflectivity. It follows that the total scattered radiation can be expressed by:

$$P_r = C\left|\frac{m^2-1}{m^2+2}\right|^2 \frac{Z}{z^2} \tag{C.11}$$

which is called the radar equation. However it doesn't take into account attenuation due to absorption and scattering. This can be corrected by introducing the two-way attenuation term that describes the basic law of extinction. In such a way, the received power is:

$$P_r = C\left|\frac{m^2-1}{m^2+2}\right|^2 \frac{Z}{z^2} \exp\left[-2\int_0^z \sigma_{ext}(z')dz'\right] \tag{C.12}$$

where σ_{ext} is the extinction coefficient at radar wavelength.

Since the received power (P_r) is several orders of magnitude lower than that transmitted, the received signal is expressed by:

$$P_r(dB) = 10\log\frac{P_r}{P_t}\,. \tag{C.13}$$

For a similar reason, radar reflectivity (in $\mathrm{mm^6 m^{-3}}$) is expressed in a logarithmic scale (dBZ):

$$Z(dBZ) = 10\log Z\,. \tag{C.14}$$

This page intentionally blank.

Appendix D

Doubling and Adding Method

One of the most used methods for solving the radiative transfer equation when dealing with multiple scattering events is the adding/doubling method. Starting from the RT equation for a plane-parallel atmosphere:

$$\mu \frac{dI(z,\mu,\phi)}{dz} = -\sigma_{ext} I(z,\mu,\phi)$$

$$+ \frac{\sigma_{scat}}{4\pi} \int_0^{2\pi} \int_{-1}^{1} P(z,\mu,\phi,\mu',\phi') I(z,\mu',\phi') d\mu' d\phi' + \sigma_{abs} B[T(z)] \tag{D.1}$$

The total radiance I can be expressed as the sum of direct and diffuse radiances:

$$I = I^0 + I^\star \tag{D.2}$$

and since at angles close to the solar angle $\mu_\odot$ we can consider that $I^0 \gg I^\star$ then the solution for the direct beam is:

$$I^0(z) = I_\odot \; exp(-\tau/\mu_\odot) \tag{D.3}$$

and the RT equation (for the diffuse beam) becomes:

$$\mu \frac{dI^\star(z,\mu,\phi)}{dz} = -\sigma_{ext} I^\star(z,\mu,\phi) + \frac{\sigma_{sca}(z)}{4\pi} \int_0^{2\pi} \int_{-1}^{1} P(z,\mu,\phi,\mu',\phi') I^\star(z,\mu',\phi') d\mu' d\phi'$$

$$+ \frac{F_\odot}{4\pi} \sigma_{sca}(z) P(z,\mu,\phi,-\mu_\odot,\phi_\odot) exp\left(-\frac{\tau}{\mu_\odot}\right) + \sigma_{abs}(z) B[T(z)] \tag{D.4}$$

In the case when the radiance $I^\star$ does not depend on the azimuthal angle and when the wavelength is in the visible range we can rewrite the above equation as:

$$\mu \frac{\partial I^\star}{\partial \tau} + I^\star = \frac{\tilde{\omega}_0}{4\pi} \int_{-1}^{1} \overline{P}(\mu,\mu') I^\star(\mu') d\mu' + \Sigma \tag{D.5}$$

with the azimuthally averaged phase function:

$$\overline{P}(\mu,\mu') = \frac{1}{2\pi}\int_0^{2\pi} P(\cos\theta)d\phi \tag{D.6}$$

and the solar term:

$$\Sigma = \frac{F_\odot}{4\pi}\sigma_{sca}\overline{P}(\mu,-\mu_\odot)exp\left(-\frac{\tau}{\mu_\odot}\right) \tag{D.7}$$

By expressing the phase function in terms of the Legendre polynomials:

$$P(\cos\theta) = \sum_{l=0}^{2N-2}\chi_l P_l(\cos\theta) \quad , \quad \chi_l = \frac{2l+1}{2}\int_{-1}^{1} P_l(\cos\theta)P(\cos\theta)d(\cos\theta) \tag{D.8}$$

and on the basis of the scattering geometry expressed as:

$$\cos\theta = \mu\mu' + \sqrt{1-\mu^2}\sqrt{1-\mu'^2}\cos(\phi-\phi') \tag{D.9}$$

and using the following expansion for the Legendre polynomials:

$$P_l(\cos\theta) = P_l(\mu)P_l(\mu') + 2\sum_{m=1}^{l}\frac{(l-m)!}{(l+m)!}P_l^m(\mu)P_l^m(\mu')\cos m(\phi-\phi') \tag{D.10}$$

and by making use of the quadrature formula:

$$\int_{-1}^{1} f(\mu)d\mu = \sum_{i=-N}^{N} w_i f(\mu_i) \quad , \quad w_i = w_{-i}\ ,\ \mu_{-i} = -\mu_i \tag{D.11}$$

we can rewrite the RT equation in the form:

$$\frac{d}{d\tau}\begin{pmatrix}\boldsymbol{I}^+\\ \boldsymbol{I}^-\end{pmatrix} = \begin{pmatrix}\boldsymbol{t} & -\boldsymbol{r}\\ \boldsymbol{r} & -\boldsymbol{t}\end{pmatrix}\begin{pmatrix}\boldsymbol{I}^+\\ \boldsymbol{I}^-\end{pmatrix} - \begin{pmatrix}\boldsymbol{\Sigma}^+\\ \boldsymbol{\Sigma}^-\end{pmatrix} \tag{D.12}$$

where

$$\begin{cases} \boldsymbol{r} = \frac{\tilde{\omega}_0}{2}\,\boldsymbol{E}\boldsymbol{M}^{-1}\,\boldsymbol{P}^-\,\boldsymbol{C} \\ \boldsymbol{t} = \boldsymbol{M}^{-1} - \frac{\tilde{\omega}_0}{2}\,\boldsymbol{E}\boldsymbol{M}^{-1}\,\boldsymbol{P}^+\,\boldsymbol{C} \\ \boldsymbol{\Sigma}^\pm = \pm\frac{\tilde{\omega}_0}{4\pi}F_\odot\boldsymbol{M}^{-1}\,\boldsymbol{P}_\odot^\pm exp\left(-\frac{\tau}{\mu_\odot}\right) \end{cases} \tag{D.13}$$

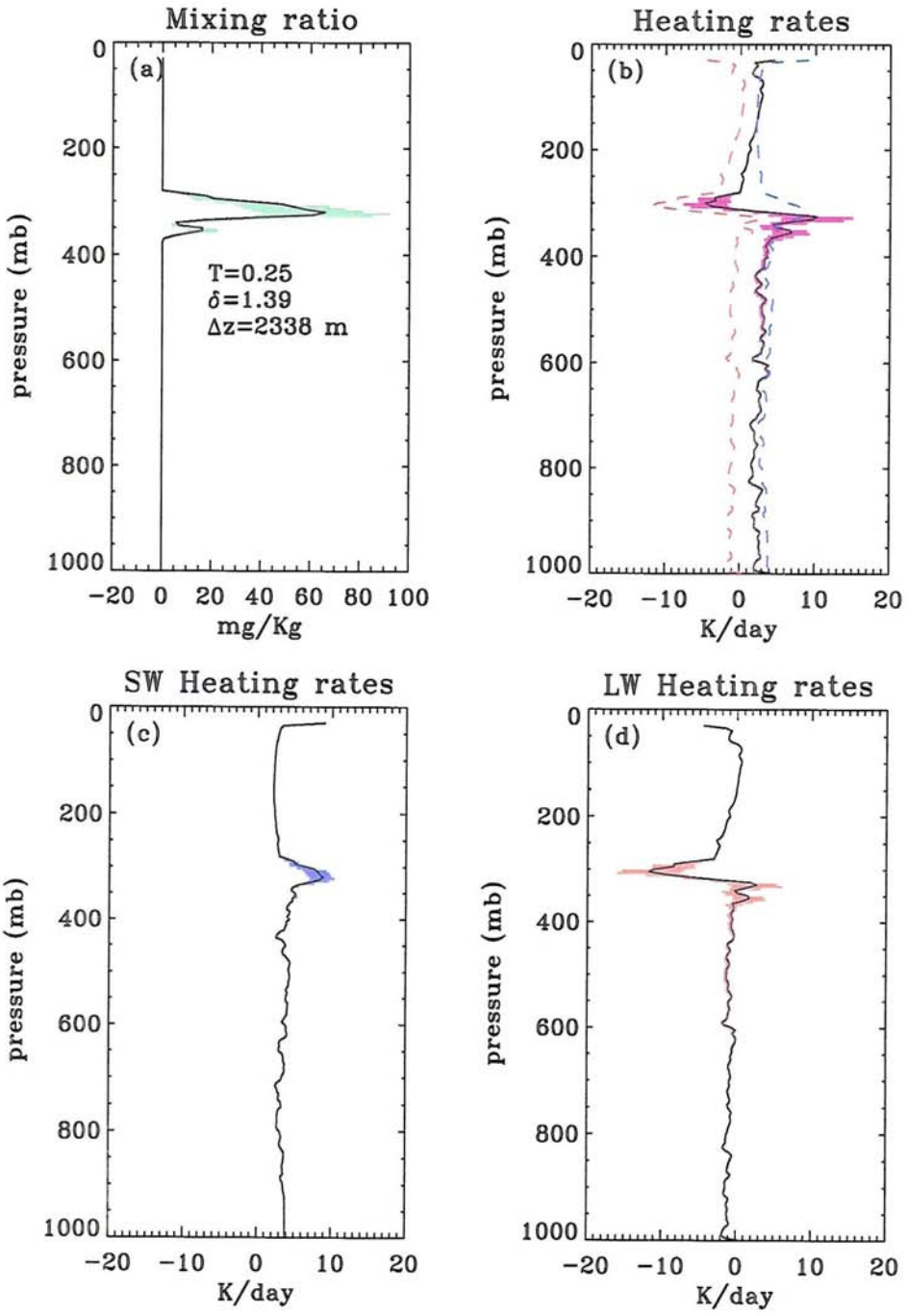

Figure 6.4: Cloudy sky heating rates and variations due to errors in mixing ratio: (a) Mixing ratio; (b) Total heating rate; (c) SW heating rate; (d) LW heating rate. In (a), cloud transmittance, optical depth and thickness are displayed. Nauru 1999/05/01 — 09:00 UTC.

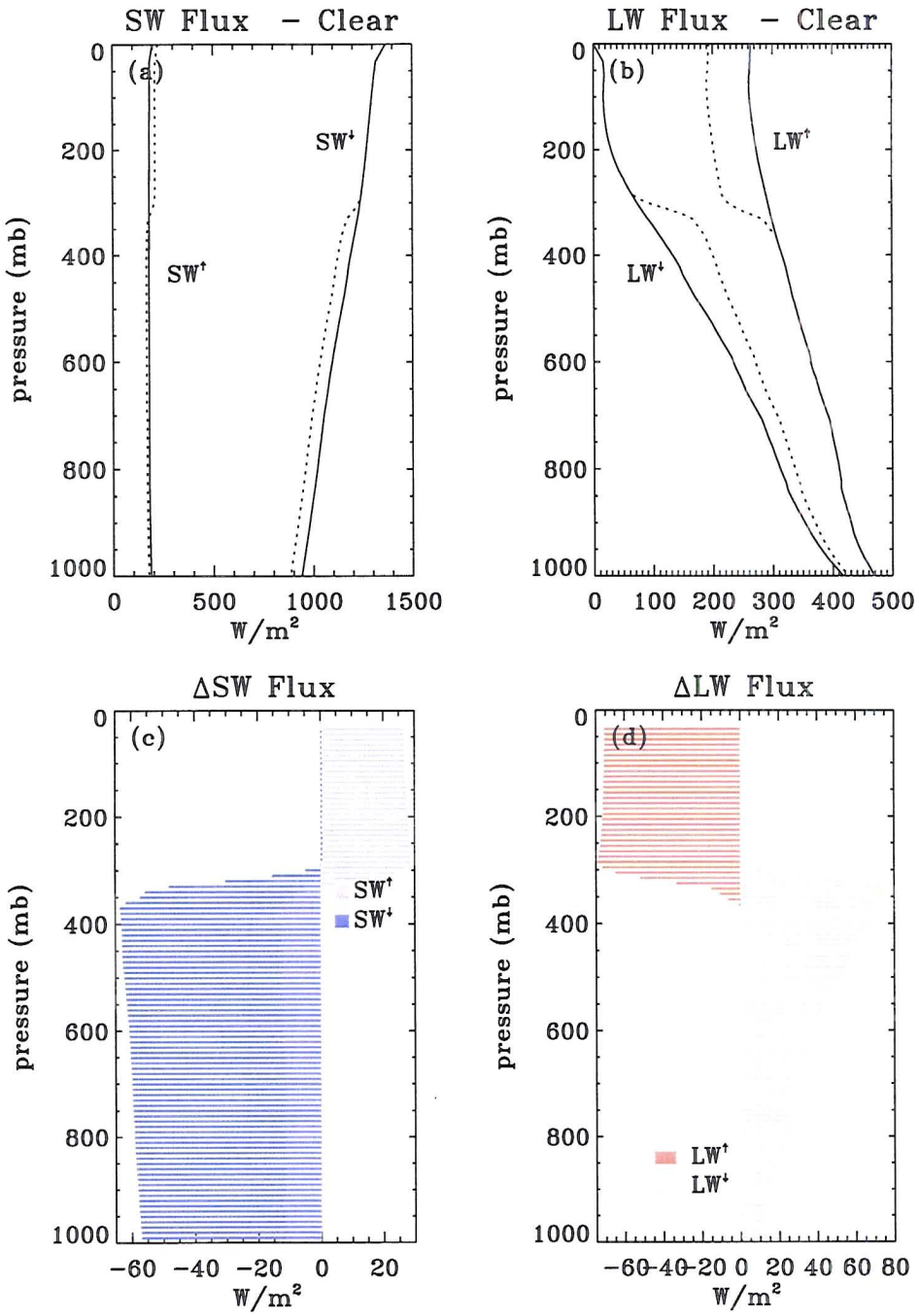

Figure 6.5: (Simulated) Clear sky computed fluxes and variations between cloudy and (simulated) clear sky: (a) SW fluxes; (b) LW fluxes; (c) ΔSW fluxes; (d) ΔLW fluxes. Nauru 1999/05/01 — 09:00 UTC.

Appendix E

Acronymns and Abbreviations

ARM - Atmospheric Radiation Measurement

BBSS - Balloon Borne Sounding System

BUGS - Beautiful General Circulation Modeling System

CPL - Cloud Physics LIDAR

CRF - cloud radiative forcing

CRM - cloud resolving model

CSU - Colorado State University

EOS - Earth Observing System

FOV - field of view

GCM - general circulation model

IDP - Instrument Development Program

IOP - intense observation period

IR, LW - infrared portion of the electromagnetic spectrum (λ = 0.7 μm - 1 mm)

IRT - IR Radiometer

ISCCP - International Satellite Cloud Climatology Project

IWC - ice water content

IWP - ice water path

LIDAR - light detection and ranging

LIRAD - LIDAR – IR Radiometer techique

LWP - liquid water path

MAS - MODIS Airborne Simulator

MMCR - Millimeter Wave Cloud RADAR

MODIS - Moderate Resolution Imaging Spectroradiometer

MPL - Micropulse LIDAR

MS - multiple scattering

MWR - Microwave Water Radiometer

NASA - National Aeronautics and Space Administration

NEΔT - noise equivalent ΔT

NOAA - National Oceanic and Atmospheric Administration

NSA - North Slope of Alaska

NWS - National Weather Service

OLR - outgoing longwave radiation

PBL - Planetary Boundary Layer

PDF - probability density function

PNG - Papua New Guinea

RL - Raman LIDAR

RADAR - radio detection and ranging

RT - radiative transfer

SAFARI - Southern Africa land–atmosphere experiment

SGP - Southern Great Plains

SNR - signal to noise ratio

SST - sea surface temperature

TOA - top of the atmosphere

TOGA - Tropical Ocean Global Atmosphere

TWP - Tropical West Pacific

TRMM - Tropical Rainfall Measuring Mission

VIS, SW - visible portion of the electromagnetic spectrum (λ = 0.4 - 0.7 μm)

UTC - universal time convention

and we used the notation:

$$\begin{cases} \boldsymbol{I}^{\pm}(\tau) = \begin{pmatrix} I(\tau, \pm\mu_1) \\ \vdots \\ I(\tau, \pm\mu_n) \end{pmatrix} \quad , \quad \boldsymbol{P}_{\odot}^{\pm} = \begin{pmatrix} P(\pm\mu_1, -\mu_{\odot}) \\ \vdots \\ P(\pm\mu_n, -\mu_{\odot}) \end{pmatrix} \\ \boldsymbol{P}^{\pm} = \begin{pmatrix} P(\pm\mu_1, \mu_1) & P(\pm\mu_1, \mu_n) \\ \vdots & \vdots \\ P(\pm\mu_n, \mu_1) & P(\pm\mu_n, \mu_n) \end{pmatrix} \quad , \quad P(\mu_i, \mu_j) = \sum_0^{2N-2} \chi_l P_l(\mu_i) P_l(\mu_j) \\ \boldsymbol{C} = \begin{pmatrix} w_1 & \dots & 0 \\ 0 & \ddots & 0 \\ 0 & \dots & w_n \end{pmatrix} \quad , \quad \boldsymbol{M} = \begin{pmatrix} \mu_1 & \dots & 0 \\ 0 & \ddots & 0 \\ 0 & \dots & \mu_n \end{pmatrix} \end{cases} \tag{D.14}$$

By integrating equation D.12 we can write the radiances at the top and bottom of a layer in the form:

$$\begin{cases} \boldsymbol{I}^{+}(\tau_1) = \boldsymbol{R}\boldsymbol{I}^{-}(\tau_1) + \boldsymbol{T}^{\star}\boldsymbol{I}^{+}(\tau_2) - \boldsymbol{\Sigma}^{+} \\ \boldsymbol{I}^{-}(\tau_2) = \boldsymbol{T}\boldsymbol{I}^{-}(\tau_1) + \boldsymbol{R}^{\star}\boldsymbol{I}^{+}(\tau_2) + \boldsymbol{\Sigma}^{-} \end{cases} \tag{D.15}$$

with $\boldsymbol{T}^{\star} = \boldsymbol{T} = (\boldsymbol{1} - \boldsymbol{t}\, d\tau)$, $\boldsymbol{R} = \boldsymbol{R}^{\star} = \boldsymbol{r}\, d\tau$, $\boldsymbol{\Sigma}^{\pm} = \boldsymbol{\Sigma}^{\pm} d\tau$. If we now add another layer, we expect that the combined equation for these two layers seen as one to be the same; therefore for two layers the combined parameters are:

$$\begin{cases} \boldsymbol{T} = \boldsymbol{T}_2(\boldsymbol{I} - \boldsymbol{R}_1^{\star}\boldsymbol{R}_2)^{-1}\boldsymbol{T}_1 \\ \boldsymbol{T}^{\star} = \boldsymbol{T}_1^{\star}(\boldsymbol{I} - \boldsymbol{R}_2\boldsymbol{R}_1^{\star})^{-1}\boldsymbol{T}_2^{\star} \\ \boldsymbol{R}^{\star} = \boldsymbol{R}_2^{\star} + \boldsymbol{T}_2(\boldsymbol{I} - \boldsymbol{R}_1^{\star}\boldsymbol{R}_2)^{-1}\boldsymbol{R}_1^{\star}\boldsymbol{T}_2^{\star} \\ \boldsymbol{R} = \boldsymbol{R}_1 + \boldsymbol{T}_1^{\star}(\boldsymbol{I} - \boldsymbol{R}_2\boldsymbol{R}_1^{\star})^{-1}\boldsymbol{R}_2\boldsymbol{T}_1 \\ \boldsymbol{\Sigma}^{-} = \boldsymbol{\Sigma}_2^{-} + \boldsymbol{T}_2(\boldsymbol{I} - \boldsymbol{R}_1^{\star}\boldsymbol{R}_2)^{-1}\boldsymbol{R}_1^{\star}\boldsymbol{\Sigma}_2^{+} \\ \boldsymbol{\Sigma}^{+} = \boldsymbol{\Sigma}_1^{+} + \boldsymbol{T}_1^{\star}(\boldsymbol{I} - \boldsymbol{R}_2\boldsymbol{R}_1^{\star})^{-1}\boldsymbol{R}_2\boldsymbol{\Sigma}_1^{-} \end{cases} \tag{D.16}$$

The above equations (D.15 and D.16) represent the basis for our RT model. The computed radiances can be further used to estimate the heating rates for a specific layer while the global reflection and transmission coefficients give some idea about the optical properties of the atmosphere.

This page intentionally blank.